The Dissertation Committee for Gilliss McNaughton Dyer
certifies that this is the approved version of the following dissertation:

# Experimental Study of the Equation of State of Isochorically Heated Warm Dense Matter

Committee:

Todd Ditmire, Supervisor

Manfred Fink

Michael Downer

Charles Chiu

J. Craig Wheeler

# Experimental Study of the Equation of State of Isochorically Heated Warm Dense Matter

by

**Gilliss McNaughton Dyer, BA Math; BA Physics**

**Dissertation**

Presented to the Faculty of the Graduate School of

The University of Texas at Austin

in Partial Fulfillment

of the Requirements

for the Degree of

**Doctor of Philosophy**

**The University of Texas at Austin**

August 2007

# Acknowledgments

There are many people without whom I can't imagine completing this work.

Above all, my parents, Michael and Charlene Dyer have been an inexhaustible source of emotional support and sound advice throughout the years. They are the best role models I could have asked for and they laid the foundation for the person I am today. My exceptional, close-knit extended family has also contributed to my positive outlook on life, and so I would like to acknowledge them as well.

My original office mates, Aaron, Will, and Greg helped me in countless ways throughout the many years that we were together. To get along so well with my office mates was truly a blessing. With them, I always felt as part of a team, and each of them was always willing to lend a hand, be a friend, or think over a tough problem with me. Along these same lines, I would like to thank Aaron Bernstein, who came along much later in my graduate career, but definitely provided the same kind of support to help me get through the final stretch. Many others in our research group, past and present, have also helped make my time here special.

I am very grateful to my collaborators and supporters at LLNL, especially Ronnie Shepherd, who provided me with the resources and expertise I needed to complete my research.

Finally, I want to thank my adviser, Todd Ditmire. His energy, intuition, and enthusiasm have always amazed and inspired me. He has worked tirelessly to provide the resources I've needed to complete my research, and to put me in a

position to succeed. Furthermore, his words of encouragement have always seemed to come at exactly the right time.

Gilliss McNaughton Dyer

*The University of Texas at Austin*
*August 2007*

# Experimental Study of the Equation of State of Isochorically Heated Warm Dense Matter

Publication No. ____________________

Gilliss McNaughton Dyer, Ph.D.
The University of Texas at Austin, 2007

Supervisor: Todd Ditmire

We have performed a series of experiments developing the techniques of volumetric, isochoric heating of matter to high energy density states, and the subsequent probing of the release isentrope. Using ultrafast, ultra intense laser systems with pulse lengths from 100fs - 1ps and pulse energies between 2 J and 100 J, we generated strong secondary radiation, in the form of $K_\alpha$ x-rays and directed proton beams, which we used to rapidly heat a foil sample to temperatures from $\sim 1$ eV to $\sim 25$ eV at solid density, thus entering the strongly coupled, partially ionized regime of warm dense matter, in which the equation of state is poorly understood. The first set of experiments examines the possibility of using laser generated $K_\alpha$ x-rays in isochoric heating experiments and concludes that this technique will require the use of higher energies and higher Z materials than were used in this thesis to achieve warm dense matter conditions. In the second set of experiments, we used an ultrafast, laser-generated proton beam with a temperature of $\sim 2$ MeV and cutoff energy of $\sim 40$ MeV to volumetrically and isochorically heat a sample foil to $> 20$ eV. With single-shot diagnostics, we measured the evolution of the temperature with 3.3 ps resolution over the first 35 ps of expansion by streaked optical pyrometry, and measured the evolution of the target expansion over the same timescale with sub-ps resolution by chirped pulse interferometry. In this way we were able to verify the equation of state and ion-balance in the SESAME equation of state tables with a Saha ionization model and distinguish this as more accurate than other, simpler models. This thesis establishes an experimental framework for acquiring equation of state data in the regime of warm dense matter that is distinct and complimentary to that acquired by the techniques of shock heating.

# Contents

# Chapter 1

# Introduction

Over the history of mankind, our sun has been the source of virtually all of the energy that has allowed us to survive and thrive on this earth. All life depends on it. Fossil fuels, the energy source upon which modern society thrives, represent millions of years of stored energy originating from that one giant fusion reactor in our sky. Although we will continue to rely primarily on the sun for energy for the foreseeable future, it is natural to strive towards generating our own energy through the same high-yield proccesses of nuclear fusion occurring there. Fusion is potentially a very bountiful source of energy, but only if it can be harnessed efficiently. In our sun and the billions of stars in the universe, gravity does the work of confining the star's fuel and generating the conditions needed for fusion, and they burn perpetually and automatically thanks to their incredible mass, which we can't hope to match.

Our advantage lies in the ability to set things up in a deliberate and calculated way, substituting precision for brute force. Along the promising avenue of inertial confinement fusion [LMC92], we find the need to understand and be able to model in great detail the collective behaviour of hot and compressed states of matter like those found deep within the stars [CB97]. This is the domain of the emerging field of high energy density physics [CoHEDPP03].

Within the field of high energy density physics lies a particularly difficult and relevant regime of density and temperature that is the target of this thesis. This regime, known as warm dense matter [LMHK+03], lies at the frontiers of plasma and condensed matter physics, where neither perfectly applies and our model for the way matter behaves must transition between these two very different descriptions. Warm dense matter is likewise out of reach from the theory of extremely dense matter, as well as the theory of partially ionized, sparse gases. Hence the problem is that warm dense matter lies in the middle of things: these four classes of theories, which are built on the extremes of density and temperature, converge awkwardly there. As a result, the equation of state - which represents the most basic and fundamental information about the material and how it interacts with its surroundings - is uncertain under WDM conditions, even for elemental materials.

Warm dense matter is generally associated with temperatures between ∼1 and 100 eV and densities from ∼.1 to 10 × solid density. The compression of a fuel pellet to the point of nuclear ignition follows a $(\rho, T)$ path that passes straight through the warm dense matter region. Likewise, the formation of stars [CB97] and giant planets [HUB81] will also involve matter at these densities and temperature. One cannot confidently model these phenomenon without first having confidence in the equation of state models.

With its characteristic complexity, theoretical advances into warm dense matter will require the verification and guideance of experimental data. Major advances in the technology of delivering massive amounts of energy to a small volume in a small amount of time, specifically pulsed electrical power technology [SYN+06] and the technology of high-power pulsed lasers [SM85, SMV+96], are making the creation and diagnostic of warm dense matter states a reality.

## 1.1 Plan for this thesis

This thesis describes an experimental campaign to produce warm dense matter through isochoric (constant density) heating of solid matter by secondary radiation sources generated by ultrashort pulsed lasers. The next chapter gives an overview of warm dense matter, including the various methods of producing and characterizing WDM experimentally. In the next chapter I will discuss our experimental tool, the sub-ps, multi-Joule CPA laser and the various laser facilities at which we've performed our experiments. This is followed by a detailed discussion of the various laser

# Chapter 2

# Warm dense matter

The term “warm dense matter” (WDM) was introduced about a decade ago [Ng:02] to draw attention to the importance of this regime in the context of our ever-increasing desire to produce highly accurate and complete models of complex systems.

## 2.1 WDM in classical plasma physics

Plasma physics is the physics of interacting, unbound, charged particles. There are three fundamental quantities of plasma physics describing where the basic rules of plasma physics apply. First, there is the characteristic length scale known as the Debye length[1]:

$$\lambda_D = \sqrt{\frac{kT}{4\pi n_e e^2}}, \tag{2.1}$$

---

[1] Note cgs units; for SI, we would have $e^2 \rightarrow 4\pi e^2/\epsilon$

where $kT$ is the plasma thermal energy, $n_e$ is the electron density[2], and $e$ is the fundamental charge. The Debye length describes the length over which the individual coulomb potential of a single particle is screened by the other components in a plasma. It is above this length scale that we see the collective behavior that plasma physics is designed to handle; conventional plasmas deal with systems with dimensions much longer than this length scale.

Next, we have the characteristic frequency, the plasma frequency:

$$\omega_p = \sqrt{\frac{4\pi n_e e^2}{m_e}}, \tag{2.2}$$

which defines the timescale over which the plasma can respond to external changes to the electric field; conventional plasma physics deals with effects on timescales longer than $1/\omega_p$.

Finally, there is the coupling parameter, defined as the ratio of the interatomic potential energy to the thermal energy, which for a one component classical plasma has the form:

$$\Gamma = \frac{Z^2 e^2}{r_0 kT} \tag{2.3}$$

Here, $Z$ is the atomic number of the constituent atom, and $r_0$ is the average interparticle distance:

$$r_0 = \left(\frac{4}{3}\pi n_e\right)^{-1/3}. \tag{2.4}$$

We see that $\Gamma$ is related to the number of particles within a Debye length of

---

[2] The Debye length and plasma frequency have equivalent definitions for the ions, but the fast motion of the electrons makes them more significant in screening effects, and so we're usually referring to electrons with these two quantities.

a given particle:

$$\left(\frac{\Gamma}{Z^2}\right)^{-3/2} = (4\pi n_e \lambda_D^3) \equiv \Lambda. \tag{2.5}$$

This commonly used fundamental plasma quantity $\Lambda$, the so-called plasma parameter, is the number of particles in a "Debye sphere". The fundamental rules of plasma physics are based on the assumption that

$$\Gamma \ll 1; \qquad \Lambda \gg 1. \tag{2.6}$$

When this assumption begins to break down, we are forced to consider more and more complex interactions of the constituent atoms. The approach for cold gases in statistical mechanics[Hua87][3] is to form a *cluster expansion*, in which the $k^{\text{th}}$ term groups together the effects of every combination of $k$ interacting particles, from 1 to $\infty$. This can then be used to form the *virial expansion*, in which the pressure divided by the temperature, $P/kT$, is expanded in powers of the density $n$, with the zero$^{\text{th}}$ order term recovering the ideal gas law, $P/kT = n$. In ionized plasmas, this approach doesn't work exactly as formulated for cold statistical mechanics, because of complications brought on by the long range of the coulomb force and, in the case of strongly coupled plasmas, electron degeneracy. However, the framework described below does form a starting point for theories [Abe59] that address the complexities of interactions in a dense plasma.

### 2.1.1 Classical cluster expansion

The ideal gas equation of state does not take into account interactions between particles, except inasmuch as they bring about thermal equilibrium. The approach of the classical cluster expansion is to take the Hamiltonian for free particles and

---

[3] Much of the following description of the cluster and virial expansions in the next section come from this reference.

add in the interaction potentials $v_{ij}$ between each of the particles:

$$\mathscr{H} \quad = \quad \sum_{i=1}^{N} \frac{p_i^2}{2m} + \sum_{i<j} \mathsf{v}_{\mathsf{ij}} \tag{2.7}$$

From the Hamiltonian is derived the gand partition function:

$$\mathscr{Q}(z,V,T) \quad = \quad \sum_{N=0}^{\infty} \left(\frac{z}{\lambda^3}\right)^N \frac{\mathsf{Z}_N(V,T)}{N!}; \tag{2.8}$$

where

$$\mathsf{Z}_N(V,T) \quad \equiv \quad \int d^3r_1 \cdots d^3r_N \exp\left(-\beta \sum_{i<j} \mathsf{v}_{ij}\right), \tag{2.9}$$

and $T$ is the temperature, $\beta = 1/kT$, $r_i$ is the position of the $i^{\text{th}}$ particle, $\lambda = \sqrt{2\pi\hbar^2/mkT}$, $z = e^{\beta\mu}$ is the fugacity ($\mu$ being the chemical potential), $V$ is the volume of the system, $N$ is the total number of particles in the system, and $\mathsf{v}_{ij}$ is the potential between the $i^{\text{th}}$ and $j^{\text{th}}$ particles. Graph theory is applied to this problem to eventually lead us to the expression [Hua87, May77]:

$$\frac{1}{V} \log \mathscr{Q}(z,V,T) \quad = \quad \frac{1}{\lambda^3} \sum_{l=1}^{\infty} b_l z^l, \tag{2.10}$$

where the dimensionless $b_l$ term represents a sum of integrals representing all possible clusters of $l$ interacting particles, e.g. [May77]:

$$b_1 \quad = \quad \frac{1}{V} \int d^3r = 1; \tag{2.11}$$

$$b_2 \quad = \quad \frac{1}{2\lambda^3 V} \iint d\mathbf{r}_1 d\mathbf{r}_2 f_{12}(r_{12}) = \frac{2\pi}{\lambda^3} \int_0^{\infty} dr f(r) r^2, \tag{2.12}$$

$$b_3 \quad = \quad \frac{1}{6\lambda^6 V} \iiint d\mathbf{r}_1 \mathbf{r}_2 d\mathbf{r}_3 (f_{31}f_{21} + f_{32}f_{31} + f_{32}f_{21} + f_{32}f_{31}f_{21})$$

where

$$f_{ij} \equiv e^{-\beta \mathsf{v}_{ij}} - 1. \tag{2.13}$$

In this way we have an expansion where each term represents higher and higher degrees of coupling between the constituents. State variables are obtained directly from the grand partition function:

$$\frac{P}{kT} = \frac{1}{\lambda^3} \sum_{l=1}^{\infty} b_l z^l \tag{2.14}$$

$$n = \frac{1}{\lambda^3} \sum_{l=1}^{\infty} l b_l z^l, \tag{2.15}$$

This is known as the cluster expansion for the EOS. Notice that we recover the ideal gas relation $\frac{P}{kT} = n$ by taking only the first term in these expansions, since then (2.14) and (2.15) are equal. If we take the term-wise[4] limit $V \to \infty$ (with $n$ held constant),

$$B_l(T) \equiv \lim_{V \to \infty} b_l(V, T), \tag{2.16}$$

then, with the assumption of a sufficiently dilute gas, we can put these equations together to expand the pressure in powers of the density $n$:

$$\frac{P}{nkT} = \sum_{l=1}^{\infty} a_l(T) \left(n\lambda^3\right)^{l-1}, \tag{2.17}$$

where $a_l$ is the $l^{\text{th}}$ *virial coefficient.* They are obtained by substituting (2.17) into (2.14) and (2.15), with $(b \to B)$, under the condition that it be true for all $z$. The

---

[4] It turns out that this destroys information about phase transitions.

first few virial coefficients are then:

$$\begin{aligned} a_1 &= B_1 = 1 \\ a_2 &= -B_2 \\ a_3 &= 4B_2^2 - 2B_3 \\ a_4 &= -20B_2^3 + 18B_2B_3 - 3B_4 \cdots \end{aligned}$$

Here we see more explicitly that by taking only the first term we recover the ideal gas EOS. For unionized cold gas, it's common to use the hard sphere potential:

$$\mathsf{v}_{ij}^{\mathrm{HS}}(r) = \begin{cases} +\infty, & r < a; \\ 0, & r \geq a, \end{cases} \tag{2.18}$$

where $a$ is the sphere radius. This easily gives us the next term in the virial expansion:

$$\begin{aligned} \frac{P}{nkT} &= 1 - n\lambda^3 \left\{ \frac{2\pi}{\lambda^3} \int_0^\infty dr \left( e^{-\beta \mathsf{v}^{\mathrm{HS}}(r)} - 1 \right) r^2 \right\} \\ &= 1 - n\lambda^3 \left\{ \frac{2\pi}{\lambda^3} \int_0^a dr (-1) r^2 \right\} \\ &= 1 + \frac{2}{3} a^3 n\pi. \end{aligned} \tag{2.19}$$

The the correction term is thus proportional to the ratio of the volume taken up by the atom to the Winger-Seitz volume, $1/n$, and it adds to the pressure.

For fully ionized plasma, the picture is somewhat complicated by the long-range coulomb field. Attractive forces between the electrons and ions tend to *reduce* the pressure relative to that of the ideal gas. One way to deal with this is to use the screened coulomb potential[5] with a finite, repulsive core radius [May77]:

$$\mathsf{v}_{ab} = \begin{cases} Z_a Z_b e^2 \exp(-r/\lambda_D)/r & (r > r_0) \\ \infty & (r \leq r_0) \end{cases} \tag{2.20}$$

where $Z$ is the atomic number, $e$ is the fundamental charge, $Z_a$ and $Z_b$ are the magnitudes of charge of the two species, and $\lambda_D$ is the Debye length (2.1) with $n_e \to n_e + Zn_i = 2n_e$. Here the Debye length expresses itself explicitly as a screening term for long range interactions, and the ion radius $r_0$ prevents the electron-ion contribution from diverging[6] at $r = 0$. With the lowest-order correction [May77], the pressure expression is:

$$\begin{aligned} \frac{P}{n_i kT} &= 1 - (24\pi)^{-1} \lambda_D^{-3} n_i^{-1} \\ &= 1 - (24\pi)^{-1} \left(8\pi\beta e^2 Z\right)^{3/2} n_i^{1/2} \end{aligned} \tag{2.21}$$

The methods of the cluster expansion are used in many treatments of dense, cooler plasmas [RD73, Ich82]. As $\Gamma$ approaches and exceeds 1, various renormalizations become important [Tra83], and calculation of the equation of state becomes more and more complex. In particular, higher order terms, ionization balance and electron degeneracy play a prominent role [IIT87, May77, Abe59, RD73].

## 2.2 WDM in condensed matter physics

In condensed matter physics, strong coupling is the cornerstone rather than the complication. Atomic energy levels are pushed together to form energy bands, which electrons fill subject to Pauli exclusion much like they fill the energy levels in a single atom, except that the energy levels no longer appear as discrete [Mar00]. Even at

---

[5] Also known as the Debye-Hückel or Yukawa potential.

[6] Properly, the electrons should be treated quantum mechanically to avoid this

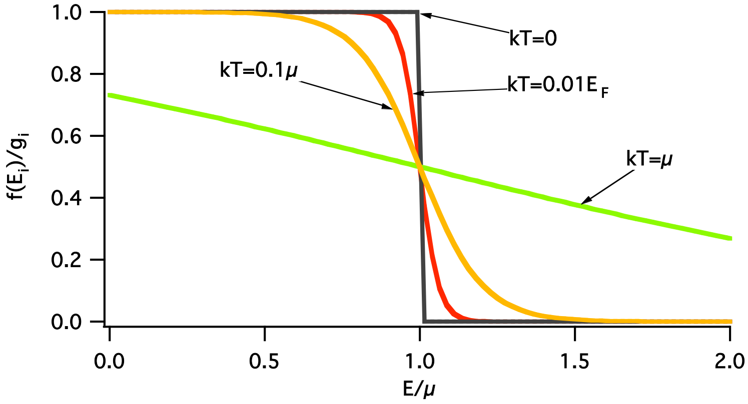

Figure 2.1: The Fermi-Dirac distribution function at various temperatures. For $kT \ll E_F$, $\mu \approx E_F$.

$T = 0$, the electrons fill the energy bands up to the Fermi energy:

$$E_F \quad = \quad \frac{\hbar^2}{2m}\left(3\pi^2 n_2\right)^{2/3}. \tag{2.22}$$

For a crystal, this is far above the thermal energy of the electrons, and so the distribution, described by Fermi-Dirac statistics (figure 2.1),

$$f(E) \quad = \quad \frac{g_i}{1+e^{\beta(E_i-\mu)}}, \tag{2.23}$$

looks very similar to the zero temperature case (where $\mu = E_F$) at moderate temperatures, meaning that only a small range of additional bands need to be considered. Furthermore, electrons at energies well below $E_F - kT$ have nowhere to go, much like inner-shell electrons in an atom. Hence their presence contributes to the screened potential experienced by the outer electrons and have a very simple relationship to the overall equation of state. The zero temperature isotherms in a crystal are calculated to high accuracy [MR79]. As temperatures increase, more and more energy bands need to be taken into account, both above and below the Fermi

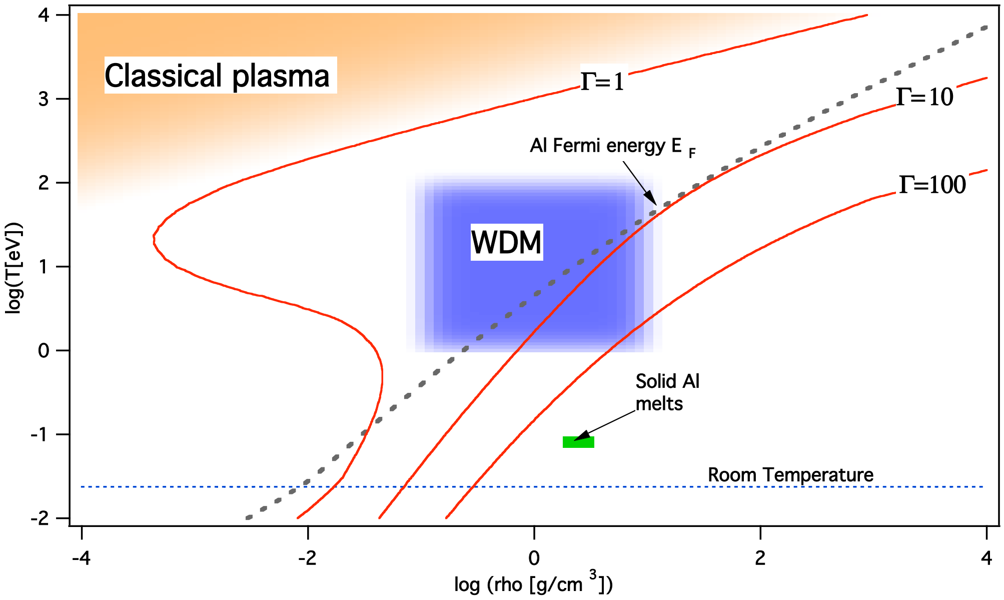

Figure 2.2: Placement of the warm dense matter in $(\rho, T)$ space in relation to various values of the plasma $\Gamma$ (2.3), the melting point, and the Fermi temperature (2.22).

energy. Reasonably accurate equations of state up to $10 \times T_{\text{melt}}$ can be produced by techniques that involve keeping track of the entropy $\Delta S$ relative to the zero temperature state [Gro71], but these approximations break down at around this point, which is still substantially below the Fermi energy.

Figure 2.2 puts warm dense matter in context with contours of constant plasma gamma, and with the Fermi and melt temperatures, for Al.

## 2.3 Sesame EOS tables

The rigorous construction of the SESAME EOS [Tra83, Hol84, Mon84] represented a monumental effort in connecting disparate EOS models, with the greatest amount of uncertainty occurring in the area which we now refer to as warm dense matter. Figure 2.3 lays out these models on a $(\rho, T)$ plot to show the limits of their applicability. This rigorous construction requires great effort and thus is not used for the

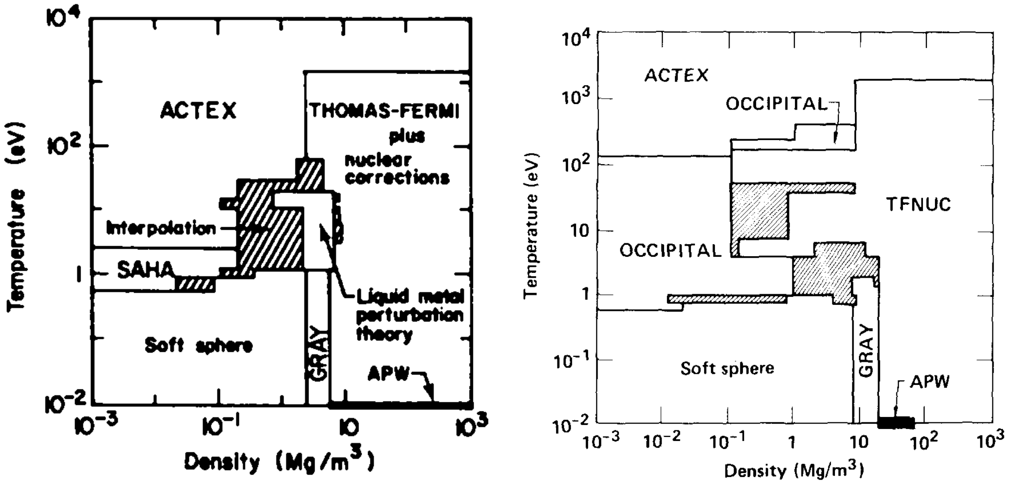

Figure 2.3: Diagram of the construction of SESAME tables for Al [Hol84, Mon84] (left) and Cu [Tra83] (right), showing ranges of applicability for constituent EOS models in the $(\rho, T)$ plane. The coverage shows the models at their absolute limits of applicability, and the crosshatched region indicates where no model applies at all. Plots are from the references.

construction of every material EOS in the SESAME database, but it is the technique applied to the more important materials. The models used in the Al expansion are as follows [Mon84]:

- **ACTEX** [RY97] The many body **act**ivity **ex**pansion method starts with a cluster expansion of the grand partition function as described above (but including spin by $z \to (2s+1)z$). In the most complete case, where needed, ACTEX takes into account quantum mechanical degeneracy effects. Because of the complexity of quantum effects, ACTEX approaches degeneracy by first determining the classical equations of a strongly coupled plasma and then inserting quantum mechanical terms to prevent the expansions from diverging where degeneracy becomes important [Rog00]. The theory is exact in the limit of high temperature, low density plasmas. The general case requires renormalizations to account for atoms that aren't fully ionized, coupling of these species to the plasma, and the strong coupling of high Z ions. The potentials are a combination of a long range term and a exponentially screened Coulomb potentials [Tra83]. The perturbation breaks down for high densities and low temperatures, as depicted in figure 2.3.

The ACTEX method has ambitions of reaching further into the dense, cool regime of EOS. However, it may have overreached slightly in attempting to mesh with a famous laser-driven shock experiment in deuterium [CDSC$^+$98], which predicted vastly greater shock compressibility in warm dense deuterium than was predicted by standard Sesame equation of state near 1 Mbar. Extending beyond its normal reach down to about 2 Mbar and $1 g/cm^3$, ACTEX seemed to show agreement with this trend, bending to the higher shock compression densities as it approached the lower pressures [Rog00]. However, the implications of this experimental result on the form of the EOS have been questioned, as some evidence has shown that a much smaller modification of the EOS tables than suggested by ACTEX and the laser experimental results (section 2.5).

- **OCCIPITAL/Saha** [Rou62] As a plasma cools to the point that electrons begin recombining with atoms, modifications to the equation of state are dominated by the ionization balance. The Saha equations come from a statistical accounting of the energy levels within an atom and finding the most favorable conditions for a given temperature. Density comes into play as atoms are brought close together and free electrons begin affecting the energy levels of the individual atoms, in a proccess called continuum lowering. The potentials of the atoms are screened by the free electrons, and thus Debye-Hückel corrections to the potential are used. A Planck-Larkin partition function is used to treat the free electrons. The Saha model is complete in principle, but its precise calculation requires good knowledge and accounting of all of the available energy levels, a technique which breaks down as we approach the conditions of condensed matter, under which the Saha treatment becomes intractable and a density-of-states formalism is needed.

- **Soft sphere** [HRJ+70] A soft sphere model fills out the low density, low temperature, non-ionized corner of the SESAME construction. Thus it covers the range from ideal gases up to the freezing point, and must handle the difficult task of modelling the liquid metal stage. Much of the region is accessible to experiments, and the equations for the thermodynamic quantities involve free parameters that are adjusted to fit experimental data. Where no experimental data are available, the model must rely on Monte-Carlo simulations of several atoms (e.g. hundreds or more), using the soft sphere potential. This potential replaces the "hard sphere" described above with a potential that rises sharply, but not infinitely fast:

$$\phi(r) \quad = \quad a\left(\frac{b}{r}\right)^n, \tag{2.24}$$

  with $4 \leq n \leq 12$, where $a$ and $b$ are constants, and $r$ the interatomic distance. The soft sphere potential is repulsive, but the equation of state must also be modified to take into account van der Waals attractive forces [HSGD75].

- **GRAY** The Gray model is an amalgam of different models and empirical fits to deal with the solid-liquid region of the equation of state, around solid density, up to about 10 times the melt temperature (which is approximately the lower bound of WDM). In particular, GRAY is designed for modelling of shocks in metals, including those which cause phase transitions. From the liquid metal side, the GRAY models are closely related to the corrected soft sphere/ van der Waals model described above [Gro71]. For solids, lattice vibrations contribute strongly to the equation of state, in particular the change in the number of vibrational modes with density, described by the Grüneisen parameter.

- **Thomas-Fermi theory with nuclear corrections** At very high densities, an EOS based on the Thomas-Fermi model, in which electrons are treated as a fluid with Fermi-Dirac statistics

  $$n(\epsilon) \quad \propto \quad \frac{1}{e^{(\epsilon - eV(r) - \mu)/kT} + 1}, \tag{2.25}$$

  where $n(\epsilon)$ is the population of electrons of energy $\epsilon$, $\mu$ is the chemical potential, and $kT$ is the thermal energy. A $V(r)$ is the potential within a sphere of radius $R_0 = (3/4\pi n_i)^{1/3}$ defined around each ion and satisfying the Poisson equation. This ion sphere is taken to contain exactly one ion and has also the condition of overall charge neutrality. The ion contribution to the equation of state takes different forms, depending on the temperature, mimicking that of the GRAY model at low temperatures and that of ACTEX for higher temperatures.

- **Liquid metal perturbation theory** A generalization by Ross [Ros80] of liquid metal perturbation theory is used to handle the transition from condensed matter to fully ionized dense plasmas in the SESAME construction of Al. Therefore this theory does extend into the higher density part of what we associate with WDM. Agreement with ACTEX at their respective temperature limits is reported as $\sim 10\%$. As with any EOS in the WDM range, this approximate theory is in need of experimental verification, but it has done relatively well with shock hugoniot data, which lands on its higher density side.

These various EOS models are assembled to form SESAME by interpolation to make isotherms transition smoothly between them. We see warm dense matter as the region of vast interpolation between the applicable ranges of these most rigorous approximations. This interpolation technique can lead to numerical instabilities and a lack of thermodynamic consistency [LBC$^+$01] (see the next section). This is problematic because hydrodynamic codes [LL94]often rely on the assumption of thermodynamic consistency to change between state variables. The other problem with this approach is that it is an extremely time consuming way to fashion an EOS. The quotidian equation of state (QEOS), described in the next section, was designed with thermodynamic consistency and speed of calculation in mind, with the goal of giving good enough EOS values for "everyday" applications.

## 2.4 QEOS

The condition of thermodynamic consistency has the form:

$$\rho^2 \frac{\partial E}{\partial \rho} = p - T\frac{\partial p}{\partial T}, \tag{2.26}$$

where $E$ is the internal energy. This follow from the formulas of the Helmholtz free energy:

$$p = \rho^2 \tfrac{\partial F}{\partial \rho}, \quad S = -\tfrac{\partial F}{\partial T}, \quad E = F + TS, \tag{2.27}$$

and holds exactly for an equilibrium system [Mor91]. It is usually a good idea to check for thermodynamic consistency in the regions of interest before running a hydrodynamic code, because the code will often use thermodynamic consistency as an assumption [LL94].

QEOS [MWYZ88] ensures thermodynamic consistency by defining its EOS in terms of the Helmholtz Free energy, through (2.27) and related thermodynamic equations. It makes the usually acceptable assumption of the additivity of the

Helmholtz free energy for the various contributions:

$$F(\rho, T_e, T_i) \quad = \quad F_i(\rho, T_i) + F_e(\rho, T_e) + F_b(\rho, T_e), \tag{2.28}$$

where the subscript $i$ refers to ions and the subscript $e$ refers to electrons. Thus the pressures and internal energies are also additive. $F_b$ is a semi-empirical correction to force the pressure to zero for the solid density zero temperature state. Ionization equilibrium and electron pressure are handled entirely by Thomas-Fermi theory, e.g. [MWYZ88]:

$$\begin{aligned}
F_e &= (Z\mu - \frac{2}{3}K - U_{ee}); \\
U_{ee} &= \frac{e^2}{2}\int \frac{n(r)n(r')}{|r-r'|} d^3r d^3r'; \\
K &= \frac{1}{2\pi^2}\left(\frac{2m}{\hbar^2}\right)^{3/2}(kT)^{5/2}\int F_{3/2}\left(-\frac{\mu + eV(r)}{kT}\right) d^3r; \\
F_v(y) &= \int_0^\infty \frac{x^v dx}{1+\exp(x+y)},
\end{aligned} \tag{2.29}$$

where $V(r)$ is the self-consistent, spherically averaged potential, including the electrostatic interaction between the electrons, and everything is contained within a spherical cavity of radius $R_0 = (3/4\pi n_i)^{1/3}$.

The ions in QEOS are treated based on the theory of Cowan [CM78], which gathers together a wide variety of models depending on the region of $(\rho, T)$ space. It uses an ideal gas law for high temperatures and low densities, fluid scaling laws related to those used in the GRAY EOS incorporated in SESAME [Gro71], and several laws to deal with melting and various laws for dealing with cooler, highly condensed states. The difference between this approach and that of the SESAME construction is that the collection of EOS models collected here are designed to be scaled to fit with the various materials, rather than being reconstructed from scratch each time.

QEOS takes as input the bulk modulus and density of the solid material. The merits of QEOS are thermodynamic consistency and speed, and it has matched shock data reasonably well [MWYZ88]. It can also be tweaked to fit with experimental results that come up in the warm dense matter regime, e.g., from additional shock experiments or isochoric heating. Still some of its results are considered questionable, and the glossing over of the warm dense matter regime has been likened to "pulling a tarp over the abyss" [LBC$^+$01].

## 2.5 Quantum Molecular Dynamics

Quantum molecular dynamics (QMD) is a heavily computational first principles theory, treating quantum effects for both electrons and the dynamics of atoms and molecules through time-dependent approaches to the Schrödinger equation [GG02]. Current limitations are largely set by the available computing power, with temperatures up to 10 eV being the current limit of applicability in temperature [CM06].

One apparent success of the method was a possible explanation for discrepancies between deuterium shock experiments accessing similar pressure regimes, the first being a famous result on the Nova petawatt laser [CDSC$^+$98], and the other a result from the Sandia Z-machine [KHB$^+$04]. The former experiment appeared to contradict greatly the accepted SESAME EOS of deuterium for compressibility in the warm dense matter regime, as mentioned above. QMD simulations which followed failed to reproduce these experimental results [LBKC00, Des03], instead agreeing closely with the original SESAME predictions. The later experiment showed compressibility more closely matching that of the QMD calculations and the original SESAME EOS, and upon further consideration and calculation it was proposed [GG02] that the discrepancy between the two experiments could be explained by non-adiabatic processes, meaning that the laser shock experiment may not have been driving an equilibrium EOS, and thus the data did not reflect a need to alter the equilibrium EOS. In fact, QMD simulations were apparently able to reproduce the Nova experiment more closely by better reproducing the initial conditions [GG02]. Deuterium shock compressibility remains a controversy in need of more experimental data.

## 2.6 Laboratory preparations of WDM

Interest in measuring WDM states is growing as experimental capabilities improve. A few techniques have been used to achieve and measure warm dense matter conditions, albeit in limited ranges.

### 2.6.1 Shock heating

The most well-developed method of measuring the equation of state material is through shock heating [ZR66]. A shock is a traveling discontinuity in the state variables, such as would be produced by a piston driving a gas above the sound speed: material before the shock wave is at the ambient pressure and density $p_0$ and $\rho_0$, and a rapid change occurs as the shock front passes over, taking the system to the final pressure and density $p_1$, $\rho_1$. The harder the shock, the higher the final pressure, and the equation of state determines the locus of points in $(p, \rho)$ space that are accessible from a given starting point $(p_0, \rho_0)$ a curve known as the principal Hugoniot. The state variables are subject to conservation laws[7]:

$$\begin{aligned} \rho_1 u_1 &= \rho_0 u_0 \\ p_1 + \rho_1 u_1^2 &= p_0 + \rho_0 u_0^2 \\ e_1 + \frac{p_1}{\rho_1} + \frac{1}{2}u_1^2 &= e_0 + \frac{p_0}{\rho_0} + \frac{1}{2}u_0^2, \end{aligned} \tag{2.30}$$

---

[7] Here and in the rest of the chapter we are using $\rho$ as the particle density, rather than the mass density.

where $e$ is internal energy density, expressing conservation of mass, momentum, and energy across the shock. Putting these together, the Hugoniot is described by the Rankine-Hugoniot equation:

$$e_1 - e_0 + \frac{1}{2}(V_1 - V_0)(p_1 + p_0) = 0. \tag{2.31}$$

One shock experiment gives one point on a Hugoniot. The most direct method of measuring the hugoniot is to drive a shock the material with a plate of the same material, measuring the shock velocity $u_s$ by the travel time across the shocked material, and the driver velocity $u_p$ as $\frac{1}{2}$ the final fluid velocity of the shocked material [Dra06]. Then:

$$p_1 - p_0 = \rho_0 u_s u_p \tag{2.32}$$

$$\frac{\rho_1}{\rho_0} = \frac{u_s}{u_s - u_p} \tag{2.33}$$

Very high pressures ($> 1Mbar$) can be obtained in flyer plate shock experiments with magnetically launched flier plates from Sandia's Z-machine [KHB+04]. Alternatively, shocks can be driven with a flier plate of a different material, or by laser ablation, in which case a reference material with a well-known EOS (e.g. Al) is needed to compare the propagation of shockwaves between the known material and the material to be measured, through a technique known as impedance matching [Dra06]. Velocities are typically measured with an optical streak camera diagnostic known as a VISAR [Hem79]. Off-Hugoniot data can be achieved with some experimental difficulty using double or triple shocks (reaching higher densities), or using a less-dense version of the starting material, such as a foam.

### 2.6.2 Static compression

Shockless, (quasi-) isentropic compression [RM06] of materials gives a different set of EOS data from shock experiments, towards higher densities than the Hugoniot [RM06]. Isentropic and quasi-isentropic compression is achieved in various ways, including the use of a density gradient in a flyer-plate type experiment, pulsed power magnetic compression [DDK+05], and diamond anvil cells with auxiliary heating.

### 2.6.3 Ultrafast isochoric heating

Isochoric heating (heating at constant volume/density) is the technique of this thesis. Because of the extreme pressures involved, warm dense matter cannot be contained forcibly at a constant density by any means available to us. Thus isochoric heating entails delivering the energy of heating (without shocks) on a timescale faster than the hydrodynamic expansion of the material. Very roughly, this entails:

$$\delta t \ll \frac{d}{c_s}, \tag{2.34}$$

where $\delta t$ is the time over which energy is deposited, $d$ is the thickness of the material sample, and $c_s$ is the sound speed in the heated material. For the >Mbar pressures of WDM, this entails an extremely fast $\delta t \sim 1$ ps for $d \sim 5\ \mu m$ . Leaving for the following chapters the mechanism by which we achieve this heating, let us observe the relationship between the response of an isochorically heated sample and its equation of state.

**Probing the release isentrope**

Consider a uniformly heated flat slab of warm dense matter that is allowed to expand freely into vacuum. Starting from the continuity equations [ZR66]:

$$\begin{aligned}\frac{\partial\rho}{\partial t}+\frac{\partial}{\partial x}(\rho u) &= 0 &(2.35)\\ \frac{\partial u}{\partial t}+u\frac{\partial u}{\partial x} &= -\frac{1}{\rho}\frac{\partial p}{\partial x}, &(2.36)\end{aligned}$$

we apply the condition of isentropic flow:

$$\left.\frac{\partial p}{\partial x}\right|_S = \frac{\partial p}{\partial \rho}\left.\frac{\partial \rho}{\partial x}\right|_S \equiv c_s^2\frac{\partial\rho}{\partial x}, \tag{2.37}$$

where $c_s$ is again the sound speed. This leads to:

$$\frac{\partial u}{\partial t}+u\frac{\partial u}{\partial x} = -c_s^2(p,\rho)\frac{1}{\rho}\frac{\partial \rho}{\partial x}. \tag{2.38}$$

Because the material is expanding into vacuum, and at temperatures $< 1000eV$ the energy lost to photon emission is not significant [Mor91], we consider the release of our isochorically heated slab to be isentropic. On the timescale defined by (2.34), the expansion is self-similar [FRS04]. Therefore we can express the expansion interms of $\xi \equiv x/t$: setting $\rho = f(\xi)$ and $u = g(\xi)$, substitution into (2.35) and (2.38) then gives :

$$\begin{aligned}f'(g-\xi)+fg' &= 0; &(2.39)\\ g'(g-\xi)+c_s^2\frac{f'}{f} &= 0. &(2.40)\end{aligned}$$

where a prime (') indicates derivative with respect to $\xi$.

The self-similar flow of the expanding material thus gives direct insight into the equation of state of the initial heated slab [FRS04]. The ideal gas flow is given

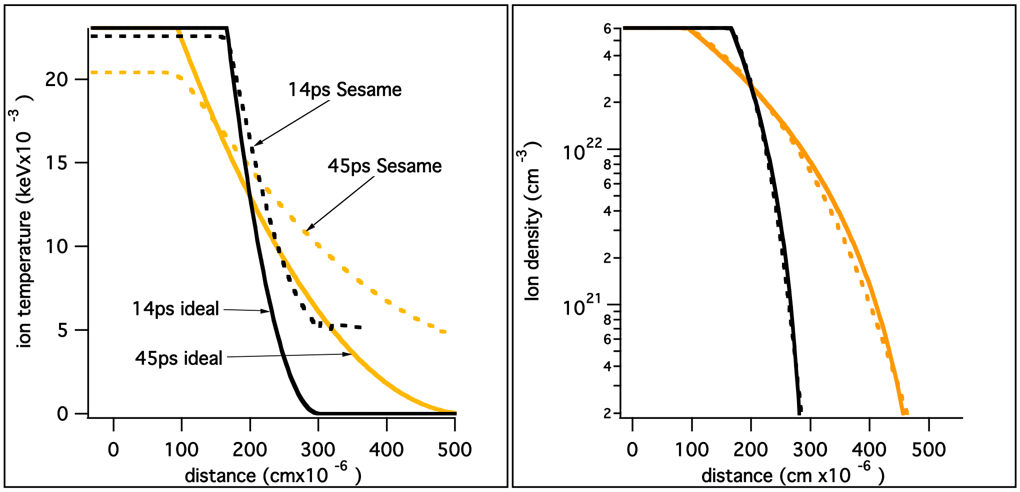

Figure 2.4: Time slices at 14 ps and 45 ps of isochorically heated warm dense Al, for the ideal gas flow given by (2.41) and for a hydrodynamics simulation using SESAME EOS tables, each having the same initial ion temperature and sound speed. The non-ideal EOS shows a similar expansion rate but for exhibits different temperature profiles (because of ionization energy loss).

by the Riemann solution [ZR66]:

$$\rho = \rho_0 \left( \frac{3}{4} - \frac{x}{4c_{s0}t} \right)^3 \qquad 3c_{s0}t \geq x \geq -c_{s0}t; \tag{2.41}$$

$$u = \frac{3}{4}(c_{s0} + \frac{x}{t}) \qquad 3c_{s0}t \geq x \geq -c_{s0}t, \tag{2.42}$$

where $\rho$ and $u$ are constant outside of their bounds. We also have the relations $T/T_0 = (\rho/\rho_0)^{2/3}$, and $c_s = \sqrt{\gamma p/m\rho}$, where $\gamma$ is the adiabatic index. A non-ideal equation of state, particularly one in which ionization and recombination during expansion become important, will give a different result. In figure 2.4, we see that for a given initial temperature, the ideal gas flow is very close to that of the non-ideal Sesame equation of state in terms of expansion rate, but differs vastly in temperature profile.

A simultaneous time resolved measurement of the progression in time of the temperature and position at a given density would thus directly probe the equation of state. That is the approach used here.

# Chapter 3

# Ultrafast lasers

Our primary experimental tool is the ultra-fast, ultra-intense pulsed laser. The technology of this field has grown rapidly over the past several decades, and opened up a number of previously inaccessible experimental possibilities. Both the short pulse length ($< 1$ ps) and the extreme light intensities achievable ($\gg 10^{18}\ W/cm^2$) have been a boon to experimentalists. Since the amplification of laser energy requires passing the laser pulse through an amplification medium, a key challenge in building more and more powerful lasers is keeping the intensity low enough so that the laser does not damage the amplifiers, and that the laser does not encounter excessive nonlinear phase modulation along its amplification path. One way to keep down laser intensity during amplification is to increase the size of the beam and the amplifiers themselves. However cost rapidly increases with the size of amplifiers and optics, and thus a revolution in the peak attainable power of laser systems followed the perfection of a technique known as chirped pulse amplification (CPA), by which the pulse is kept stretched out in time during the amplification process and compressed in the final stage.

## 3.1 CPA lasers

The uncertainty relation of waves requires a short laser pulse to contain a certain amount of bandwidth. To see this, consider a laser pulse envelope whose amplitude takes the shape of a Gaussian with time:

$$A(t) \quad = \quad A_0 \exp\left\{-4\ln 2\frac{t^2}{\Delta t^2}\right\}. \tag{3.1}$$

Here, $\Delta t$ is the FWHM of the intensity $I = |A|^2$. A Fourier transform shows the bandwidth content of this pulse shape:

$$\tilde{A}(\nu) = \mathcal{F}\{A(t)\} \quad = \quad A_0 \exp\left\{-\frac{\pi^2 \Delta t^2 \nu^2}{2\ln 2}\right\}. \tag{3.2}$$

If we define the FWHM in frequency $\Delta\nu$ in the same way as $\Delta t$, we have:

$$\Delta\nu = \frac{2\ln 2}{\pi\delta t}. \tag{3.3}$$

The value of the time bandwidth product (TBWP) $\Delta t \Delta\nu \approx 0.44$ is specific to this envelope function, and it describes the minimum possible pulsewidth $\Delta t$ for a given bandwidth content $\Delta\nu$. Laser pulses are sometimes considered to have more of a $sech^2$ shape, which gives a TBWP of $\approx 0.315$. A pulse exhibiting the TBWP of its envelope function is said to be "transform limited" and has no frequency dependence in its phase.

Thus it is possible through dispersion to lengthen arbitrarily an initially transform-limited pulse. Dispersion is equivalent to imparting a frequency dependent phase to the envelope function:

$$\tilde{A}(\nu) \quad = \quad A_0 \exp\left\{-\frac{\pi^2 \Delta t^2 \nu^2}{2\ln 2} - i\phi(\nu)\right\}. \tag{3.4}$$

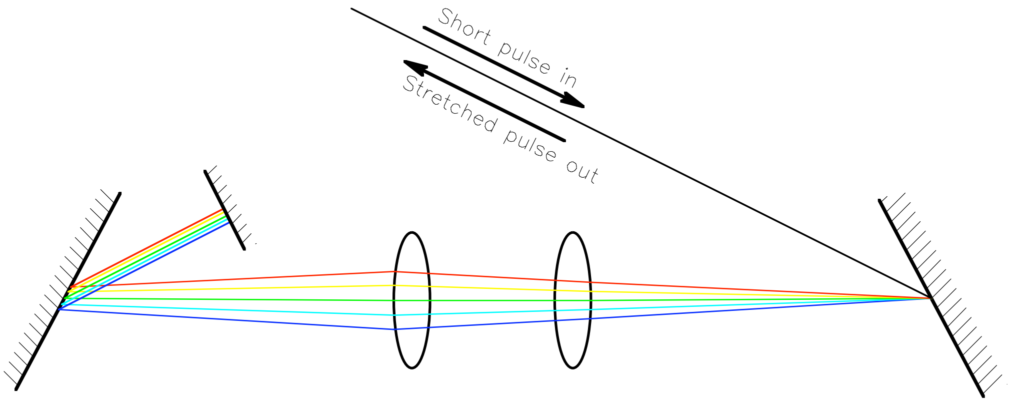

Figure 3.1: Conceptual diagram of a two-grating stretcher, involving two optical gratings, focusing optics, and a vertical retro mirror (which offsets the incoming and outgoing beam vertically). Notice that the red path is shorter.

The idea that this can be done in a controlled and reversible manner is the concept behind CPA [SM85]. Modern CPA lasers use an optical grating configuration, known as a stretcher (figure 3.1), to extend a pulse in time by a factor of $\sim 10^3 - 10^4$ before amplification, and an inverse configuration, known as a compressor (figure 3.2), to return the pulse to nearly its original pulsewidth.

I say "nearly" because the process of amplification destroys the potential symmetry through nonlinear dispersion of the pulse frequencies, and also lengthens the output pulse through gain-narrowing of the bandwidth caused by nonuniform amplification of the laser frequencies.

### 3.1.1 Phase dispersion compensation

The index of refraction $n$ of any material will be nonlinear with respect to wavelength, as can be seen in the commonly used empirical fit known as the Sellmeier equation [Sie86]:

$$n^2(\lambda) \quad = \quad 1 + \sum_i \frac{B_i \lambda^2}{\lambda^2 - C_i}, \tag{3.5}$$

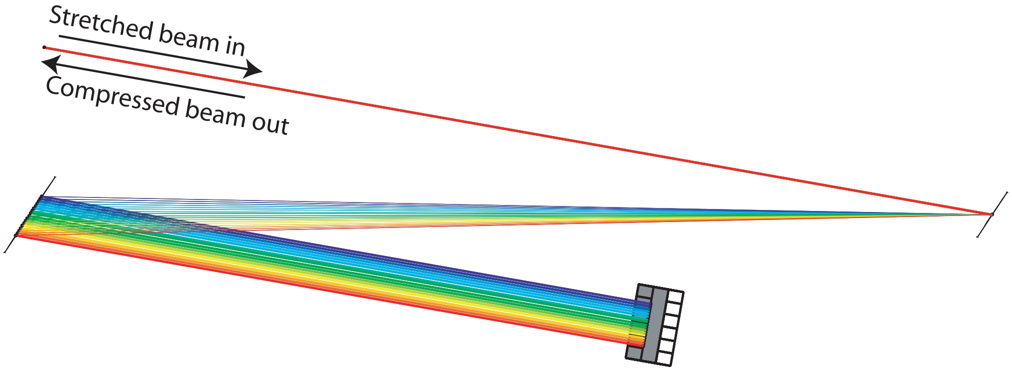

Figure 3.2: False-colored ray-trace of a two-grating compressor, involving two optical gratings and a vertical retro mirror. Each grating is hit twice. Notice that the blue path is shorter.

where $i$ continues for as many terms as needed (usually 2). Relative to a central frequency $\nu_0$, we have an optical path length difference $\mathrm{OPL}(\nu) = \Delta(n \cdot d)$, where $n$ and $d$ are the frequency-dependent index of refraction and distance, respectively. Passage through material will incur a difference primarily through $\Delta n$, and an optical grating compressor through $\Delta d$. The shift in phase is then just $\Delta\phi(\nu) = \Delta(\mathrm{OPL} \cdot \nu/c)$. The overall phase can be Taylor expanded into the polynomial phase orders:

$$\phi(\nu) = \phi(\nu_0) + \varphi^{(1)}(\nu - \nu_0) + \frac{1}{2!}\varphi^{(2)}(\nu - \nu_0)^2 + \frac{1}{3!}\varphi^{(3)}(\nu - \nu_0)^3 + \cdots , \tag{3.6}$$

where $\varphi^{(i)} = \frac{\partial^i \phi}{\partial \nu}\Big|_{\nu=\nu_0}$. The delay accumulated by a given frequency is then $\tau(\nu) = \frac{\partial \phi(\nu)}{\partial \nu}$, or:

$$\tau(\nu) = \varphi^{(1)} + \varphi^{(2)}(\nu - \nu_0) + \frac{1}{2!}\varphi^{(3)}(\nu - \nu_0)^2 + \cdots , \tag{3.7}$$

where $\varphi^{(2)}$ is known as the linear frequency chirp, or quadratic phase term; $\varphi^{(3)}$ is the cubic phase, and so on. In a grating compressor, the grating spacing and angle both affect all orders of the phase to some degree, but the grating angle affects $\varphi^{(3)}$ more strongly relative to $\varphi^{(2)}$ than does the grating spacing. Thus the grating spacing and angle can be perturbed from their stretcher-symmetric positions to eliminate the accumulated quadratic and cubic phases. Fittinghoff, *et al.*[FWS$^+$98] discuss the problems of phase compensation in CPA systems and find that for laser systems of pulse length 100 fs or higher, this is sufficient, but for shorter pulses a more detailed optimization must be performed to minimize higher orders of phase. In some cases this can involve adding material with the appropriate dispersion function to the laser chain.

These calculations of the the stretching and compression of a CPA system can be made easier with the help of a ray-tracing program, such as Mathematica/Optica[WR], which can keep track of the wavelength-dependent OPL. Figure 3.2 and figure 3.8 were generated in this process.

### 3.1.2 Self phase modulation

Intensity dependence in a material's index of refraction causes acute problems only at very high intensities, which CPA systems are designed to avoid throughout amplification. However, the gradual accumulation of nonlinear phase the laser chain can still be detrimental to the output pulse, causing an overall broadening, and a long pedestal in the recompressed pulse [PDS94]. Nonlinear phase accumulation tends to be more difficult than dispersion to eliminate [BKN97], and spatial variation in the amount of phase modulation further complicates the task [KM98].

Below, I present a simple mathematical model for predicting the effects of cumulative nonlinear phase on the output of a CPA laser system, and show a few sample calculations.

### B integral

We express the accumulation of nonlinear phase through the so-called "B-integral":

$$\mathsf{B}(\mathbf{r},t) = \frac{2\pi}{\lambda}\int n_2|\mathbf{E}(\mathbf{r},t)|^2 dz, \tag{3.8}$$

where $n_2$ is the nonlinear term in the index of refraction $n = n_0 + n_2|\mathbf{E}(\mathbf{r},t)|^2$, $\mathbf{r}$ is the transverse coordinate of the laser, $t$ is the local time, and the integral is taken along the path of the light pulse. For a laser pulse with electric field $\mathbf{E}(\mathbf{r},z,t) = \mathbf{E}_0(\mathbf{r},z,t)\exp\{-i[kz-\omega_0 t]\}$, the effect of self phase modulation is found by multiplying by the phase term: $\mathbf{E}(\mathbf{r},z,t) \rightarrow \mathbf{E}(\mathbf{r},z,t)\exp\{i\mathsf{B}(\mathbf{r},t)\}$ [CZM93]. The contribution of $\mathsf{B}$ to the instantaneous frequency of the pulse is $\delta\omega = -d\mathsf{B}/dt$. Since most [KM98] materials have a positive $n_2$, the leading edge of a pulse will be red shifted, and the trailing edge blue shifted due to the $\mathsf{B}$ integral [Boy92].

The stretcher in a CPA laser effectively maps the ultrashort input pulse to its fourier transform. To lowest order, the stretched pulse has an instantaneous frequency which varies linearly with time. Its form can be obtained through fourier transforms between time ($t$) and frequency ($\omega$) space:

$$\mathbf{E}_s = \mathcal{F}^{-1}\{\mathcal{F}\{\mathbf{E}_i\}e^{-i\phi_s(\omega)}\}, \tag{3.9}$$

where $\mathbf{E}_i$ is the initial pulse, $\mathbf{E}_s$ is the final pulse, and $\mathcal{F}$, $\mathcal{F}^{-1}$ are the Fourier transform ($t \rightarrow \omega$) operator and it's inverse ($\omega \rightarrow t$), respectively. $\phi(\omega)$ describes the phase function of the stretcher, and for a purely linear chirp (quadratic phase shift), $\phi_s(\omega) = \beta\omega^2/2$ [MSB$^+$88].

In the ideal case, the amplification would be uniform without phase modulation, and the compressed pulse would then look like:

$$\mathbf{E}_c = \mathcal{F}^{-1}\{\mathcal{F}\{A\mathbf{E}_s\}e^{i\phi_s(\omega)}\}, \tag{3.10}$$

where $A^2$ is a uniform amplification. Thus the ideal result is $\mathbf{E}_c = A\mathbf{E}_i$. Of course, this ideal is never fully achieved, due to gain narrowing, gain saturation, dispersion, clipping, self-phase modulation, and so on [CZM93]. In practice, amplification is never perfectly uniform and it is always accompanied by phase terms. In the simple model that follows, only self-phase modulation is treated: We assume that the dispersion has minimized to the point that it can be neglected. Thus, for our purposes (3.10) becomes [MSB⁺88]:

$$\mathbf{E}_c = A\mathcal{F}^{-1}\{\mathcal{F}\{\mathbf{E}_s e^{i\mathsf{B}}\}e^{i\phi_s(\omega)}\}. \tag{3.11}$$

We can exploit the assumption that the pulse is stretched to $> 1000$ times its initial duration by the phase function $\phi_s(\omega) = \beta\omega^2/2$. For large enough $\beta$, we can use the approximation:

$$\mathbf{E}_c = A\mathcal{F}^{-1}\{\mathcal{F}\{\mathbf{E}_i\}e^{i\mathsf{B}_{\max}\tilde{S}(\omega)}\}, \tag{3.12}$$

where $\mathsf{B}_{\max}$ is the value of $\mathsf{B}$ at peak intensity ($t = 0$, $r = 0$), and $\tilde{S}(\omega)$ is the spectrum of $\mathbf{E}_i$, normalized so that $\tilde{S}(\omega_0) = 1$. Fig. 3.3 shows that (3.11) converges to (3.12) as the stretched pulse length increases towards the typical 500 ps.

In fig. 3.4, the temporal distortion calculated for various values of $\mathsf{B}_{\max}$ are compared. The relative pulse broadening and shaping caused by the various values of $\mathsf{B}_{\max}$ do not depend strongly on the initial pulse length, as can be seen by comparing this figure for 30fs pulses to a similar figure that assumed 100fs initial pulses in [PDS94].

It should also be noted that self phase modulation can affect the quality of the focal spot, as the intensity of the beam will have spatial variation. To achieve maximal intensities, we want to focus the output of a CPA laser system to the smallest practically attainable spot size. To this end, a lowest order Gaussian profile

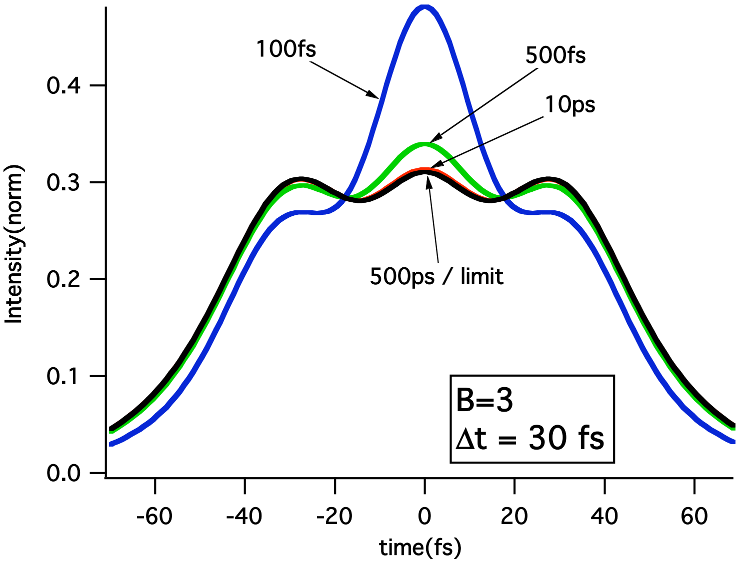

Figure 3.3: A 30 fs pulse recompressed after having been stretched to various lengths and accumulating $\mathsf{B}_{\max} = 3$. Profiles calculated with the more exact formula (3.11) converge to a limit (3.12) as the amount of stretching increases. Typical CPA pulses are stretched to 500ps or longer.

is most desirable. Spatially filtering the pulse at various stages of amplification maintains an approximately Gaussian profile, discarding pulse energy which would not be focused down to a spot [MSB$^+$88]. Unfortunately, the distortions caused by accumulated nonlinear phase manifest upon re-compression, at which point no further spatial filtering or amplification is possible (because this requires passing through material). Radial dependence of the phase accumulation threatens the spatial coherence of the pulse, and thus the quality of the focused spot [BKN97]. However, this effect is generally not as significant as the effect on the pulse length.

A few methods have been suggested for overcoming B-integral accumulation in certain laser systems. Calculations [BKN97] have shown that linear pulse shaping prior to amplification could radically improve the temporal shape of a pulse along the central axis or on average. Experimental measurements [KM98] have demonstrated

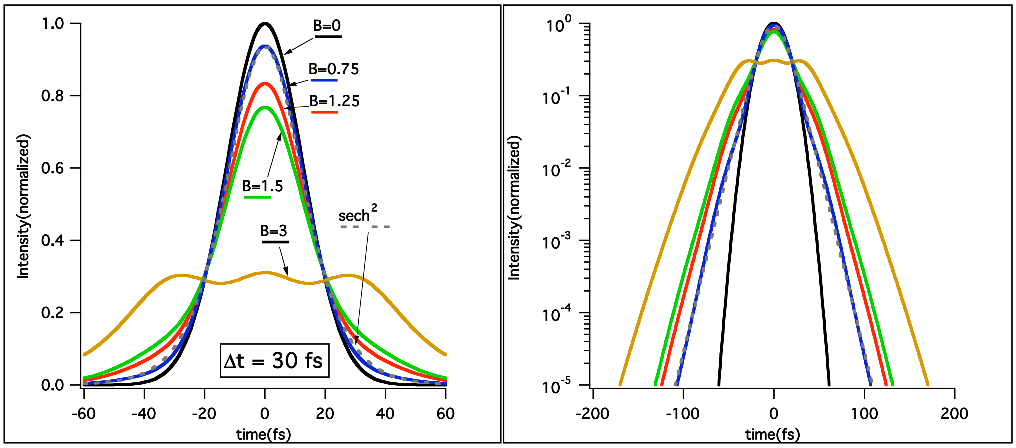

Figure 3.4: Compressed pulse shape of an initially 30fs FWHM pulse for various values of $\mathsf{B}_{\text{max}}$. For reference, a sech$^2$ pulse with FWHM = 30fs is also shown.

the use of a semiconductor wafer with negative $n_2$ can be cut to the right width so as to reverse, almost entirely, the accumulation of the B-integral for pulses of appropriate central wavelength. Also, electrical feedback mechanisms [PHA$^+$01] designed to completely control the phase of ultrashort pulses may also help. In general, B integral is a difficult problem, and laser systems must be designed to keep its effects to a minimum.

As a general rule of thumb, we will usually try to keep the B integral of the system less than 1. Even air has a nonlinear index of refraction, so high power CPA systems will always have their main compressor in vacuum.

### 3.1.3 Gain narrowing

Since the laser gain of an amplifying medium is nonuniform in wavelength, the process of amplification will narrow the spectrum of the laser pulse. Thus to get ultrashort pulses, we need as broadband an amplification medium as possible. For its broad gain bandwidth around 800nm, the crystal Ti:sapp is the common choice for tabletop, sub-100fs laser systems [ZHMK95]. However, it has a short fluorescence lifetime, meaning that it must itself be pumped by larger and larger pulsed ($\sim 5ns$) lasers. Also, Ti:sapp has to be grown, which is a relatively slow process. Both of these factors drive up the price of Ti:sapp, generally limiting the pulse energy to the vicinity of 1 J.

Glass amplifiers can be made larger, have longer fluorescence lifetimes at high gain, and can be flashlamp-pumped, and thus can achieve higher energy levels, but with a narrower bandwidth than Ti:sapp. Glass CPA lasers, typically Nd:glass amplifying near $\lambda = 1\ \mu m$ , are characterized by much higher energies for a given cost, but will also have longer pulsewidths. The nonlinear wave-mixing technique of optical parametric amplification (OPA) [CHGR$^{+}$99] allows for very broadband pre-amplification up to a few mJ reducing the amount of amplification to be done in glass, and leads to CPA laser systems which can achieve hundreds of Joules in a sub-ps ($\sim 500fs$) pulse. Such systems are called OPCPA lasers. The emerging technique of using mixed-glasses [HGMD07] in the amplification process to support a higher bandwidth spectrum is leading to a new class of $>$ 100J lasers at pulsewidths closer to 100 fs.

### 3.1.4 Autocorrelation

CPA lasers allow unprecedented measurements of extremely short timescales. The question arises how we measure the duration of a laser pulse that occurs much faster than the temporal resolution of our measuring devices. The answer is that we use the pulses themselves to measure their pulselengths, through a process called autocorrelation. The polarization **P** inside a material is, in general, driven nonlinearly by the electric field of the laser. For example, it is possible for two frequencies of laser passing through a medium to form a third wave at the sum of their frequencies, in a process known as sum frequency generation [Boy92]:

$$P(\omega_1 + \omega_2) = 2\chi^{(2)} E_1(\omega_1) E_2^*(\omega_2) + c.c. \tag{3.13}$$

Here, $\chi^{(2)}$ is the second-order susceptibility tensor. We define

$$\Delta\Omega = n_1\omega_1 + n_2\omega_2 - n_2\omega_3, \tag{3.14}$$

where $\omega_3 = \omega_1 + \omega_3$, and $n_1$,$n_2$, and $n_3$ are the respective indices of refraction. Normal dispersion (where there is no absorption) dictates that $n$ is a monotonic increasing function of frequency. Thus the phase matching condition for constructive interference, $\Delta\Omega = 0$, appears impossible, except that crystals can exhibit polarization dependent indices of refraction, a property known as birefringence. In the simple case of a uniaxial birefringent crystal, one crystal axis, $\hat{c}$, has an "extraordinary" index of refraction, $\bar{n}_e$, which is different[1] from the "ordinary" index of refraction $n_o$ for polarization along the other two axes. Light propagating in the $\hat{k}$ direction that is polarized in the plane of $\hat{c}$ and $\hat{k}$ will experience an extraordinary index of refraction [BW75]

$$n_e(\theta)^2 = \left(\frac{\sin^2\theta}{\bar{n}_e^2} + \frac{\cos^2\theta}{\bar{n}_o^2}\right)^{-1}. \tag{3.15}$$

An appropriate birefringent crystal is cut at the right angle to set the desired value of $n_e$ for the phase matching condition. In this case there are two types of phase matching:

- Type-I phase matching, in which $\mathbf{E}_1$ and $\mathbf{E}_2$ are polarized along the higher index axis (typically ordinary waves), and $\mathbf{P}$ is polarized along the orthogonal axis, or,

- Type-II phase matching, in which $\mathbf{E}_1$ and $\mathbf{P}$ are polarized along the same axis (typically extraordinary waves) and perpendicular to $\mathbf{E}_2$.

---

[1] The case ($n_e > n_o$) is called "positive uniaxial" while ($n_e < n_o$) is called "negative uniaxial."

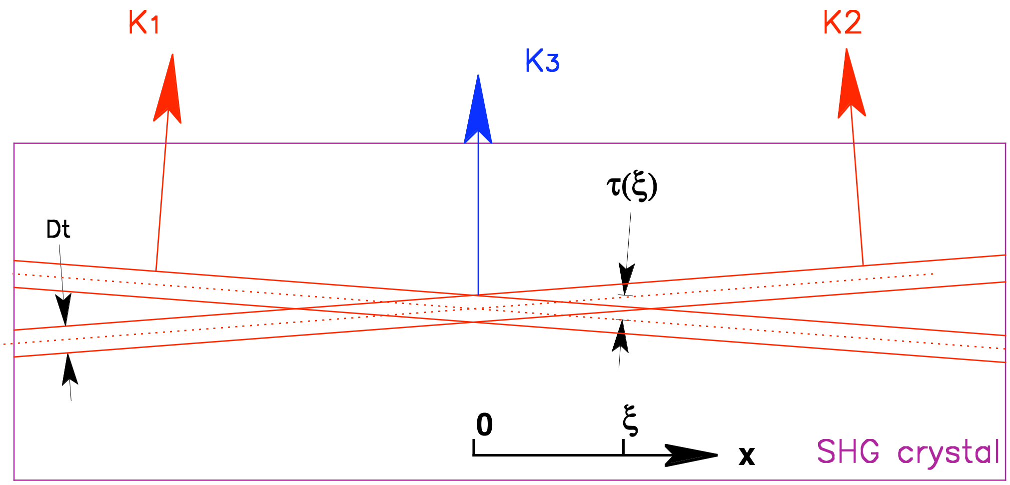

Figure 3.5: Schematic of two pulses interacting in a SHG crystal to output the autocorrelation function as a function of horizontal position $\xi$, by $\tau(\xi) \approx c/(\xi\theta)$, where $\theta$ is the small angle between the two beams.

Two special kinds of SFG are used to measure the laser pulse. Second harmonic generation (SHG), where $\omega_1 = \omega_2$, and third harmonic generation (THG), where $\omega_1 = 2\omega_2$ and the wave of frequency $\omega_1$ was generated by SHG. With SHG we are able to produce a second order autocorrelation:

$$I_{2\omega}(\tau) \quad \propto \quad \int_{-\infty}^{\infty} |E(t)E(t-\tau)|^2 = \int_{-\infty}^{\infty} I(t)I(t-\tau), \tag{3.16}$$

Where $I_{2\omega}$ is the output $2^{\text{nd}}$ harmonic intensity measured on a detector, and $\tau$ is the delay between two copies of the laser pulse entering the SHG crystal. By varying $\tau$ we can trace out the autocorrelation function, which has a width that is $\sqrt{2}$ as long (FWHM) as the original pulse, in the case of a Gaussian pulse shape, and 1.54 times as long in the case of a $\text{sech}^2$. The delay $\tau$ can be varied manually by splitting and recombining a beam colinearly with a delay stage in one arm, or in a single shot, by crossing two beams in the crystal at a small angle, as depicted in figure 3.5. Because the second order autocorrelation is symmetric in time, it does not

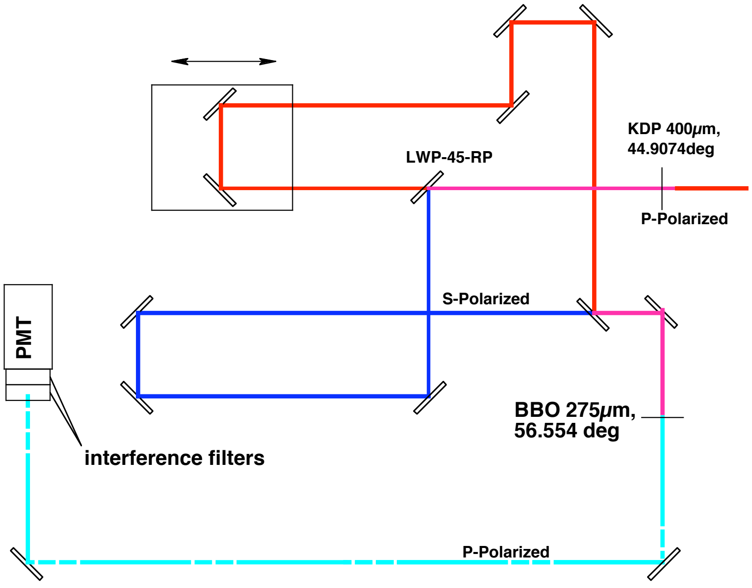

Figure 3.6: Schematic of a scanning third order autocorrelator. A SHG KDP crystal doubles the laser light by Type-I SFG and the $2\omega$ and remaining $1\omega$ are split and then recombined with a variable delay and then combined to form $3\omega$ by Type-II SFG in BBO. The signal is read on a PMT.

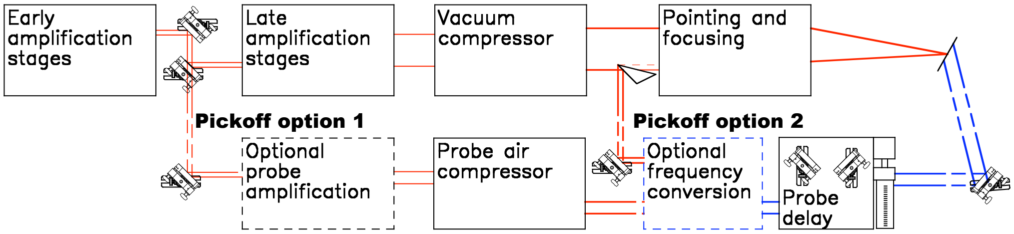

Figure 3.7: Schematic of two options for picking off a probe beam from the main laser. Option 1: Leak-through of partially amplified probe light is further amplified and independently compressed. Option 2: A small fraction at the edge of the beam profile of the fully compressed, large diameter beam is picked off. In either case, frequency up-conversion with decent efficiency can be achieved after compression, and an actuator stage with $\mu m$ precision is used for pump-probe synchronization.

distinguish between undesired light arriving before the pulse (prepulse), which can be disastrous to an experiment, and light arriving after the main pulse (post pulse), which is generally less detrimental. For that reason a third order autocorrelator is often used to diagnose prepulses and postpulses. The pulse is doubled so that the laser beam contains similar intensities of $2\omega$ and leftover, unconverted $1\omega$. They are then recombined with a relative delay in a THG crystal, and the signal gives the third order autocorrelation:

$$I_{3\omega}(\tau) \quad \propto \quad \int_{-\infty}^{\infty} I(t)^2 I(t-\tau). \tag{3.17}$$

This function is asymmetric and can be used to distinguish between prepulse and postpulse. A scanning third order is depicted in figure 3.6. It is also possible to construct a single-shot third order autocorrelator [CHGA$^+$01].

### 3.1.5 Probe beams

A great advantage of laser-driven experiments is that the laser pulse which generates the radiation to heat our sample can also be used to probe it. By picking off a small amount of laser light upstream for a probe, the relative timing of pump and probe is determined by path lengths, independent of any timing electronics, and so $\sim 100\mu m$ stability in path length gives $<$ 1ps temporal precision.

As illustrated in figure 3.7, we have used two different techniques for obtaining a probe beam in the various experiments. Many laser facilities (THOR, Calisto, Titan, Sandia) the beam will often be picked off at an early stage and independently compressed (option 1). If the laser facility does not have an independent probe beam (as was the case in the JanUSP experiments), a probe beam can be picked off from the edge of the large beam profile after compression and before focusing (option 2). Option 1 has several advantages, including the possibility of leaving the probe beam partially compressed (as used in the Titan and Sandia experiments in chapter 7), more stable probe beam profile and energy (since in option 2 shot-to-shot variations in main beam profile greatly affect the probe brightness), and saved setup time.

## 3.2 Laser systems in this thesis

### 3.2.1 THOR

The **T**exas **H**igh Intensity **O**ptical **R**esearch (THOR) laser is a workhorse research laser at the University of Texas, delivering 600 mJ 800nm pulses of 35 fs duration at a maximum rep rate of 10 Hz. With a tightly focusing parabolic mirror, the laser intensity can exceed $10^{19}\ W/cm^2$. Ultrashort pulses are originated in a commercial Femtosource[2] Kerr mode-locked oscillator, which generates a 75Mhz pulse train that triggers a photodiode, the signal of which is divided down to 10 Hz for the timing of the system. A 10 Hz pulse train is isolated by an electrooptic pockels cell pulse slicer and faraday rotator combination [Sie86]. The pulse is stretched in a folded, single grating stretcher (figure 3.8) and passed through 4 m of optical fiber for

---

[2] `http://www.femtolasers.com/Pages/Oscill_FS.html`

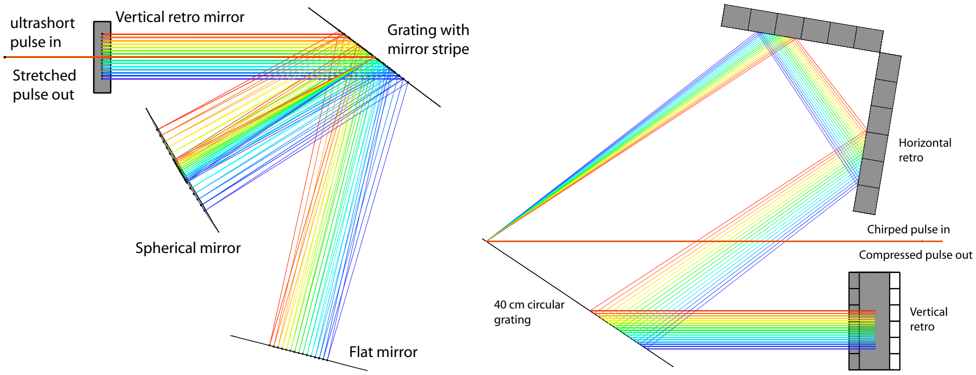

Figure 3.8: Ray trace images of the THOR single-grating stretcher (left) and compressor (right). The stretcher utilizes a large grating with a mirror stripe at its center. Light enters, and reflects in the following order: grating (top), spherical mirror, mirror stripe, flat mirror, mirror stripe, spherical mirror, grating (top), vertical rooftop, grating (bottom), spherical mirror, mirror stripe, flat mirror, mirror stripe, spherical mirror, grating. In the folded single grating compressor, which is operated under vacuum, the stretched laser hits the grating on the right side just below the equator and is turned around by a horizontal retro mirror where the wide beam hits the grating to the left of the first hit. The wide beam is offset vertically by a vertical retro mirror, hits the grating and returns through the horizontal retro mirror to the final spot, on the other side of the equator from the original spot. This last hit on the grating is the most intense hit on an optic in the laser chain. Unlike the representation here, the actual incoming and outgoing beam diameter is 3”.

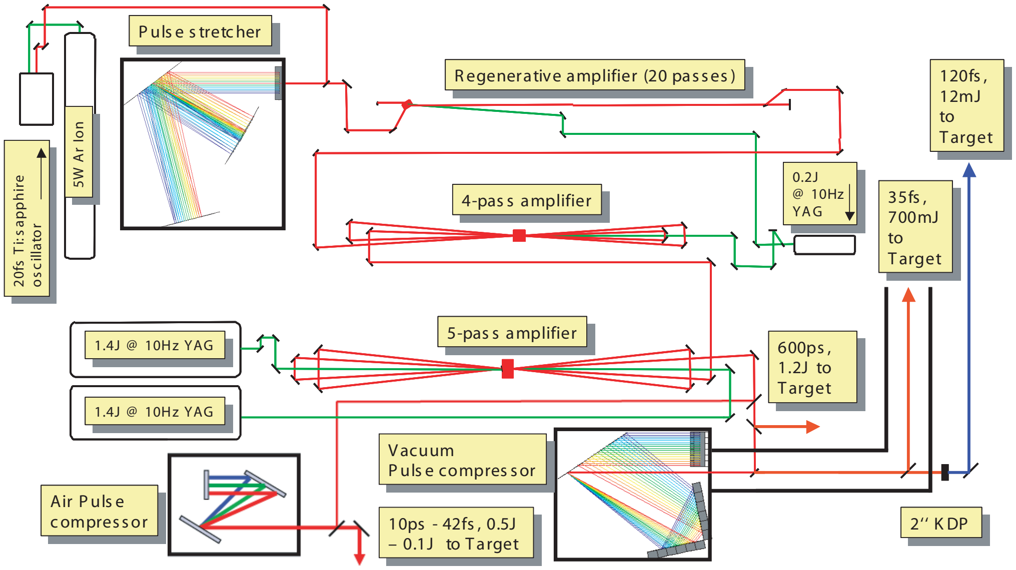

Figure 3.9: Overview of THOR laser system, courtesy Dr. Ditmire, modified by S. Kneip.

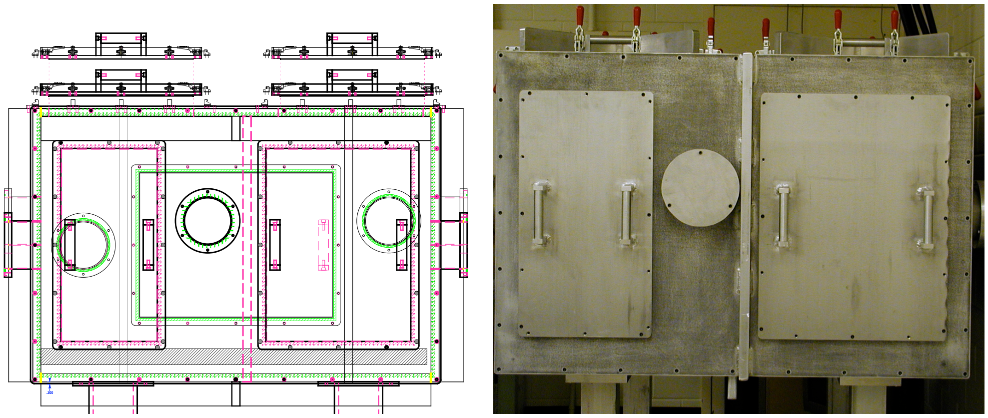

Figure 3.10: Compressor vacuum chamber, manufactured from Al by the UT Physics machine shop. LEFT: From CAD drawings. RIGHT: Photograph

dispersive phase compensation purposes. The pulse is then injected into a Ti:sapp laser cavity, the regenerative amplifier (regen), which is pumped by approximately 60mJ from a Nd:YAG laser. After about 20 passes through the cavity, the pulse is switched out by a pockels cell and thin film polarizer and isolated from the long timescale continuous emission of the cavity (amplified spontaneous emission; ASE) by a second pulse slicer. The first amplification stage takes the pulse from several nJ to several mJ.

The beam is expanded for the next amplifier stage, which consists of 4 passes through a brewster-cut Ti:sapp crystal pumped with the remaining ~160mJ from the Nd:YAG laser that pumps the regen. This amplifier stage brings the pulse energy up to ~20mJ. In its initial setup, the amplified beam emerged from the four pass with a slightly elliptical shape, with $1/e^2$ radius of 1.7 mm in the horizontal direction and 1.23mm in the vertical direction. Because of thermal lensing, this beam size was smaller than the unamplified beam leaving the 4-pass, which had horizontal radius of 2.77mm and vertical radius of 2mm. The pump beam was more circular with a $1/e^2$ radius of 1.42 mm. The gain for passes 1 through 4 were 2.13, 1.87, 1.56, and 1.4 in order, for a total overall gain of 8.75.

A second expansion of the beam is done with a vacuum telescope with a pinhole at focus, which acts as a spatial filter, removing the higher frequency modes in the beam profile to reduce the risk of damage to laser optics from hot spots. The 1cm beam then takes 5 passes through an AR coated Ti:sapp crystal pumped on either side by two 1.4 J Nd:Yag lasers (impressive lasers in their own right), to reach a pulse energy of up to 1.1 J.

Up to 200 mJ of the laser energy can be diverted into an air compressor (which is preceded by a non-expanding spatial filter) for use as a probe beam. The main laser energy is expanded to 3” in a vacuum spatial filter telescope and passed into the 3’×4’×5’ vacuum chamber containing the folded compressor, where it is

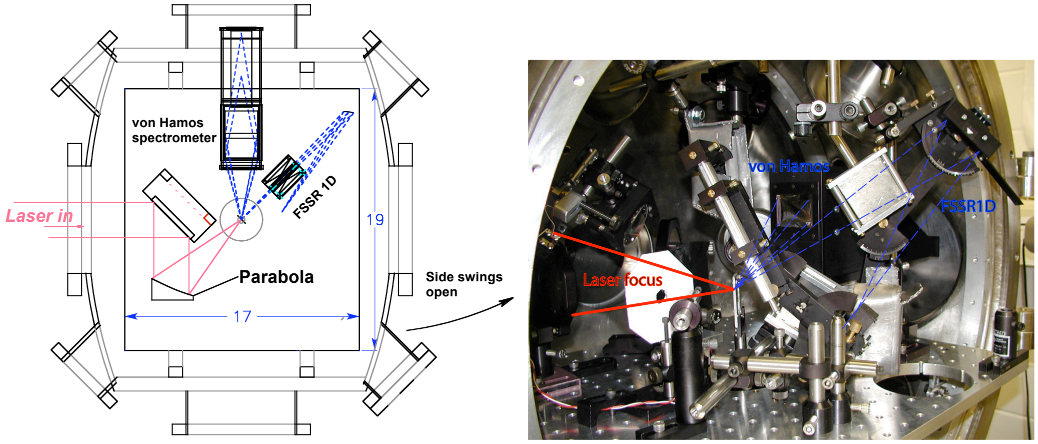

Figure 3.11: LEFT: Top view drawing of the THOR solid target chamber, in one of many possible configurations. The dimensions are in inches. This was the configuration used for the experiment described later. RIGHT: Photograph of the same layout.

compressed to 35fs. The laser pulse is delivered under $10^{-4} - 10^{-5}$ vacuum to the experimental target chamber.

A vacuum switchyard containing a turning mirror allows selection between various target chambers. A layout of the solid target chamber used for the experiments in this thesis is shown in figure 3.11

### 3.2.2 JanUSP/Calisto

The JanUSP laser at Lawrence Livermore National Laboratory (LLNL) was named for the **Jan**us laser, which pumps its final amplifier stage, and the **U**ltra **S**hort **P**ulses it produces as a high energy Ti:sapp laser. Now renamed Calisto, this laser was designed to deliver 10 J pulses of 800nm light in a 100 fs pulse. When it was built, JanUSP broke the laser intensity record with a tightly focusing f/2 parabolic optic producing a focal spot of $< 4\,\mu m$ , 15J and 80 fs, for $\approx 2 \times 10^{21}\ W/cm^2$.

JanUSP / Calisto is a Ti:sapp laser system which can operate at 10 Hz with 100 mJ, or in a single shot mode, pumped by JanUSP at $\sim 1$ shot per 30 minutes.

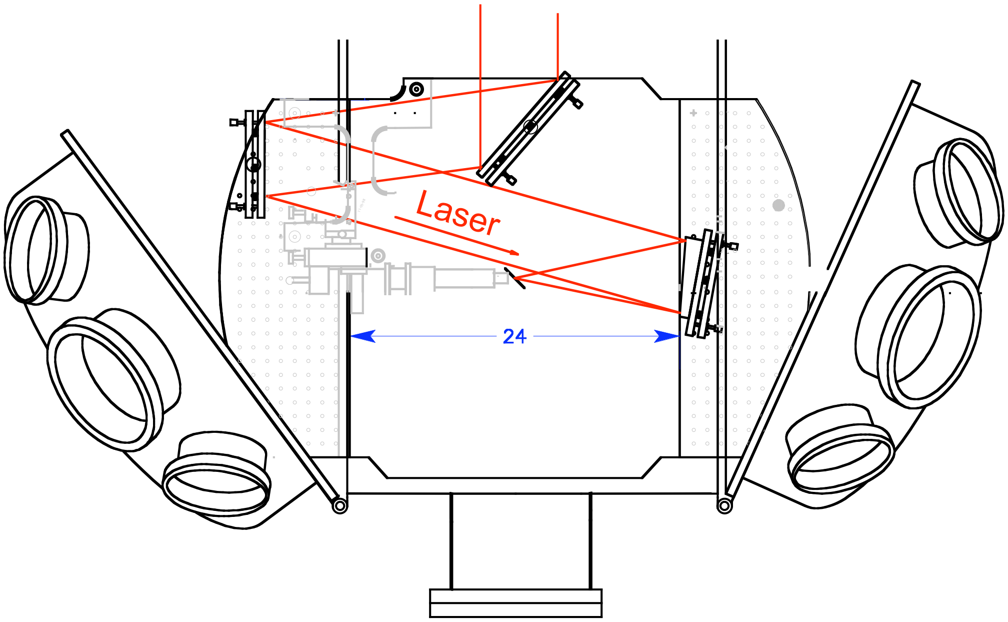

Figure 3.12: Top view of main target chamber of JanUSP/Calisto. Produced at LLNL and provided courtesy J. Bonlie

Its 6” final Ti:sapp amplifier crystal was originally pumped by 100 J from the Janus laser system. Recently, JanUSP was renamed Calisto when the Janus laser was upgraded to 1kJ and independent rod amplifiers were installed to pump Calisto’s final Ti:sapp crystal separately. An independent air compressed probe beam, and a separate, 2-parabola target chamber were also installed in recent years.

As discussed later in the thesis, JanUSP/Calisto has gone through various states of disrepair in recent years, with energies not always reaching 10 J, and signs of a destructive prepulse.

### 3.2.3 COMET

The **Com**pact **M**ultipuls**e** **T**erawatt (COMET) laser at LLNL was designed to drive Ni-like collisionally-driven x-ray laser [DLO$^+$00] at wavelengths in the range of 139Å-203Å. Its main CPA beam can deliver between 5 and 7 J at 1.054$\mu m$in a 500fs pulse

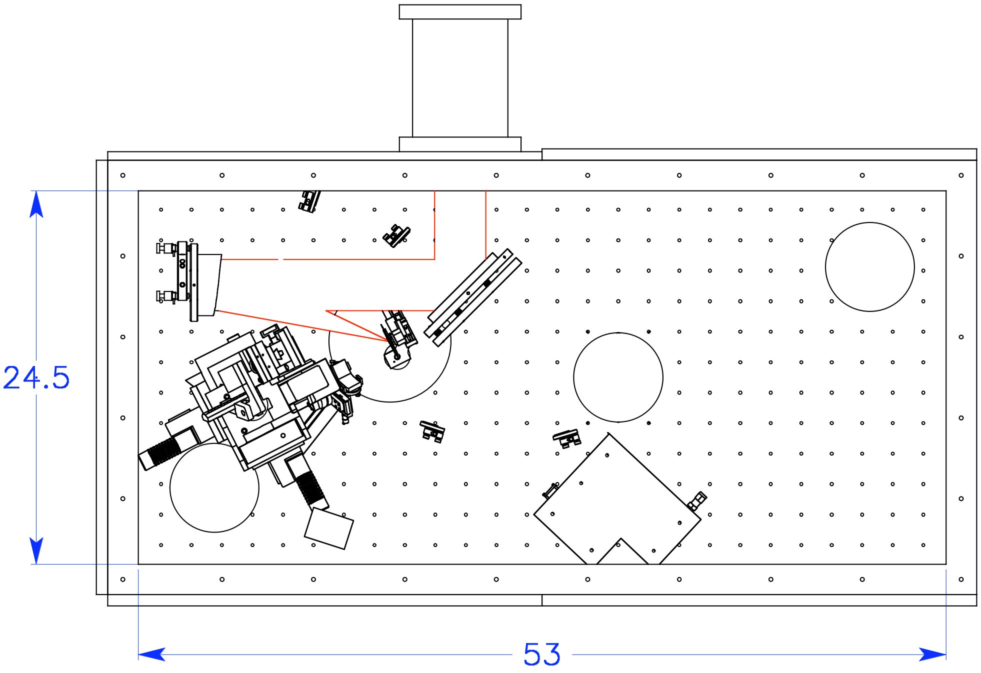

Figure 3.13: Top view of the COMET target chamber for standard target shooting. CAD courtesy Robert Berry, LLNL. Units in inches

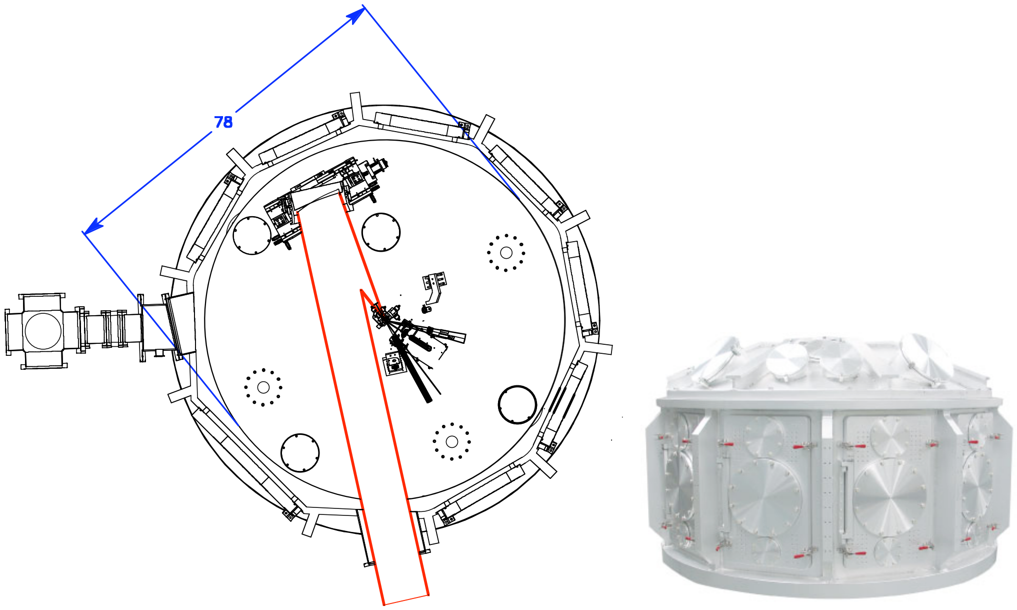

Figure 3.14: The target chamber of the Titan laser facility. The interior breadboard is supported directly from the ground and thus is unaffected by the stresses in the target chamber going from air to vacuum. Thus, alignment done at air will match with high precision the final alignment at vacuum, which is not the case for a target chamber in which the breadboard is supported by the vacuum vessel itself. Detailed drawings of the target chamber can be found at the Jupiter Laser Facility website (`http://jlf.llnl.gov/titan.html`). The chamber was manufactured from aluminum by precision metal works of Canada (`http://www.precisionmetalworks.com/press/lawrence.2005.08.23.html`). Units in inches.

once every 5 minutes. In 2004, a separate target chamber was installed allowing the COMET laser to run also as an ordinary parabola focused target shooter (figure 3.13).

### 3.2.4 Titan

The recently completed Titan laser [Ng07] of the Jupiter laser facility (JLF) at LLNL is a two beam laser system combining an ultrashort pulse OPCPA laser with a longer pulse kJ laser. The shorter pulse laser is designed to approach, eventually, 1 PW in power at 400 J in 400 fs. It is currently operated at up to 150 J and 600 fs. The combination of long and short pulse beams allows for shock/probe experiments to measure EOS and dynamic material properties. The shot rate in Titan is currently limited to at most 5 shots per day. An independently air-compressed probe beam of $\sim$ 5mJ is available and can be frequency doubled.

As the laser power exceeds 100 TW at several 10s of J, some additional experimental difficulties arise:

### Nuclear activation within the target chamber

One of the issues of laser systems approaching PW powers with 100 J or more of laser energy is undesired nuclear activation of materials around the target. On such systems, the large number of gamma rays emitted from a target can lead to nuclear activation of the surrounding materials and even the target chamber walls. Because the level of activation is lower for Al and lower- Z materials than for higher-Z materials [PCC+99], the target holder mount and any diagnostics close to the target should be made from Al or plastic if at all possible. This is also the reason that the target chamber itself is made of Al. Because radiation safety is a concern, upon venting after a system shot, a radiation sweep is performed and access to the target chamber by experimenters is prohibited until dose rates fall to acceptable levels. Changing out a steel optics post near the target for one made of Al has meant the difference between a 2-3 hour wait and a 30 minute wait for clearance.

### Electromagnetic pulse (EMP)

Terawatt and sub-TW electromagnetic pulses (EMP) [SGJ+06, MNG+04] from shots on $>$ 100 TW laser facilities can cause severe problems in electronic diagnostics, such as CCDs. On interaction with the large number of high energy electrons emitted from a target, various components of the target chamber act as antennae to drive an EMP, and electrical components connected to the devices, including the ground loop, can act as an antenna to deliver the pulse into the electronic measuring device, often causing it to malfunction. Low-tech solutions to this problem involve fashioning a Faraday cage for the instrument and disconnecting it from the ground loop by powering the diagnostics by battery during a shot. On Titan shots at 100J/600fs, Computers were kept at a distance of several meters from the target chamber, surrounded in wire mesh[3], and plugged into battery packs. Oscilloscopes must be kept in a completely electromagnetically shielded copper box to operate properly. Interestingly, we found that one CCD which was reliably failing on system shots was able to function properly upon direct line-of-site placement of a thick lead barricade between target chamber center and the CCD. This allowed it to function properly, thus indicating a directionality to the problematic radiation, which was causing problems despite nearly a foot of other materials along the path (e.g. the glass of the parabola, the target chamber wall and the walls of the CPI box). This suggested that bremsstrahlung gamma rays in the backwards laser direction may have been directly responsible for the camera's failure.

### 3.2.5 Sandia Petawatt

The Sandia Z-beamlet laser facility exists in support of the Z-machine there [HVC+02]. It is also equipped to operate several laser-based experiments between Z shots. The 100TW target chamber is an example of this, where a 60 J, 600fs 1.053 $\mu m$ OPCPA laser is provided. A typical shot rate is 3 or 4 per day, working around the laser schedule of the other lasers and Z. The independently compressed probe beam operates at 10 Hz with pulse energy of $\sim$ 5mJ, or at 1 shot per 10 minutes (rod shots or system shots) amplified to $\sim$ 50 mJ.

---

[3] It's not clear how much the mesh helped, but you over-engineer to avoid problems because shots come so infrequently.

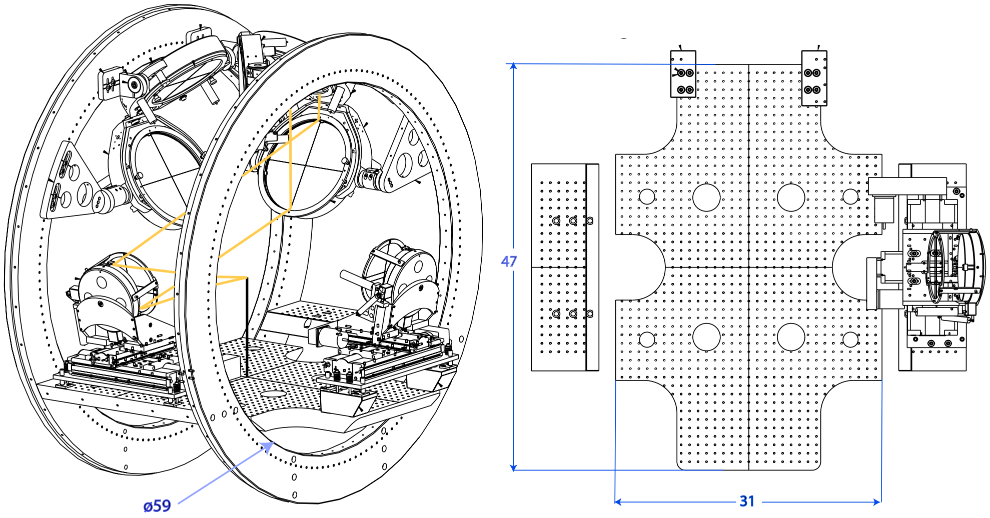

Figure 3.15: The Sandia 100TW target chamber will have the option of splitting the beam energy into two focused beam paths for high energy pump-probe. The front and back panels of the target chamber sit on rails to allow full access to the target chamber insides. The drawing were produced at Sandia and provided courtesy Dr. Edens Units are inches.

## 3.3 Limitations of direct laser heating

We are interested in isochoric heating of solid density matter to warm dense matter temperatures, and modern high intensity, ultrafast lasers are an obvious candidate for their ability to deliver an extreme high energy density to a precise location in a very short period of time. We run into a limitation with direct laser heating in that the laser frequencies available to us (near optical) are significantly below the critical frequency of heated material. As such, the laser intensity dies off exponentially from the surface of the solid material we're trying to heat with a characteristic length called the skin depth, which for a conductive material is given by:

$$\delta = \sqrt{\frac{2}{\mu\sigma\omega}}, \tag{3.18}$$

where $\mu$ is the permeability, $\sigma$ is the conductivity, and $\omega$ is the angular frequency of the laser. Typically this depth will be only a few or a few tens of nm; as materials are heated and partially ionized, their conductivity tends to increase (the interaction of lasers with solid materials is further discussed in the next section). The result is that to create warm dense matter under controlled and well-characterized conditions by direct laser irradiation requires using extremely thin materials, on the order of the laser skin depth. Leaving aside the difficulty of working with foils so thin that wind currents could break them, surface contamination and uncertainty in the exact thickness of the foil will affect predictions of the energy deposition [WAF$^+$04, WGF$^+$01]. Good results have been achieved from direct laser heating [YMUM06, APW$^+$06], but deeper, volumetric heating of solid density matter [AFA$^+$06, PMK$^+$03] leads to a more persistent WDM state giving better flexibility in measurements. Also, as discussed in section 5.5, a target must be thick enough to be totally opaque to the observed wavelengths in a streaked optical pyrometer in order for that diagnostic to serve as a viable temperature diagnostic.

### 3.3.1 Free electron lasers

Direct, deep, isochoric heating of solid samples will be made possible by the Linac Coherent Light Source (LCLS) x-ray free electron laser (FEL) [MGA$^+$01] being built on the Stanford linear accelerator [LBC$^+$01]. The facility will deliver tunable to photon energies between 800eV and 8keV, with transverse coherence and far, far higher brightness than current x-ray sources in a 200 fs pulse. Isochoric heating and subsequent probing of solid density plasma and warm dense matter states is one of the principle research thrusts of the facility. It is quite likely that LCLS will contribute enormously to the study of warm dense matter, but the pursuit of ordinary laser-driven WDM isochoric heating experiments will continue to be valuable for two reasons:

- The LCLS is only one, very large facility that will open up a huge range of experimental possibilities, of which isochoric heating and EOS studies is only one. By contrast, numerous laser facilities capable of using proton heating for isochoric heating of matter are available.
- Construction of LCLS is not complete. Although it is likely to succeed, this laser system is unprecedented, and as such will have some bugs to work out as it comes online. In particular, fabrication and use steering optics at these x-ray photon energies will be a challenge.

Of course, there is plenty of room for a variety of methods to study WDM, and narrowing down the EOSes will require a large body of data to which experiments from many different facilities can contribute.

In the next section, I discuss the laser generation of secondary sources which can be used to volumetrically heat solid density materials to WDM temperatures, thus overcoming the skin depth limitation of optical lasers.

# Chapter 4

# Laser-generated sources

A large part of high intensity laser science concerns the conversion of laser energy into another useful form, which is achieved through the interaction of the intense laser light with matter. Some examples are high harmonics of the laser extending into the uv and xuv from gas jets, MeV neutrons from fusion events in irradiated deuterium clusters, and GeV electrons accelerated in plasma filaments. This thesis concerns solid target sources, from which one can generate high energy electrons, bremsstrahlung x-rays, hard x-rays from inner-shell emission, or directed ion beams. A major advantage of sources generated with ultra-short pulsed lasers is that they are themselves pulsed on a similar time scale to the laser, which greatly expands the scope of ultra-fast science.

In this chapter I will discuss the sources that I have investigated for isochoric, volumetric heating of solids to warm dense matter temperatures, namely $K_\alpha$ x-rays and proton beams. After establishing the benchmarks that must be met by a source to achieve isochoric heating to WDM temperatures, I will describe the mechanisms by which a huge number of super-thermal electrons are accelerated by an intense laser pulse incident on a solid target, and how the energy distribution and number of these electrons are thought to depend on the laser parameters. Treating the electrons statistically, I will describe their path through the material of the foil as they lose energy, radiate bremsstrahlung and create K-shell holes. These analyses will lead to theoretical estimates for the amount of $K_\alpha$ radiation we can expect to see for given laser conditions, and thus what laser conditions will be needed to meet the benchmarks for WDM heating. Next I consider the hot electrons leaving the back surface of a foil, which are so great in number that they actually produce enormous electric fields that pull back the electrons and accelerate ions from the back surface. The most readily liberated ions are single protons from the light hydrogen atoms in water and hydrocarbon contaminants on the back surface of the foils. These protons are accelerated to MeV speeds over just a few microns and exhibit high directionality and energy content. In the final section, I show that proton beams easily reach our requirements for heating to WDM temperatures, but that velocity dispersion can cause the overall timescale of heating to be longer than we'd like, unless sufficient steps are taken to eliminate the slower protons and ions from the picture.

## 4.1 Source requirements

Although the boundaries defining warm dense matter aren't firm, a temperature of $\sim$1 eV (or $\sim$10,000 K[1]) is usually quoted for the lower boundary of temperature in metals such as aluminum. From statistical mechanics [Rei98] we know that a temperature of 1 eV implies an energy content of $\frac{1}{2}$ eV per degree of freedom, which in a 3-dimensional ideal gas would be $\frac{3}{2}$ eV *per atom.* In the non-ideal case the number of degrees of freedom is a complicated problem depending on the model used for the equation of state and the level of ionization. For simplicity, I will set the bar that a viable heating source should deposit at least 1 eV/atom in the sample.

Let $\mathsf{E}$ be the deposited energy per atom into a volume element our heated

---

[1] 1 eV = k·11,604.5 K, where k is Boltzmann's constant

sample. This energy is due to an absorbed flux:

$$\mathcal{F}_{abs} \quad = \quad \mathsf{E} n\Delta x,$$

where $\Delta x$ is the thickness of material over which the absorption takes place, and $n$ is the atomic density. Let's assume that we're only dealing with one type of heating particle (e.g., protons or x-rays), and that they are all coming from the same direction. Then the absorbed flux depends on the number per unit area $\mathcal{N}$ of heating particles and their average energy deposition $\Delta\mathcal{E}$ over the length $\Delta x$ of our volume element, and we have $\mathcal{F}_{abs} = \mathcal{N}\Delta\mathcal{E}$. Taking the volume element to be infinitesimally small, we can frame the problem in terms of differentials. For a given material composition, the quantity $\frac{1}{n}\frac{d\mathcal{E}}{dx}$ will usually be a function of the heating particle's energy $\epsilon$, so that for a monoenergetic source:

$$\mathsf{E}(x) \quad = \quad \mathcal{N}\frac{1}{n}\frac{d\mathcal{E}}{dx}[\epsilon]. \tag{4.1}$$

More generally, there will be a distribution of energies, so let $\mathcal{N}_\epsilon$ be the number per unit area per unit energy of the heating particles with energy $\epsilon$. This gives:

$$\mathsf{E}(x) \quad = \quad \int_\epsilon \mathcal{N}_\epsilon \frac{1}{n}\frac{d\mathcal{E}}{dx}[\epsilon]. \tag{4.2}$$

### Example: Si $K_\alpha$ heating Al

Consider the case of silicon $K_\alpha$ - the production of which I describe later in the chapter - heating solid density aluminum sample, where the source is taken to be a uniformly emitting disk of radius $R$ that is a distance $D$ away from the sample (figure 4.1). This approximately models our two-foil experiments in which a thin laser-irradiated silicon foil is separated by a vacuum gap from a foil of aluminum. Since an atom emitting a $K_\alpha$ photon does so in a random direction, we can use the

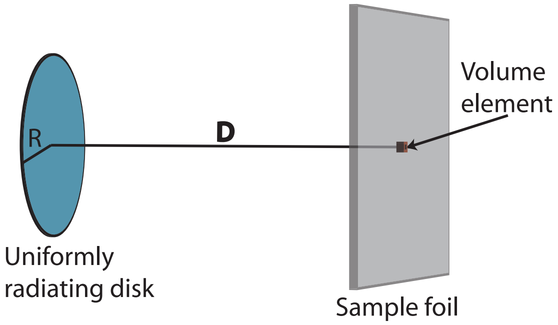

Figure 4.1: Geometry of the uniformly radiating disk source. Source is taken to be flat with radius R, each point of the source radiating equally in all directions. The sample is a distance R away and we focus on a point centered over the middle of the disk.

equation for a disk that uniformly emits $N$ photons[2]:

$$\mathcal{N}(D;R) \quad = \quad \frac{N}{2\pi R^2}\left(1-\frac{D}{\sqrt{D^2+R^2}}\right) \tag{4.3}$$

A silicon $K_\alpha$ photon has an energy of 1740 eV [Vau86], which is strongly absorbed due to photo-ionization of the K-shell in aluminum (figure 4.9) [HGD01]. The $1/e^2$ attenuation length $\mu_L$ of Si $K_\alpha$ in solid density Al is 1.154 $\mu m$, e.g. $I[SiK_\alpha] = e^{-x/\mu_L} = e^{-x/1.154\,\mu m}$. Thus, we have:

$$\begin{aligned}
\frac{1}{n}\frac{d\mathcal{E}}{dx}[Si\,K_\alpha : Al] &= \frac{1}{n_{Al}}\frac{\epsilon_{[Si\,K_\alpha]}}{\mu_L}e^{-x/\mu_L} \\
&= \left(\frac{1}{6.02\times 10^{10}\,\mu m^{-3}}\right)\left(\frac{1740\,eV}{1.154\,\mu m}\right)e^{-x/1.154\,\mu m} \\
&= \left(2.5\times 10^{-8}\,eV\cdot\mu m^2\right)e^{-x/1.154\,\mu m} \qquad (4.4)
\end{aligned}$$

---

[2] When I speak of the "total" $K_\alpha$ emission, I am actually referring to the emission per $4\pi$ steradians measured in the normal direction behind the foil. The actual total emission will be less because photon reemission at off-normal angles is greater. This is common practice in the literature, I suppose because it gives higher numbers than "per steradian."

Plugging (4.4) and (4.3) into (4.1), we obtain:

$$\mathsf{E}(x) \;\approx\; \frac{N}{2\pi R^2}\left(1-\frac{D}{\sqrt{D^2+R^2}}\right)\left(2.5\times10^{-8}\,eV\cdot\mu m^2\right)e^{-x/1.154\,\mu m}, \quad (4.5)$$

where $x$ is the distance into the Al foil, $N$ is the "total" number of Si $K_\alpha$ photons (extrapolated into $4\pi$ str.), $D$ is the distance between the two foils, and $R$ is th radius of our disk source. The equation is approximate because we ignored the 2-D nature of the photon absorption from various angles, but this approximation will lead us to the same general conclusions as the more rigorous result while giving a clear picture of the parameter space.

Now equation 4.5 leads us to an expression for the number of $K_\alpha$ photons we would have to produce to reach a given energy content $\mathsf{E}_{req}$:

$$N \;\geq\; \left(2\pi R^2\right)\left(1-\frac{D}{\sqrt{D^2+R^2}}\right)^{-1}\left(4\times10^7\right)e^{x/1.154}\cdot\mathsf{E}_{req}, \quad (4.6)$$

where distances are given in units of $\mu m$ and $\mathsf{E}_{req}$ is in $eV/atom$.

In figure 4.2, I have used equation 4.6 to plot the required Si $K_\alpha$ to heat an Al foil to a minimum internal energy of 1 $eV/atom$ for various two-layer target configurations. In the figure I have replaced $N$ with the $K_\alpha$ conversion efficiency from a 10 J laser pulse, by $\{\text{conv. eff.}\} = \left(\frac{N\cdot 1740eV}{10J}\right)\left(\frac{1.602\times10^{-19}J}{eV}\right)$. The heating is evaluated at the back side of the sample foil. For reference, I have included three published values for conversion efficiency into $K_\alpha$ photons that give a representative range. We see that heating to lower WDM temperatures using a foil laser generated $K_\alpha$ source is at least feasible.

In the next section I will discuss intense laser-solid interactions, which give rise to the fast electrons that are responsible for generating x-rays and proton beams from a foil source.

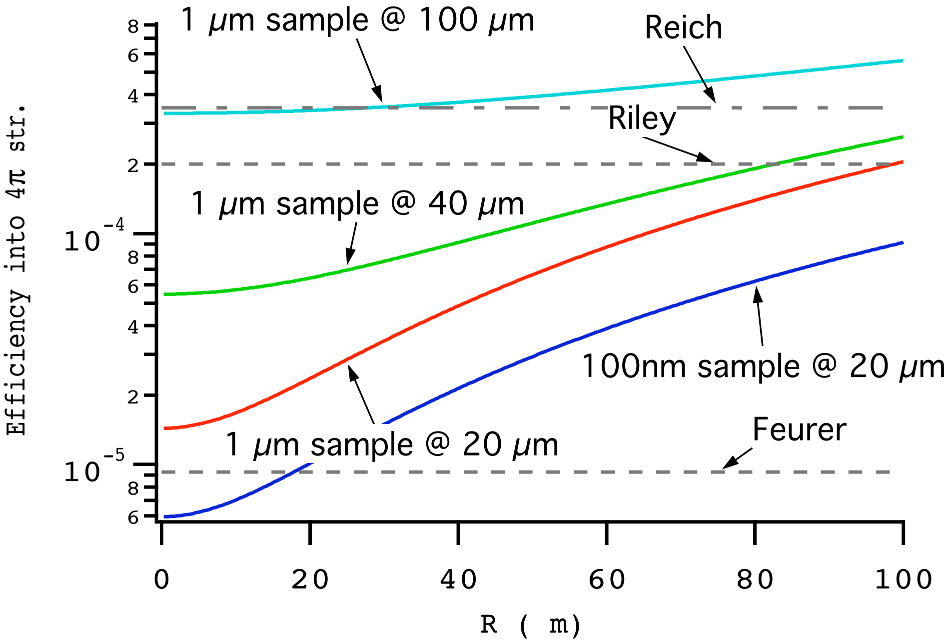

Figure 4.2: Required conversion efficiency into Si $K_\alpha$ to heat an Al sample by 1 eV/atom as a function of source radius R for various target configurations. Foil separations of 20, 40, and 100 $\mu m$ are considered for Al sample foils of thickness 1 $\mu m$ and 100 nm. For reference, conversion efficiencies from Reich, et al.[RGUF00], Riley, et al.[RKPdS$^+$06], and Feurer, et al. [FMU$^+$01] are plotted.

## 4.2 Intense laser-solid interactions

The physics of ultra-intense laser interaction with solids is almost always framed in terms of interaction of the laser with a pre-formed plasma. Indeed, the electric field of a focused terawatt laser pulse is much higher than the field binding electrons to the atoms in the material, and ionization will occur well in advance of the main pulse. This is evident in the semi-classical expression for the threshold intensity needed to ionize an atom to a charge state $\tilde{Z}$ and ionization potential $I_p$ [Mal04][3]:

$$I_{\text{threshold}}[W/cm^2] \approx 4 \times 10^9 \frac{(I_p[eV])^4}{\tilde{Z}^2}. \qquad (4.7)$$

So that, e.g., we'd expect hydrogen ($I_p = 13.6\ eV$) to be fully ionized at just over $10^{14}\ W/cm^2$, which is several orders of magnitude less than the intensities shot on terawatt and petawatt facilities. Equation 4.7 represents an extreme case, in which the classical potential well binding the electron in is completely suppressed, which is referred to as above threshold ionization. In fact, quantum tunneling allows ionization to begin at even lower intensities[ADK86]. Once an electron is free, the laser field can accelerate it so that it collides with an atom and frees another electron, which can also be used in this way to free other electrons, and so on, in a proccess known as "avalanche" ionization. The threshhold intensity to produce a critical density of free electrons in this way is $\sim 10^{12}\ W/cm^2$ [AAB$^+$06, SFH$^+$96].

Thus for the arrival of an ultrashort, ultraintense laser pulse we expect a plasma to already be in place, and we also expect it to have a density gradient in which the electron density goes smoothly from zero, to the so-called critical density surface, and beyond to solid density (solid density being more than an order of magnitude higher than the critical density). The laser will reflect at or before the critical density surface, with only an exponentially decaying evanescent wave

---

[3] The reference has a typo in leaving out the fourth power of $I_p[eV]$ in his equation (1.6) but is otherwise correct.

continuing beyond the reflection plane. The electrons under the influence of the laser will oscillate in sync at the so-called "quiver velocity," given by[WK97]:

$$\frac{v_{osc}}{c} = \frac{eE}{m_e\, c\, \omega} \quad = \quad \sqrt{\frac{I\lambda_\mu^2}{1.37 \times 10^{18}}}, \tag{4.8}$$

Where $v_{\mathrm{osc}}$ can exceed $c$ and is hence not a true velocity in the relativistic case; $v_{\mathrm{osc}}/\gamma$ gives the true peak velocity expected in oscillation. Without any absorption mechanisms whatsoever, the electron's energy would travel into and out of the plasma with no heating. In fact, collision cross sections are quite low at the extreme quiver velocities implied by the laser's peak power, and energy absorption by the most straightforward method we can think of, collisions between ions an electrons (e.g., inverse bremsstrahlung), is indeed rather low. And yet ultra-intense laser pulses can be absorbed very strongly, under the right conditions by well over 50%.

I will start with the basic fluid treatment of plasmas to introduce plasma waves, which play a key role in transporting energy away from the oscillations of the laser field under the mechanism of resonance absorption. I will then describe the propagation of the laser wave in a 1-dimensional plasma gradient (i.e. a slab), which leads into that resonance. I will then discuss two other important absorption mechanisms, vacuum heating and $J \times B$ heating. I will then discuss how a real laboratory CPA system affects the plasma scale length which, along with laser intensity, is a key parameter in determining which absorption mechanism dominates.

### 4.2.1 The fluid treatment of plasmas

A great deal of intuitive and computational simplicity can be obtained by modeling a plasma in terms of a fluid with charged constituents[HW98]. Then instead of imagining a collection of quintillions of charged particles, each with their own position and momentum, we can think in terms of macroscopic quantities such as charge density, temperature, and current. We start, in much the same fashion as is done in hydrodynamics, by representing our system of charged particles with single-particle distribution functions $\mathcal{F}_s(\mathbf{x}, \mathbf{v}, t)$. Here $s$ represents the various species, i.e., the electrons and various charge states of ions involved. In the *two-fluid* description, which is used in the initial derivations of laser-plasma interactions, we assume that we are dealing with a fully ionized and overall neutral plasma of one element, and hence we'd have only $s = e$, for the electrons and $s = i$ for the fully stripped ions, with $n_e = Zn_i$, $Z$ being the atomic number.

$\mathcal{F}_s$ integrates to the particle density:

$$\int d^3v \mathcal{F}_s(\mathbf{x}, \mathbf{v}, t) \quad = \quad n_s(\mathbf{x}, t).$$

Saying that particles are neither created nor destroyed in our system is equivalent to the equation[4]:

$$\frac{\partial \mathcal{F}}{\partial t} + \mathbf{v} \cdot \nabla \mathcal{F}_s + \mathbf{a}_s \cdot \frac{\partial \mathcal{F}_s}{\partial \mathbf{v}} \quad = \quad 0, \tag{4.9}$$

where the species acceleration $\mathbf{a}_s$ is dominated by the Lorenz force:

$$\mathbf{a}_s \quad = \quad \frac{e_s}{m_s}(\mathbf{E} + \mathbf{v} \times \mathbf{B}), \tag{4.10}$$

and $m_s$ is the mass and $e_s$ is the charge. At this point we haven't done much: $n_s(\mathbf{x}, t)$ looks like a collection of delta functions at the individual particle positions, so this is still a lot like treating each individual particle separately. The key to having a fluid treatment is to consider a statistical ensemble of equivalent systems and average over them, preserving only density fluctuations of interest and paying less close attention to the exact positions and velocities of each particle. Thus we

---

[4] when particles *can* be created or destroyed, as in processes such as ionization or recombination, we can replace the 0 on the right hand side with a source term $I_s(\mathbf{x}, \mathbf{v}, t)$.

want to use the ensemble-averaged distribution function:

$$f_s = \langle \mathcal{F} \rangle_{ensemble}. \tag{4.11}$$

We'd like to plug $f_s$ into (4.9), but the last term on the left hand side brings correlations between particles into play. Thus the correct version of (4.9) for $f_s$ is actually:

$$\frac{\partial f}{\partial t} + \mathbf{v} \cdot \nabla f_s + \mathbf{a}_s \cdot \frac{\partial f_s}{\partial \mathbf{v}} = C_s(f), \tag{4.12}$$

where $C_s(f)$ is the so-called *collision operator*, a complicated and challenging term designed to collect the relevant effects of correlations between particles. For a problem in which collisions are negligible, $C_s(f) = 0$, and we get back to the same form as (4.9) in what is known as the Vlasov equation:

$$\frac{\partial f}{\partial t} + \mathbf{v} \cdot \nabla f_s + \mathbf{a}_s \cdot \frac{\partial f_s}{\partial \mathbf{v}} = 0. \tag{4.13}$$

As much of a simplification as it implies, the Vlasov equation can be useful as a starting point in many problems, especially the electrostatic oscillations of plane waves within the plasma.

The distribution function is used by taking its *moments*, or velocity integrals of different order. This gives tensors of increasing rank, the first few of which have simple interpretations:

$$\begin{aligned} n_s(\mathbf{x},t) &= \int d^3v f_s(\mathbf{x},\mathbf{v},t) \\ \mathbf{V}_s(\mathbf{x},t) &= \frac{1}{n_s}\int d^3v f_s(\mathbf{x},\mathbf{v},t)\mathbf{v} \\ \mathbf{P}_s(\mathbf{x},t) &= \int d^3v f_s(\mathbf{x},\mathbf{v},t) m_s \mathbf{v}\mathbf{v} \\ &\text{...etc.} \end{aligned} \tag{4.14}$$

We already know the zeroth-order moment, $n_s$, as the particle density. With the first-order moment, $\mathbf{V}_s$, is the plasma flow velocity. The second-order moment $\mathbf{P}_s$, called the stress tensor, describes the flow of momentum. We retrieve the ordinary pressure from

$$\mathrm{p}_s = \frac{1}{3}Tr(\mathbf{p}_s); \qquad \mathbf{p}_s \ = \ \mathbf{P}_s - m_s n_s \mathbf{V}_s \mathbf{V}_s. \tag{4.15}$$

The moments continue on and the next few also have conceptually meaningful interpretations. However, for simplicity I will leave them out of my discussion, since I won't need to refer to the higher moment equations. The next step is to take the moments of the Vlasov equation (4.13):

$$\begin{aligned} \int d^3v \left( \frac{\partial f}{\partial t} + \mathbf{v} \cdot \nabla f_s + \mathbf{a}_s \cdot \frac{\partial f_s}{\partial \mathbf{v}} \right) &= 0 \\ \int d^3v \mathbf{v} \left( \frac{\partial f}{\partial t} + \mathbf{v} \cdot \nabla f_s + \mathbf{a}_s \cdot \frac{\partial f_s}{\partial \mathbf{v}} \right) &= 0 \\ &\text{...etc.} \end{aligned} \tag{4.16}$$

With integration by parts, and using the values I just defined, we obtain the following for the first two moments:

$$\begin{aligned} \frac{\partial n_s}{\partial t} + \nabla \cdot (n_s \mathbf{V}_s) &= 0 \\ m_s \frac{\partial n_s \mathbf{V}_s}{\partial t} + \nabla \cdot \mathbf{P}_s - e_s n_s (\mathbf{E} + \mathbf{V}_s \times \mathbf{B}) &= 0 \end{aligned} \tag{4.17}$$

A trend that continues through all moments becomes evident here: the first expression involves both the zero- and first- order moments of the distribution function, $n_s$ and $\mathbf{V}_s$, while the next equation also needs the second-order moment $\mathbf{P}_s$. Closure then requires some statement about how the moments might either drop off or truncate as we go further. Without some form of closure, all we have are an infinite chain of coupled equations that don't solve anything. Truncation is the simplest form of closure, and that is what is used in the description of electrostatic plasma waves.

### The Debye Length

The Vlasov equation (4.13) ignores collisions and focuses on collective motion in order to simplify the equations for wave propagation in a plasma. Whether or not a process in a plasma is relevant is a question of relative rates. In [Kru88] a convenient expression for the separation between collective and collisional regimes is given:

$$\frac{\nu_{90}}{\omega_{pe}} \propto \frac{Z}{N_D}, \tag{4.18}$$

where $\nu_{90}$ is the rate of significant (90°) collisions, $\omega_{pe}$ is the plasma frequency, and $N_D = n_e 4\pi\lambda_D^3$ is the number of electrons in a Debye sphere. Clearly, as $N_D \rightarrow \inf$, plasma collisions become unimportant relative to collective motion. The quantity $\lambda_D$, known as the Debye length, is an important plasma quantity describing the length scale over which an electron's individual coulomb field is shielded by the other electrons in the plasma. If $\phi$ is the potential due to a particular electron in a plasma, then

$$\phi = \frac{q}{r}e^{-r/\lambda_D}. \tag{4.19}$$

For a classical, isothermal plasma,

$$\lambda_D = \sqrt{\frac{kT_e}{4\pi n_e e^2}}. \tag{4.20}$$

The Debye length sets the length scale above which we can ignore the individual electrons and treat the plasma as a fluid. Perhaps counter-intuitively, more electrons are present in a Debye sphere as the density *decreases*: $N_D \rightarrow \inf$ as $n_e \rightarrow 0$. This simply means that in a very hot and/or very sparse plasma, collisions become unimportant.

As is normally done, I will introduce plasma waves in the context of the Vlasov equation, and bring collisions into the picture only when necessary.

### 4.2.2 Plasma waves

In a non-magnetized plasma, there are two types of waves: high frequency electron waves and low frequency ion-acoustic waves. Both rely on truncation of the moment equations through a simple equation of state approximation.

#### Electron plasma waves

These waves are modeled as high-frequency/cold-plasma waves, where the phase velocity $\omega/k \gg v_e$, the electron thermal velocity. Because they are electrostatic, the waves are longitudinal, and we can operate in one dimension. The high phase velocity relative to thermal velocity means that we can ignore heat flow and still have a pretty good approximation. This truncates the moment equations by way of a (one dimensional) adiabatic equation of state:

$$\frac{\mathrm{p}_e}{n_e^3} = \text{constant.} \tag{4.21}$$

Again, we are treating the ions as a stable neutral background, and focusing on the electrons ($s \to e$). Writing equations (4.17) with (4.15) in one dimension and substituting $\mathbf{V}_e \to u_e$, the 1-dimensional velocity, we have [Kru88]:

$$\frac{\partial}{\partial x}(n_e u_e) + \frac{\partial n_e}{\partial t} = 0 \tag{4.22}$$

$$\frac{\partial}{\partial t}(n_e u_e) + \frac{\partial}{\partial x}(n_e u_e^2) + \frac{n_e e E}{m_e} + \frac{1}{m_e}\frac{\partial \mathrm{p}_e}{\partial x} = 0. \tag{4.23}$$

Taking $\frac{\partial}{\partial t}$ of the first and $\frac{\partial}{\partial x}$ of the second to eliminate the first term:

$$\frac{\partial^2 n_e}{\partial t^2} - \frac{\partial^2}{\partial x^2} - \frac{e}{m_e}\frac{\partial}{\partial x}(n_e E) - \frac{1}{m_e}\frac{\partial^2 \mathrm{p}_e}{\partial x^2} = 0 \tag{4.24}$$

To first order in small perturbations of the electron density $n_e = n_0 + \tilde{n}$, velocity $u_e = \tilde{u}$, pressure $\mathrm{p}_e = \mathrm{p}_0 + \tilde{\mathrm{p}}$, and electric field $E = E_0 + \tilde{E}$, equations (4.21), (4.24), and Poisson's equation become, respectively:

$$\tilde{\mathrm{p}} = 3\frac{\mathrm{p}_0}{n_0}\tilde{n} \tag{4.25}$$

$$\frac{\partial^2 \tilde{n}}{\partial t^2} - \frac{n_0 e}{m_e}\frac{\partial \tilde{E}}{\partial x} - \frac{1}{m_e}\frac{\partial^2 \tilde{\mathrm{p}}}{\partial x^2} = 0 \tag{4.26}$$

$$\frac{\partial \tilde{E}}{\partial x} = -4\pi e\tilde{n} \tag{4.27}$$

Substituting (4.27) and (4.25) into (4.26) and recognizing that $\frac{\mathrm{p}_0}{m_e n_0} = v_e$, the electron thermal velocity of the stationary (isothermal) background plasma, we obtain the wave equation:

$$\left(\frac{\partial^2}{\partial t^2} - 3v_e^2\frac{\partial^2}{\partial x^2} + \omega_{pe}^2\right) = 0, \tag{4.28}$$

where $\omega_{pe} = \sqrt{4\pi e^2 n_0/m_e}$ is the electron plasma frequency. Solving this with, $\tilde{n} \sim e^{ikx - i\omega t}$, we find the dispersion relation:

$$\omega^2 = \omega_{pe}^2 + 3k^2 v_e^2. \tag{4.29}$$

We started with the assumption $\omega \gg v_e$, we see that all such waves are very close to the plasma frequency, with small corrections depending on the temperature and wave number.

**Ion acoustic waves**

The low frequency ion acoustic wave is derived in a similar fashion. With the assumption $v_e \gg \omega/k \gg v_i$, the electrons are taken to stay close with the oscillating ions and follow an isothermal equation of state, $\mathrm{p}_e = n_e\theta_e$, while the ions follow the adiabatic EOS seen earlier $\frac{\mathrm{p}_i}{n_i} = constant$. The resulting dispersion relation for ion-acoustic waves is:

$$\omega \quad = \quad \pm k v_s, \tag{4.30}$$

where $v_s = \sqrt{(Z\theta_e + 3\theta_i)/M}$, $\theta_s$ being the species temperature, $Z$ the atomic number, and $M$ the ion mass.

### 4.2.3 Laser propagation in a slab plasma

An incident laser field will drive the electrons in a plasma to oscillate at the laser frequency $\omega_0$, where $\omega_0 \gtrsim \omega_{pe}$. At these frequencies we continue to consider the ions as a stationary neutralizing background. We start by working with the assumption that electron motion is non-relativistic, so that products of quantities involving $\mathbf{V}_e$ and $\mathbf{B}$ can be neglected, and motion of the electrons is driven by the electric field. We consider a single-frequency laser oscillation:

$$\mathbf{E} = \mathbf{E}(\mathbf{x})e^{-i\omega t} \quad , \quad \mathbf{B} = \mathbf{B}(\mathbf{x})e^{-i\omega t}. \tag{4.31}$$

The electric field drives the electrons [Kru88]:

$$\frac{\partial \mathbf{V}_e}{\partial t} \quad = \quad -\frac{e}{m_e}\mathbf{E}(\mathbf{x})e^{-i\omega t}. \tag{4.32}$$

Rewriting this in terms of the current density $\mathbf{J} = -n_e(\mathbf{x})e\mathbf{V}_e$ and the plasma frequency, $\omega_p^2 = 4\pi e^2 n_0/m$ [Kru88]:

$$\begin{aligned} \frac{\partial \mathbf{J}}{\partial t} &= \frac{\omega_{pe}^2(\mathbf{x})}{4\pi}\mathbf{E} \\ \Rightarrow \mathbf{J} &= \sigma \mathbf{E}, \end{aligned}$$

where $\sigma = i\omega_{pe}^2/4\pi\omega$ is the high-frequency conductivity. Thus, the electric field is driving current, which will drive a magnetic field, which will in turn affect the electric field. Applying Maxwell's equations, specifically Faraday's law and Ampere's law (linearized), one will arrive at wave equations for the electric and magnetic fields [Jac98, Kru88]:

$$\nabla^2\mathbf{E} - \nabla(\nabla\cdot\mathbf{E}) + \frac{\omega^2}{c^2}\epsilon\mathbf{E} = 0 \tag{4.33}$$

$$\nabla^2\mathbf{B} + \frac{\omega^2}{c^2}\epsilon\mathbf{B} + \frac{1}{\epsilon}\times(\nabla\times\mathbf{B}) = 0, \tag{4.34}$$

where $\epsilon = 1-\omega_{pe}^2/\omega^2$ is the plasma dielectric function. In a uniform density plasma, $\nabla\epsilon = 0$ and $\nabla\cdot\mathbf{E} = 0$, and with $\exp(i\mathbf{k}\cdot\mathbf{x})$ spatial dependence of the waves, we arrive at the dispersion relation for both $\mathbf{B}$ and $\mathbf{E}$ of:

$$\omega^2 = \omega_{pe}^2 + |\mathbf{k}|^2 c^2. \tag{4.35}$$

The fact that $|\mathbf{k}|$ must be negative for frequencies $\omega < \omega_{pe}$ means that $\mathbf{k}$ is entirely imaginary and any light wave would decay exponentially. Hence the density at which $\omega_{pe} = \omega$ is referred to as the critical density $n_{cr} = \omega^2 m_e/4\pi e^2$.

### 4.2.4 Collisional absorption

Electrons oscillating under the influence of an electromagnetic wave can dissipate the wave's energy into the plasma by undergoing collisions. The most important form of collisional absorption is known as inverse bremsstrahlung, because it is a process by which an electron absorbs a photon in the vicinity of an ion. Based on a simple theoretical model fractional intensity absorption of this process is given by [WK97]:

$$f_{ib} \quad \approx \quad 1 - \exp\left(\frac{32}{15}\frac{L_n}{c}\nu_{ei}(n_{cr})\right), \tag{4.36}$$

where $\nu_{ei} \propto \frac{n_{cr}Z}{(kT_e)^{3/2}}$ is the electron-ion collision frequency and $L_n \equiv n_e(\nabla n_e)^{-1}$ is the plasma scale length (linear profile). Thus $L_n/c$ is a characteristic time for a photon traversing the plasma, and we are basically comparing that time to the time between electron-ion collisions.

At very high intensities, the above expression becomes far too large due to incorrect assumptions about the electron motion. For very fast moving electrons, collision cross sections are reduced greatly, and collisional absorption fails to explain the high absorption that occurs for intensities exceed $10^{15}W/cm^2$ [GF96]. To explain this, *collisionless* models are needed.

### 4.2.5 Resonance absorption

Let an incident electromagnetic wave be incident with an angle $\theta$ relative to the $z$ direction on a slab plasma that is uniform in the $x$ and $y$ directions and has a density gradient in the $z$ direction. Let the density increase continuously from $n_e = 0$ at $z = 0$ to $n_{cr}$ at $z = L$, and continue to grow above $n_{cr}$ for $z > L$ (fig. 4.3). The electric field of the wave can either be in the $x$ direction (s-polarization) in which case it oscillates along a constant density, or it can have a component in the $z$ direction (p-polarization), along the density gradient, which leads to charge density fluctuations. I'll start with the former case.

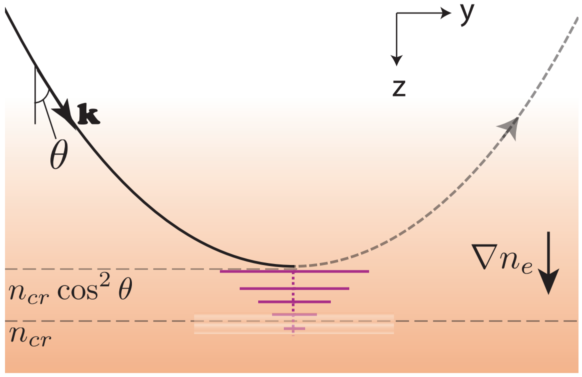

Figure 4.3: Geometry of the resonance absorption problem. A plane light wave incident at an angle $\theta$ to a uniform plasma gradient in the $z$ direction. The wave reflects at $n_e = n_{cr}\cos^2\theta$ but persists past that plane with an exponential falloff.

### S-polarization

When the electric field $\mathbf{E}$ is entirely in the x direction, $\mathbf{E} = E_x\hat{x}$. With $\epsilon$ a function of $z$ only, $k_y$ never changes, e.g., $k_y = (\omega/c)\sin\theta$. Thus eqn. (4.33) becomes[Kru88]:

$$\frac{\mathrm{d}^2E(z)}{\mathrm{d}z^2} + \frac{\omega^2}{c^2}\left(\epsilon(z) - \sin^2\theta\right)E(z) \quad = 0 \quad . \tag{4.37}$$

The light wave can propagate no further in the z-direction when $\epsilon(z) = 1 - \omega_{pe}^2(z)/\omega^2 = \sin^2\theta$, and so $n_e = n_{cr}\cos^2\theta$ defines a plane of reflection, beyond which $\mathbf{E}$ decays exponentially.

### P-polarizaton

When the electric field $\mathbf{E}$ is P-polarized, we have $\mathbf{E} = E_y\hat{y} + E_z\hat{z}$. Poisson's equation for the neutral plasma, $\nabla(\epsilon\mathbf{E}) = 0$ gives:

$$\nabla\cdot\mathbf{E} \quad = \quad -\frac{1}{\epsilon}\frac{\partial\epsilon}{\partial z}E_z. \tag{4.38}$$

This implies an electrostatic oscillation that has a resonance at $\epsilon = 0$, e.g., at the critical density surface. A plasma wave is excited there by whatever portion of the $z$ component of the electric field reaches that point. A key assumption here is that the density not change appreciably over the path of the oscillating electrons in the plasma wave. Thus this model is most accurate when $L_n \equiv n_e(\nabla n)^{-1} \gg \lambda_0$.

The electric field decays exponentially past $n_{cr}\cos^2\theta$, as in the s-polarized case, and so there is a balance: when $\theta = 0$ there is no $z$ component of the electric field to start with. However, the larger the value of $\theta$ the further the reflection plane at $n_{cr}\cos^2\theta$ gets from the critical density surface, meaning that the wave suffers more exponential decay in getting to the resonance plane. It is clear that the details of $\nabla n$ are important in determining this balance.

Now $\mathbf{B} = B_x\hat{x}$ is the s-polarized wave and we can use $k_y = (\omega/c)\sin\theta$ for it.

$$B_x = B(z)e^{-i\omega t + i(\omega/c)y\sin\theta} \tag{4.39}$$

Ampere's law gives:

$$\begin{aligned} -\frac{i\omega}{c}\epsilon\mathbf{E} &= \nabla\times\mathbf{B} \\ \implies E_z &= \frac{B(z)\sin\theta}{\epsilon(z)} \end{aligned} \tag{4.40}$$

Using the approximation $E_z = E_d/\epsilon(z)$, where $E_d$ is evaluated at the critical density, one finds [Kru88]:

$$\frac{E_d}{\epsilon(z)} = \frac{E_L}{\sqrt{2\pi\omega L_n/c}}\phi(\tau) \tag{4.41}$$

Where $L_n \equiv n_e(\nabla n_e)^{-1}$ is the plasma scale length, $\tau = (\omega L_n/c)^{1/3}$, and $\phi(\tau) \approx 2.3\tau\exp(-2\tau^3/3)$. We aren't actually dividing by zero at the critical density layer because $\epsilon$ will always contain a small damping term $\nu \ll \omega_{pe}$:

$$\epsilon(z) \quad = \quad 1 - \frac{\omega_{pe}^2(z)}{\omega(\omega + i\nu)}. \tag{4.42}$$

In this equation, $\nu$ usually refers to a collisional damping term, but other phenomenological damping can also be included in eqn (4.33) to account for collisionless effects, such as particle trapping or wave breaking [FKL$^+$75, Kru88]. The fraction of absorbed energy can then be approximated as [WK97]:

$$f_{ra} \approx \frac{\phi^2(\tau)}{2}; \qquad \phi(\tau) \approx 2.3\tau \exp(-2\tau^3/3) \tag{4.43}$$

This expression for $\phi(\tau)$ is very close to the exact result [Gin64] and has the same shape, with a peak at $\tau \approx 0.8$ reaching $\approx 50\%$ absorption. Resonance absorption was studied by many authors through the 80s and 90s, by numerical or particle-in-cell simulation and many experiments. Summarizing a large number of papers, Wilks, *et al.* [WK97] summarize the parameters for which resonance absorption is expected to be a dominant mechanism of laser light absorption:

$$\begin{aligned} I\lambda^2 &< 10^{17}\, W \cdot \mu m/cm^2; \\ L_n &\geq 0.1\lambda. \end{aligned} \tag{4.44}$$

In this range it is estimated [FKL$^+$75] that the temperature of electrons heated by way of resonance absorption should scale as :

$$T_{hot} \quad \propto \quad (I\lambda_\mu^2)^{1/3}, \tag{4.45}$$

With temperatures in the 10s of keV in the range given in (4.44) [WK97]. In ultra-short pulsed lasers resonance absorption continues to contribute at even higher intensities, although other mechanisms begin to take over. Next I will describe a short scale length process, which was originally called "'not so resonant' resonant absorption" [Bru87]:

### 4.2.6 Vacuum heating

In the opposite extreme of plasma scale length, we may imagine a plasma with a density gradient that is very sharp relative to the electron excursion distance. Then, rather than exciting a plasma wave, the laser pulls electrons out into vacuum, with the stationary ions staying behind. This leads to a charge separation, and hence a field given by Poisson's equation. This field is balanced by the combined field in the $z$ direction of the incoming and outgoing laser wave, which in the case of perfect reflection would be $E_d = 2E_L \sin\theta$, where $E_L$ is the vacuum laser field. In fact, this driving field is better approximated by taking absorption into account, in which we would have $E_d = E_L[1 + (1-f)^{1/2}]\sin\theta$, where $f$ is the fraction of laser intensity absorbed (by whatever mechanism). When the field reverses direction, the electrons are thrown back into the over-dense plasma, where the electric field of the laser on the next cycle can no longer grab them and turn them around. Thus on the next laser cycle, new electrons are being dragged out into vacuum. The absorbed laser intensity due to vacuum heating under this model was given by Brunel [Bru87]:

$$f_{vh} = \frac{\eta}{\pi} c\tilde{v}_d \left( \sqrt{1 + \frac{\tilde{v}_d^2}{c^2}} - 1 \right) \Bigg/ (\tilde{v_L}^2 \cos\theta), \tag{4.46}$$

where $\tilde{v}_L = eE_L/m_e\omega$ and $\tilde{v}_d = eE_d/m_e\omega$ are just shorthand symbols for $\gamma v_d$ in eqn. 4.8 for the respective laser fields. Here $\eta \approx 1.75$ is derived from simulations [WK97]. Note that this expression still implicitly contains the absorption, through $v_d$. Since vacuum heating isn't necessarily the only absorption mechanism, $E_d$ is only calculated when all absorption mechanisms are taken into account.

Simulations [Bru87, GB92] have shown demonstrated that the hot electron temperature due to electrons receiving these vacuum heating "kicks" scales as:

$$T_{hot} \propto (I\lambda_\mu^2)^{1/3-1/2}. \tag{4.47}$$

This seems to indicate a smooth transition between the scaling of resonance absorption and ideal vacuum heating as described above. The range of intensities and scale lengths for which vacuum heating is considered a major contributor to laser absorption is:

$$\begin{aligned} 10^{15}\, W \cdot \mu m/cm^2 < \quad I\lambda_\mu^2 &< 10^{18}\, W \cdot \mu m/cm^2; \\ L_n &\leq 0.1\lambda. \end{aligned} \tag{4.48}$$

In this range, vacuum heating can lead to electron temperatures from 10s to 100s of keV [WK97]. It's important to note that in vacum heating hot electrons are expected to be launched in the target normal direction. I'll now consider an absorption mechanism which tends to accelerate very hot electrons in the laser direction, for very high intensities.

### 4.2.7 J×B heating

When the laser intensity is high enough, it is not sufficient to consider laser acceleration only in terms of the electric field: we need also to consider the forces due to the laser's magnetic field $\mathbf{B} = \omega^{-1}\mathbf{k} \times \mathbf{E}$, as well as relativistic effects. For this we refer to the Lorentz force due to an electromagnetic field:

$$\mathbf{F} = \frac{d(\gamma m \mathbf{v})}{dt} = q\left(\mathbf{E} + \mathbf{v} \times \mathbf{B}\right). \tag{4.49}$$

Here I include the relativistic $\gamma = \left(1 - \frac{|\mathbf{v}|^2}{c^2}\right)^{-1/2}$ to emphasize that relativistic effects may come into play. Notice that if an electron is accelerated to a significant velocity by the $\mathbf{E}$ field, the $\mathbf{v} \times \mathbf{B}$ component of the force will push it in the forward ($\mathbf{k}$) direction, with peak forces occurring twice per laser cycle. This aspect of the Lorentz force is distilled by perturbation analysis to give an equation for the *longitudinal* component of electron fluid motion [WK97]:

$$\begin{aligned} \mathbf{F}_p &= \frac{\partial \mathbf{p}_L}{\partial t} = -\nabla U_p; \\ U_p &= (\gamma - 1) m_0 c^2, \end{aligned} \tag{4.50}$$

where $\gamma_L = \left(1 - \frac{\langle v_{osc} \rangle^2}{c^2}\right)^{-1/2}$ is the relativistic term for the *average* velocity of the oscillating electrons, and $\mathbf{p}_L$ is the electron's longitudinal momentum. Considering the relativistic expression for $v_{osc}$, we can solve for $\gamma_L = (1 - \langle v^2 \rangle / c^2)^{-1/2}$ in terms of the l.h.s. of equation 4.8 to obtain[5] $\gamma_L = \sqrt{1 + \gamma_L v_{osc}^2 / 2c}$ . If we equate $U_p$ to our expected "temperature" of hot electrons created by this method, we arrive at a crude but useful estimate for the accelerated electrons[WK97][6]:

$$T_{hot} \approx \left( \sqrt{1 + \frac{I \lambda_\mu^2}{2.74 \times 10^{18}}} - 1 \right) 511\text{keV}. \tag{4.51}$$

Computer simulations show that the distribution, while not Maxwellian, looks similar to a Maxwellian with an energy cutoff [MM96]. Electrons oscillate in the laser direction under the $J \times B$ forces and can escape the influence of the laser if they are kicked far enough into the over-dense region of the plasma (away from laser influence). This scaling gives us a range of intensities for which this heating method would give us "temperatures" that start to be interesting for x-ray production (e.g.

---

[5] This is for linearly polarized light - in the circularly polarized case the factor of 2 in the denominator is left out.

[6] The reference contained some mildly confusing rounding errors which I have corrected in eqns (4.51) and (4.8)

$T_{hot} > 10$keV):

$$I\lambda_{\mu}^{2} \quad \gtrsim \quad 10^{17}\, W \cdot \mu m/cm^{2} \tag{4.52}$$

Some important features of $J \times B$ heating are more easily seen using the non-relativistic case:

$$\mathbf{F}_{p} \quad = \quad -\frac{e^{2}}{4m\omega^{2}} \nabla E^{2}. \tag{4.53}$$

$$\tag{4.54}$$

Then the force on a plasma fluid element becomes [WK97]:

$$f_{p} \quad = \quad -\frac{\partial}{\partial z} \left( \frac{mv_{osc}^{2}}{2} \frac{4\omega^{2}}{\omega_{pe}^{2}} e^{-2\omega_{pe} z/c} \left[ \frac{1+\cos 2\omega t}{2} \right] \right) \tag{4.55}$$

First, we see that the frequency of the ponderomotive force is twice the frequency of the laser, and hence electrons are launched twice per cycle. Second, the magnitude of the force depends on $n_{cr}/n$, meaning that at higher densities absorption is less efficient. Thus the range of effectiveness for $J \times B$ heating also depends on density. The criteria for $J \times B$ heating to not be overshadowed by vacuum heating can be expressed as [WK97] :

$$\frac{v_{osc}}{c} \frac{\omega}{\omega_{pe}} > \sin \theta. \tag{4.56}$$

Obviously, at $\theta = 0$, this effect is stronger than the previous two discussed until intensities and pulse-lengths are high enough to cause ion motion and distort the surface. Typically, when a ultra intense laser pulse is focused at an angle on a solid target, electrons are seen to be accelerated in two directions. Hot electrons accelerated in the target normal direction are attributed to a vacuum-heating like effect, while the hottest electrons are found to be accelerated predominantly along the laser axis, which is attributed to $J \times B$ acceleration. We will see experimental evidence of the hottest electrons escaping a solid target in the laser axis direction in section 7.2.

### 4.2.8 Precursors and scale length

As we have seen, the density scale length $L_n = n_e(\nabla n_e)^{-1}$ plays an important role in the absorption of laser energy. The short scale length requirement (eqn. 4.48) for vacuum heating, for example, is often used as a criterion for desirable scale length. If a large cloud of sub-critical plasma exists in front of the target, it can even cause defocusing laser through the nonlinear (intensity dependent) index of refraction, or deplete the laser energy through collisional absorption.

Once a plasma is formed by the laser, it will tend to expand outward, increasing in scale length. The hotter the plasma, the faster it will expand. Thus we are concerned with the low-power precursor of the laser pulse. As I discussed in section 3.2.1, in a CPI laser system precursor laser energy must be carefully monitored. Recall that this extraneous laser energy consists of two parts: pre- (and post-) pulses, which are low-intensity echos of the main pulse occurring from zero to several tens of ps before (and after) the main pulse, and the ASE pedestal, which is the uncompressed energy spontaneously emitted from the amplifier stages[7]. A *contrast ratio* of prepulses to main of less than $10^{-5}$ is often considered good, even though at a peak intensity exceeding $10^{18}\,W/cm^2$ such a precursor would still ionize. It is sometimes frustrating that, as Wharton, et al. [WBK$^+$01] have demonstrated, even if the pedestal and prepulses are suppressed to below ionization intensities, the ns-timescale pedestal can heat a foil target to the point of vaporization at well below ionization intensities, leading to a cloud of atoms which is instantly ionized by the rising edge of the laser pulse to create a much longer scale length plasma than would

---

[7] Usually, both of these are referred to as a "prepulse" (or postpulse), but I prefer to refer to the former as "prepulse", and the latter as "ASE pedestal" to distinguish between them.

be expected from early ionization alone. They report that non-ionizing prepulses can have an effect at ASE intensities as low as $10^8\ W/cm^2$, which would require a contrast ratio of $10^{10}$ on even a modest $10^{18}\ W/cm^2$ shot to avoid! Achieving contrast ratios in the $10^{-6}$ range is a challenge [OCR$^+$05]; getting to $10^{-10}$ requires extreme measures.

## 4.3 X-ray generation

As we've seen, the ultrafast laser does not penetrate very far into a solid material, but it can accelerate very fast electrons which do escape the laser plasma interaction region and travel into the cold bulk material behind it. Thus, we have a hot electron source and the generation of x-rays is a somewhat decoupled problem from the laser interaction. The science of fast electrons interacting with matter was well-established by the time ultra-intense lasers entered the picture, and so the same physics that is used in other fields to deal with electron beam interaction with matter can be applied to our predictions about x-ray generation in laser-solid interactions. We will be dealing with an extremely large number of electrons $\sim 10^{12}$, and so in this treatment electrons will be treated statistically. If we followed a single electron through the material, it would suffer a large number of very small collisions which would slow it down gradually as it passed, and with a certain probability a large collision such as one causing $K$-shell ionization or full-energy bremsstrahlung would take place. Rather than tracking an electron up to a large collision and then starting over with a new electron, it is acceptable, because of the large number of electrons, to use the average stopping power of the material as a continuous drain on the electron's energy, turning cross sections for the large, x-ray producing collisions into a fractional rate of emission. Thus an electron of a given energy passing through $1\mu m$ of material would generate a certain fractional number of "photons". When added up over the enormous number of electrons, the difference from a whole number of photons will be negligible. I will start with a description of electron stopping power in a material, to establish how an electron's energy will change as it passes. In the process we will encounter equations for bremsstrahlung, a source of continuous band x-rays which can become significant at high electron energies (requiring very high laser intensities). Next I'll present the cross sections for K-shell ionization, leading to the so-called $K_\alpha$ source of $keV$ x-rays. Putting them all together we can make an optimization routine for a $K_\alpha$ source and see how this source can measure up, in theory, to the requirements presented at the beginning this chapter.

### 4.3.1 Electron energy attenuation by cold material

A high energy electron passing through matter will lose energy through interaction with that matter. The rate of energy loss, which depends on the incident electron velocity (energy) and the material properties, is referred to as the *stopping power* of that material at a given electron energy. Stopping power scales linearly with density for a given material, and so it is often given in a density-normalized form (e.g. $[MeV cm^2/g]$) which can be multiplied by the density $\rho$ to give energy loss per unit distance (e.g. $[MeV/g]$):

$$\begin{aligned} \frac{dE}{dz} &= -S_{mat}(E,\rho) && (4.57) \\ &= -\rho\mathcal{S}_{mat}(E). && (4.58) \end{aligned}$$

At many keV and MeV energies, an electron will experience a large number of very small angle collisions and virtually no large angle collisions. For this reason the electron trajectory through a material can often be considered one-dimensional, with a continuous slowing down by the material. Thus a very close approximation of how far an electron will penetrate into a material is given by the "continuous slow down approximation" (CSDA) range:

$$\text{CSDA range} \;=\; \rho^{-1}\int_{E_0}^{E_{min}} (\mathcal{S}_{mat}(E))^{-1} dE. \qquad (4.59)$$

Here, $E_{min}$ is the minimum energy at which an electron could be considered absorbed by the target. The theory of electron stopping power in materials is semi-empirical, with two theoretical foundations: inelastic collisions with bound (ionizing) and free (plasmon generating) electrons, and bremsstrahlung emission. Inelastic collisions dominate stopping power up to $1MeV$, at which point bremsstrahlung contributes. Bremsstrahlung dominates electron stopping above $100MeV$ $(1-\frac{v}{c} \sim 10^{-5})$. An excellent database [BCZC05], provided online by NIST provides stopping powers separated into collisional (inelastic scattering) and radiative (bremsstrahlung), CSDA ranges, radiation yield, and density effect parameter for elements 1-98, as well as a wide range of compound materials, such as polypropylene and water. The mean excitation energies, which are empirical cannot be derived from first principles, for each material in the database are kept up-to-date, based on the best available experimental data. The database, known as "estar" is extremely useful resource in modeling electrons passing through cold material. Data is provided in tables or plots; an example plot is shown in figure 4.4.

### Collisional electron stopping

The scattering of an electron from an ion does not impart much energy to the ion because of the huge difference in mass. Therefore the theory of collisional stopping of hot electrons deals with electron-electron collisions. The electrons in the material are treated as a set of oscillators which interact with the incident electron through the coulomb force through ionization or promotion to an open energy level. The

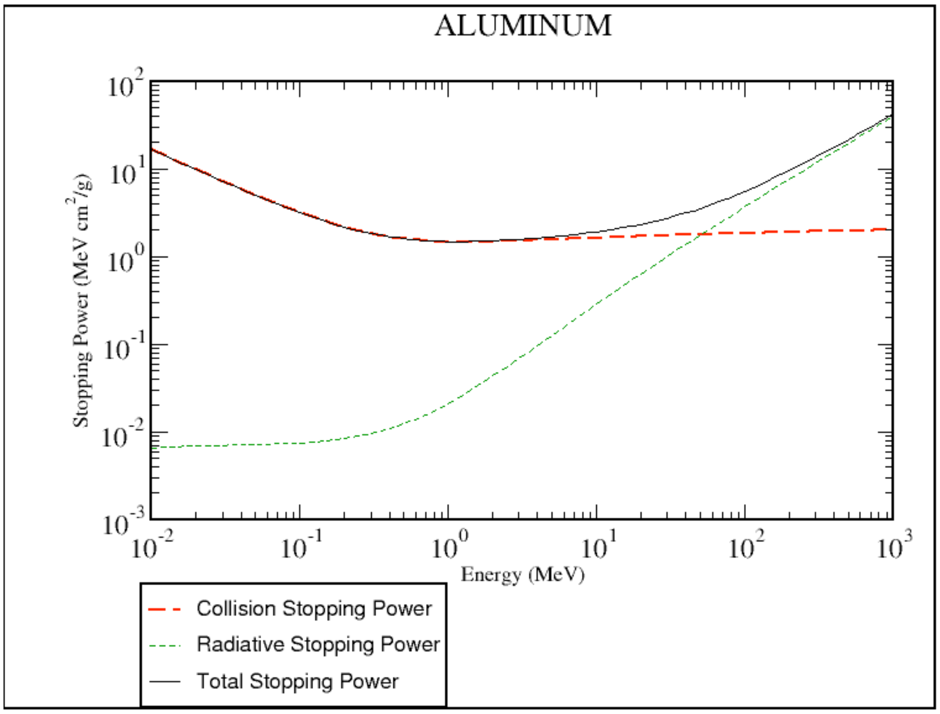

Figure 4.4: A plot of electron stopping powers in Al provided by the NIST estar database, and generated using the online tools [BCZC05]. Collisional, radiative, and total stopping powers of $\mathcal{S}_{Al}(E)$ are shown on a log-log plot.

Bethe equation is the quantum mechanical solution to this problem [Dap03]:

$$-\frac{dE}{dz} = \frac{2\pi e^4 NZ}{E}\ln\left(\frac{CE}{\bar{I}}\right), \tag{4.60}$$

where $\bar{I}$ is the mean ionization potential, and $C \approx 1.166$. This equation is modified by a density effect correction [SSB82], which slightly lowers the stopping power at higher energies. The mean ionization potential can't be determined from first principles and is empirically determined.

### Bremsstrahlung

An electron's collision with an atomic nucleus cannot actually be inelastic, because the acceleration of the electron causes a change in the electromagnetic field that necessitates emission of a photon. The spectrum of bremsstrahlung from electrons of given energy is continuous up to the initial electron energy. Solving the [KM59]

$$d\sigma = \frac{137 r_0^2}{(2\pi)^4}\frac{p\mathsf{E}_0\mathsf{E}}{p_0}\left|\int \psi_f^*(\mathfrak{p}^*\cdot\mathfrak{a})e^{-ik\cdot r}\psi_i d\tau\right|^2 \times k dk d\Omega_k d\Omega_p, \tag{4.61}$$

where $p_0$, $p$, $\mathsf{E}_0$, and $\mathsf{E}$ are the electron's initial and final momentum, and initial and final *total* energy, $k$ and $\mathfrak{p}$ are the wave vector and unit polarization vector of the outgoing photon, $\mathfrak{a}$ is the Dirac matrix, $\psi_i$ and $\psi_f$ are the Dirac wave functions of the initial and final electrons, $r_0$ is the classical electron radius, and $d\tau$ is the unit volume element. Solving this equation requires knowledge of the Dirac wave function in a screened, nuclear coulomb field, which does not have a closed-form solution. Therefore a wide variety of approximations for the wave functions are used, depending on what assumptions can be made [KM59]. Below 2 MeV, accurate numerical results for bremsstrahlung are tabulated [PTL$^+$81], whereas above $\sim 50$ MeV, analytical formulas work well. Numerical interpolation is used to bridge this gap [SB85]. One can get a good qualitative feel for the behavior of bremsstrahlung

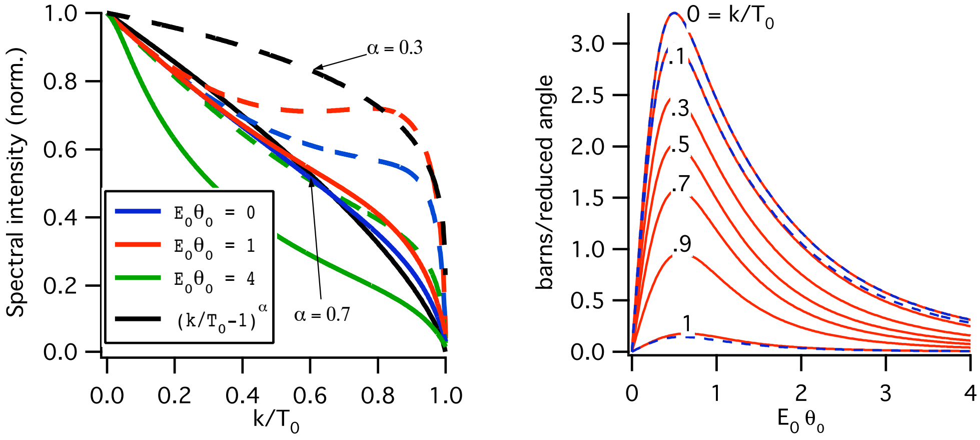

Figure 4.5: Characteristic features of bremsstrahlung radiation from eqn. 4.63 for $Z = 22$ (Ti), with dashed curves for $T_0 = 100$ MeV and solid curves for $T_0 = 10$ MeV. Left: shape of spectral intensity vs. $k/T_0$ for various values of $\mathsf{E}_0\theta_0$, compared to the simple estimate in eqn. (4.63). Right: plot of $\frac{kd\sigma_{k,\theta_0}}{dkd(\mathsf{E}_0\theta_0)}$ vs $\mathsf{E}_0\theta_0$ for various ratios of $k$ to $T_0$

radiation using, e.g., equation 2BS from Koch, et al. [KM59][8], which gives the differential cross section, also differential in photon energy and incoming electron energy:

$$\begin{aligned} d\sigma dk d\theta_0 &= \frac{4Z^2r_0^2}{137}\frac{dk}{k}ydy\left\{\frac{16y^2\mathsf{E}}{(y^2+1)^4\mathsf{E}_0} - \frac{(\mathsf{E}_0+\mathsf{E})^2}{(y^2+1)^2\mathsf{E}_0^2}\right. \\ &\quad \left. + \left[\frac{\mathsf{E}_0^2+\mathsf{E}^2}{(y^2+1)^2\mathsf{E}_0^2} - \frac{4y^2\mathsf{E}}{(y^2+1)^4\mathsf{E}_0}\right]\ln M(y)\right\}, \\ &\quad y = \mathsf{E}_0\theta_0, M(y) = \left\{\left(\frac{k}{2\mathsf{E}_0\mathsf{E}}\right)^2 + \left(\frac{Z^{1/3}}{111(y^2+1)}\right)^2\right\}^{-1} \end{aligned} \tag{4.62}$$

In their notation, $T_0 = \mathsf{E}_0 - m_ec^2$ is the initial kinetic energy of the incoming electron[9], $k$ is the energy of the emitted bremstrahlung photon, with all energies expressed in units of $m_ec^2$, and $\theta_0$ is the angle of emission relative to the incoming

---

[8] This equation was obtained by Koch, et al. from L.I. Schiff, Phys. Rev. 83, 252. Koch summarizes many other equations and discusses their respective ranges of applicability.

[9] I use $E_e$ for this in other sections, but overuse of the letter $E$ here would be confusing.

electron trajectory. $\mathsf{E}_0\theta_0$ is referred to as the "reduced angle". From this equation, which is most accurate for very high energy electrons and high $Z$ values, one can produce plots of the spectral and angular characteristics of bremsstrahlung emission. I have done this in figure 4.5 for incoming electrons of 10 and 100 MeV. The first plot gives the spectral shape of bremsstrahlung emission for various reduced angles (color coded by reduced angle). For comparison, the black curves show the approximation quoted by McCall, et al. [McC82][10]:

$$I \quad \propto \quad Z\left(\frac{k}{T_0}-1\right)^{\alpha}. \tag{4.63}$$

In the second plot of figure 4.5, we see that the cross section for photon production as a function of reduced angle follows a pattern that is nearly independent of electron angle when plotted in terms of $k/T_0$. The salient point of this plot is that emission is directed more towards the axis of the incident electron's motion as energy increases. Coupled with radiative stopping power from NIST (see figure 4.4) these plots let us make reasonable approximations for the bremsstrahlung yield.

### 4.3.2 K-shell ionization and relaxation

Ionization of the innermost electron shell, or the K-shell, of an atom can be achieved by an incoming electron with energy greater than the binding energy of the K-shell, typically several keV. An excellent bibliography of work on this problem is given in the introduction of Hombourger, *et al.* [Hom98]. For high incident electron energies, where the ratio of electron energy to K-shell ionization energy, or overvoltage[11] $U = E_e/I_K \gg 1$, the incoming and outgoing scattered electron can be treated in a relatively simple way as a plane wave interacting with the bound electron. How-

---

[10] He attributes this to Jakshik (probably Jakschik) but I cannot find his cited reference.

[11] $E_e$ is now the kinetic energy of the incoming electron, for which I used $T_0$ in the previous section

ever, as $U$ approaches 1 various corrections need to be made to account for the more complex interactions between the incoming electron and the bound electrons of the atom, as well as the nucleus. As Hombourger, *et al.* note, reasonably accurate theoretical models are available, but they do not lead to simple and convenient analytical expressions. This motivates an empirically fit cross-section formula [Hom98]:

$$\sigma_K(U, I_K) = n_K \pi a_0^2 G_r \left(\frac{I_0}{I_K}\right)^{C_U} D_U \frac{\ln U}{U} \tag{4.64}$$

Here, $n_K$ is the number of K-shell electrons in the atom (e.g. 2), $a_0$ is the Bohr radius, and $I_0 \approx 13.6$ eV is the Rydberg constant. The term $\frac{\ln U}{U}$ is the signature of the Bethe equation, also seen in eqn. 4.60. The expression contains a relativistic term:

$$G_r = \left(\frac{1+2J}{U+2J}\right)\left(\frac{U+J}{1+J}\right)^2 \left(\frac{(1+U)(U+2J)(1+J)^2}{J^2(1+2J)+U(U+2)(1+J^2)}\right)^{3/2} \tag{4.65}$$

$$J = \frac{.511 \text{ MeV}}{I_K}$$

and two fitting parameters:

$$D_U = \left(a + \frac{b}{U} + \frac{c}{U^2}\right) \qquad C_U = \left(d + \frac{e}{U} + \frac{f}{U^2}\right) \tag{4.66}$$

| | |
|---|---|
| a=3.125; | d=2.0305; |
| b=-4.172; | e=-0.3160; |
| c=1.877; | f=0.1545 |

A practically identical form of the above expressions was used by Casnati, *et al.*[CTB82], with slightly different values for the fitting parameters. The updated values reflect new experimental and computational data at lower electron impact energies, and result in slightly lowered cross sections.

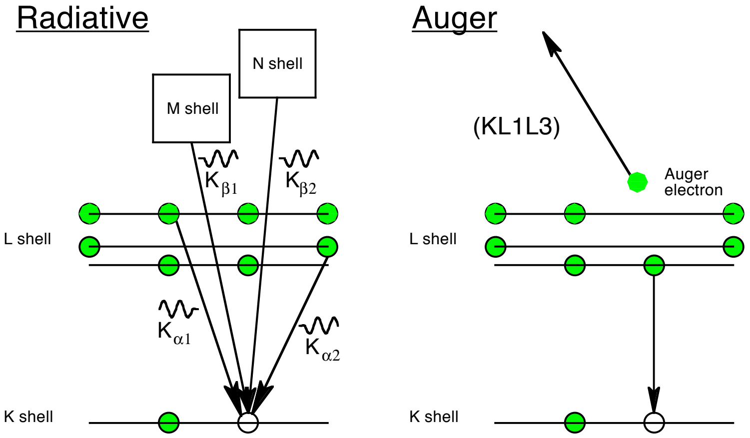

Figure 4.6: Competing processes for filling the K-shell vacancy. Left: photoemission transitions are given subscript letters to differentiate between L-shell ($\alpha$) and M- or N- shell ($\beta$) transitions, and each subscript is numbered in order of relative intensity. Right: auger transition, by which the energy of the K-hole filling transition is delivered into the ionization of another bound electron (specific case of KL1L3 process shown).

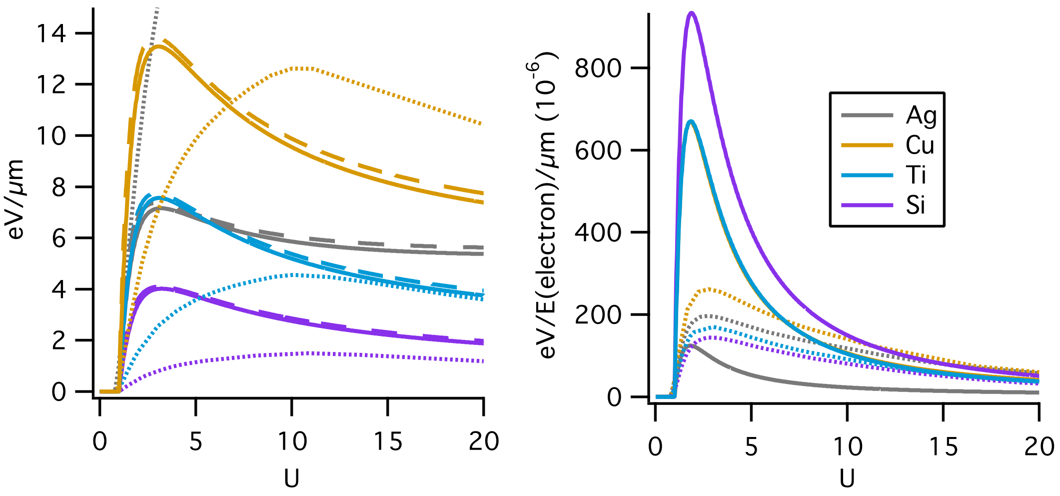

Figure 4.7: K$_\alpha$ yields vs. the "over-voltage" $U \equiv E_e/I_K$, obtained from empirical K-shell ionization cross sections (dashed = [CTB82], solid = [Hom98], see eqn. 4.64) and photoemission probabilities [Kra01]. Dotted lines = Bremsstrahlung yields of photons from $0.9E_{K_\alpha} \leq\ k \leq\ 10E_{K_\alpha}$, calculated using NIST tables [BCZC05] and eqn. 4.63... Left: eV/ $\mu m$ of photons generated; Right: "efficiency," obtained by dividing the left plots by $E_e$.

### Photoemission vs Auger

Once the K-shell is ionized, the vacancy is filled by an electron from one of the other shells. The energy of that transition can be released either in the form of a photon ($K_\alpha$ or $K_\beta$) or ionization of an electron from the donor shell (Auger). These possibilities are illustrated in figure 4.6. For low $Z$ materials such as Si, Auger is much more likely than photoemission, but the photoemission probability $\omega_K$ approaches 1 as $Z$ increases [Kra01]. This is balanced to some extent by the cross section for $K_\alpha$ photo-ionization, which decreases as $Z$ (and hence $I_K$) increases. To obtain the statistical $K_\alpha$ photon yield $dN_K$ of an electron of kinetic energy $E$ passing a distance $dx$ through material of density $n$ and K-ionization potential $I_K$, we use:

$$\frac{dN_K}{dx} \quad = \quad \sigma_K(E/I_K, I_K)\omega_K n. \tag{4.67}$$

We can multiply this value by the average $K_\alpha$ photon energy[12] to get the rate of energy radiation, and divide that by the electron energy to give a sort of radiative energy efficiency. Both of these are plotted for various materials in figure 4.7, which includes for reference the same values estimated for the production of bremsstrahlung photons in the energy range $0.9E_{K_\alpha} \leq k \leq 10E_{K_\alpha}$. It's worth noting that in a silver target, bremsstrahlung in this range by far outweighs $K_\alpha$ production, even for near-threshold electrons. The narrow $K_\alpha$ peaks would still show up above the continuous bremsstrahlung background, but only if the measuring device has good spectral resolution.

### Photon reabsorption

The material can reabsorb the $K_\alpha$ photons that it produces, although this absorption is somewhat weak since the material can't re-ionize its $K-$ shell with its own $K_\alpha$ emission. Data for x-ray attenuation lengths, as well as a wealth of other x-ray data tables, are available from Berkeley's Center for X-ray Optics website [HGD01]. X-ray propagation through matter is given in terms of an attenuation length, as discussed in section 4.1. The trend of $K_\alpha$ self-absorption vs. Z for a source material is plotted in figure 4.8

We now have the basic data needed to estimate optimal conditions for a $K_\alpha$ heating source.

---

[12] Of course if we want to be more precise, we consider the relative rates of $K_\alpha$ and $K_\beta$ and add them together appropriately. For low Z, $K_\alpha$ far outweighs $K_\beta$ .

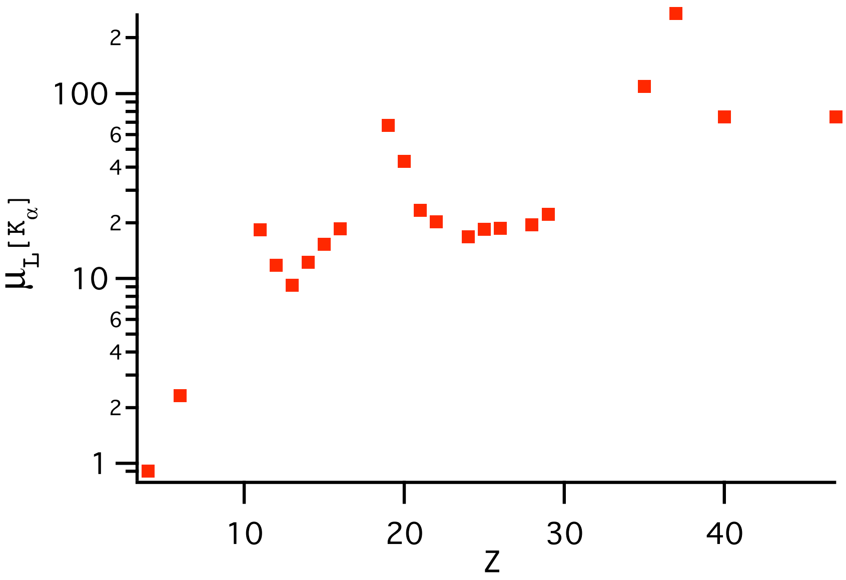

Figure 4.8: Reabsorption lengths of $K_\alpha$ in a source for some solid-density elements, by Z.

### 4.3.3 $K_\alpha$ source optimization

We can put together stopping power, x-ray attenuation, $K$-shell ionization cross sections and photoemission probabilities, and laser to electron scalings to predict $K_\alpha$ output from a laser irradiated solid. After choosing an appropriate source/sample combination, we can model $K_\alpha$ generation in the source starting with the monoenergetic case, giving $K_\alpha$ output as a function of target thickness and electron energy, and then move on to finding optimal combinations of electron temperature distribution and target thickness. Finally, we want to to tie hot electron temperature distributions and conversion efficiencies to laser parameters to see where we land on plots such as figure 4.2.

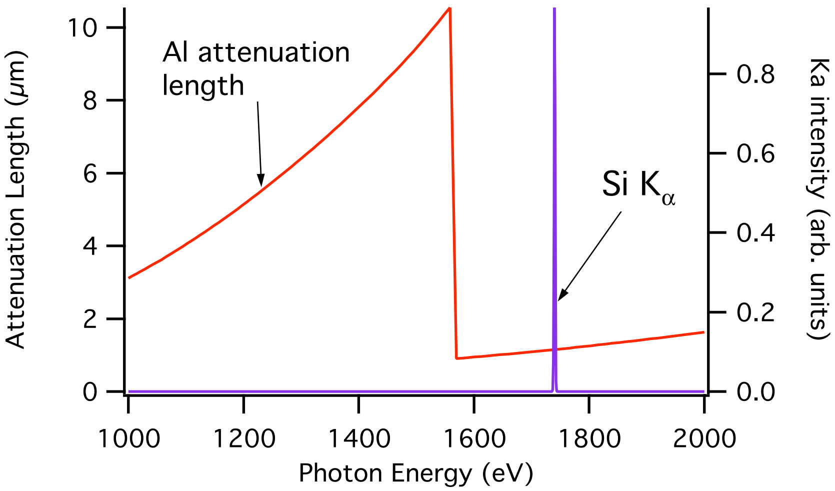

Figure 4.9: Plot of $\mu_L$, the $1/e^2$ falloff distance of x-rays in aluminum as a function of x-ray energy. Si $K_\alpha$ lands just past the threshold of photo-ionization of the Al K-shell, causing it to be more strongly absorbed [HGD01]. The energy of an individual x-ray photon is not depleted: it is either absorbed or not, and so $\mu_L$ is a statistical quantity.

### Energy matching

At the beginning of this chapter (section 4.1) I gave the example of Si K$_\alpha$ heating Al. This was motivated by the desire to study Al, since it is the most studied of the metals in terms of material properties, and is thus a good material to start with in establishing a new technique of EOS measurement. Although Si was never studied extensively as a K$_\alpha$ source, energetically it is the best choice among convenient target materials for heating Al, because it is absorbed quite strongly, being just above the $K$-shell ionization energy of Al (fig. 4.9). In general, we want to use a material combination in which the $K_\alpha$ of the source has an attenuation length $\sim 2\mu m$, so that we can achieve high enough temperatures in a thick enough foil. A few examples with feasible (e.g. available as foils) source and sample material combinations are given in table 4.1.

| source | sample | $\mu_L$ |
|---|---|---|
| Si | Al* | 1.2 |
| Ti | Sc* | 3.9 |
| Ni | Fe* | 3.5 |
| Ti | Ag | 1.0 |
| Fe | Ag | 2.5 |
| Cu | Ag | 4.6 |
| Ni | Au | 2.1 |
| Cu | Au | 2.5 |

Table 4.1: Example source/sample combinations with $\mu_L \sim 2\mu m$ for source $K_\alpha$ in the sample material. The "*" indicates that the combination takes advantage of strong K-shell absorption in the sample.

### Electrons of a given start energy

I will start with electrons of a constant start energy. As I mentioned at the beginning of this section, the large number of hot electrons involved in laser-solid interactions allows us to model all electrons of a given start energy with a single particle which moves through the material, continuously slowing down and radiating fractional numbers of $K_\alpha$ photons based on the cross sections. For a given electron start energy, material composition, and target thickness, advance the electron through the material in small steps ($d \ll CSDA(E)$), decreasing the energy of the electron at each step based on the material stopping power [BCZC05] and adding up the $K_\alpha$ emission from the $K$-shell cross sections [Hom98] and radiative transition probabilities [Kra01] (eqn 4.67). Since we're interested in emission from the back side of the target, the $K_\alpha$ photon number must then be reduced due to the x-ray attenuation [HGD01] of the remaining target material. For small enough step size, this is equivalent to the integral:

$$N_K(E_0, D) \quad = \quad n \int_0^D dx \left( \sigma_{K,I_K}\{E(E_0, x)\} \omega_K e^{-(d-x)/\mu_L} \right), \tag{4.68}$$

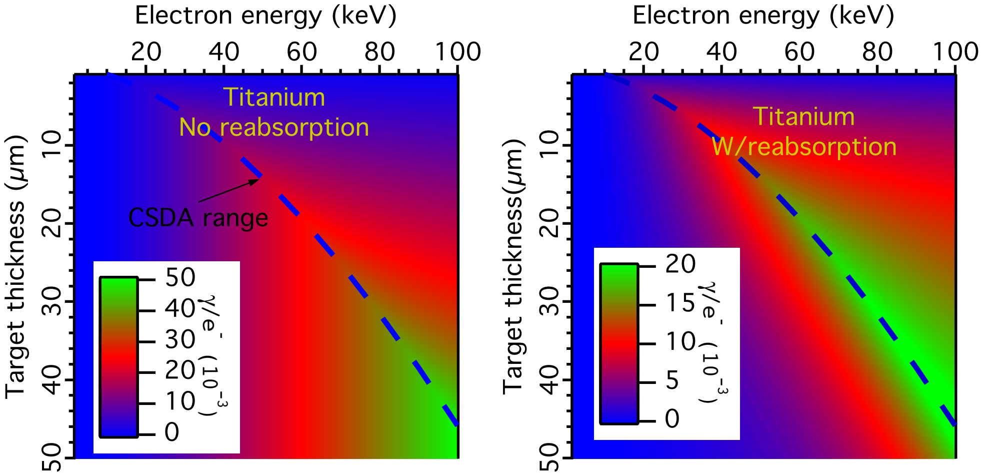

Figure 4.10: Per-electron x-ray output in Ti as a function of electron energy and target thickness. Left: Case where photon reabsorption is left out (color scale 0 to .05 $\gamma/e^-$); Right: Output at the back side of a target when self attenuation of $K_\alpha$ is used (color scale 0 to .02 $\gamma/e^-$). The dashed line shows the CSDA range of the electron in the material.

where $D$ is the target thickness, $n$ is its atom density, and $E(E_0, x)$ is the solution to $x = \int_E^{E_0} \frac{dE}{S_{\mathrm{mat}}(E,\rho)}$ for a given starting electron energy $E_0$ and depth $x$ into the target.

Figure 4.10 shows the $K_\alpha$ output per electron in a false-colored image plot of electron energy vs. target thickness. When photon reabsorption is ignored, the output increases until the target thickness reaches the range of the electron in the target (CSDA range), and then becomes constant. When photon reabsorption is included, the output at the back side of the target increases with target thickness until the CSDA range, and then drops off for thicker targets. Although higher energy electrons with thicker targets give more $K_\alpha$ photons, we are more interested in conversion efficiency. Figure 4.11 shows the energy conversion efficiency, calculated from the number $N_K$ and energy $E_K$ of the $K_\alpha$ photons produced and the initial energy $E_0$ of the electron as: eff $= N_K E_K / E_0$. Then we see the optimal target thickness and electron temperature for a monoenergetic beam of electrons in a given

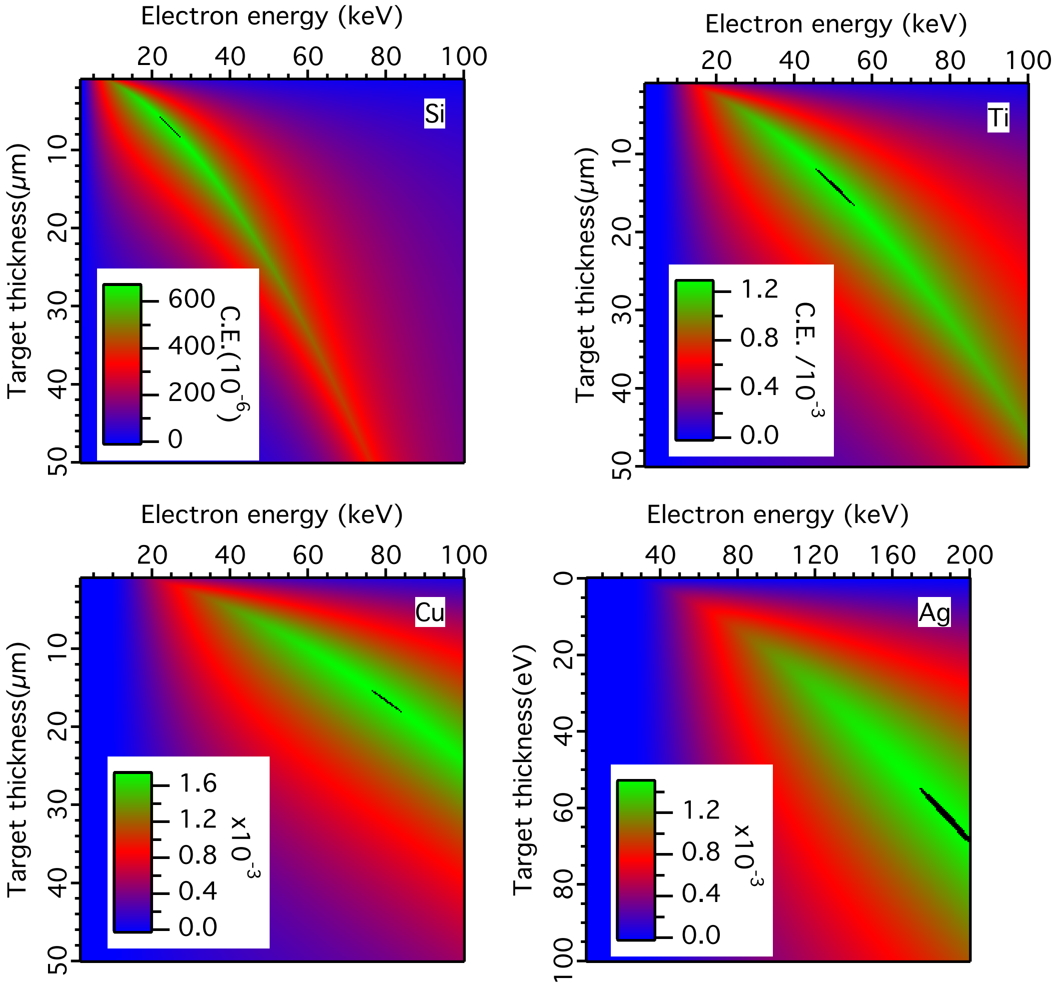

Figure 4.11: Conversion efficiencies for single electrons passing through targets of various materials and various thicknesses. Color scale indicates conversion efficiency $E_\gamma/E_e$; black is used to highlight the peak values. Note that the axis scaling for Ag is different since it is optimized at higher temperatures and thicknesses.

material.

### Electron energy distribution

Since the electrons produced in laser-solid interactions aren't monoenergetic, we must now consider the optimization problem in terms of electron energy distributions. Most authors will assume that the electron energy distribution follows a Maxwell-boltzmann shape, since measured energy spectra tend to have an exponentially decaying tail at high energies [McC82]. Recall that a Maxwellian of d dimensions takes the form [Kit58]:

$$f_d(E, \Theta) \quad = \quad \Gamma(d/2)\Theta^{-d/2}E^{d/2-1}\exp(-E/\Theta), \qquad (4.69)$$

where $\Theta = kT$ and $\Gamma$ is the gamma function $\Gamma(n) = (n-1)!$, $n \in \mathbb{Z}$. The choice of dimensionality will affect slightly the results of our optimization, since the higher dimension maxwellians are weighted more towards higher energies, but the difference isn't substantial. The average number of photons per electron from a Maxwellian energy distribution is just:

$$N_d(D, \Theta) \quad = \quad \int_0^\infty dE_0 f_d(E_0, \Theta) N_K(E_0, D), \qquad (4.70)$$

and the conversion efficiency is $N_d(D, \Theta)E_{K_\alpha} \big/ \left(\frac{d}{2}\Theta\right)$.

In figure 4.12, I show color scaled image plots of the conversion efficiency from electrons into $K_\alpha$ photons for Cu foils, for 1, 2, and 3 dimensional Maxwellian distributions. In figure 4.13, I plot the optimization for Si, Ti, Cu, and Ag. Note that although Cu has the best conversion efficiency of the group, it is by less than a factor of 3. With an attenuation length of over 75 $\mu m$, Cu $K_\alpha$ would be a poor choice for heating of Al. However, it could be suitable for heating high Z materials such as Ag or Au (see table 4.1).

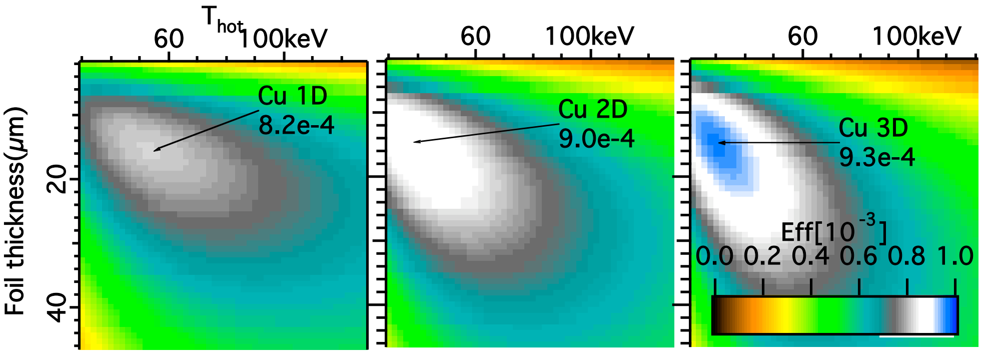

Figure 4.12: Conversion efficiency from hot electron energy into Cu $K_\alpha$ for 1-, 2-, and 3-D (L to R) Maxwellian distributions. Peak values are indicated in each.

We must now consider the conversion of laser energy into these hot electrons in order to predict the efficacy of a given $K_\alpha$ heating source.

### Electron temperature and conversion efficiency from laser parameters

We saw in section 4.2 how the temperature and conversion efficiency from the laser into hot electrons is expected to scale for various models (see eqns.4.45, 4.47, 4.51). However, as I mentioned, no single model perfectly describes the laser-solid interaction: theory must be supplemented by empirical data are needed to make predictions for what temperature and conversion efficiency will be given at a given laser irradiance. Information about the hot electron temperature and absorption can come from measurements of, e.g., the high energy bremsstrahlung tail [McC82, YJKK99], the spectrum of emitted hot electrons [Fil04], total laser absorptivity measurements, or the output of various $K_\alpha$ sources (various Z) buried in a compound target [WHW$^+$98], or from simulations such as PIC codes [RGUF00].

In table 4.2, I've listed the functions $T_{h.e.}(I\lambda_\mu^2)$ and $N_{h.e.}(I\lambda_\mu^2)$ used by various authors for scaling hot electron generation. As can be seen by considering a laser irradiance of $10^{18}\ W \cdot \mu m/cm^2$, the predicted electron temperatures varies greatly between these functions, from 40 to 410 keV [YJKK99, RGUF00]. Hot elec-

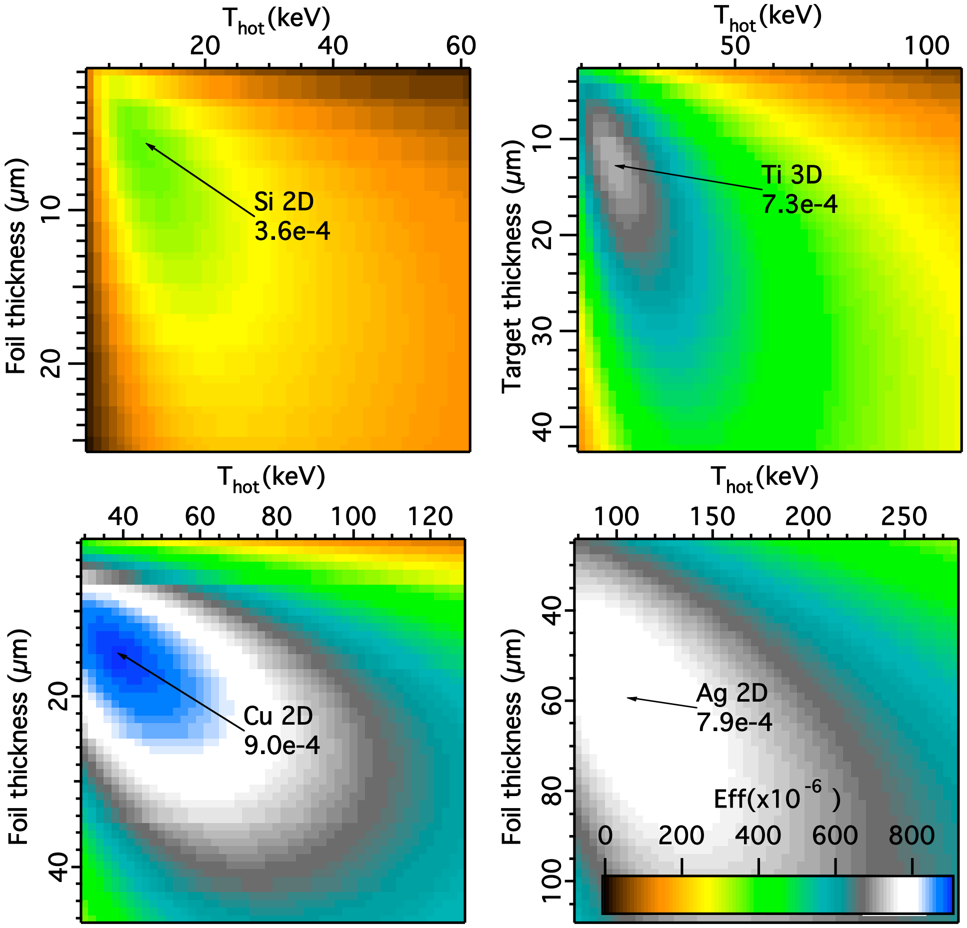

Figure 4.13: Conversion efficiency from hot electron energy into $K_\alpha$ for Si, Ti, Cu, and Ag using 2D Maxwellian distributions. Peak values are indicated in each.

| reference | kT scaling (MeV) | hot e eff ($E_{hot}/E_{Las}$) | d | $I\lambda_\mu^2$ range ($W\mu m^2/cm^2$) |
|---|---|---|---|---|
| Riley, *et al.* | $.32\sqrt{\frac{I\lambda_\mu^2}{10^{18}}}$ | eqn. 4.46 | ? | $\lesssim 1.8 \times 10^{18}$ |
| Salzmann, *et al.* | N/A | 0.1 | 2 | N/A |
| Guo, *et al.* | eqn. 4.51 | 0.3 | ? | $\lesssim 5 \times 10^{18}$ |
| Reich, *et al.* | $.41\sqrt{\frac{I}{10^{18}}}$ | 0.5 | 1 | $10^{15} - 10^{19}$ |
| Yu, *et al.* | $.04\left(\frac{I\lambda_\mu^2}{10^{18}}\right)^{\frac{1}{3}}$ | $.146\left(\frac{I\lambda_\mu^2}{10^{18}}\right)^{\frac{3}{4}}$ | 3 | $10^{16} - 10^{19}$ |

Table 4.2: Semi-empirical estimates of hot electron and $K_\alpha$ generation by various authors (respectively): [RKPdS+06], [SRU+02], [GSWB01], [RGUF00], [YJKK99]

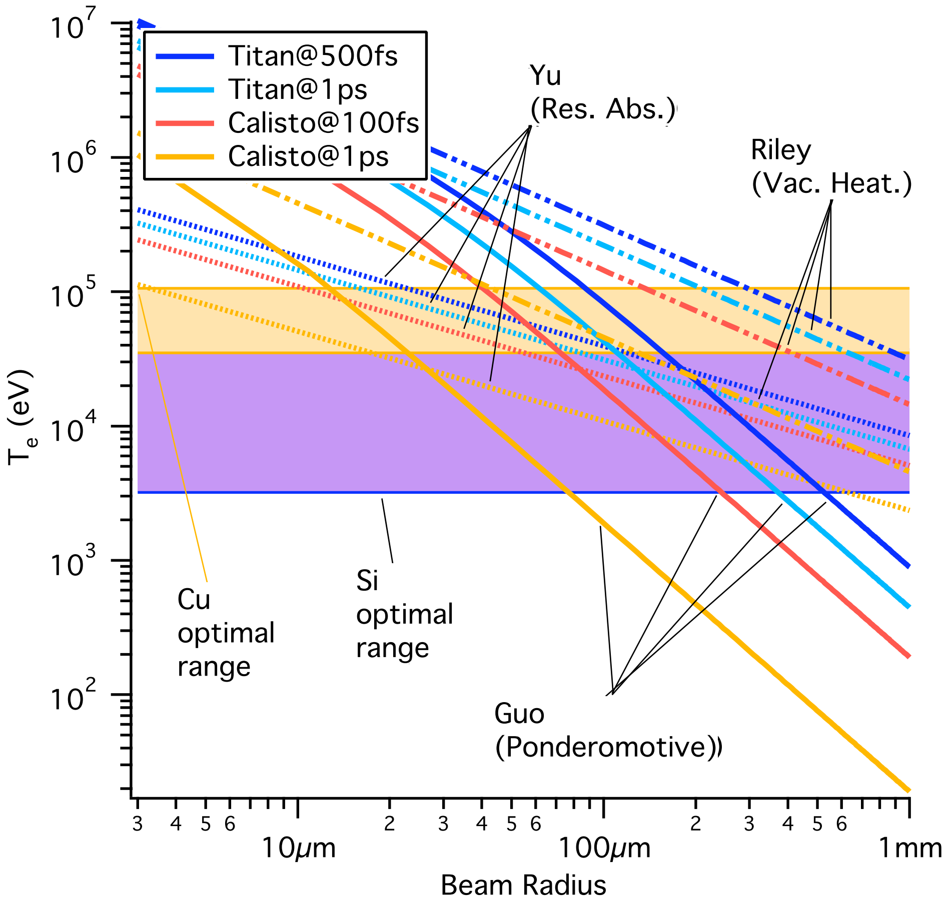

Figure 4.14: Hot electron temperature as a function of spot size for various temperature scalings from Reich, *et al.*[RGUF00], Guo, *et al.*[GSWB01], and Yu, *et al.*[YJKK99], and laser systems (Calisto = 10 J, 800 nm; Titan = 150 J, 1 $\mu m$ ). Optimal temperature ranges (above half maximum) for Si and Cu $K_\alpha$ are shown for reference.

tron conversion efficiencies are taken by the authors to be in the range of .1 to .5, some assuming constant conversion efficiencies, and others giving scalings based on experimental data, or the model of vacuum heating (section 4.2.6). Salzmann, *et al.*[SRU$^+$02] declined (perhaps wisely) to speculate about how the hot electron spectrum might depend on the laser irradiance and focused only on electron temperature and target thickness.

### Consequences of scaling

The scalings of laser conversion efficiency into electrons and electron temperature as functions of $I\lambda^2$ in 4.2 have a major effect on predictions about proton heating, because as we increase the energy to get a higher $\mathrm{K}_\alpha$ output, we must also increase the spot size to maintain the intensity that gives an optimal temperature. Different scalings of $T_e(I\lambda^2)$ give very different predictions for just how large the spot size should be (figure 4.14). Revisiting the falloff in intensity with source radius illustrated in figure 4.2, we can use the $T_e(I\lambda^2)$ and $\mathrm{eff}_{L,e}(I\lambda^2)$ scalings of table 4.2 to translate the efficiency plots of 4.13 into the space of $\mathrm{eff}_{L,\mathrm{K}_\alpha}$ vs. $R_{\mathrm{src}}$, since the source size roughly scales with the laser spot size for larger focal spots. The results are shown in figures 4.15 and 4.16. We see that scalings for which $T_e \propto (I\lambda^2)^{1/3}$ (e.g. Reich, *et al.*[RGUF00]), electron temperature falls slowly with increasing spot size, negatively impacting our ability to heat with $\mathrm{K}_\alpha$ . However, until we reach the limit of $R_{\mathrm{src}} \gg$ (separation distance), increasing the laser energy- and the spot size, accordingly - does improve our heating capability.

The effect of target thickness is taken into account in those plots by assuming that thicker targets also increas source size, by $R_{\mathrm{src}} = R_{\mathrm{las}} + \tan(\theta)$, where $\theta$ is a spreading angle, in this case taken to be $20^\circ$.

I have left out a discussion of Bremsstrahlung heating largely because it takes away the advantage of the very narrow $K_\alpha$ bandwidth, and hence easy determina-

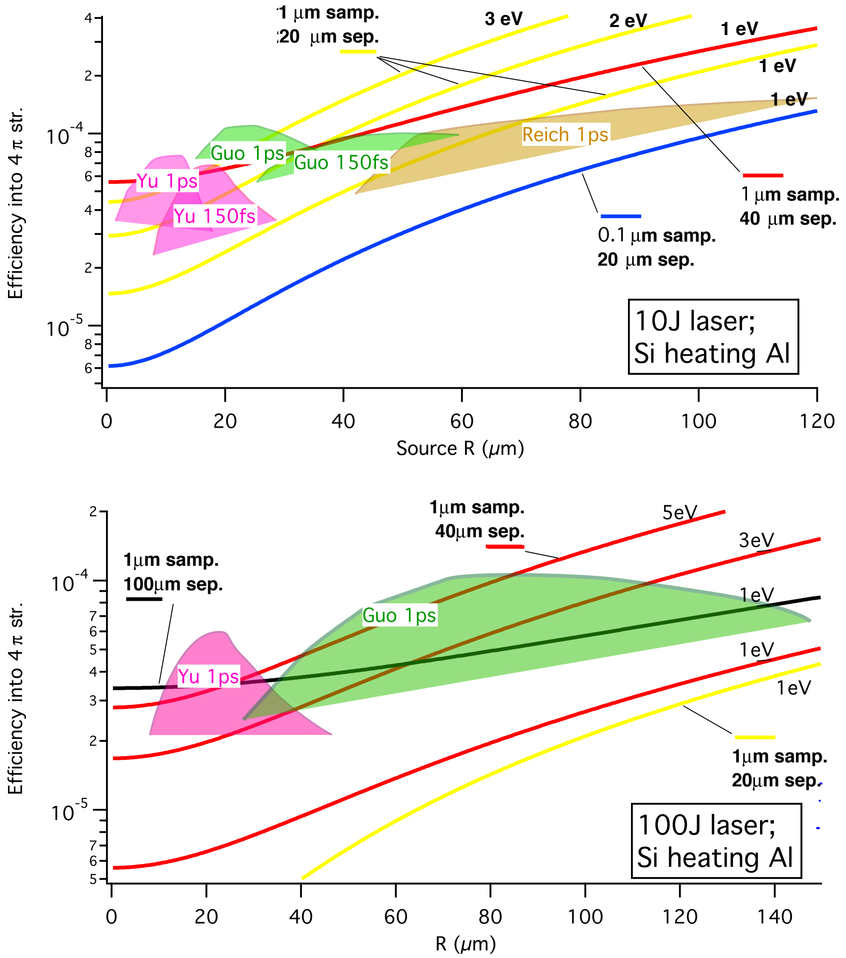

Figure 4.15: COLORED REGIONS: Shows where the various laser intensity to electron temperature models in table 4.2 and figure 4.14 predict optimal $K_\alpha$ production. Here, target thickness $d$ is taken to affect the source size by $R_{\text{src}} = R_{\text{las}} + d\tan(20°)$. LINES: Contours of minimum efficiency needed to heat a sample of given distance and thickness to a given temperature (labeled on right side of the contour) are shown for reference. TOP: Si heating Al on a 10 J (800 nm) laser; BOTTOM: Si heating Al on a 100 J (1 $\mu m$ ) laser.

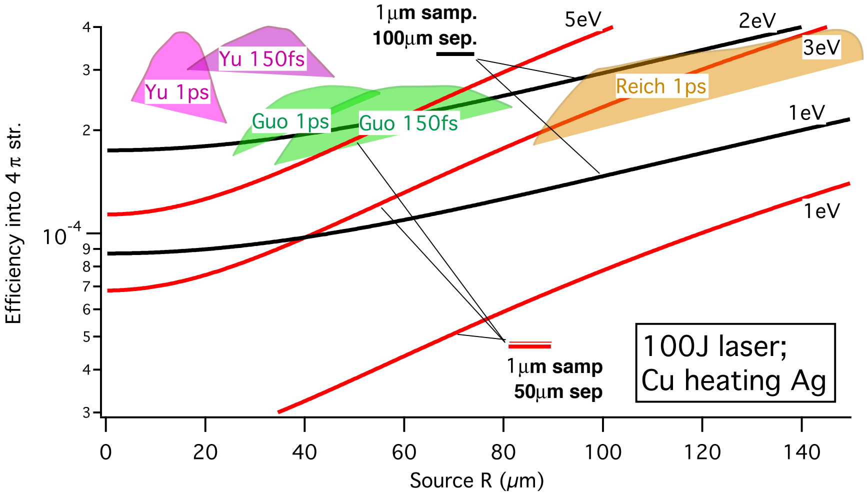

Figure 4.16: The same considerations as in figure 4.15, except for Cu heating Ag.

tion of the deposited energy in the sample. However bremsstrahlung is a viable heating source when enough laser energy an intensity are available, and it is used for example in the hohlraum geometry for compressing and heating fusion ignition capsules [LIN95].

### 4.3.4 Return current

In the above considerations I have tacitly assumed that the background cold material has perfect conductivity and an effectively infinite electron density, so that the current due to hot electrons passing in one direction through the material can be exactly cancelled by a slow return current. A return current is not only necessary to balance the charge being left behind, but also to cancel the strong azimuthal magnetic field of the hot electron beam in the source material [BDGR97]. Although the hot electrons have a long mean free path, the cold return current electrons are quite collisional, and they are subject to the resistivity of the underlying material. This is where the one-electron model we've been using breaks down: the return current $\mathbf{j}_{ret} = \mathbf{j}_{fast}$ encounters a resistivity $\eta$, leading to an electric field [DBHG97]:

$$\mathbf{E} \;=\; -\eta \mathbf{j}_{fast}. \tag{4.71}$$

If the current of our fast electrons or the resistivity of our background material is too large, this electric field will significantly slow the hot electrons. The current $I$, in amperes, of our hot electron distribution (dimension $d$), where $T_0$ is the electron temperature *in electron Volts*, $\epsilon_e = (\text{eff}) \times \epsilon_L$ is the total energy in the hot electrons *in Joules*, and $\tau$ is the pulse length [BDGR97]:

$$I \;=\; \frac{\epsilon_e}{\tau(\frac{d}{2})T_0}. \tag{4.72}$$

So that, in a $100J$, 1 ps laser pulse with conversion efficiency of 30% and hot electron temperature of 100 keV, the current would be about 200 $MA$. If, for example, as suggested in one of the more "effective" models in figure 4.15 (e.g., Guo), the electrons are traveling in a cylinder of radius 40 $\mu m$ , we have $\mathbf{j} = 4 \times 10^{16} A/m^2$. The resistivity will vary greatly depending on the source material and how much it has been heated by the electrons. Optimistically, we might expect the resistivity to be somewhere in the vicinity of $10^{-7}\Omega m$ [BDGR97] for a well heated, slightly ionized source material, leading to an electric field $E \approx 4 \times 10^9 \, V/m \;=\; 4\,\text{kV}/\,\mu m$ . Such a field will add substantially to the effective stopping power relative to that of the single electron approximation, making the optimal source thicknesses and final conversion efficiency of the source lower.

Even more important than the electric field experienced by the electrons inside the material is the electric field experienced in the vacuum at the back side of the target.

### 4.3.5 Electrons entering vacuum

There can be no more immediately acting return current when the electrons escape into vacuum. Because the electrons move in such great numbers, the static electric fields get very large, very quickly, and a large number of the electrons will be forced to return to the target. This electric field is also responsible for accelerating high energy protons from the back side of a foil target, as described in the next section.

Ernst Fill has described analytically two limiting cases of electrons leaving a foil into vacuum [Fil01, Fil05], that of a monoenergetic source with finite temporal length, and that of an energy distribution with negligible temporal length. The scenario of finite energy spread and temporal extent is a complicated problem that isn't solved analytically. However, some insight can be gained by observing these two limiting cases.

#### Monoenergetic source with finite temporal duration

Let the monoenergetic source [Fil01] have width $d$ immediately before leaving the back side of a foil, with infinitely fast rise and fall (hence, a block of electrons moving together). At this moment, $t = 0$, the Lagrangian coordinate $x_0$ is equal to the cartesian coordinate $x$, which is taken to be 0 at the back side of the foil and $-d$ at the tail end of the pulse. The Poisson equation takes the form

$$E = -4\pi e N_b x_0, \tag{4.73}$$

where $N_b$ is the initial hot electron density. The Lagrangian treatment breaks down when the first electron is stopped, and he finds that this occurs at a real space distance of:

$$x_r = \frac{c}{\omega_p}\frac{\gamma - 1}{\beta_0}\sqrt{\gamma_0}, \tag{4.74}$$

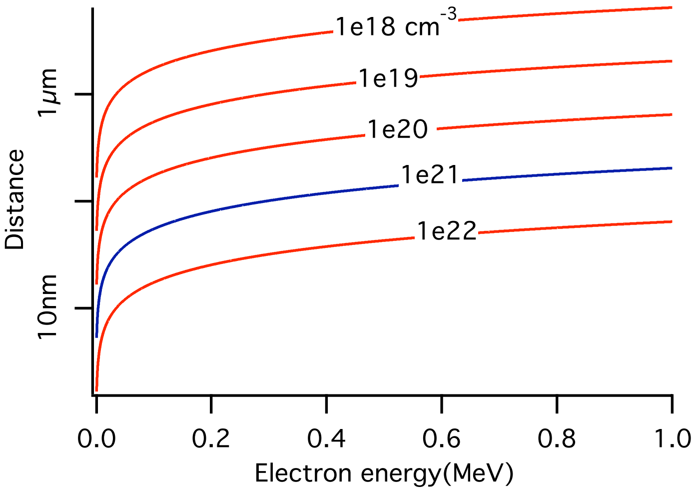

Figure 4.17: Values of $x_r$ from equation 4.74. A typical value of the hot electron density for intense laser matter interaction is $1 \times 10^{21}\text{cm}^{-3}$ [DBHG97] (blue line).

where $\beta_0 = \frac{v_0}{c}$ and $\gamma_0 = (1 - \beta^2)^{-1/2}$ are functions of the initial electron velocity, and $\omega_p = (4\pi N_b e^2/m_e)$ is a "plasma frequency" for the initial electron pulse. The values of $x_r$ are plotted in figure 4.17.

### Ultrashort pulsed electron source with electron energy distribution

In the case that all of the hot electrons are produced in a time $\Delta t \ll d/\bar{\beta}$, where $d$ is the foil thickness $\bar{\beta}$ is the average normalized velocity of the electrons, we can apply Fill's approximation of the instantaneous release of an electron energy distribution into vacuum [Fil05]. The equations allow for a finite source size, giving a more realistic geometry. With a finite source size, the hottest electrons can leave the target to an arbitrary distance. The Poisson equation is now written in terms of the *areal* density $N_a$:

$$E = -4\pi e\xi N_a, \tag{4.75}$$

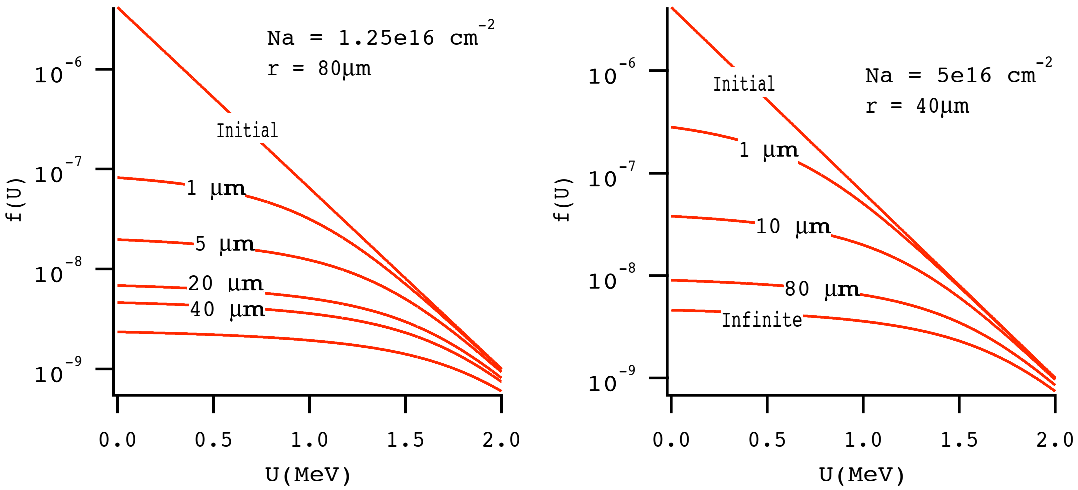

Figure 4.18: Exponential electron energy distributions at various distances for an initial electron temperature of 240 keV. Left: $N_a = 5 \times 10^16$ cm$^{-2}$, $r = 40\,\mu m$ Right: $N_a = 1.25 \times 10^16$ cm$^{-2}$, $r = 80\,\mu m$ (in both cases contain $\sim$ 0.1 J of electron energy).

where $\xi(U)$ is the new Lagrangian coordinate, giving the fraction of hot electrons with energy $\geq U$. If $U$ is the electron energy at a distance $x$ from the source back side, where the electrons left the target from a source spot of radius $r_0$ with initial energy $U_0$, then:

$$U = U_0 - 4\pi e^2 \xi N_a x r_0/(r_0 + x) \tag{4.76}$$

and

$$\frac{\partial U}{\partial \xi} = \frac{\partial U_0}{\partial \xi} - 4\pi e^2 N_a x r_0/(r_0 + x). \tag{4.77}$$

If the electron distribution is given as a 2D maxwellian (eqn. 4.69), then

$$\xi(U) = \exp(-U/kT_e). \tag{4.78}$$

The distribution for source radius $r_0$ at a given $x$ is obtained by plotting $-(\frac{\partial U}{\partial \xi})^{-1}$ vs $U(\xi)$, parameterized by $\xi$. The results for various distances for two electron densities and spot sizes, both containing 100 mJ of hot electrons, are shown in figure 4.18. These equations are best suited to ultrashort pulses ($<$ 100 fs) and thin foils $\sim 10\,\mu m$ .

### Second-chance electrons

The fact that a large fraction of the hot electrons are constrained to the target by electric field suggests that hot electrons may be able to pass several times back and forth through a target, potentially receiving a new kick from the laser if they return to the front in time. This effect has been hypothesized as a potential way to enhance proton production with very thin foils and very high contrast laser pulses [MSP$^+$02]. The lengthening of $K_\alpha$ pulses observed in time resolved measurements as also been attributed to this phenomenon [RKPdS$^+$06]. I will touch on this second point in chapter 6.

The extreme electric fields which pull back the hot electrons also propel forward ions from the target, as I discuss in the next section.

## 4.4 Proton acceleration

A very hot topic in high intensity laser matter interactions is the acceleration of high energy, directed proton beams from foil targets [SKH$^+$00]. Protons of many 10s of MeV have been observed on high energy laser systems with a laser to proton energy conversion efficiency of up to several percent. The low emittance that can be exhibited by these proton beams [CFR$^+$05] has led to a large number of experiments in which the proton beam is used for time-resolved radiography [MPT$^+$04], or electromagnetic field mapping [BCS$^+$02]. It is also a quite potent rapid heating source [PMK$^+$03, AFA$^+$06].

The protons originate from hydrogen atoms contaminating the laser target foil and are emitted in the target normal direction. In this section I will discuss the mechanism by which they are accelerated, the characteristics of the proton beams generated in 100 TW and PW class laser systems, their interactions with a sample foil to be heated, and the problems associated with velocity dispersion which can lead to a lengthened heat deposition times.

### 4.4.1 Protons accelerated from the back surface

The mechanism by which protons were accelerated from solid later targets was an issue of some debate until recently [APM$^+$04], when the model of electron sheath acceleration from the back side of the target won out over front side ponderomotive acceleration as the dominant mechanism. Over 99% of the high energy protons are accelerated by the electric field of electrons leaving the back surface of a target. This electric field has the form:

$$E \approx \frac{kT}{e\lambda_D} \tag{4.79}$$

where $\lambda_D$ is the Debye length (eqn. 4.20)[13]. Typical values of this electric field can easily exceed $10^12\,V/m = 1$ MeV/ $\mu m$ , which is sufficient to accelerate a proton to MeV kinetic energies in less than 100 fs.

Protons were demonstrated to originate from the back surface of a foil by Allen, *et al.*[APM$^+$04] when they used an argon-ion sputter gun to clean the back side of a target in vacuum before a shot without substantially heating it and measured an almost complete drop off in proton production. As they note, ohmic heating can also be used to remove contaminants if a proton beam is not desired, but their method showed very clearly that the vast majority of the protons accelerated from a foil target originate from the back surface and hence must have been accelerated

---

[13] The factor of $\epsilon_0$ in the reference comes from using SI rather than cgs/Gaussian units.

by the electron sheath. This mechanism of acceleration is now commonly referred to as target normal sheath acceleration (TNSA).

### 4.4.2 Beam characteristics

Accelerated proton beams take on an energy distribution that is roughly exponential with an energy cutoff. In petawatt laser experiments [SKH$^+$00], up to $2 \times 10^{13}$ protons with energy $> 10$ MeV were produced in a 4 MeV distribution with a cutoff energy of 58 MeV from [CH] targets. This staggering proton output of 48 J of protons represented a conversion efficiency of 12% into very high energy protons. With a high-contrast, 10 J 100fs pulse from the JanUSP laser system, cutoff energies of $> 20$ MeV and conversion efficiencies of a few percent were achieved [MBH$^+$01].

A two dimensional image of the proton beam, as well as a measurement of the energy distribution, can be achieved with a stack of radiochromic film (RCF) [BBG$^+$04]. To the extent that RCF film can be calibrated by dosage, a reasonable estimate of the number of protons in the beam can be made with this method, assuming an exponential distribution. As might be expected from a source of finite size, there is a correlation between emission angle and proton energy, with the highest energy protons being emitted in a cone of narrowest angle. Typical values are $2^\circ - 4^\circ$ for the highest energy protons and $\sim 20^\circ$ for the lowest energy protons.

### 4.4.3 Absorption by matter

As with electrons (section 4.3.1), proton stopping power can be obtained from the NIST databases [BCZC05] , and a similar plot to figure 4.4 can be generated, as shown in figure 4.19, which shows both nuclear (proton-ion collisions) and electronic (electron excitation and ionization) contributions to the stopping power. Like electrons, cross sections for collisions with atomic electrons are based on the Bethe theory (c.f. eqn. 4.60). Being much heavier than electrons, the protons don't lose

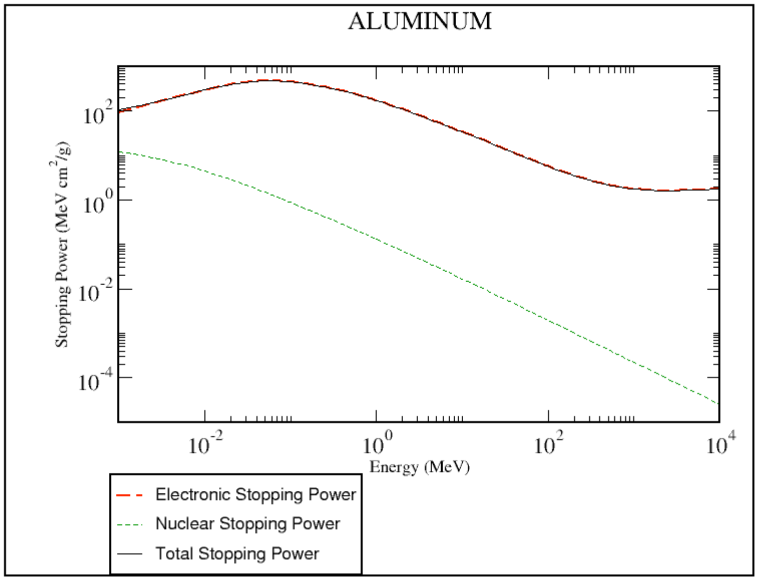

Figure 4.19: Proton stopping power as plotted by the NIST pStar databases [BCZC05]. Protons of energy $>$ 1 keV are plotted here and it is clear that electronic stopping power dominates in this range.

energy to bremsstrahlung, and the vast majority of absorbed proton energy goes into the electrons of the material. Near 1 keV, nuclear collisions account for only 10% of the energy loss.

### Bragg peaks

The concept of the Bragg peak [BA53], which is vital in medical applications of high energy *monoenergetic* proton beams is less important when the protons start with a wide energy spread, as is the case with laser generated protons[14]. .

The Bragg peak describes the fact that a proton being slowed down will deposit most of its energy near the end of its trajectory in the material. With a tunable monoenergetic proton beam, this allows deposition of energy to be peaked

---

[14] Indeed, even the so-called "monoenergetic" laser proton sources reported recently [HAC$^+$06] actually have a rather large energy spread of $\Delta E/E \sim 0.25$

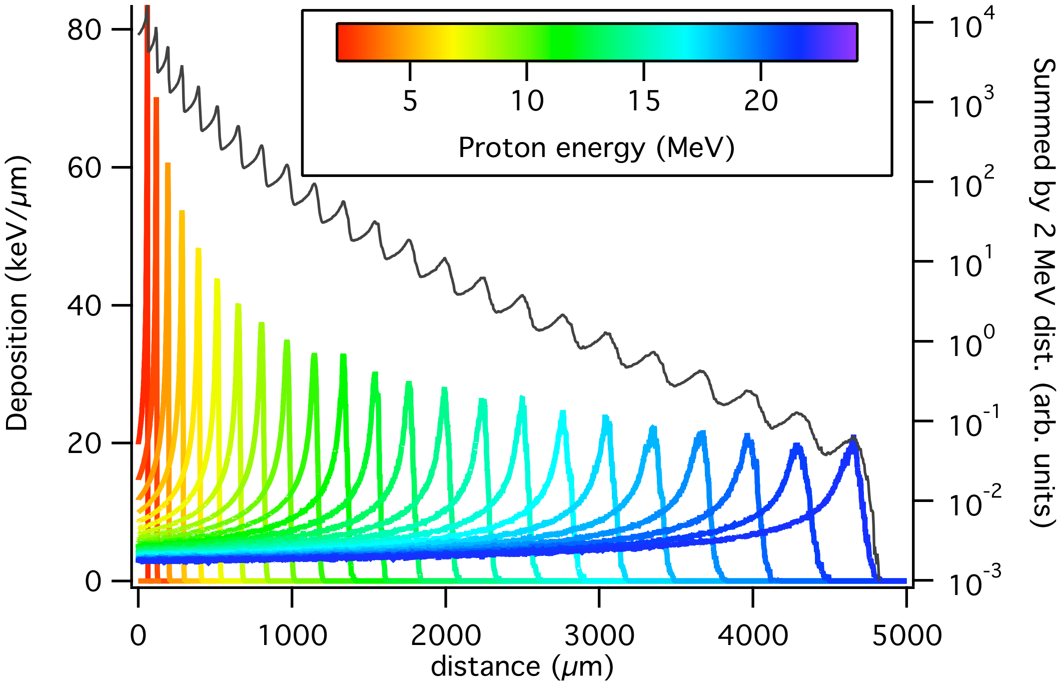

Figure 4.20: Proton energy deposition as a function of distance into the material of various energies, and their summation over a Maxwellian distribution of energies. For each individual proton energy, the bragg peak is the point of maximum deposition. In a continuous distribution of proton energies, the summation curve would be perfectly smooth.

a certain depth into a target, perhaps meeting a threshold dosage for damage at the bragg peak, while leaving the intervening material undamaged with a sub-threshold dose (e.g., to destroy a tumor). As can be seen in figure 4.20, Bragg peaks smooth out when summed together in an energy distribution. In the figure I added together a discreet set of energies, and a degree of smoothing can already be seen.

Energy straggling comes from the fact that scattering is a statistical process and the stopping power is just an average. The number and energy loss of collisions experienced by a given proton both vary significantly. Again, this effect is smoothed out when we are only concerned with the total energy deposition of a large number of protons of continuously varying energy, most of which are expected to pass through the material.

### 4.4.4 Timescale of heat deposition

The weakness of proton heating as a means to isochorically preparing a warm dense matter state is that velocity dispersion causes the proton pulse, which starts with a pulsewidth approximately the same as that of the laser, to spread out in time because of its wide range of energies, and hence velocities. For example, crossing a 50 $\mu m$ gap, a 500 keV and a 3 MeV proton which start at the same time will arrive separated in time by 3 ps (= 5.1 ps - 2.1 ps). In a two-foil proton heating setup, this can be mitigated partially in two ways: 1) reducing the gap between the foils, and 2) block slower protons with intermediate material. In reducing the gap between the foils, one must be sure that enough space is left for the electron sheath to build up and accelerate the electrons; generally several 10s of $\mu m$ are left to be safe. In adding material, the barrier layer can't be far separated from the sample, because the barrier slows down all proton energies, causing a new velocity dispersion problem across the barrier-sample gap. Therefore, the barrier might as well be right up against the sample, or simply consist of a thickening of the sample

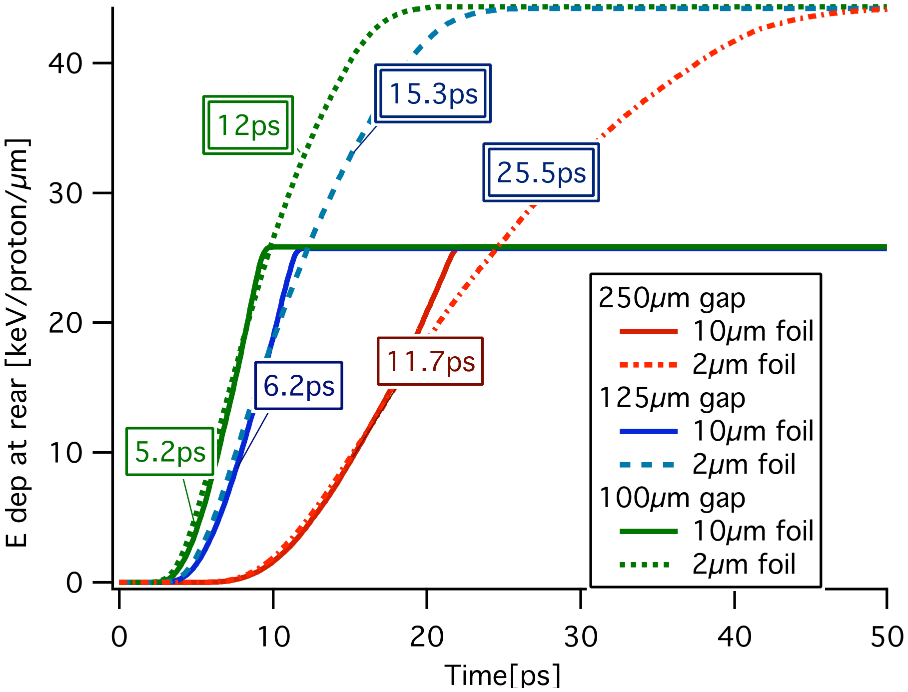

Figure 4.21: Energy deposition timescales for various sample thicknesses and gap distances for a proton energy distribution of 1.5 MeV with a 50 MeV cutoff. Labels on the curves are the time for heating to go from 10% to 90% of total.

itself. The integrated energy deposition as a function of time for 2 $\mu m$ and 2 $\mu m$ sample thicknesses and various gap distances for 1.5 MeV proton distributions are shown in figure 4.21. The choice to use a 50 MeV cutoff energy has negligible effect. We can see that a large gap and a thin sample foil can lead to deposition timescales of several 10s of ps. This wouldn't be long enough for a 2 $\mu m$ foil to completely dissipate, but a significant amount of hydrodynamic expansion of the surface of the sample foil will have taken place by the time the deposition is finished.

It's easy to see from figure 4.21 why proton heating is still an attractive option. We see here a deposition of 25 keV/proton/$\mu m$. With a modest laser to proton conversion efficiency of only 1% on a 10 J laser, we expect to see $4.2 \times 10^{11}$ protons in our 1.5 MeV distribution, amounting to $10^{16}$ eV of deposited energy per $\mu m$ of material. Typical proton source radius of 150 $\mu m$, crossing a 100 $\mu m$ gap with a typical angle of 20° implies a heating region of 185 $\mu m$ diameter, or $2.7 \times 10^4\, \mu m^2$ area, implying $\approx 3.6 \times 10^{11}$ eV/$\mu m^3$. The atom density of Al being $6.02 \times 10^{10}\, \mu m^{-3}$, we easily obtain 6.1 eV/$atom$ with these assumptions. Indeed, on the 10 J JanUSP laser, Patel, *et al.*achieved heating to 4 MeV with a gap separation of 250 $\mu m$, confirming the conversion efficiency of $\sim 1\%$. By ballistically focusing the protons using a spherically shaped source target, he was able to increase this heating to 23 eV in a very small spot.

# Chapter 5

# Diagnostics

In this chapter I describe the diagnostics used in our experiments. Although experiments on many different laser systems are presented in this thesis, the diagnostics described here could have been used on any of them, and there was in fact a great deal of overlap. This chapter will present the detailed operating procedures for the diagnostics, as well as representative images of raw data and techniques for analyzing the data. Quantitative numerical results are reserved for the later chapters. For diagnostics fielded by other experimenters, I go into less detail, and the reader is encouraged to follow the references.

I start with the diagnostics for laser focusing and alignment. Later sections describe diagnosis of x-rays, protons, heated material expansion, and thermal emission.

## 5.1 Focusing on a solid target

In solid target experiments, a single shot typically destroys the target requiring a new target to be brought into position. On most laser systems, the laser focus established at a fixed point and the target is moved into position using motorized stages. Some laser systems (e.g. Sanidia, Titan) allow for sub-mm corrections in the position of the laser focus by motorizing the focusing mirror and the mirror before it. In this section I will briefly describe the experimental techniques needed to reliably achieve good focus on our solid targets.

### 5.1.1 Diagnosing the focal spot

Unless a target chamber is specially designed to avoid it, the strain of having the target chamber under vacuum will shift the relative positions of various optics causing significant changes relative to air, and so the process of diagnosing the beam and locating the position of best focus should be done under vacuum, necessitating vacuum positioning of the target and the beam diagnostic optics. However, initial rough alignment is easier to do at air.

The focal spot is measured using a low $f/\#$ optic imaging the laser in the focal plane onto a CCD[1]. The optic is moved along the focal axis, the $z$ direction, until the sharpest image of the beam is found. Often in a new setup the beam will be nowhere near perfect. Two principal causes for a bad focal spot are astigmatism from a misaligned off-axis parabolic mirror, and non-parallelism of compressor gratings[2]

#### Parabola astigmatism

The focusing optic of choice in high energy USP lasers is the off-axis parabola (fig. 5.1). This setup allows the target to be placed such that it doesn't interfere with the incoming beam. A parabola can give a very good focus, but the incoming beam must be incident at a precise angle. The back surface of the parabola will be flat and that can be roughly aligned normal to the incoming beam. To get close, an

---

[1] Of course, the laser is sent in highly attenuated so as not to damage the CCD or optics.

[2] Some laser systems (e.g. Titan, Sandia) also have a vacuum window in the beam path, allowing the compressor to stay at vacuum while the target chamber is aligned with the laser at air. The quality of focal spot through such windows is usually horrible, and so it's important to confirm that the status of the window is known before adjusting the parabola.

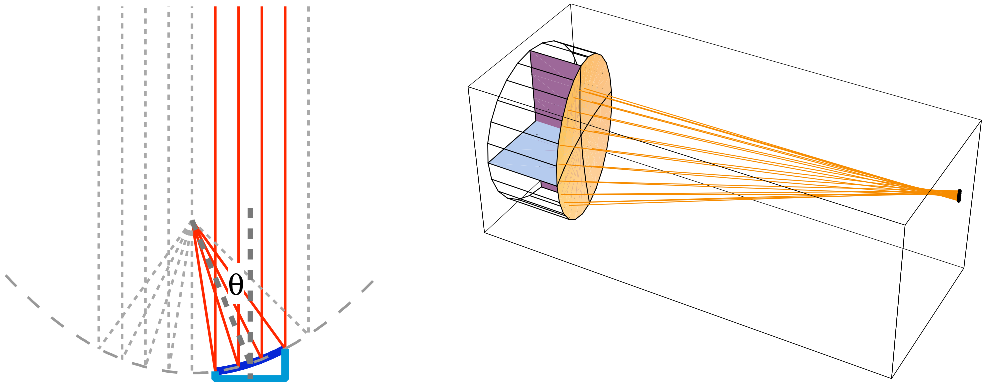

Figure 5.1: The off-axis parabola. The off-axis angle $\theta$ is measured between the incoming beam and the line from the center of the mirror face to the focal point.

adjustment in air can be made to maximize white light generation at low pulse energy. Even then, the parabola may be several $10^{\text{th}}$s of a degree off, and the focal spot diagnostic should be used.

Figure 5.2 shows real and ray-traced images of a focal spot for which the reflection angle off the parabola is too narrow. The spot looks wide before focus and narrow after focus. If the reflection angle is too wide, the beam will be narrow before focus and wide after. A vertical misaligment leads to diagnonal beams immediately before and after focus.

In certain situations it may be hard to determine whether the angle is being narrowed or widened by a given adjustment of the optics, and so I sometimes use a trick for grossly misaligned parabolas. A geometric effect causes a bright point to move across the screen as the focus diagnostic scans from before to after focus (see fig. 5.2). To fix horizontal misalignment when the beam starts wide (too-small angle case), the optics should be adjusted so that the focal spot moves in the opposite direction of the point's motion. In the narrow start (wide angle) case, adjust the beam in the same direction as point motion. In vertical misalignment, the spot may be seen twice in a progression through the focal plane; in this case the spot travelling

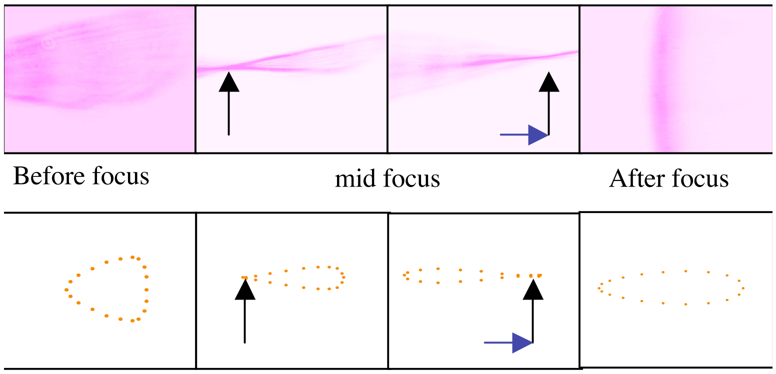

Figure 5.2: A horizontally misaligned parabola. Top: real beam images. A bright point is seen to move from left to right on the screen. Bottom: geometric ray tracing shows this spot to be a geometric effect.

down and then up indicates that the spot should be adjusted up; opposite for the other case.

If the parabola is properly adjusted and the beam still looks distorted, there may be a problem with grating parallelism in the compressor.

#### Grating parallelism

We had this difficulty on the COMET laser, which had previously been used as an x-ray laser system and thus used a line focus for which perfect parallelism of the gratings was less crucial and never tested for. Figure 5.3 shows how the non-parallelism of compressor gratings can cause a widening of the focal spot. This can occur in a two grating compressor, or even a 1-grating compressor if the horizontal retro mirror is misaligned (see section 3.2.1).

### 5.1.2 Target alignment

If we want to position a flat target at best focus, our precision is set by the properties of the focal spot. Using the approximation of a gaussian beam profile [Sie86], we

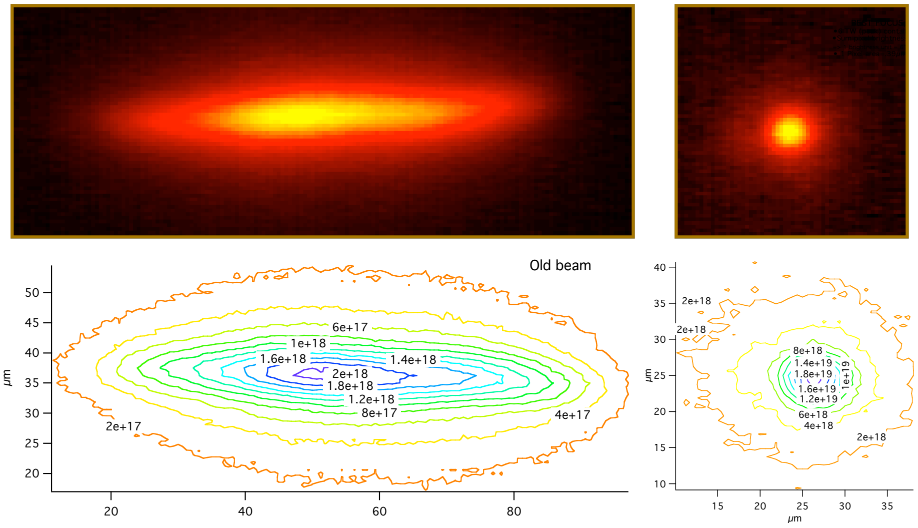

Figure 5.3: Left: after best adjustment of the parabola, the focal spot was still wide. Right: Slight adjustment in the angle of one of the compressor chamber gratings made the beam circular and small. Contour plots show that the peak intensity is increased by an order of magnitude.

know that if a gaussian laser beam travelling in the $z$ direction is perfectly columnated at $z = 0$ then its *beam waist*, defined as its $1/e^2$ intensity radius as a function of $z$ is given as:

$$w(z) \quad = \quad w_0\sqrt{1+\left(\frac{\lambda z}{\pi w_0^2}\right)^2}, \tag{5.1}$$

which asymptotically approaches a linearly changing beam waist:

$$\frac{w(z)}{w_0} \quad \rightarrow \quad \frac{\lambda z}{\pi w_0^2}\ (z \gg 0). \tag{5.2}$$

This is illustrated in figure 5.4, where the $x$ axis is $\frac{\lambda z}{w_0^2}$ and the $y$ axis is $\frac{w(z)}{w_0}$. Going from right to left, we see $z = 0$ as the geometric focal plane of a beam focused down with a cone angle of $\theta$, and the asymptotic line is the geometric focus. The

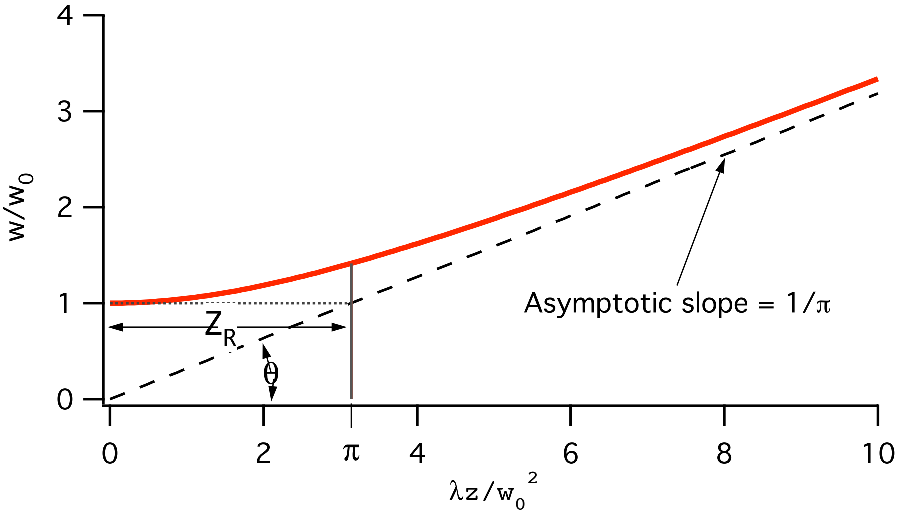

Figure 5.4: Geometry of a gaussian beam focus.

minimal beam waist $w_0$ is then the *diffraction limited* focal radius for a given cone angle and wavelength $\lambda$. We define the Raleigh range $z = z_R$ as the distance for which $w(z_R) = \sqrt{2}w_0$. As we see in the figure, this is also the range at which the geometric focus reaches $w_0$. The intensity at this point will be about half maximal at this point, and so we'd like to set $z_R$ as our maximum uncertainty in positioning our target:

$$\Delta z_{\max} = z_R \quad = \quad \frac{\pi w_0^2}{\lambda}. \tag{5.3}$$

The focusing optic and incoming beam have an associated "f-number" ($f/\#$), defined by the geometric focal length over the initial beam diameter, or:

$$\begin{aligned} f/\# &= \frac{1}{2}\lim_{z\to\infty}\frac{z}{w(z)} \\ &= \frac{w_0\pi}{\lambda}. \end{aligned} \tag{5.4}$$

Therefore, in terms of the f-number:

$$w_0 = \frac{2(f/\#)\lambda}{\pi}; \qquad z_R = \frac{4(f/\#)^2\lambda}{\pi}. \tag{5.5}$$

On JanUSP/Calisto, we had $f/\# \approx 3.1$ and $\lambda = .8\,\mu m$ , so therefore $w_0 \approx 1.58\,\mu m$ and $z_R \approx 9.8\,\mu m$ . So, we needed to be more precise than $10\,\mu m$ with our target alignment to ensure the best focus.

### Scattered or reflected light alignment

Our preferred technique of flat solid target alignment is to image the focal spot from an off angle, either through the reflection or scattering of a coaxial alignment beam off of our solid target. The coaxial beam can be any type of CW laser that's convenient, but a wavelength different from the laser wavelength won't survive too many reflections from dielectric mirrors. On the focal spot diagnostic, when the main beam and alignment beam hit the same focal spot, the beams are colinear; they will then be sufficiently coaxial if the alignment beam is visibly hitting the center of the parabola. The Titan and Sandia systems both provide coaxial CW alignment beams from the laser bay; other systems required them to be set up by the user.

Once best focus of the main beam is found and imaged in the beam diagnostic, an alignment target can be moved into place. Usually this is a $< 10\,\mu m$ wire or a very thin sheet of plastic. In either case, the alignment target is moved so that it is in focus in the beam diagnostic, which is still imaging the focal plane. The alignment target is then back-lit at the laser wavelength. If the alignment target is plastic, small specs of dust are brought into focus. With the alignment target in focus on the beam diagnostic, which is imaging the focal plane, let the alignment laser land on the target and scatter or reflect light into the alignment optics. The scattered or reflected focal spot is then imaged at 20× or greater magnification onto

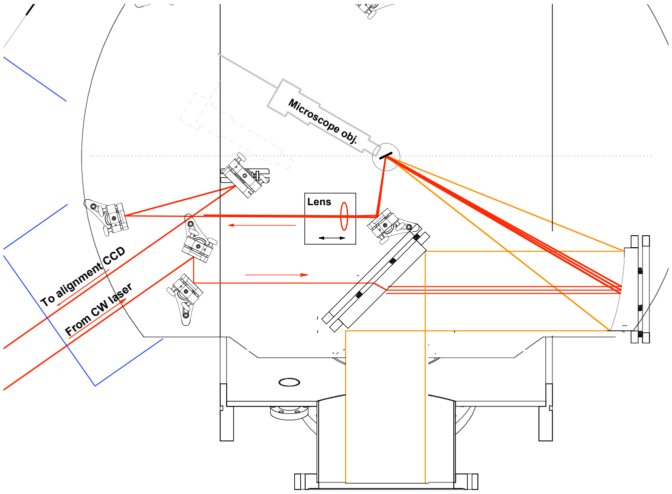

Figure 5.5: CAD drawing showing the layout of alignment diagnostics within the Calisto/JanUSP chamber. The microscope objective was on a long travel stage allowing it to clear out of the way in vacuum. The scatter diagnostic lens was placed on a translation stage for focusing.

a CCD, and the position of the spot (left to right) on the screen is marked. An example chamber layout (JanUSP/Calisto) for an incoming and outgoing alignment beam is shown in figure 5.5.

This alignment procedure was found to be repeatable to better than 5 $\mu m$ on the JanUSP laser. Any scattering surface placed at the focal point without obscuring the line of sight of the alignment lens can be brought into focus with this technique. On high energy lasers, a blast shield should be used to protect the alignment lens. It is always neccessary to block the alignment CCD before a shot, since scattered light from the laser focal point would otherwise be imaged onto it, destroying the CCD.

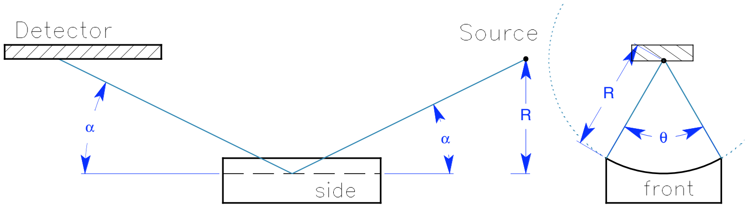

Figure 5.6: The Von Hamos geometry. The size of the crystal is exaggerated relative to most systems.

## 5.2 Measuring $K_\alpha$

In this section I will briefly describe the diagnostics that we have used used to measure laser generated x-rays (section 4.3) in our experiments.

### 5.2.1 Von Hamos crystal spectrometer

*Von Hamos* refers to a cylindrically bent crystal defraction geometry in which a point source of x-rays is focused to a line, with spectral resolution along the line. Reflection of order $n$ occurs at the Bragg angle (see figure 5.6):

$$2d\sin\alpha = n\lambda. \tag{5.6}$$

The focusing quality of the von Hamos crystal will generally depend on the bragg angle $\alpha$, the spread in angle $\delta\alpha$ (e.g., the width of the "rocking curve"), and the crystal radius $R$ by [Kne05]:

$$\Delta y = \frac{2R\Delta\alpha}{\sin^2\alpha}. \tag{5.7}$$

Under the right conditions and with the right crystal, one can achieve sub-100 $\mu m$ spatial resolution in the von Hamos geometry [YB83]. However, such pre-

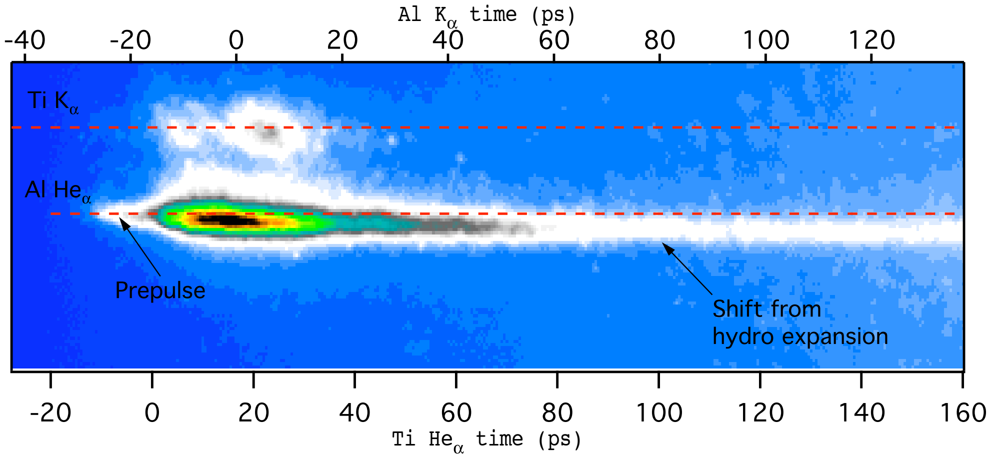

Figure 5.7: Example output of the x-ray streak camera. The target was 2 $\mu m$ Ti with a 1000 Å overcoat of Al, observed from the Al/laser side. One von Hamos crystal focused the Al He$_\alpha$ while the other (less reflective) crystal focused Ti K$_\alpha$ . The effects of the COMET prepulse can be seen in the streak image. Hydrodynamic motion of the heated plasma towards the streak camera causes the position of the Al He$_\alpha$ line to apparently shift in the spectral direction, although no change in wavelength is occuring.

cisely focusing crystals are more expensive to make and harder to find. For the von Hamos crystals in our experiments, the focusing was solely for the purpose of inproving signal-to-noise, and the spatial resolution was generally larger than the source size. Spatial resolution was achieved in experiments at UT and Livermore using a spherically bent crystal spectrometer (see section 5.2.3). Details about the film-based, time integrated Von Hamos x-ray spectrometer used in experiments at THOR can be found in the thesis of S. Kneip [Kne05].

### 5.2.2 X-ray streak camera

The von Hamos geometry was employed [SAB$^+$04] on the Jupiter facility's in-house x-ray streak camera [SBP$^+$95], which was fielded by Ronnie Shepherd in the experiment on COMET. As I will discuss in additional detail later in this chapter, a streak camera is a device employing a photocathode, an accerlation mesh, sweep plates, electron imaging optics, and a detection screen screen to produce a 1-D spatial, 1-D temporal image of the incident light. The Livermore (T-REX) streak camera, which sits entirely under vacuum inside the target chamber, uitilizes a potassium iodide photocathode and a very high, pulsed extraction voltage to achieve sub-ps temporal resolution.

Two von Hamos crystals are used to focus the x-ray radiation from the source onto the streak camera slit for two distinct spectral ranges. Readout was achieved with an MCP/vacuum CCD combination. The high voltages of the streak camera mandated that the chamber be operated below $10^{-6}$ Torr, which in the case of COMET run was expediated by a cold finger (i.e., a liquid nitrogen cooled surface that collects atoms and quickly brings the pressure down from the $10^{-4} - 10^{-5}$ Torr range to $\sim 10^{-6}$ Torr).

### 5.2.3 Spherically bent crystal spectrometer

Focusing Spectrometers with Spatial Resolution in one dimension (FSSR1D) [MAD+02] were fielded on the COMET experiment by Anatoli Faenov and Tanya Pikuz, and on the THOR experiments by Sergei Pikuz. By bending the crystal along two axes to form a spherical optic, high spectral and spatial resolution can be achieved simultaneously when the source size is small. In both of our experiments, the crystals were high quality spherically bent mica configured to resolve the $K_{\alpha 1}$ and $K_{\alpha 2}$ of the target material (Ti or Al) with spatial resolution equal to or better than $30\,\mu m$.

The FSSR1D is aligned such that the detector is on the so-called "Rowland circle" (a circle in the plane of reflection that touches the crystal at its center and has diameter equal to the crystal radius of curvature), and the source is positioned

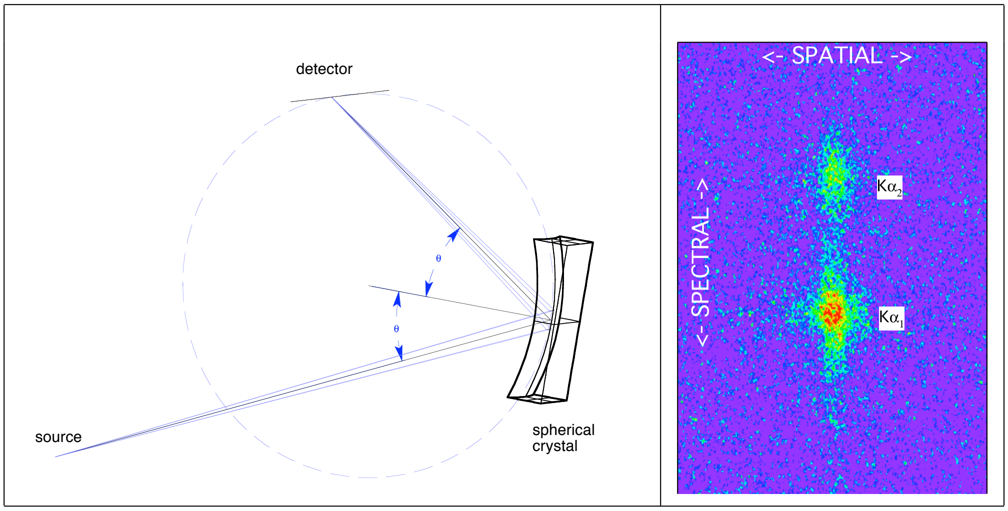

Figure 5.8: Left: Diagram of the spherical crystal spectrometer, in the FSSR1D configuration. Right: example image of $K_{\alpha 1}$ and $K_{\alpha 2}$ on film. The on-film resolution was better than $10\,\mu m$; resolution with a CCD (as on the COMET experiment) was limited by the pixel size .

for specular reflection from source to detector off the crystal, so that [GAR$^+$96]:

$$\begin{aligned} a &= R\sin\theta/(2\sin^2\theta - 1) \\ b &= R\sin\theta, \end{aligned} \tag{5.8}$$

where $R$ is the crystal radius, $a$ is the source to crystal distance, $b$ is the detector to crystal distance, and $\theta$, which satisfies the Bragg condition for our wavelength of interest, is the angle of incidence and reflection with respect to the crystal normal at its center (fig. 5.8). Note that the form of $a$ requires that $\theta < 45°$, and that the magnification $M = -b/a = -\cos 2\theta$ will be less than 1.

In an alternate scheme, reffered to as FSSR2D [GAR$^+$96], the crystal is aligned with the intent of producing a 2D image of a monoenergetic source (e.g., $K_{\alpha 1}$ only). Thus we want $\theta$ to be as small as possible, for both axes to focus in nearly the same plane, but the detector is allowed to be at any distance from the crystal. In this case, for example, the distances $a$ and $b$ in (5.8) could be swapped, giving a (slight, since $\theta$ should be small) magnification of $-1/\cos 2\theta$.

The above restrictions on the FSSR 1D and 2D alignments make it difficult to match the Bragg condition for an arbitrary x-ray wavelength. Mica is a popular material for this because several Bragg orders ($n$ in eqn. 5.6) give good reflection, meaning that one well-chosen crystal radius can be chosen cover several wavelength ranges. In figure 5.8, I show an example of an FSSR 1D image of Al $K_\alpha$ from the THOR experiments in which $R = 160mm$ and $n = 7$.

### 5.2.4 Pinhole camera

An x-ray pinhole camera has the potential to measure the spatial extent and intensity of x-rays radiated from a target. To balance diffraction and geometric blurring in the pinhole camera, we need

$$d \approx 2\sqrt{\lambda f}, \tag{5.9}$$

where $d$ is the pinhole diameter, $\lambda$ is the wavelength of light being measured, and $f$ is the pinhole to film distance. While this calls for $\sim 100\,\mu m$ in a visible light pinhole camera, shorter wavelenth x-rays allow for better spatial resolution in a pinhole camera and hence have a smaller optimal pinhole size, on the order of several to several tens of $\mu m$ depending on the x-rays being viewed. The resolution is $\sim 2 \times d$, and the magnification is $f/o$, where $o$ is the object distance. The pinhole camera relies on us having a very bright source, since the light intensity on the film will be greatly reduced by the small aperture size:

$$I_{\text{film}} \approx \frac{I_{\text{src}} d^2}{16\pi o \cdot f}. \tag{5.10}$$

The intensity on film will also be reduced by the filter placed in front of the pinhole to block out the bright visible light from the target and only admit the high energy x-rays we're interested in. Often the filter is Be or thin Al, since we are most concerned with blocking visible light and want to let in as many of our x-rays as possible.

Secondary radiation by the pinhole camera itself is a concern, since electrons and hard x-rays hitting the outer casing of the pinhole camera could cause emission within the tube, leading to noise on the film. The pinhole camera used in the first JanUSP experiment (see section 6.1.3) was conically shaped to allow for a low surface of the camera close to the target.

An x-ray pinhole camera can be difficult to align, and so it's usually helpful to fix the pinhole camera alignment while switching out the film. One option is light-tight film packs which can be replaced at the back of the pinhole camera. The other option is placing the pinhole camera on a kinematic base plate and taking the whole camera down to the dark room for film removal.

### 5.2.5 Photon counting CCD

The single photon counting CCD is a well-established diagnostic for measuring the hard x-ray spectrum from laser targets in the 1 - 100 keV range [ESS02, STS$^+$04, PIK$^+$04]. A back-illuminated[3] CCD is kept light-tight and operated at vacuum, with a thin filter between the CCD and the target. When an x-ray photon hits a CCD pixel, it excites a number of electrons proportional to the energy of the photon, which register as brightness counts in the CCD readout (see figure 5.9). Usually the CCD material is silicon, which has a bandgap of $\sim 1.09$ eV, and only a few electrons are needed to register a count on the CCD. Thus, a single K$_\alpha$ photon gives rise to thousands of counts on a single pixel. When the number of significant-energy

---

[3] Back illuminated CCDs have much higher quantum efficiencies into the x-ray, making them favorable for this purpose.

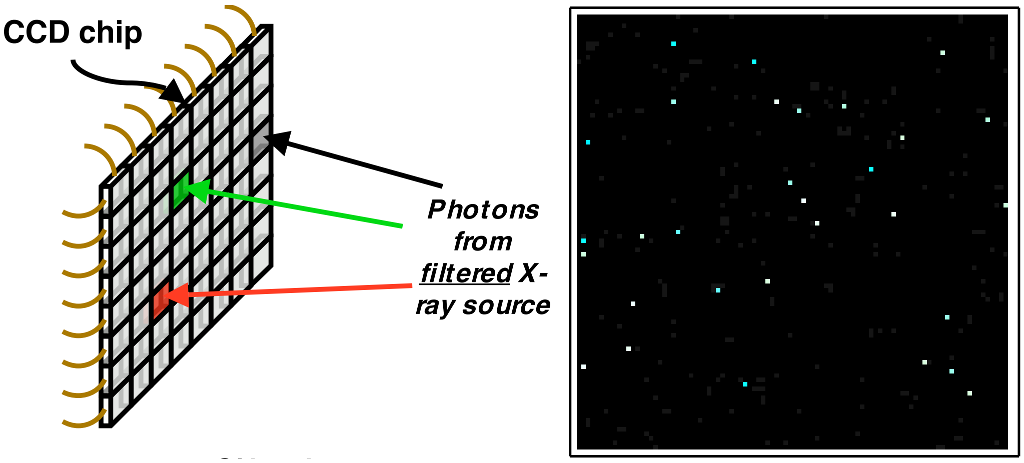

Figure 5.9: Photon counting CCD spectrometer concept. Left: A single x-ray photon hitting a pixel creates a number of counts on the pixel proportional to the photon energy; Right: Small section of a typical photon counting image (this example comes from COMET) in which $K_\alpha$ photons have been highlighted. It is important that the distribution be sparse.

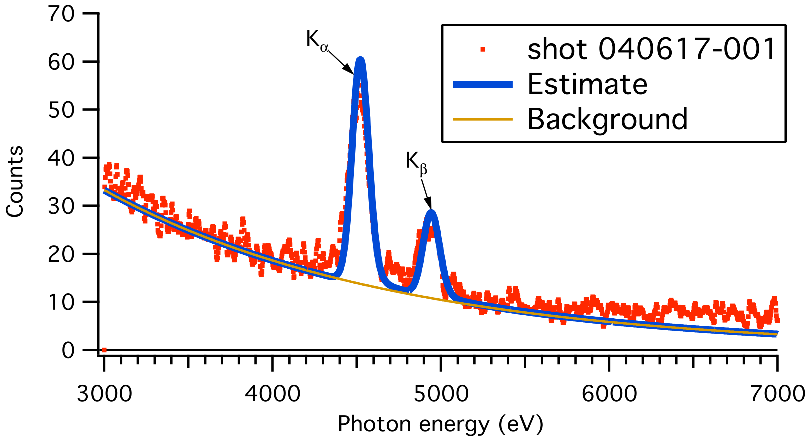

Figure 5.10: Typical histogram from photon counting CCD (from the COMET experiment).

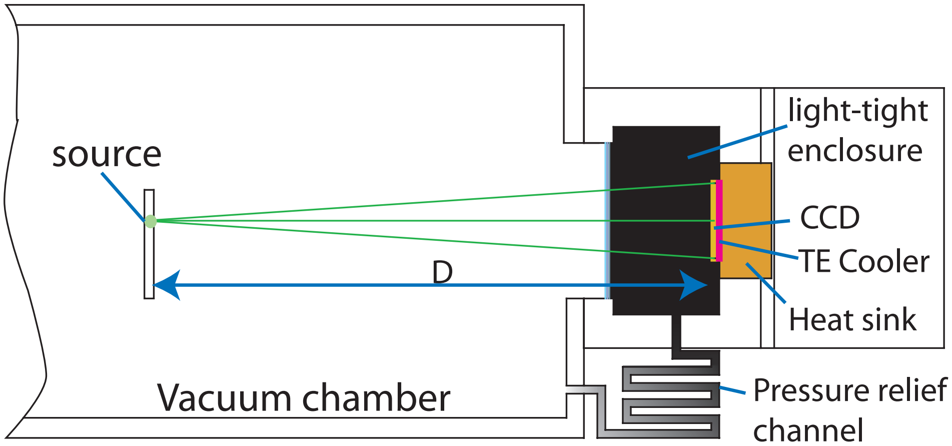

Figure 5.11: CCD in relation to x-ray source. Filters keep the CCD enclosure light-tight while allowing through the x-rays of interest.

photon hits is much less than the number of pixels on the CCD, a histogram of the CCD image can become a spectrum with well-defined $K_\alpha$ and $K_\beta$ peaks (figure 5.10). The spectral resolution of photon counting is somewhat poor in practice, for reasons to be described below, but the main strength of this diagnostic is that it allows, under the right conditions, an absolute count of the $K_\alpha$ x-ray output of our target, in photons/str in the direction of the CCD. The histogram gives $f(h)dh$, which is the number of pixels with brightness between $h$ and $h + dh$ counts. To "zeroth order", backing out this absolute number from the histogram requires: the number of pixels $N$, the CCD area $A$ (or, equivalently, the pixel area $a = A/N$), the source-to-CCD distance $D$, the thicknesses $d_i$ and attenuation lengths $\lambda_i(E)$ of the filter foils, the CCD quantum efficiency[4] $Q(E)$, and the analog-to-digital (ADC) scaling factor (number of electrons per count) $C$ of electrons to pixel counts[5], giving $h(E) = E/C$. The inferred number $\mathcal{N}_{\text{str}^{-1}}(E)dE$ of photons per steradian per unit

---

[4] Q.E. is essentially the odds of absorption of a single photon incident on a pixel, and is usually available from the manufacturer.

[5] ADC factors are usually available from the manufacturer, but can also be inferred from a low count calibration using a known x-ray spectral line (e.g. a low energy shot on a $K_\alpha$ source)

energy $E$ in the direction of the CCD is then given by:

$$\mathcal{N}_{\mathrm{str}^{-1}}(E)dE = \frac{D^2}{AC}Q(E)e^{\left(\frac{d_1}{\lambda_1}+\frac{d_2}{\lambda_2}+\cdots+\frac{d_k}{\lambda_k}\right)}f\left\{h(E)\right\}dE. \tag{5.11}$$

Various factors can distort the histogram and cause the above interpretation to fail. It is important to minimize and account for all of them.

### Dark current

The CCD will have a natural background signal, caused by dark current counts and flaws in the CCD. Imperfections are minimized by using a very high grade CCD, and accounted for in a dark reference image. Dark current is minimized bycooling to very low temperatures, usually below $-30°$C. At such a low temperature the number of dark current counts for a given exposure time will be very stable, giving a spread of a few counts (typically $< 10$ or $< 50$ eV FWHM) after background subtraction. The histogram of two dark images subtracted from one another gives the natural spread due to dark current.

### Light leaks

The photon counting spectrum can be ruined by a failure to properly block out visible light. The CCD is extremely sensitive to any light that sneaks in, and so the enclosure of the CCD should be completely light sealed. X-ray CCDs are often made with a permanent Be filter that is strong enough to hold a vacuum in the light-tight enclosure of the CCD. The advantage of this approach is that the CCD can be kept perpetually at independent vacuum, alleviating the danger of venting while the CCD chip is still being cooled (which leads to condensation and even damage to the CCD). If this option isn't available (e.g., if your filters are too thin to hold vacuum), it's neccesary to provide a pressure relief channel between the chamber and the enclosure of the CCD. This can be achieved with a long spiraling tube or a

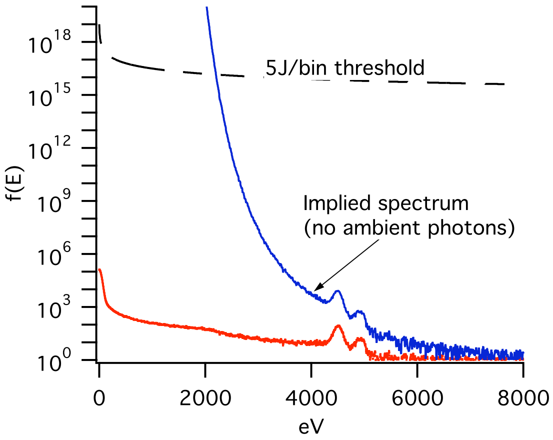

Figure 5.12: Red: measured histogram, in counts/eV; blue: implied spectrum if all counts are interpreted as photons passing through the filters; dashed: line for all laser energy being in a single histogram bin worth of x-rays. Where the blue curve approaches and crosses the dashed line, the photons must have come from ambient flourescence inside the CCD enclosure (including any pixel "leaking" effects).

cleverly machined channel on the face of the filter holder.

To test for light leaks, take successive dark images with the camera with a bright light source held next to various suspected points of light entry. The image histogram should never change if the CCD enclosure is appropriately light sealed. Certain materials, such as very thin filters with pinhole defects, or white ceramic electrical insulating tube, may appear opaque to the naked eye but fail this test.

### Ambient flourescence

The trickiest problem of the single-photon-counting CCD diagnostic in a high intensity laser environment is the fact that materials throughout the target chamber, including the x-ray filters, will be driven to flouresce soft and hard x-rays through excitation by bremsstrahlung and hot electrons.

Ambient flourescence shows up on the count histogram as a thermal background which can't be explained in terms of radiation coming directly from the source and passing through the filters, as in eqn. 5.11, since the filter term would imply more energy in soft x-rays than were available in the laser. As shown by figure 5.12, the softer x-rays must be originating from within the CCD enclosure.

Harder x-rays and hot electrons can penetrate the filters and even the thick walls of the vacuum chamber and CCD enclosure leading to lower energy flourescence from the filters, inner enclosure walls, or even the copper heat sink behind the CCD chip. Various techniques are used to minimize these effects:

- *Distance* is the best remedy, and photon counting CCDs are often kept several meters from the target; the further the better. The uniform $1/r^2$ falloff of all photon energies is generally superior to filtering, which adds a slope to the histogram.

- *Reducing high-Z materials* Any surface area of a high-Z material such as lead or even steel can lead to re-radiation of high energy photons that penetrate the CCD enclosure and contribute to the background. Thus it is important to minimize the amount of surface area of high Z material that is within line of sight of both the target and the CCD enclosure.

- *Enclosing the target in thick, low-Z material* was suggested by Stoeckl, *et al.*[STS$^+$04], as a way to cut down on available high-Z surface area, but it was not implemented in their experiments.

- *Successive apertures* are often used to prevent radiation from objects near the source from re-radiating to the CCD. This is tricky because any material placed in the line of sight of the CCD can potentially re-radiate, including apertures[6]. Any material close to the CCD should be low-Z, leading to a

---

[6] In fact, CCDs have been permanently affected by experimenters putting a non-knife-edged lead aperture within 10 cm of a CCD chip for high energy shots, as evidenced by a faint ghost image visible in dark images.

common suggestion of using progressively lower Z apertures, or increasing from low to high and then back to low Z. To avoid surface area in the aperture in direct line with both the source and the CCD, the apertures should be knife-edged. The improvement I've seen using apertures has been visible but not dramatic.

- *Outer lead shielding* was found to significantly improve $K_\alpha$ contrast over background by Stoeckl, *et al.*[STS$^+$04]. Their technique consisted of lining the *outer* walls of the vacuum chamber near the photon counting CCD with several cm of lead, blocking hard x-ray paths originating from some point inside the target chamber and away from the source and travelling *through the chamber walls* to affect the CCD.
- *Magnets* are often used [ESS02], particularly when the photon-counting-CCD is in the so-called "cone of death" - a 10 to 20° cone along the laser axis in either direction - in an attempt to divert the very hottest electrons from hitting the filters or CCD. The "cone of death" is so named because electrical diagnostics such as photon counting CCDs have been known to be completely ruined by radiation in the forward laser direction behind a solid target, presumably because of extremely hot electrons ponderomotively accelerated in the forward direction by the laser.

The importance of blocking out ambient flourescence goes beyond just a signal-to-noise concern at the photon energy of interest: a very high count of soft x-rays reaching the CCD can lead to pileup which can distort and bury $K_\alpha$ peaks.

### Count pileup

Multiple photon hits on a single pixel must be considered in the photon counting measurement to properly interpret the count histograms. The rigorous treatment

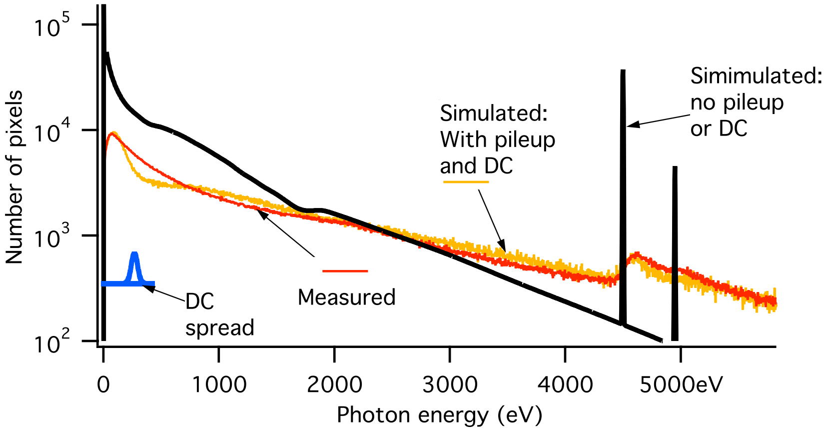

Figure 5.13: Example of the effects of pixel count pileup on a Ti $K_\alpha$ spectrum. The black curve shows the histogram input into the CCD photon counting simulation, taking into account the CCD quantum efficiency; the yellow curve shows the results of the simulation, which mimics pile up and dark current broadening; the red curve shows the measured spectrum of the shot being simulated.

of this problem can be very complicated [Dav01][7], but we can achieve sufficient accuracy using a number of simplifications. First, since the photon energies of interest are well below 100 keV, I use the approximation that a single photon only affects the single pixel that it hits, without bleeding over into neighboring pixels[8]. Thus I take the function $R(h, E)$, which representing the distribution of incident photon energy $E$ into the number of photon counts on a pixel to have the shape of a delta function, and neglect the question charge cloud grading, instead treating the problem pixel-by-pixel. Each sample pixel is treated as equivalent, and I take the source to be far enough away such that angle of incidence can be taken as normal.

With these assumptions, the problem lends itself to a simple Monte Carlo approach, modelling the CCD as an array of bins that each have an equal chance of receiving a given photon. Photons are chosen randomly from a guess of the actual

---

[7] Since the CCD cameras I used on experiments were borrowed, there was no chance to do the calibrations called for in the cited article, which was written for a x-ray observatory for which photon counting is of central importance.

[8] pixel bleeding generates low-count pixels which are treated as part of the ambient flourescence

photon energy distribution, and the appropriate number of photons are distributed randomly on the array and allowed to add up. Gaussian noise is then added to simulate dark current. Dealing with $\sim 1 \times 10^6$ pixels and $\sim 1$ count per pixel, a reasonable faxcimile of the actual CCD chip can be simulated in this way with a calculation time of less than 1 minute on a desktop computer, although finding a good enough start distribution can take several iterations.

An example of such an analysis is shown in figure 5.13. The red curve is a measured distribution with significant but managable pileup. The black curve shows a guess for the actual distribution of photons absorbed by the CCD, and the yellow curve shows the resulting distribution after dark current spreading is taken into account. Note that pileup causes the slope of the background, by which we would infer the bremsstrahlung temperature, to flatten out , mimicing a higher background temperature than was actually present.

## 5.3 Diagnosing expansion and reflectivity with interferometery

In the experiments covered in this thesis, expansion and reflectivity were measured using a probe beam whose light was derived from the main laser pulse (see section 3.1.5). This section describes the considerations involved in operating a reflecting interferometric probe for observing an expanding solid target, as well as the specific designs of interferometers fielded in the experiments.

### Reflecting the probe beam

In our experiments we were interested in measuring the immediate response of our sample material to being isochorically heated to WDM temperatures, during the first few ps of expansion. This calls for the measurement of $\sim 1\ \mu m$ motion of the sample surface. Such fine expansion is essentially impossible to see looking at a profile of the sample target surface (side-on probe beam) due to resolution limitations and diffraction from the target edges. Rather than attempt side-on imaging, we reflected our probe from the back surface of the sample. In reflection, $\sim 1\,\mu m$ of motion is similar to the probe wavelength, and shows up as a shift in the phase front which can be measured by interferometry. At these early times, the expanding plasma[9] (see section 4.2) has a short scale length, and we can safely apply the WKB approximation to find the phase shift from the expanding plasma, relative to the flat, unheated surface, for a probe beam with $k(x) = \cos\theta n(x)\omega/c$:

$$\begin{aligned} \phi_{\mathrm{WKB}} &= 2\int_{x_v}^{x_{\mathrm{tp}}} k(x)dx + 2k_0\cos\theta(x_v - x_i) && (5.12)\\ &= 2\int_{x_v}^{x_{\mathrm{tp}}} [k(x) - k_x]dx + 2k_0\cos\theta(x_tp - x_i), && (5.13) \end{aligned}$$

where $x_{\mathrm{tp}}$ is the position of the critical density reflection point, $x_v$ is a point in vacuum, and $x_i$ is the initial position of the surface. According to our hydrocode simulations (see chapter 7), the WKB approximation is very similar to the approximation of treating the critical surface as a moving reflective surface and ignoring the plasma out front, for our timescales and plasma scale lengths. At later and later times of expansion, the WKB treatment becomes more important.

The reflectivity of the heated region is also interesting, as it is related to the electronic properties of the material. This will depend more strongly on the properties of the plasma out front and should be treated by the formalism of Milchberg, *et al.*[MF89].

Our heated region will be $\sim 100\,\mu m$ across, and so we require a surface that is uniform and smooth on that scale. Thus it was important for the target material to have a mirror-like finish. In addition, it is useful for the surface to be very flat,

---

[9] warm dense matter, with lower density plasma out front

so that interference fringes on undisturbed material will show up as straight lines. For many of our targets, this was achieved by vapor depositing our sample material onto a layer of silicon or silicon nitride that is either negligibly thin or etched away.

### Short coherence length

Interferometry relies on the interference of two coherent laser fields, one of which encodes the phase from interacting with our target, while the other contains an undisturbed reference phase. The beam paths of the reference and interacting beams must be equal to within less than the coherence length of the laser for interference to occur. Since the coherence length of CPA lasers is very short (typically $\lesssim 50\mu m$), a convenient strategy is used to achieve this overlap: rather than having one beam interact with the target while another follows a separate path of equal length, a single beam interacts with the target, and then two regions of that single beam are interfered with each other, one part of the beam interacting with a dynamic region of the target (e.g. heated material) and the other with a static region (unheated material). This is achieved by splitting the beam after interaction with the target and either shifting the two beams relative to each other (as with the Wollaston and Mach Zehnder) or inverting one of the two beams (as with the Michelson).

### Non-probe light polution

The laser pulse itself will generate a lot of light which scatters around the chamber and towards the interferometer CCD. Usually, a bright enough probe beam is available so that interference and ND filters can be placed at the CCD to eliminate the scattered light.

Since the probe and pump are initially of the same wavelength, doubling the probe could help prevent scattered laser light from affecting our image, since then the interference filter would block out the fundamental wavelength of the pump pulse

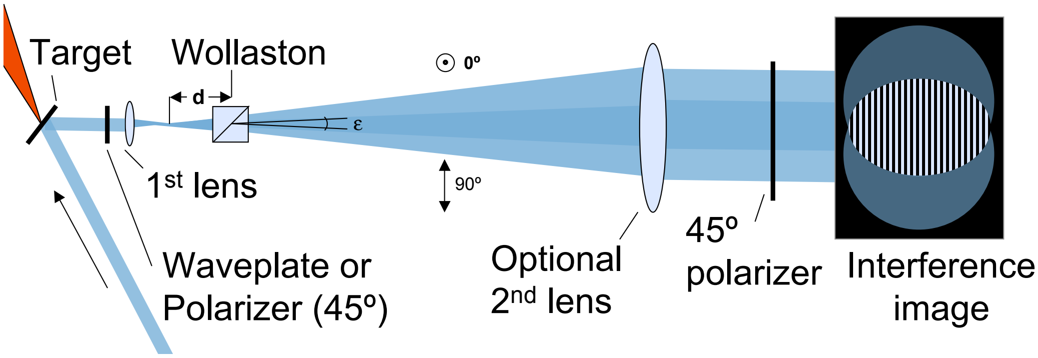

Figure 5.14: Schematic of the Wollaston prism interferometer. A Wollaston prism inserted in an imaging beam path splits the 45° polarized beam into 90° and 0° polarized beams diverging at an angle $\epsilon$. A polarizer converts both to 45°, allowing them to interfere. Note that theparation of the two beams relative to the beam diameter is exaggerated here.

scattering around the chamber. However, if doubling comes at the cost of having a much weaker probe beam, it can make the problem of light polution greater (as was seen in the second run of JanUSP x-ray heating experiments): self-emission from heated material at warm dense matter temperatures and beyond will be brighter at the $2\omega$ wavelengths than at $1\omega$ (see eqn. 5.25). Thus as the probe gets dimmer the emitted light from the source gets brighter. Some stray light can be eliminated by placing an iris behind the lens at the focal length. Then the probe light, which is columnated before entering the lens will pass through the iris while other light is blocked. The iris can only be closed as much as precision in alignment and flatness of the target allow, but this can be as much as 90%.

The best solution to light polution is to have a sufficiently bright probe pulse to allow heavy filtering. The several mJ available in the independently compressed probe pulses of major laser systems is generally sufficient to beat out stray light.

### 5.3.1 Wollaston prism interferometer

In our x-ray heating experiments, we utilized a shearing interferometer in which a Wollaston prism is placed along an imaging beam path between crossed polarizers [BPS]. A Wollaston prism is a variety of cube polarizer which separates the two polarization by a small angle $\epsilon$ at the interface between its two wedges [10]. Placing the Wollaston in an imaging path, typically just behind the focal point of the first imaging lens (figure 5.14), causes the probe beam to split into its 90° and 0° components with a slight shear. Using a 45° polarizer then allows the two components to interfere. With a waveplate or polarizer placed before the Wollaston, we can adjust initial polarization and hence the two components to make them equal in brightness.

In terms of distances *in the object plane*, we are interested in the fringe spacing $\eta$ as well as the separation $e$ between equivalent points in the two images. These are given by [Kog, May94]:

$$\eta = \frac{f}{w}\frac{\lambda}{\epsilon}; \tag{5.14}$$

$$e = 2f\tan\frac{\epsilon}{2}, \tag{5.15}$$

where $f$ is the focal length of the first lens, $w$ is the separation between the center of the Wollaston and the focal point behind the lens, $\lambda$ is the beam wavelength, and $\epsilon$ is the splitting angle of the Wollaston.

Thus we see that our choice of collecting lens and Wollaston prism fix our image separation in the object plane for a given probe wavelength, but the fringe spacing can be adjusted by moving the Wollaston back and forth along the beam axis. Another nice feature of the Wollaston interferometer is that the fringe angle is adjusted very easily relative to other interferometers, requiring only rotation of the

---

[10] The related Nomarski prism has one optic axis tilted towards the input face, moving the point from which the distance $d$ to the focal point is measured to a point outside of the prism, compared to the center of the prism in the Woolaston case. Either type of prism could be used for our purposes, but Wollaston prisms are more commonly available.

Wollaston (and associated adjustment of the polarizers/waveplate).

In practice, the diameter of the beam should be much larger than ($\gtrsim 4\times$) the separation $e$ given in eqn. 5.15, which in turn should be larger than the expected interaction region. An example image in which these conditions have been met is shown in figure 5.15. A 2 mm target window is overfilled with the probe beam, and $e \sim 1$ mm, while the expanding region is $\lesssim 100\,\mu m$ .

### 5.3.2 Timing of 2D-imaging interferometers

Unlike the chirped pulse interferometer discussed in section 5.3.7, a 2D imaging interferometer takes only a single time snapshot of the heated target as it expands. While a precise delay stage can adjust the relative timing of pump and probe with $\sim 10$ fs precision, it is important to find an accurate timing which gives a delay of zero, where the pump and probe are known to arrive simultaneously. This alleviates the uncertainty inherent in trying to track back the zero time at which heating starts from a large number of data shots at different delay, and also helps us distinguish between heating by instantaneous (x-rays) and delayed (protons and other ions) sources.

#### Timing by air breakdown

As discussed in chapter 4, atoms can be instantaneously field-ionized by the laser pulse in focus. In the JanUSP x-ray heating experiments, I exploited this fact to find the relative timing of pump and probe arrival by back-filling the vacuum chamber slightly with nitrogen and using the interferometer to observe the change in index of refraction caused by the ionized gas at the laser focus.

The index of refraction in neutral nitrogen is $N_{\mathrm{neut.}} \approx (1.000297)(P/1\mathrm{atm})$, so we should check that the addition of the nitrogen backfill doesn't significantly change the position of the focus. We find that $(N_{60\ \mathrm{Torr}} - 1) \approx 2.4 \times 10^{-5}$, and so

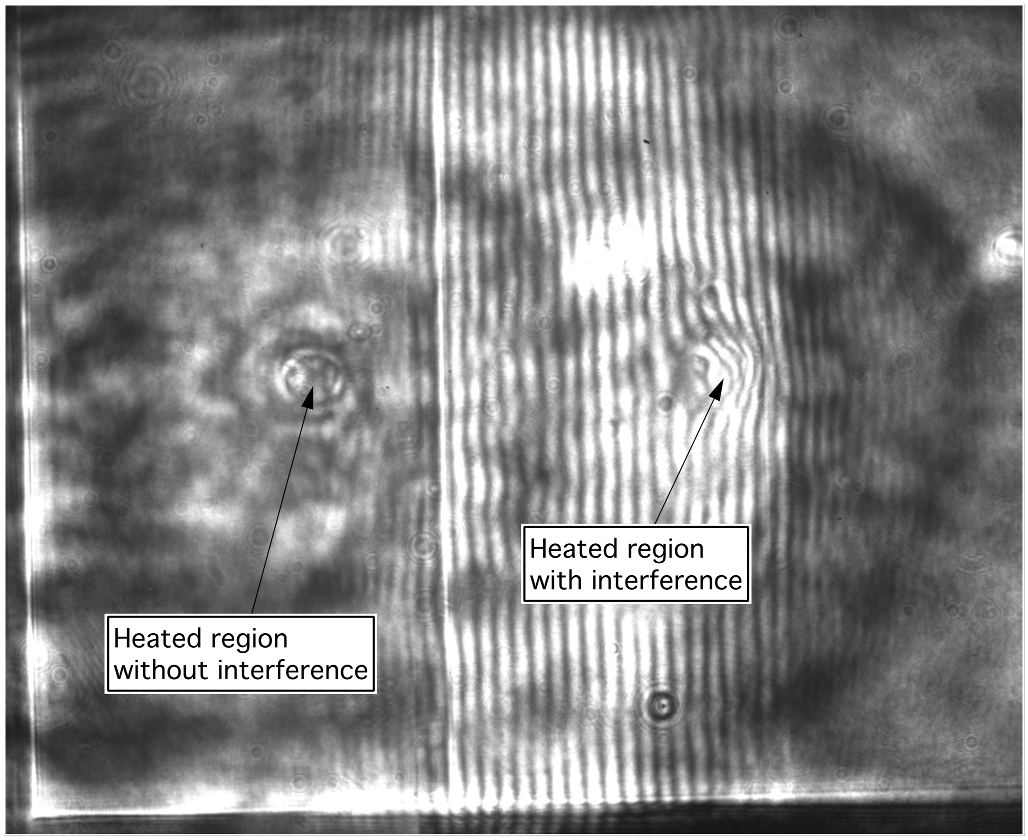

Figure 5.15: An example image from a wollaston prism interferometer used on a JanUSP shot. Two images of the heated expanding region are seen, one with interference fringes, and the other without. In this case the overlap of the two beams covers the entire CCD; the non-interfering region consists of areas in which one of the two beams is on a non-reflecting part of the target and also areas in which one reflecting surface is raised by more than a coherence length relative to the other.

for our half-meter focal length parabola, the position of the focus would move about 8 $\mu m$ , which is negligible for timing considerations.

The atom density of nitrogen at a background pressure $P$ is $\approx 2.5 \times 10^{19} cm^{-3}$ $\times (P/1\text{atm})$. We calculate the index of refraction of partially ionized nitrogen in terms of a plasma with electron density $n_e$ equal to the atom density times the average ionization state [Hub00]:

$$N(n_e) \quad = \quad \left(1 - \frac{\omega_p}{\omega}\right)^{\frac{1}{2}} = \left(1 - \frac{n_e}{n_c}\right)^{\frac{1}{2}}, \tag{5.16}$$

where $n_c = \omega^2 m_e / 4\pi e^2$ is the critical density of the laser wavelength (see section 4.2.3). Since $(n_e/n_c)$ is small, the phase shift due to the probe beam passing a distance $d$ through an average electron density $\bar{n}_e$ is reasonably well-approximated by [Hut87]:

$$\Delta\phi = 2\pi \int \frac{(N(n_e) - 1)}{\lambda} dl \quad \approx \quad -\pi \frac{\bar{n}_e}{n_c} \frac{d}{\lambda}. \tag{5.17}$$

Because of the definition of $n_c$, the expression on the r.h.s. scales linearly with $\lambda$, as well as with distance across the ionized region, average ionization level, and atomic density. A 10 $\mu m$ thickness of once-ionized nitrogen in a 60 Torr background leads to a fringe shift of only -0.04 radians, which would not be seen by our interferometer; we need about 20 times as much phase shift to see something significant. Thus we can't simply bring in the laser with a peak intensity at the bottom threshhold of $1\times$ ionization: we need a peak intensity more like $10^{16}\, W/cm^2$, which of course is easily attainable with a few mJ of laser energy. Timing in this way is much simpler in a transmitting probe beam geometry, but our interferometer was set up for reflection, so our options were to either build a second interferometer along the transmission direction just for timing, or to precisely position a target to allow viewing of the field ionization upon reflection. We used the latter approach, which is schematically

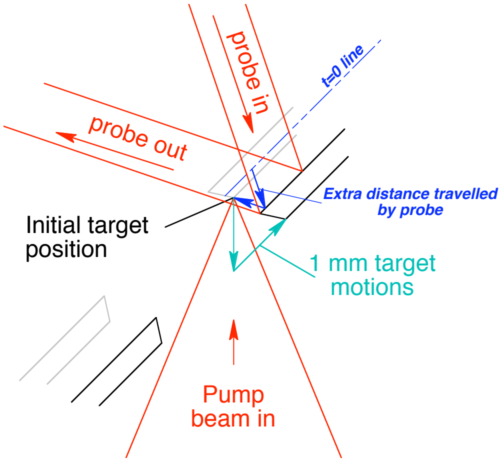

Figure 5.16: Schematic of the translations used to view the breakdown of air at the focus of the laser in the reflecting probe geometry. The distances were represented in a CAD drawing so that the extra distance travelled by the probe beam before reaching the beam focal point could be easily accounted for.

diagramed in figure 5.16. This approach relies on the fact that the target was on an encoded positioning stage, and so could be moved a precise known distance along the laser axis direction and the horizontal direction along the target surface. By focusing on the edge of a hole in the target and then moving the target 1 mm in both of these directions, we were able to pass the laser through the hole and reflect the probe beam so that it passed over the focus of the laser.

Empirically, we found a good balance on JanUSP with a back pressure of $\sim$ 60 Torr and an energy somewhere below the maximum 10 Hz rep rate energy from that laser (few mJ). At higher pressures, the focus shifted noticably and laser energy was lost to the air before reaching the focal point. In figure 5.17, I show the progression of fringe shifts at the main beam focus, which is seen in real time with a video camera as the probe delay is shifted. Viewing the fringes on a video camera rather than the interferometer's capture CCD allows us to more easily pinpoint the initial onset of fringe shifting.

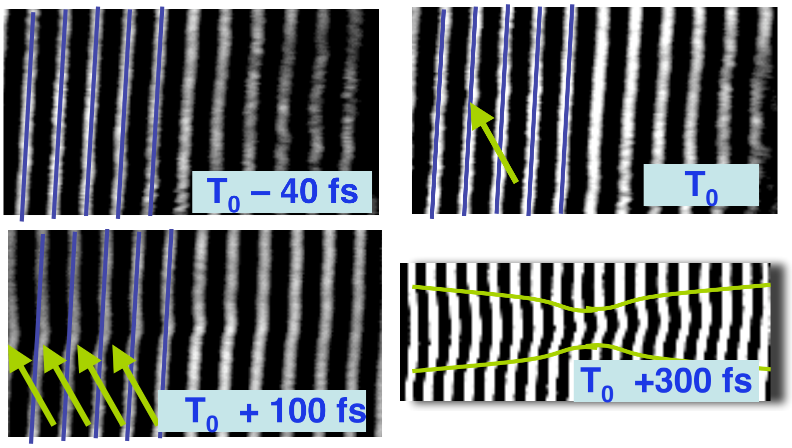

Figure 5.17: A sequence of images identifying the instant of air breakdown by the probe. $T_0$ indicates the onset of visible fringe shifts. Within 100 fs the fringe shifting is very clear, and by 300 fs the shape of a beam focus can be made out and the ionization.

### Timing by streak camera

If a streak camera is available, the relative probe and pulse timing can be measured by scattering them both off of a very thin, heavily scattering piece of material such as a small piece of lens tissue paper. Place a scatter at the focal point of the main beam (keeping the main beam energy low so that it doesn't a hole) and orient it so that the probe and main are illuminating the same narrow region of scatter target. Next, take a series of images with different relative probe timings (precisely set on an actuator stage), until the probe and main pulse switch positions. Finally, fit a line to a plot of relative pixel position of the two beams in the streak image, versus stage position. The intersection of this line gives the zero time delay position of the stage. Error is set by the uncertainty in finding the middle points of the streak images for the two beams (see figure 5.18).

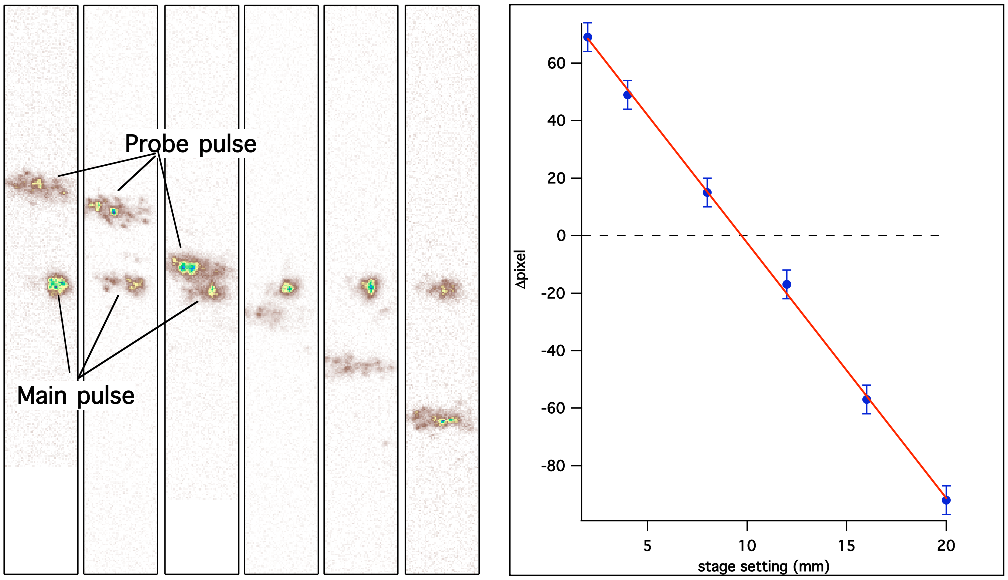

Figure 5.18: Timing of probe and pulse relative arrival time at the focal point using the SOP optics and streak camera. Left: streak images, centered on the main pulse for visual clarity; Right: plot of separation in pixels vs. stage position, with a linear fit that identifies the zero delay position of the stage.

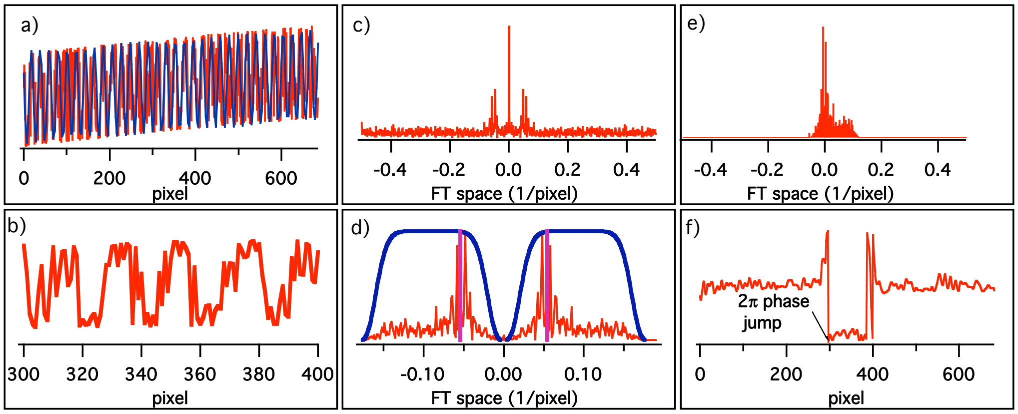

Figure 5.19: Steps in the process of extracting phase from one lineout of an interference image. a) Lineout across a phase image; b) zoom-in of lineout; c) fast fourier transform of lineout; d) gaussian window applied to FFT of lineout, and markers identifying the position of the primary frequency peak; e) rotated primary frequency peak in FFT; f) Phase obtained from inverse fast fourier transform of (e)

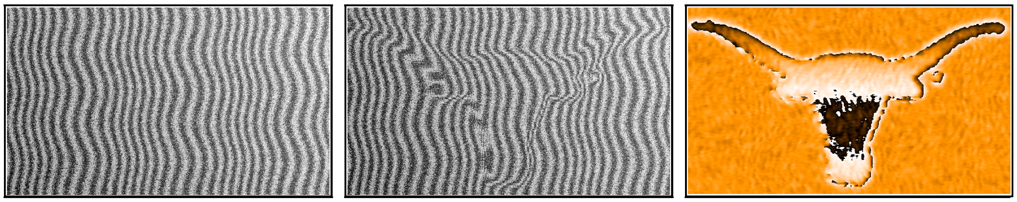

Figure 5.20: Simulated interference images. Left: background phase image with no disturbance; center: fringes with phase imposed; right: phase from central minus phase from left.

### 5.3.3 Extracting phase

The fringes in an interferometer represent the interference between the two beams arriving at the detector. Straight fringes indicate two identical phase fronts tilted at a slight angle, and tracing from one peak to the next takes us through $2\pi$ radians of phase. The straight fringes in the undisturbed region of our interference region help us quickly interpret the bent fringes in our region of interest.

See figures 5.19 and 5.20 for the steps in the phase aquisition process. The simulated interference image used for the figures was given artificial noise, as well as low frequency variations in both the phase and brightness. For simplicity, we orient the fringes run primarily the $y$ direction (the image can be rotated). Then a lineout in the $x-$ direction will appear as a sinusoidal function over a DC background and some noise (both imperfections in the interference). The base frequency of this oscillation, the fringe spacing, is set by the angular separation of the two interferometer beams. A fast fourier transform of the lineout will show peaks at the dominant frequencies: a strong peak around zero frequency for the DC background, peaks at $\pm\nu$, where $\nu$ is the base frequency of the fringe spacing, and various additional noise. With a super-gaussian windowing function, we isolate the peak representing the base frequency, letting in a wide band of other frequencies, but blocking out the zero frequency peak and very high frequency oscillations (how much of the high frequency region to keep depends on the nature of your signal). Next, rotate one of the base frequency peaks into the zero frequency position (this is equivalent to subtracting out the linear phase), and remove the other peak (which contains no additional information because the orignal function was real-valued). An inverse fast fourier transform of the rotated array yields a complex array. Expressing the complex values in the array as $A(x) = r(x)e^{i\phi(x)}$, $\phi(x)$ is our phase, and $r$ is the brightness [TIK82]. We can do better than this if there is a reference interference map of the same field with the disturbance we want to measure being absent (as in figure 5.20). We then take $A(x)/A_{\mathrm{ref}}(x)$ to isolate the disturbance. Doing this line by line (or with thicker lineouts representing an average over our resolution in the $y$ direction, if that is larger than 1 pixel), we obtain the phase of our disturbance, modulo $2\pi$.

Removing the "modulo $2\pi$" is generally more complicated than tracing through the image looking for $2\pi$ jumps, due to noise and other errors in the measurement and finite resolution. Fortunately, the algorithms of phase unwrapping are now well developed, as discussed in the next section.

### 5.3.4 Phase unwrapping

The theory of two-dimensional phase unwrapping is the subject of an excellent book by Ghiglia and Pritt [GP98]. I will give an overview of the theory and some brief examples and encourage the interested reader to find this book and the associated source code.

Let $\phi(\mathbf{x})$ be the true phase at point $\mathbf{x}$ (e.g. the total path length difference between two interfering light fields at that point). Then the wrapped phase $\varphi = \mathcal{W}\{\phi(\mathbf{x})\}$, is defined by $\mathcal{W}\{\phi(\mathbf{x})\} = \phi(\mathbf{x}) + k(\phi(\mathbf{x})) * 2 * pi$, where $k$ is an integer function that ensures $-\pi < \mathcal{W}\{\phi(\mathbf{x})\} \leq \pi$. This is the "modulo $2\pi$" effect that we want to undo with phase unwrapping.

#### One-dimensional phase unwrapping

In one dimension, phase unwrapping is a matter of tracing through the phase data and adding or subtracting $2\pi$ point-by-point where needed. There are two obstacles to successful 1-D phase unwrapping:

- Sample rate must be sufficient such that the real phase never jumps more than $\pi$ between sampling points. The rate at which the maximum phase jump between sample points is less than $\pi$ is the so-called "Nyquist rate," and we would strive to stay well above that sample rate with higher measurement resolution.

- When signal to noise ratio drops too low, (e.g., $\lesssim 2$), it becomes hard to distinguish noise from wrapping effects. At this point a simple unwrapping algorithm is likely to fail.

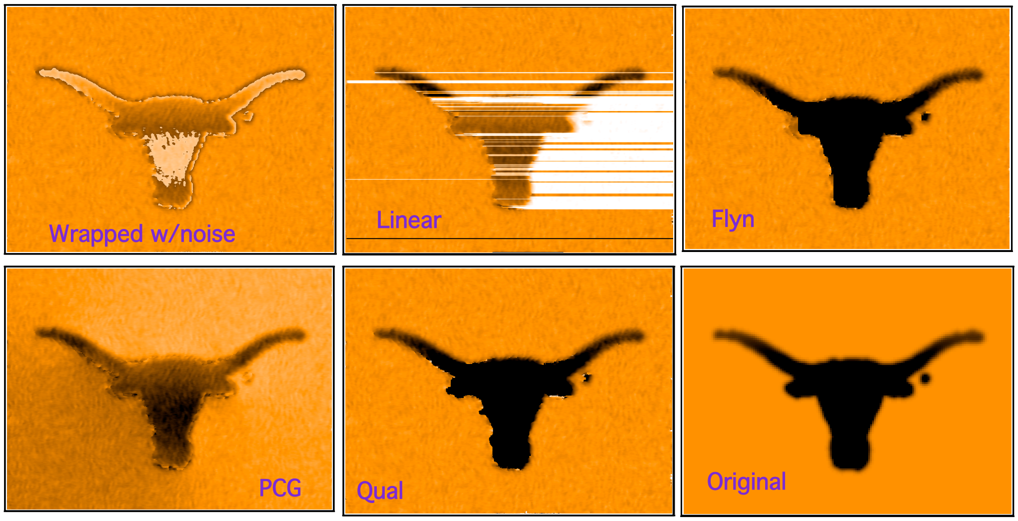

Figure 5.21: Examples of various unwrapping algorithms applied to simulated data. Noise in the phase data makes the unwrapping non-trivial and leads to residues in the phase data. An attempt to linearly unwrap the phase line-by line leads to very unsatisfactory results. Other algorithms, discussed by Ghiglia and Pritt [GP98], show better success: Qual = quality guided algorithm; Flyn = Flyn's minimum discontinuity algorithm; PCG = Preconditioned conjugate gradient algorithm

### Two-dimensional phase unwrapping

The essence of phase unwrapping is the integration a long a path of the phase gradients, plus a known phase at some point $\mathbf{r}_0$:

$$\varphi(\mathbf{r}) = \int_C \nabla\varphi \cdot \mathbf{dr} + \varphi(\mathbf{r}_0), \tag{5.18}$$

where $\nabla\varphi$ is a phase gradient. For a 2D matrix of data points, the gradient is obtained by wrapping the difference between two adjacent points. So a discretized definition the phase gradient could be written as $\nabla\varphi(p,q) \equiv \mathcal{W}\{(\varphi(p+1)-\varphi(p))\}\hat{p}+\mathcal{W}\{(\varphi(q+1)-\varphi(q))\}\hat{q}$, where $p$ and $q$ are the indecies of the point.

The crucial fact in this equation is that the integral is, in general, *path dependent.* The problem is framed in terms of non-zero residues (simply called "residues"), in close analogy with the residues of complex analysis. A simple example of a point of residue 1 is the phase function

$$\varphi(x,y) = \arctan\frac{y}{x}, \tag{5.19}$$

with the residue existing at the origin. Mathematically, the origin in this function has non-zero curl. Path-independent phase unwrapping will only occur for completely irrotational (zero curl) phase. Residues can occur in noisy or undersampled data, especially where the true phase changes sharply. Algorithms to unwrap phase in real data can be separated into two classes: *path following* methods, where the optimal integration path is determined by mapping out residues and other features of the wrapped phase map, and *minimum-norm* methods, which produce unwrapped phase maps with derivatives that match those of the measured, wrapped phase "as closely as possible." Some examples of unwrapping algorithms as applied to the wrapped phase map originally seen in figure 5.20 are shown in figure 5.21. Different algorithms will be appropriate depending on the nature and quality of the data, and

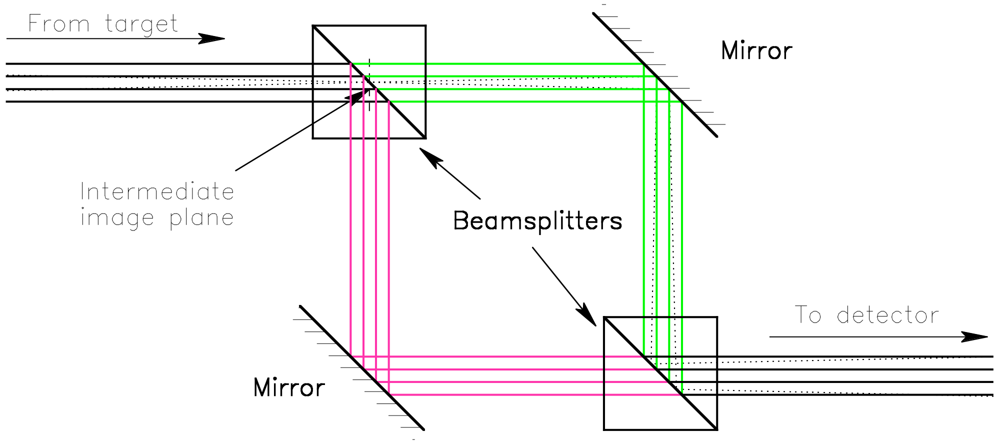

Figure 5.22: Diagram of a Mach Zehnder interferometer. In our setup, the beam is split at the intermediate image plane to simplify alignment.

it is usually worthwhile to try several of them.

### 5.3.5 Mach Zehnder

A Mach Zehnder interferometer formed the front end of the chirped pulse interferometer used on in the Titan proton heating experiment. Two 50/50 beamsplitters (in our case cubes) which split and recombine the incoming laser beam. Our target is imaged to an intermediate image plane on the first beam splitter. Tilting either of the two beam splitters adjusts the fringe spacing and tilting the second beam splitter affects the relative positions of the two images. Attention must also be paid to the relative path lengths in the two arms of the interferometer. Our strategy of alignment involved starting with very wide fringes and the two images overlapped, and itteratively adjusting the tilt (yaw and pitch) of the two beamsplitters to achieve the desired fringe spacing and contrast with the pulsed probe beam, as well as the desired separation between the images.

Figure 5.23 shows an example image from the Mach Zehnder interferometer

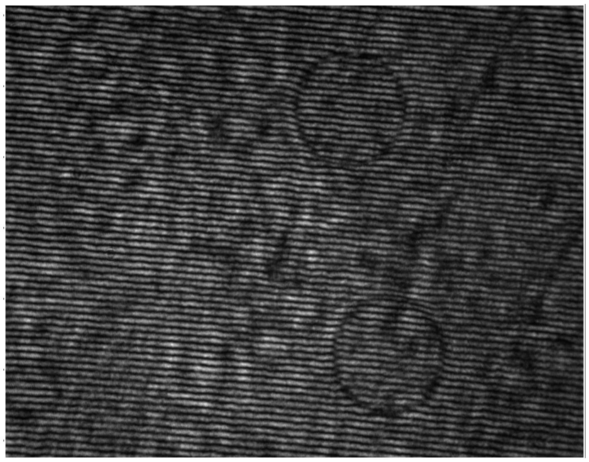

Figure 5.23: Example image from a Mach Zehnder interferometer, in which the probe beam reflects off of a smooth surfaced target with a single etched circle. Careful tilting of the beamsplitter displaces the two images of the circle from each other while producing horizontal fringes while maintaining good fringe contrast.

used on Titan, taken during the initial alignment phase. The fringes were later projected on the slit of a high resolution spectrometer to complete the CPI described in section 5.3.7.

### 5.3.6 Inverting Michelson interferometer

We used an inverting Michelson interferometer in the proton heating experiment at Sandia, as the front end to our chirped pulse interferometer. Rather than splitting the two beams of an interferometer by a small angle, the inverting Michelson interferometer design inverts one of the beams in a rooftop mirror or prism, interfering each half of original beam profile with the other (figure 5.24). The disadvantage of this approach is that the space between the two mirrors in the rooftop - or the chamfering of the edge of the 180° reflecting prism - produces a line in the middle of the image, with the useful regions being on either side of this line. However, it may be easier to align than the Mach Zehnder

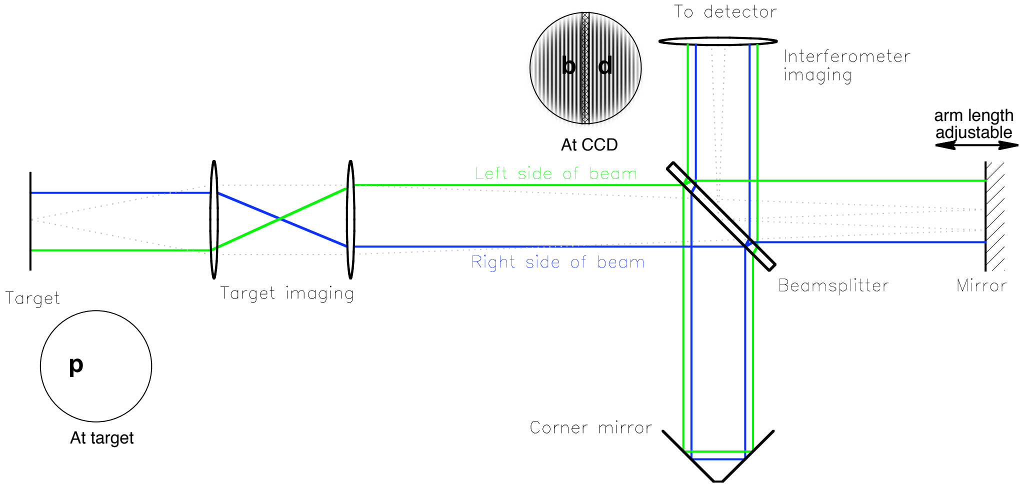

Figure 5.24: Schematic of the inverting Michelson interferometer. As in a standard Michelson, the target is imaged to a point inside the interferometer (e.g. the second pass of the beamsplitter), and that image plane is relay imaged onto a CCD. In the inverting Michelson, the left and right sides of the beam are swapped in one of the arms, allowing interference between opposite halves of the beam.

### 5.3.7 Chirped pulse fourier domain interferometer

As discussed in chapter 3, the laser pulse in a CPI system is given a linear chirp during amplification in order to reduce the size of optics needed to reach a given intensity level. Recall that the linear chirp is a group velocity dispersion applied to our high bandwidth pulse. The chirped pulse will be much longer than the transform limited pulse, and the instantaneous phase can be written as:

$$\omega_i(t) \quad \approx \quad \omega_0 + bt,$$

where $b$ is the inverse of the quadratic phase $\phi^{(2)}(\omega_0)$. This linearly changing instantaneous frequency suggests a way to encode the time history of a dynamic target: a stretched pulse reflecting from a changing surface will encounter a time-dependent phase shift $\delta\phi(t)$, which will be encoded as a frequency-dependent phase shift $\delta\phi(\omega_i)$.

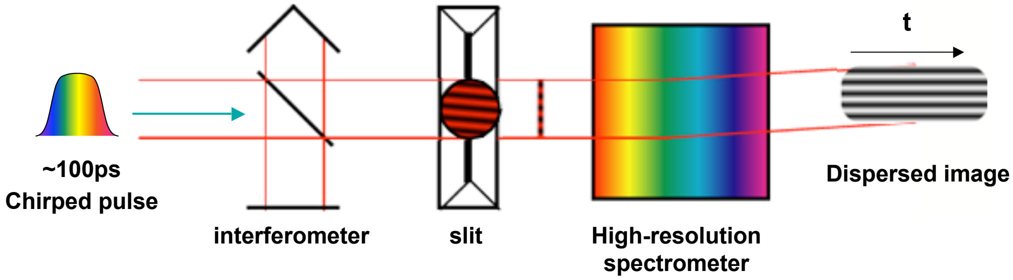

Figure 5.25: Conceptual layout of the CPI. Fourier analysis on the output image gives a 1D spatial + temporal map of the phase shift.

In earlier works [BMKB+99] this phase shift was measured by sending in two chirped pulses that were time-delayed such that one arrived early and reflected from the unperturbed target and the second interacted with the expanding target. These two chirped pulses were then sent into a high-resolution spectrometer, producing interference fringes perpendicular to the spectral/temporal direction. In this setup, fringe spaceing was set by the relative delay between the pulses, and good fringe resolution relied on a high resolution spectrometer. We refer to this as a temporally shifted, chirped pulse fourier domain interferometer (FDI)

We use an alternative to the temporally shifted configuration, in which two pulses are spatially, rather than temporally separated, was discussed by Geindre, *et al.*. This is accomplished with an interferometer such as the ones described above imaged onto the slit of a high resolution spectrometer (figure 5.25). Then the fringes are formed in the spectral/temporal direction, and the fringe spacing is set by the external interferometer. This relaxes somewhat the spectral resolution requirements compared to the time-delayed variety. This space-shifted chirped pulse fourier domain interferometer is thus more flexible than the time-shifted variety . I refer to this design simply as the chirped pulse interferometer (CPI).

Example raw images from the CPI we built at Sandia national laboratory are shown in figure 5.26. Even in the raw form the image gives a good impression

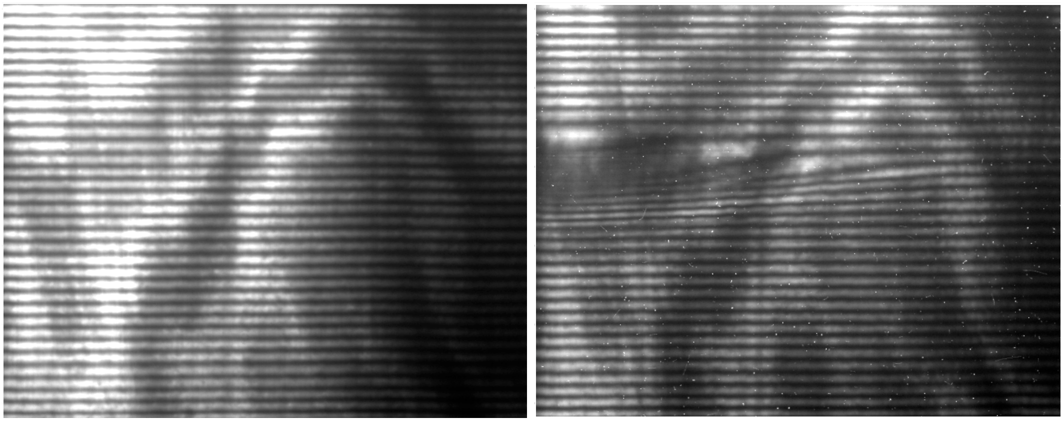

Figure 5.26: Example CPI images. Left: A reference image showing the static target. Right: The same target, showing the time history immediately before and after the onset of expansion (time goes right to left).

of the rate of change in the target and the spatial extent of the expanding region. Fringes are harder to make out at late times in the center of the heated region, mostly because of the strong drop in reflectivity. At these late times (several 10s of ps), a 2D imaging interferometer would also have issues with fringe contrast.

### CPI reconstruction procedure [GAR$^+$01]

Since the frequency, phase shift, and time are intrinsically coupled, we can't make a direct translation of $\omega \rightarrow t$ when the rate of phase shift is changing with time. Indeed, any perturbation of duration $\delta t$ should be represented by a bandwidth[11] $\delta\omega \gtrsim (4\ln 2)/\delta t$, but will only sample a range of frequencies $d\omega = b\delta t$. For this perturbation to show up properly in uncompensated data, we would have to insist that [GAR$^+$01]

$$\begin{aligned} \delta t &\geq \sqrt{\frac{4\ln 2}{b}}, \\ \Rightarrow \frac{\delta t}{T_0} &\geq \sqrt{2}\sqrt{\frac{\Delta T}{\Delta T_0}}, \end{aligned} \tag{5.20}$$

---

[11] the specific numbers used here come from the assumption of Gaussian pulses

where $\Delta T_0$ and $\Delta T$ are the pulse durations of the compressed and stretched pulse, respectively.

We should be able to do better than this if our spectrometer and probe pulse are calibrated so that we know the precise dispersion of the spectrometer (pixel $\rightarrow \omega$) and spectrum and degree of chirp in the probe pulse. Suppose we have this information, and we have mapped the fringed image into a (still wrapped) phasemap by the technique of section 5.3.3, preferably having subtracted out a reference phase from a pre-shot image. Then along a lineout in the spectral direction we have the phase shift $\Delta\varphi(\omega)$, and also the reflectivity[12] $R(\omega)$. Then we calculate the purturbation as:

$$P(\omega) \quad = \quad \sqrt{R(\omega)}e^{i\Delta\Phi(\omega)}, \tag{5.21}$$

and using the field of the unperturbed chirped pulse:

$$E_0(\omega) \quad = \quad \mathcal{E}_0(\omega)e^{i(\omega-\omega_0)^2/b}, \tag{5.22}$$

we calculate the signal by multiplying the two quantities together:

$$E(\omega) \quad = \quad E_0(\omega) \times P(\omega), \tag{5.23}$$

which yields the perturbation in time through an inverse fourier transform:

$$P(t) \quad = \quad \mathcal{F}^{-1}[E(\omega)]/\mathcal{F}^{-1}[E_0(\omega)]. \tag{5.24}$$

---

[12] The measurement of reflectivity from a fringed image won't be very good, but I've found that this procedure is not very sensitive to the reflectivity function used. In an inverting Michelson, one might try blocking one of the two halves of the beam in the flat mirror arm to obtain two images of the disturbance, one with fringes and one without (we had insufficient CCD area to fit both images in the Sandia experiments).

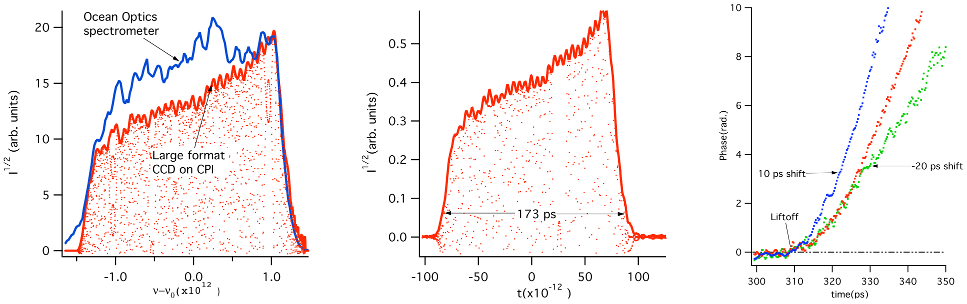

Figure 5.27: Left: Spectrum in CPI spectrometer compared to calibrated spectrum; center: Fourier of transform of spectrum using chirp parameter $b = 5.07 \times 10^{21}$, to obtain the emperical chirped pulse width of 173 ps; right: shots with known relative delay demonstrate that our timing is correct, because the onset of expansion is offset by the expected amounts (blue: -10 ps, green +20 ps).

This procedure is to be done line-by-line with lineouts along the spectral direction in the phase and reflectivity images. In the Titan experiments, we obtained a calibrated spectrum of the probe beam which we used to calibrate the spectrum of the CPI spectrometer (figure 5.27, left). The length of the chirped pulse reported by the laser crew was 173 ps, based on the grating spacing. We match this pulswidth in $\mathcal{F}^{-1}[E_0(\omega)]$, thus setting the value of $b$ (figure 5.27, center). We verify the timing by using the above prescription to proccess three shots, with three different and known probe delays, and checking that the onsets of expansion are separated by the expected amount (figure 5.27, right).

We can cut down on noise in the phase map by using thicker lineouts in the conversion of fringes to phase. Determine the approximate number of pixels that corresponds to the length of the compressed pulse (in the case of Titan $\sim$ 700 ps) and average over that many lines when producing each lineout for phase extraction (in the case of Titan, this was 8 pixels). This will help cut down on errors in the phase caused by random noise in the image. If a clean unwrapping can be performed before the reconstruction procedure of this section, lineouts along the spectral direction can also be averaged out to the spatial resolution of the optical system (assuming it is worse than 1 pixel). If the unwrapping procedure doesn't work well on the raw phase map, however, the reconstruction procedure should be applied line-by-line, to avoid smoothing out $-\pi$ to $\pi$ jumps.

## 5.4 Measuring proton beams

To diagnose the proton beams generated in laser-foil interaction (section 4.4), we can exploit either their energy-dependent penetration depths (section 4.4.3) or their charge. In this section I describe the various types of detection methods we've used to characterize the protons we've produced.

### 5.4.1 Radiochromic Film

Radiochromic film (RCF) is direct exposure film (DEF) used for densitometry [MYS+91] of any form of ionizing radiation, available commercially in various forms (e.g., from ISP [Gaf]). A single film will generally consist of three regions, with two regions of thin, clear plastic sandwiching an active layer that changes color following exposure to ionizing radiation. The film is weakly sensitive to ordinary light, and so should be stored in the dark. However, it doesn't neccessitate the use of a darkroom, as brief exposures to light will have negligible impact on the optical density [Gaf]. RCF is ordinarily cut into a series of squares and stacked, with marked orientation and ordering, and wrapped in thin foil. The thin foil serves to protect from the bright visible and UV light from the laser shot, as well as debris and heavy ions. The thicknesses and compositions of the layers in the film are carefully controlled and reported from the manufacturer [Gaf], allowing judgement of the maximum energy of protons present based on the number of films in the stack that are exposed. For an example, the composition of Gafchromic$^{\text{TM}}$MD55 film [CP00], which is a very common choice of RCF film, is given in table 5.1. The active layer has a well-calibrated and linear response to ionizing radiation, measured in grays (1 Gy

| Material | Thickness<br>( $\mu m$ ) | $\rho$<br>($g/cm^3$) | COMPOSITION (ATOM%)<br>C | <br>H | <br>O | <br>N |
|---|---|---|---|---|---|---|
| polyester film base*** | 67 ±2.5 | 1.35 | 45.50 | 36.40 | 18.20 | 0.00 |
| active layer* | 16** | 1.08 | 29.10 | 56.80 | 7.10 | 6.90 |
| adhesive | 20 ±2.5 | 1.2 | 33.30 | 57.10 | 9.50 | 0.00 |
| film base | 25 ±2.5 | 1.35 | 45.50 | 36.40 | 18.20 | 0.00 |
| adhesive | 20 ±2.5 | 1.2 | 33.30 | 57.10 | 9.50 | 0.00 |
| active layer* | 16** | 1.08 | 29.10 | 56.80 | 7.10 | 6.90 |
| polyester film base | 67 ±2.5 | 1.35 | 45.50 | 36.40 | 18.20 | 0.00 |

Table 5.1: Composition of Gafchromic$^{TM}$MD55 film, available on request from the manufacturer, in order from front to back. Note that this film is symmetric. Notes: * The active layer contains gelatin, which may vary slightly in elemental composition; ** Thickness ±2 $\mu m$ batch-to-batch, and ±0.5 $\mu m$ within a batch

= 1 J/kg). The optical density[13] as a linear function of dose for a given film will be available from the manufacturer [Gaf].

With this detailed calibration of the RCF film, the stack can be modeled such that, for a given spectrum and angular distribution of protons, we can predict the dosage in each layer of the stack [BCZC05], which translates into optical density in the active layer. This can be done in reverse, to a certain extent, by accounting for absorbed energy starting from the deepest film (which ideally would be sufficiently far back to have zero exposure) and working towards the front. An algorithm to accomplish this is outlined by Breschi, *et al.*[BBG+04]. Even if a proton beam has too low a cutoff energy to penetrate several RCF films in a stack (e.g. $E_{\text{cutoff}} <$ 4 MeV), RCF film is still a quick and useful way to diagnose the shape and strength of the proton beam. Examples of RCF images taken during the Calisto experiment, for which proton energy was low, are shown in figure 5.28. The films showed evidence of a prepulse, in the distorted shape of the proton beams, which indicated that the rear surface of the foil may have been distorted by premature heating. Deeper films in the stack showed evidence of large amounts of electron dosage, which is

---

[13] for best precision, this is measured at a specific wavelength

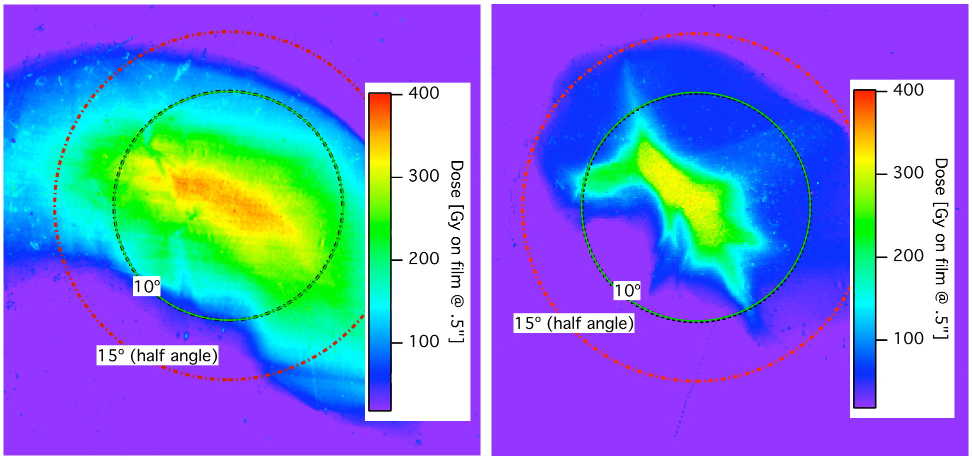

Figure 5.28: RCF scans from system shots on Calisto. Left: from 4 $\mu m$ Al; right: from 20 $\mu m$ Si.

also indicitive of prepulse. Electron dosage on the film stack is characterized by weak dosage that changes very little from film to film in the stack. The electrons responsible for this dosage have energies $\gtrsim$ 1MeV .

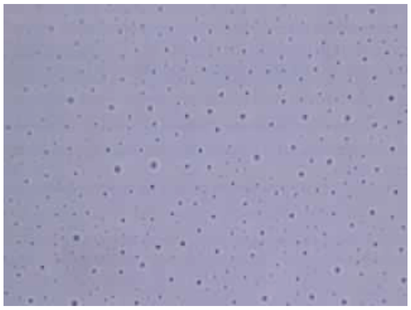

Figure 5.29: Example scan of an etched CR39 plate. Pits are well spaced; this plate could be accurately read by CR39 scanner.

### 5.4.2 CR39 plastic

CR39 is clear and colorless plastic that has been used for decades to detect various ions with energies greater than 100 keV. An energetic ion damages the CR39 along its tragectory until it is stopped. The damaged tracks can then be etched out with an appropriate solution and etching time of NaOH. The resulting pits scatter transmitted light in the plastic and affect the optical density. The pit will be conical as etching proceeds along the damaged track, and round out after the end of a track is reached. Gaillard, *et al.*have shown that there is a maximum fluence of ions for which CR39 can be useful in determining the proton count. This maximum is set by the need to avoid excessive overlap between adjacent pits, since overlap affects the scattering in a nonlinear fashion. Shorter etching times for smaller pits can only be used up to the point at which the pits would be too small, and the etching time too short to reliably control. This occurs at a fluence of about $10^8/cm^2$. An example of etched CR39 in a tractible fluence regime is shown in figure 5.29.

One of the manufacturers of CR39, Track Analysis Systems, Ltd.[14], provides systems for automatic track counting of etched CR39. Laser facilities such as Jupiter and Sandia's Z-Petawatt own such systems. In using these systems, the fluence limits discussed above should still be considered.

The major advantage of CR39 is that it is unaffected by radiation other than ions and protons. Thus it is unneccessary to block UV and white light with a foil, or to account for a low level electron or x-ray background as with RCF or other types of film.

### 5.4.3 Magnetic proton spectrometer

We used a magnetic spectrometer to measure the proton spectrum on the Titan experiment, as well as on THOR. The principal of operation of a magnetic proton

---

[14] `http://www.tasl.co.uk/`

spectrometer is simple. A magnetic field in the $\hat{y}$ direction is established between two strong magnets. The proton, travelling in the $\hat{z}$ direction, pass through a slit which narrows the beam in the $\hat{x}$ direction. The magnetic field dispurses the protons by velocity in the $\hat{x}$ direction via the Lorenz force, $\mathbf{F} = e\mathbf{v} \times \mathbf{B}$, with the fastest protons being deflected the least even though the force is greatest, because they spend the least time in the magnetic field. If $\mathbf{B}$ were constant and completely transverse, the trajectory of the ion would be given simply by the gyroradius $r_g = mv_\perp / |q| \mathbf{B}$, where m, q, and $v_\perp$ are the mass, charge, and velocity of the ion, respectively. Heavy ions follow an almost straight path in the spectrometer, because of their lower charge-to-mass ratios.

The two magnets of the spectrometer are usually placed in an iron yolk, in order to reduce the fringe fields in the path of the protons. Unfortunately, the ideal case of straight uniform magnetic field lines confined only to the region between the two magnets cannot be exactly realized, and it's important to map out the magnetic field as a function of position inside of a magnetic spectrometer, e.g. with a Hall probe, unless a comprehensive calibration with proton beams of known energies can be performed.

### 5.4.4 Thomson Parabola

Although it was never fielded in our experiments, the Thomson parabola [MNP+00] remained an intriguing diagnostic for its ability to distinguish protons from other ion species. The Thomson parabola is essentially a magnetic proton spectrometer with a pinhole instead of a slit and an additional strong pulsed electric in the magnetic field direction (usually between electrodes placed just after the magnets). The name comes from the parabolic shape of the tracks from the various ion species which are dispersed by energy in the $\hat{x}$ direction, as in a plain magnetic spectrometer, and also in the $\hat{y}$ direction by species. A basic Thompson parabola is currently available at the Sandia 100TW laser chamber.

## 5.5 Streaked optical pyrometry

Determining the temperature of the high energy density states created in high intensity laser experiments is very difficult, due to their transient nature. Often in plasma physics the temperature is inferred through the rate of expansion of a heated material, using some assumed equation of state. However, since we're interested in *measuring* the equation of state, we need a method that is decoupled from the pressure. In plasmas created by a high energy pulsed free electron laser, Thompson scattering might be a viable temperature diagnostic [LBC$^+$01], measuring electron temperature through doppler broadening. However, this isn't an option in our experiments, as it requires a very low divergence $< 12$ Åx-ray source. Temperature determination through analysis of K$_\alpha$ satellites is possible for temperatures $> 20-30$ eV [HFP$^+$05], but this technique won't work for colder temperatures with no resolvable sattelites. Furthermore, this technique is still in a very preliminary phase, particularly for streaked measurements[15]. Various groups have also made rough estimates of the temperature of warm and hot plasmas by measuring the maximum energy of XUV light emitted by a sample [GZK$^+$06], which indicates the maximum temperature reached.

In our proton heating experiments on Calisto and Titan, we used a temperature diagnostic known as a streaked optical pyrometer (SOP). The SOP is designed to infer the (surface) temperature of a heated sample by imaging a single wavelength of self-emitted light from the sample onto an ultrafast streak camera, thus measuring the instantaneous spectral intensity emitted from the sample.

---

[15] this part is the thrust of the research of Ronnie Shepherd, whose laser time on Titan concerning preliminary measurements testing this technique also accommodated our temperature / expansion measurements featured in this thesis

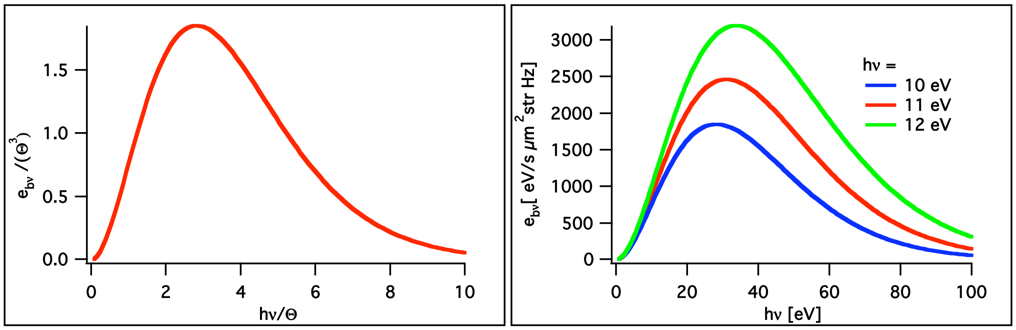

Figure 5.30: Left: The invariant Planck function, showing a peak at $E \approx 3\Theta$; Right: Spectral emissive power vs. photon energy for 10, 11, and 12 eV

### 5.5.1 Thermal self-emission

The relationship between temperature and spectral intensity starts with Planck's blackbody function for the directional spectral emissive power [Mah02]:

$$\begin{aligned} e_{bE}(E,T,\theta) &= \frac{2E^3}{h^3c^2}\left(\frac{1}{e^{E/\Theta}-1}\right)\cos\theta \quad \left[\frac{eV}{s\cdot\mu m^2\cdot eV\cdot \mathrm{str}}\right]; \\ &\equiv i_{bE}(E,T)\cos\theta \end{aligned} \tag{5.25}$$

Here, $\theta$ is the angle from the surface normal direction, $E = h\nu$ is the photon energy and $\Theta \equiv kT$. Plots of $e_{bE}$ are shown in figure 5.30. The left plot is invariant, obtained by plotting $e_{bE}/\Theta^3$ vs. $E/\Theta$, and shows that the peak blackbody radiation occurs at a photon energy about 3 times the thermal energy $\Theta = kT$. This invariant plot is known as the Plank function. The right plot demonstrates how quickly the blackbody emission function changes with temperature by showing $e_{bE}$ at three close temperatures. The total radiation from all frequencies into the hemisphere from a blackbody surface goes as the fourth power of the temperature $T$:

$$\int_{E=0}^{\infty}\int_{2\pi} e_{b\nu}(E,T,\theta)d\Omega dE = \sigma T^4, \tag{5.26}$$

where $\sigma = 5.6696 \times 10^{-8} W/m^2 \cdot K^4$ is the Stefan-Boltzman constant. However, note that when $\Theta \gg E$, the emissive power at the photon energy $E$ varies only linearly with temperature:

$$e_{bE}(E, T, \theta) \approx \frac{2E^2\Theta}{h^3c^2} \cos\theta, \; (\Theta \gg E). \tag{5.27}$$

Therefore for WDM temperatures (several eV), the ideal case would see us measuring the emitted light in the XUV range. Unfortunately, standard ultrafast streak cameras tend to be sensitive only in the visible and, more importantly, an absolute calibration (see below), necessary for reliably determining the temperature, would be much more difficult in the XUV. The additional challenge of using XUV optics prevented us from taking that route, and our measurements were done at visible wavelengths.

### Real surfaces

A blackbody is the ideal case of an object in thermal equilibrium that is a perfect absorber, neither transmitting nor reflecting incident light. In this limit, matter of temperature $T$ emits light as given by equation 5.25. This equation represents the *maximum* directional, spectral emissive power that can be emmitted from a given surface of temperature $T$. A real surface has an *emissivity* $\varepsilon_E(E, T, \theta, \phi)$ less than 1, and the directional spectral emissive power becomes:

$$e_{\mathrm{r}E}(E, T, \theta, \phi) = \varepsilon_E(E, T, \theta, \phi) e_{b,E}(E, T, \theta). \tag{5.28}$$

By Kirchoff's Law, we know that the directional, spectral emissivity is equal to the the directional, spectral *absorptivity*:

$$\varepsilon_E(E, T, \theta, \phi) = \alpha_E(E, T, \theta, \phi) \tag{5.29}$$

Now, the absorptivity is just the fraction of incident light intensity that is neither transmitted nor reflected. Thus for an opaque target, a measurement of the reflectivity $R$ (this should include scattered light) at a given incident angle and wavelength is a measurement of the absorptivity and hence the emissivity: $1 - R = \alpha = \varepsilon$.

I use the term *brightness temperature* to describe the temperature that would be inferred if we simply assumed that a light emitter were a blackbody source, with no concern for emissivity.

### Calculating emissivity

For the results of the data presented in this thesis, the reflectivity at the SOP wavelength was calculated from simulations. The alternative would be to measure reflectivity at the wavelength and angle of the SOP. However, we prefer to set the SOP to a wavelength away from any of the main beam harmonics to avoid light contamination from scattering of the main beam. Therefore, the reflectivity measurement would either have to be extrapolated to the SOP wavelength, or somehow performed with an off-harmonic wavelength ultrashort probe (by white light generation, for example). In the analysis of the Titan proton heating experiments (see chapter 7), we calculated the SOP signal from a hydrodynamic code. The code predicted a temperature and density profile at each time step, both of which decrease monatonically from the bulk foil to vacuum. The proper blackbody surface to use in this geometry is the critical density for the wavelength in question [NAP$^{+}$05]. Emissivity of the SOP wavelength was calculated by way of equation 5.29 and the prescripton for determining reflectivity described by Milchberg, *et al.*[MF89], which is based on Maxwell's equations in a short scale-length plasma and a Drude conductivity model. Figure 5.31 shows a plot of the actual electron temperature at the critical surface (for 470nm light) and the calculated brightness temperature from a simulation of a proton heated foil. The model predicts substantial reflectivity at

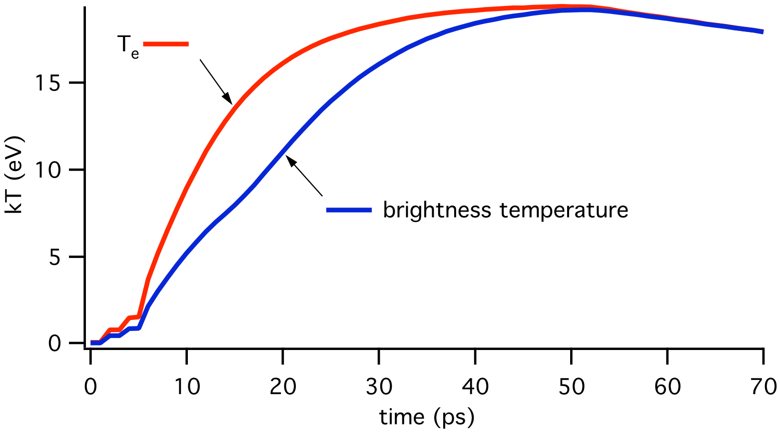

Figure 5.31: Plot of brightness temperature and critical surface electron temperature $T_e$ at 470nm vs. time, as calculated using a 1-D hydrodyamics code and the equations of Milchberg, *et al.*[MF89]

intermediate times, causing the brightness temperature to be much lower than the actual temperature. At late times, the plasma becomes more absorptive and the brightness temperature approaches the actual temperature.

### 5.5.2 Streak cameras

A streak camera operates by converting incident light on a photocathode into electrons which are accelerated across a vaccuum tube to a converter plate - a phosphor screen and/or microchannel plate (MCP) - which converts the signal back to light to be recorded. Electronics image the electron beam such that an image on the photocathode is transferred to the converter. In sweep mode, a transverse voltage deflects the electrons away from the phosphor screen until a sweep signal is received at which point the transverse voltage rapidly and linearly changes sign so that the deflection of the electrons is swept in time over the phosphor screen (figure 5.32). Hence on the phosphor screen is produced an image with temporal resolution in one direction and spatial resolution in the other. In ultrafast streak cameras the

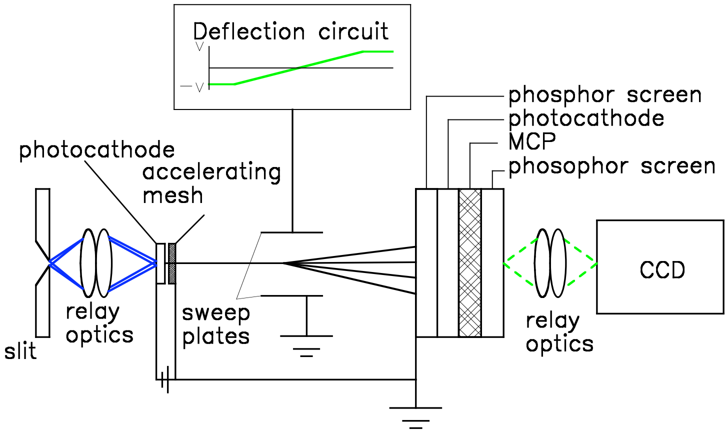

Figure 5.32: Schematic of the C7700 streak camera. Adjustable input optics image an adjustable slit to a photocathode. Photoelectrons from the photocathode are accelerated towards a phosphor screen upon which the photocathode surface is electronically imaged. During sweep operation a fast linear voltage sweeps electrons across the phosphor screen. An image intensifier consisting of a photocathode, MCP, and phosphor screen boosts the light intensity considerably, and the sweep image is relayed to a CCD by the output optics.

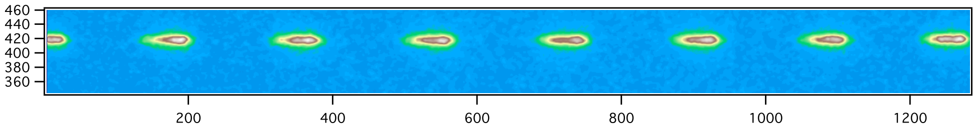

Figure 5.33: Example streak image of a 3GHz comb generator laser (image cropped in vertical direction). In this case, a 2 ns nominal sweep window was used. Temporal resolution is highly uniform in this streak camera (C7700).

sweep time across the converter can be 1 ns or even shorter, leading to a temporal resolution on the order of a few ps or less. An example streak image, from a comb generator, is shown in figure 5.33.

Most commercially available streak cameras also feature electronic gating of the photocathode, acceleration mesh, and/or the MCP, creating a short time window during which light incident on the photocathode can lead to signal. Even with electrons being deflected away from the converter plate, scattering of electrons within the tube can lead to unwanted light signal, and gating helps minimize this noise.

### Space charge effect

When excessive electrons are produced by the photocathode in a given unit of time, from excessive light intensity, space charge effects can cause an apparent temporal stretching of the signal, causing the streak camera to overestimate greatly the temporal extent of the feature being measured. The problem occurs when the number of electrons in a pulse is large enough so that the collective charge pushes electrons apart along their trajectory as they traverse the streak tube, causing leading electrons to be accelerated more than trailing electrons [QEA02]. The threshhold brightness for the onset of space charge effects can be tested by observing streak images of an ultrashort laser pulse (of a wavelength within the photocathode's sensity range) as the pulse energy is slowly increased. Eventually the streak image will spread out in time, indicating the brightness limit. The upper limit of the dynamic range reported by the manufacturer is usually set by this effect, and marked by the brightness level at which temporal resolution worsens by a factor of $\sqrt{2}$.

| Model | used on | $\Delta t_{\max}$ | $\Delta t_{\min}$ | $\delta t_{\min}$ | p.c. | dynamic range | response $\left(\frac{\text{count}}{10^{-18}J}\right)$ |
|---|---|---|---|---|---|---|---|
| C1587<br>+ M1952 | Calisto | 10 ns | 300 ps | 1 ps | S-20 | $10^3 : 1$ | 0.92<br>@ 633 nm |
| C7700 | Titan | 1 ms | 1 ns | 3 ps | S-20 | $10^4 : 1$ | 170<br>@ 470 nm |
| C6138<br>(FESCA) | Sandia<br>100 TW | 1.2 ns | 60 ps | $\lesssim$ 200 fs | S-1 | $10^3 : 1$ | $\sim 6$<br>@ 470 nm |

Table 5.2: Comparison of the Hamamatsu streak cameras used on various experiments. The C1587 and C7700 were calibrated on site, while the response value for the FESCA is estimated based on expected relative response between the FESCA and the C7700 as reported by Hamamatsu. The lower response is due to the S-1 photocathode, which is more than an order of magnitude less sensitive in the visible but, unlike the S-20, is sensitive to 1 $\mu m$ light.

### 5.5.3 Models of streak camera used

We used three different models of streak cameras in our experiments. All of these streak cameras were manufactured by Hamamatsu Photonics K.K. and manuals for all of them are available from the company. Key properties of the streak cameras are listed in table 5.2.

#### Hamamatsu C1587 with M1952 high speed streak unit

This streak camera, which was used on the Calisto proton heating experiments, functioned despite having a damage spot on its S-20 photocathode[16] (figure 5.34). After many years in service, the phosphor screen also had a faded band along the center, where the photoelectrons hit in unstreaked ("focus") mode. Of course, this fading had to be taken into account in calibration. The converter plate consisted of an MCP followed by a phosphor screen, and both the MCP and photocathode

---

[16] A second C1587 unit was available for the Calisto experiments but it was in more serious disrepair (with an even worse damage spot on its photocathode), and used an S-1 photocathode, which is more than an order of magnitude less sensitive across the visible, and was not sensitive enough for our measurements.

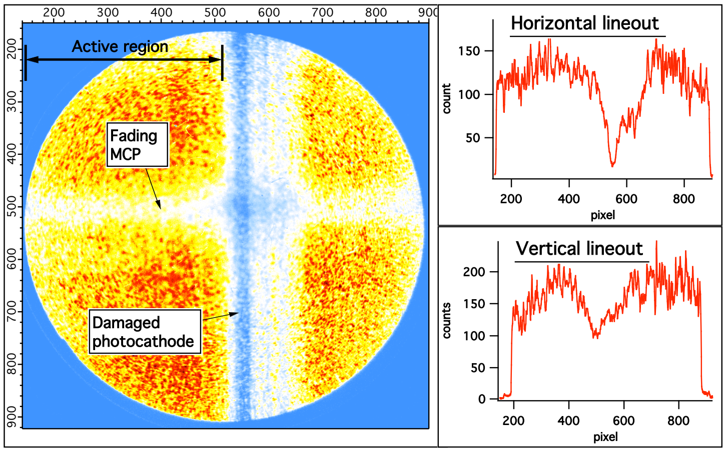

Figure 5.34: Spatially and temporally uniform light from a Xe flashlamp as registered by the C1587 streak camera in 5ns sweep mode. Damage to the photocathode restricted our active range to the right region of the image, corresponding to about 6 mm spatially along the slit. Fading in the phosphor screen had to be accounted for in data analysis.

could be electronically gated. The MCP gain had 5 settings (1-5), as did the sweep speed (10 ns - 300 ps). Some other notes on this streak unit:

- Triggering of the streak unit required a 40 V, fast rising trigger, which we supplied using an ultrafast avalanche photodiode positioned at the stretcher. The signal was carried with low dispersion over special BNC cable known as “foam flex.”
- The effective f/# was 4.1
- The gate could be set to switch off immediately after sweep, or stay open for a specified amount of time, variable from .1 $\mu s$ to 100 $\mu s$ and monitored with an oscilloscope.
- The front slit width was adjustable, but the reading did not correspond to the actual opening size of the slit. I performed a separate calibration of slit width

to determine that the reading scale was correct, but offset by 180 $\mu m$ .

- The sensitivity of this streak camera was insufficient to view self-emitted light through a narrow band interference filter. However, as seen in figure 5.40, using the full visible spectrum of emitted light, dispersed onto the slit with a prism did provide enough light (but not at the fastest sweep speed).

### C7700 High Dynamic Range Streak Camera

This streak unit was used in the Titan proton heating experiments. Although the shortest temporal resolution achievable on this streak camera was relatively long (3 ps), this unit worked very well because of its very high sensitivity ($>30\times$ more sensitive than the other streak cameras I've used) and dynamic range ($10\times$ better dynamic range than the other two streak cameras described here). The conversion plate consisted of a phosphor screen followed by an image intensifier consisting of a photocathode, MCP and phosphor screen stack. The gain could be set between 1 and 55. The input optics were coated for 400 nm - 900 nm light, and had an effective F/# of 1.2 with 1:1 magnification onto the photocathode.

The C7700 required only a 5 V fast rise-time, which was provided by a fast photodiode in the laser bay of titan with signal relayed into the target room on low-dispersion BNC cable. At Titan, the streak camera triggers were set up in advance by the laser facility and worked well without modification.

### C6138 (Fesca-200)

This streak camera, which we attempted to use at Sandia's 100 TW laser, features extremely fast temporal resolution of $\lesssim$ 200 fs at the fastest speed, a resolution which is considered superior for measuring transient states of warm dense matter such as those produced in our experiments [NAP$^+$05]. The specific unit, newly purchased by Sandia at the time of our experiments, uses an S-1 photocathode to

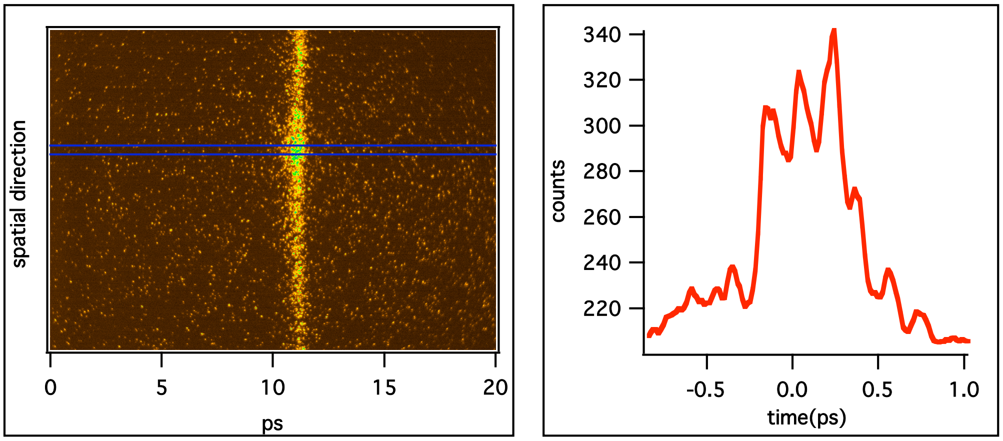

Figure 5.35: Left: streak image of main Sandia pulse filling the slit of a Fesca-200, run at maximum sweep speed. The size of the slit is much narrower than the band shown, so the extent in the temporal direction comes from the duration of the ultrashort pulse. Right: A lineout shows that the pulse is close to where they want it to be (500fs FWHM).

allow it to measure the fundamental wavelength of the laser.

While sensitivity to 1 $\mu m$ laser light made this streak camera extremely helpful in reducing the Sandia laser's pulse width from several picoseconds down to a range accessible by an autocorrelator (see figure 5.35), it made the response to the blackbody emission of our source so low that no self-emission signal was seen from proton heated targets[17]. Note that although the signal in terms of pixel counts per unit energy incident is estimated to be higher than the unit used on Calisto, the faster sweep time leads to lower brightness on the CCD, as did the use of an interference filter instead of the low-dispersion prism used on Calisto (see below).

### 5.5.4 Setup of the monochromatic SOPs

The streak unit should be bolted in place to an optical table, if possible. Initial alignment is done in focus mode in which the sweep plates are turned off. It is cru-

---

[17] Sandia Petawatt now has a C7700 unit with an S-20 photocathode available for use

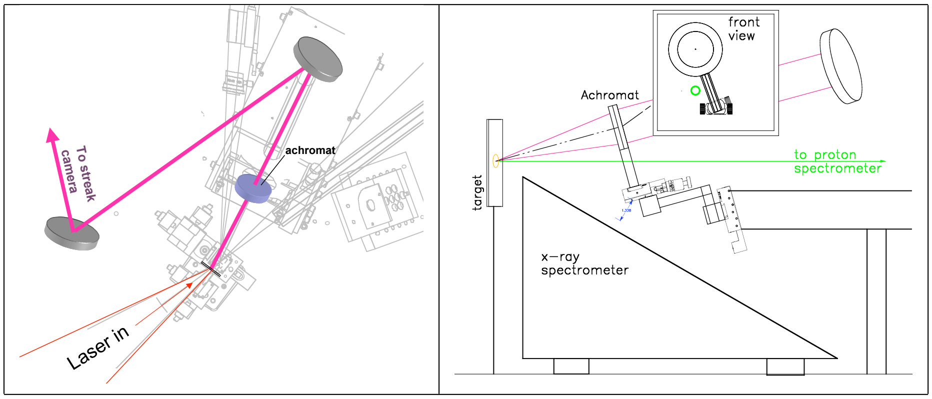

Figure 5.36: Layout of SOP collecting lens in Titan target chamber. Left: Top view, showing achromat and two mirrors to direct the light out of the target chamber; Right: side view (front view inset) showing positioning of achromat to avoid other diagnostics.

cial to ensure that the light entering the streak unit is sufficiently filtered, because excessive light can damage the intensifier or even the photocathode (as evidenced by the older C1587 at Calisto). The output optics can usually be focused on random MCP noise when gain is at its highest setting an input optics are shuttered. Adjusting the focus of the input optics is done by closing down the slit to a narrow line and illuminating with the wavelength of interest. These procedures for the initial setup of the streak unit itself will be provided in the manuals for the unit.

We wish to observe the thermal emission at as shallow an angle as possible in order to collect the brightest emission (small $\theta$ in eqn. 5.25) and to be able to clearly pinpoint and image the central part of the heated region of the target. One should also use as low an f/# optic as allowable by our setup (e.g., the streak camera), again to collect as much light as possible. Unfortunately, the desire to measure the protons (or x-rays) on each shot precludes placing the SOP lens directly behind the target normal, and shallow angles in the horizontal plane will be taken up by the probe beam. This neccessitates orienting the lens out of plane, as shown in figure 5.36. In our setup, the first lens collected and columnated light of the measured wavelength and a second lens near the streak camera (outside the chamber) focused and re-imaged the light from the back surface of the target onto the streak camera.

For precise alignment, a good fiducial target is needed. We have a strategy to align precisely a target to the laser focus (section 5.1.2), but the position of laser focus is not exactly the position of the heated material. Therefore the fiducial should either be on an encoded stage which allows precise translation from the position of laser focus to the center of the heated region (normal from the source target's surface), or have the appropriate thickness and be precisely marked on both sides, e.g. by a pinhole drilled straight through. The latter option is much more convenient, as it eliminates the time consuming task of translating the fiducial, and since more light can be scattered from a surface with a small hole than from a small pin, the thick target will be easier to see on the streak camera. Most modern streak cameras will have a fast capture rate and can be operated in focus mode with the slit wide open (at low gain) to find the image of the fiducial quickly after rough alignment.

### 5.5.5 Calibration of monochromatic SOPs

Recall that the output of equation 5.25 is in the form of energy per unit time, per unit area, per unit photon energy (e.g. frequency) per unit solid angle. Ideally, calibration could be obtained using a uniformly emitting calibrated light standard, which could be placed at the target position. However, such sources are very faint compared to the heated sample that we will be measuring. For example, the Optronics Laboratories, Inc.[18] Model 455-12-1 12-inch diameter inetgrating sphere standard delivers a known, uniform spectral irradiance that, when calibrated, is considered accurate to within .5% of the NIST standard. On a C7700 streak camera operated at 10 ns sweep speed, a $\sim 100nm$ band interference filter centered at around 633 nm,

---

[18] online at `http://www.olinet.com/`

and and about a 500 $\mu m$ slit opening, enough brightness could be achieved to make a calibration measurement on the streak camera[19]. An in-situ calibration of this type would be very satisfying because a known spectral emissive power at the target position could be measured as a reference. However, the low light intensity actually reaching the streak camera could potentially lead to uncertainty in the calibration.

We did not have a calibrated light standard available during our runs, and so we had to use a series of other calibrations. The calibrations consisted of obtaining the sensitivity of the streak unit by producing a streaked image of a source with known power, the timescale by measuring light sources with known relative delays, the mangification by imaging features of known size at the target plane through the SOP optics, and the throughput of the optics by measurement and documentation (in the case of precision filters). Uniform illumination was also tested to check the uniformity or response. This was significant in the calibration of the C1587, as noted in figure 5.34.

### Streak camera light sensitivity

To calibrate light sensitivity of the streak cameras, I required bright, directed light sources, and a calibrated and accurate power meter. The primary source of calibration light was a collection of three CW lasers of different wavelengths, one of which was an intensity-stabilized HeNe[20] at 633 nm, which varied in power output by far less than 1% during calibration measurements. Sensitivity at different wavelengths can be extrapolated using the wavelength response curve, available from the manufacturer.

We measured the power of the light sources with a calibrated Silicon power

---

[19] With these assumptions I calculate that the light source should give about 10 counts per pixel in a band across the streak camera, allowing for good statistics. An alternative to the broadband filter is to use much the slower sweep times available on the C7700

[20] online at `http://www.newport.com/Frequency-and-Intensity-Stabilized-HeNe-Laser/139678/1033/catalog.aspx`

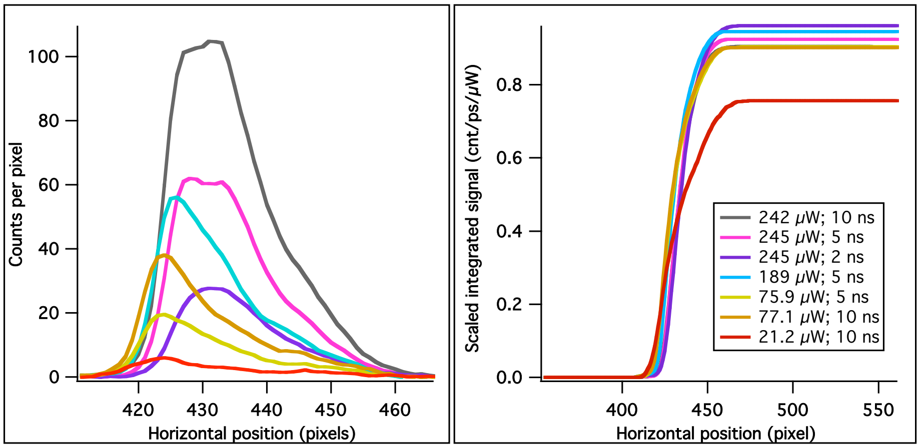

Figure 5.37: SOP calibration; Left: Transverse lineouts from various incident light powers and sweep speeds, showing a range of count rates; Right: Integrated lineouts divided by time scale and incident light power. The measurements were consistent within 6%, except for a very low light shot, which was likely affected by being near the threshhold of light detection on the camera (this was the C1587, which was not sensitive enough to detect single photo-electrons).

meter (Newport 840C meter with 818UV head), which was considered accurate to within 1 - 2%. The power incident on the streak camera was less than 1 mW and was focused to a small spot and shuttered to less than 1 ms to cut down on noise. Sweeps were taken at various light source intensities and sweep speeds, with many shots integerated. With a good calibration of the temporal scale, transverse lineouts could be integrated to give counts/ps/$\mu W$ → counts/J. Figure 5.37 gives an example of this, showing consistency for various sweep speeds and incident laser powers.

### Time scale

For sweep windows $\gtrsim 500ps$, a comb generator provides pulses with very stable spacing. We had access to comb generators up to 3 GHz (see figure 5.33). On longer sweep windows, a single image of a comb generator pulse train allowed us to check easily the uniformity of the timescale across the streak window (very uniform

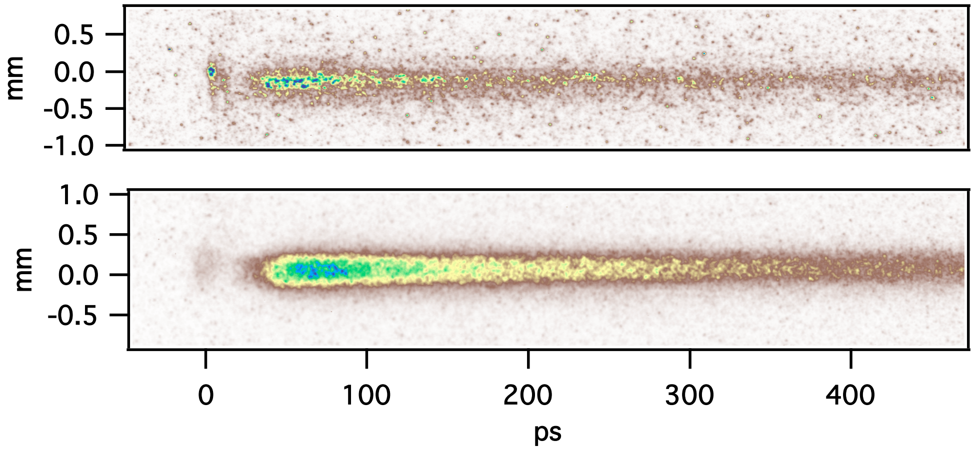

Figure 5.38: Two SOP images of proton heated targets from the Titan experiments. The high dynamic range C7700 streak camera handled both shots well, despite very different light levels (color scales were adjusted). Optical transition radiation (OTR) can be seen at 0 ps, with thermal emission following.

on the newer streak units but varying somewhat on the C1587). Calibrations of the temporal scale were also provided in a test report from Hamamatsu along with the specific streak unit, in the case of the newer streak units.

### Optics throughput

We measured optics throughput at various wavelengths using CW lasers of various wavelengths and the calibrated silicon power meter. The transmission curve of our interference filter ($\sim$ 50% throughput over $10nm$ bandwidth) was verified using a white light source and an ocean optics spectrometer.

### Spatial scale

Our targets contained apertures of well-controlled size which were imaged by the streak cameras in focus mode to give a spatial scale. Determining an accurate spatial scale is crucial, since intensity goes as the square of distance. I recommend

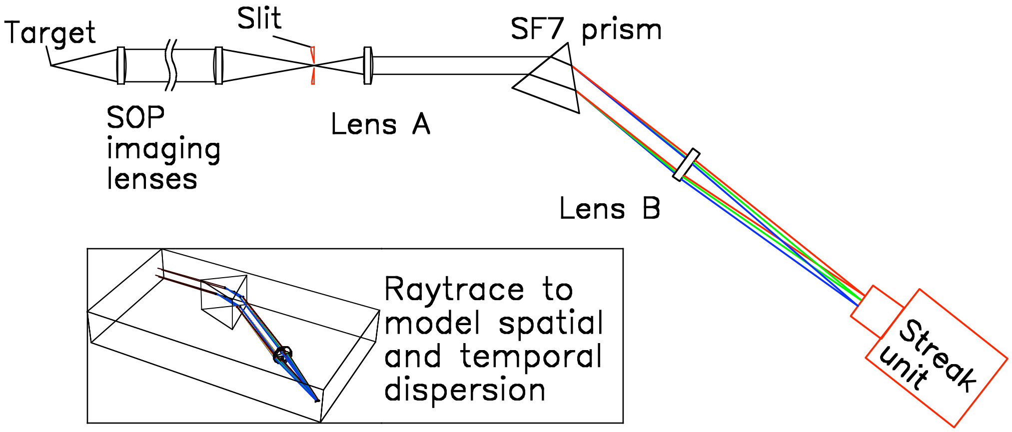

Figure 5.39: Layout of the spectrally resolving SOP. Two lenses, a prism, and a slit were added to the SOP configuration to view the visible spectrum. Ray tracing allowed us to model the spatial and temporal dispersion, which fit well with measured results.

using resolution targets with precise periodic patterns, in addition to single objects of known size.

Two example images of the spatial SOP output viewing proton heated samples are shown in figure 7.20.

### 5.5.6 Setup of the prism spectrometer SOP

For the first Calisto proton heating run, we added spectrometer consisting of additional imaging optics, a slit, and a large prism. This allowed us to cover the active region of the C1587 with light in the range 450 nm to 750 nm, with 800 nm light (the fundamental frequency of Calisto) visible on the other side of the damage spot on the photocathode. We used a large SF7 [Inc02] 50° prism to disperse the light. The standard optics of the spatially imaging SOP image the target back surface to an intermediate vertical slit (perpendicular to the streak camera slit), and two lenses after this slit relay the image at the slit onto the streak camera, with the

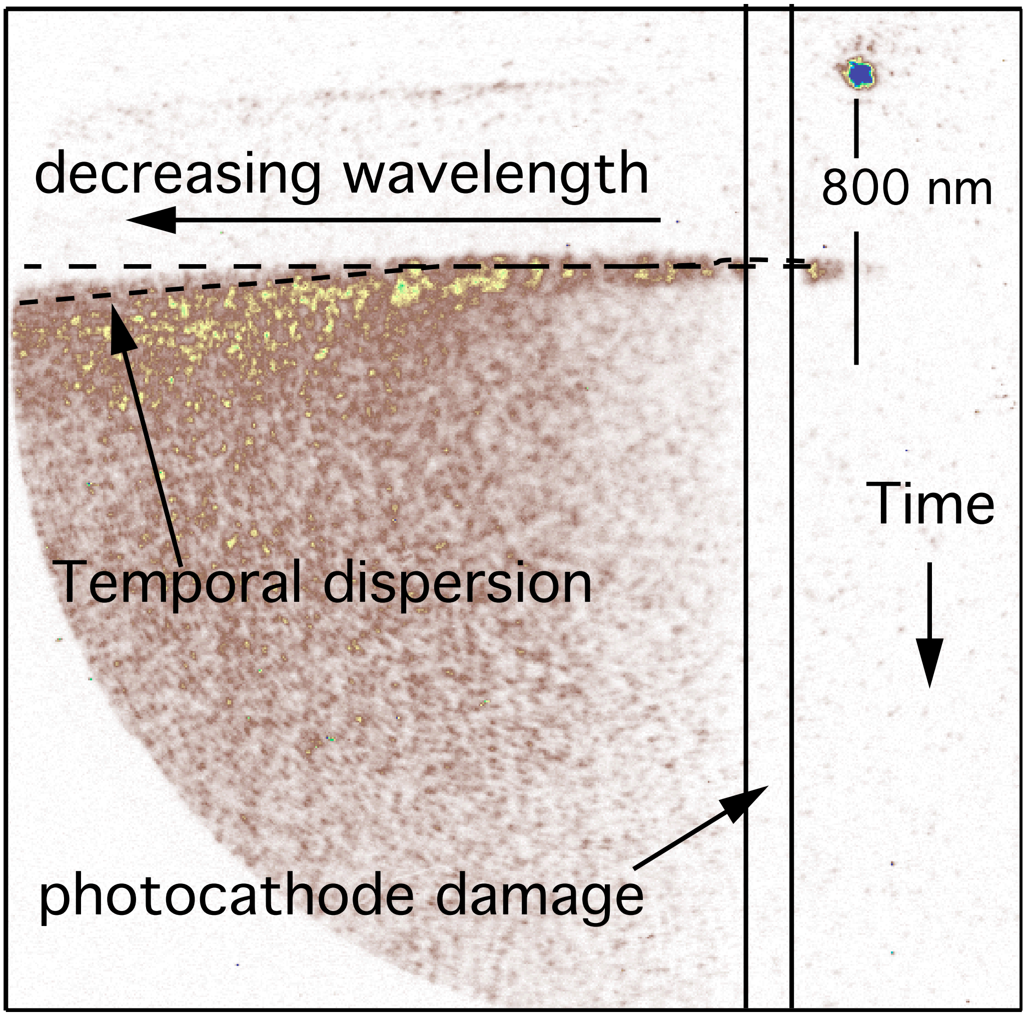

Figure 5.40: An example streak image from the spectrally resolving SOP, in which protons from a Silicon source target heat a Silicon sample target. The different arrival times of different wavelengths are a result of dispersion, which can be modelled for. An 800nm prepulse is seen to scatter through the target.

prism between them (fig. 5.39).

Raytracing with the Mathematica Optica package, knowing the material composition of all lenses (including those in the streak camera input optics) and windows and the prism, allowed us to not only predict the spatial dispersion, but also the temporal dispersion of the system. The spatial dispersion found by the ray trace model allowed us to map horizontal position along the slit to wavelength, comparing to reference wavelengths measured at 468 nm, 570 nm, 633 nm, 656 nm, and 800 nm (which landed on the other side of the damage spot). Temporal dispersion led to a bent line of simulteneity which could be seen in faster sweeps. By passing a point source through the ray-tracing simulation, we also got a an idea for how well the various wavelengths would focus, setting the spectral resolution. A sample image from the spectrally resolved SOP is shown in figure 5.40

# Chapter 6

# X-ray heating experiments

In this chapter I discuss the results of experiments concerning x-ray generation in laser solid interactions and experiments attempting to heat a sample foil to WDM temperatures with the x-rays from a $K_\alpha$ source while monitoring the expansion of the sample target. As discussed earlier, heating with $K_\alpha$ photons was appealing because a narrow band source is much more tractable than a continuous one, allowing in principle for more precise determination of the deposited energy. An x-ray heating source also has the advantages of not being subject to velocity dispersion, as with protons and other ions, and not being radically affected by the electromagnetic fields near the target, like electrons are, allowing an unambiguous straight line path to our detectors.

The $K_\alpha$ heating experiments were all conducted on the JanUSP laser (now called Calisto), and additional studies of $K_\alpha$ production were conducted on the COMET and THOR lasers. Based on the modeling of section 4.3, temperatures at the lower boundary of warm dense matter were expected from JanUSP. Results from JanUSP could then be scaled up to higher energy lasers.

The sections are divided by the laser on which experiments were performed, with the final section discussing the prospects for going forward with $K_\alpha$ heating

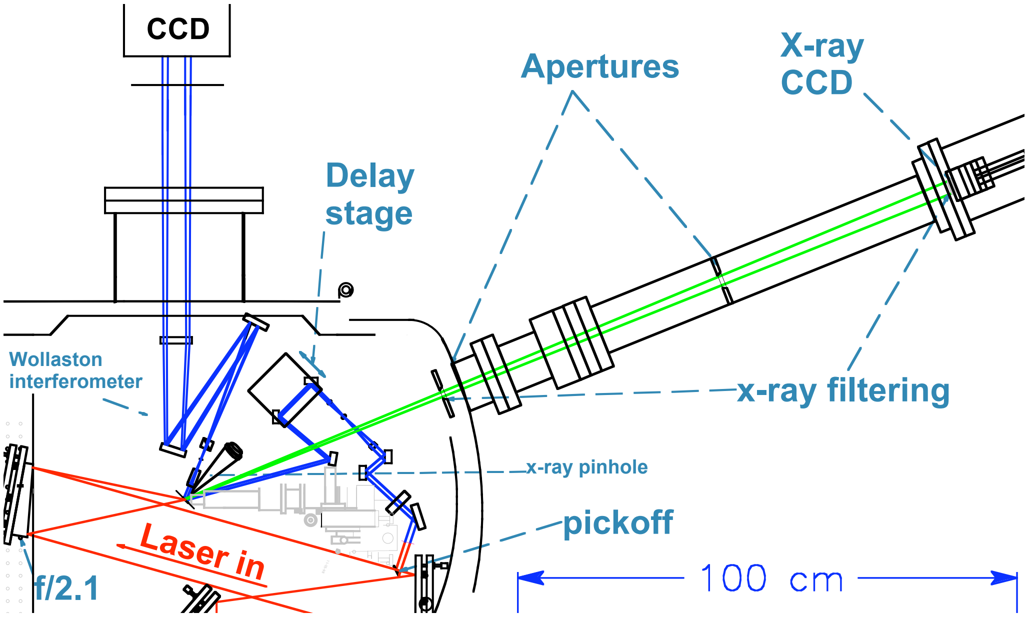

Figure 6.1: An x-ray CCD is mounted on the chamber on a long vacuum arm, which had its own gate valve and roughing pump to isolate it from the vacuum chamber. The Wollaston prism imaged the back side of the chamber to a CCD outside the chamber, using a probe beam which was picked off from the main laser and optionally doubled and spatially filtered. A motorized delay stage controlled the timing of the probe.

experiments. Recall that more detailed descriptions of the apparatus can be found in chapter 5.

## 6.1 JanUSP experiments

Our two $K_\alpha$ heating experiments on the JanUSP laser at LLNL were performed in summer of 2002 and spring of 2003. From the outset the experiments were designed to measure the internal energy deposition, by way of absolute $K_\alpha$ counting (section 5.2.5), as well as the target expansion, by a 2-D imaging Wollaston interferometer (section 5.3.1).

The experimental layout is shown in figure 6.1. The pinhole camera was used

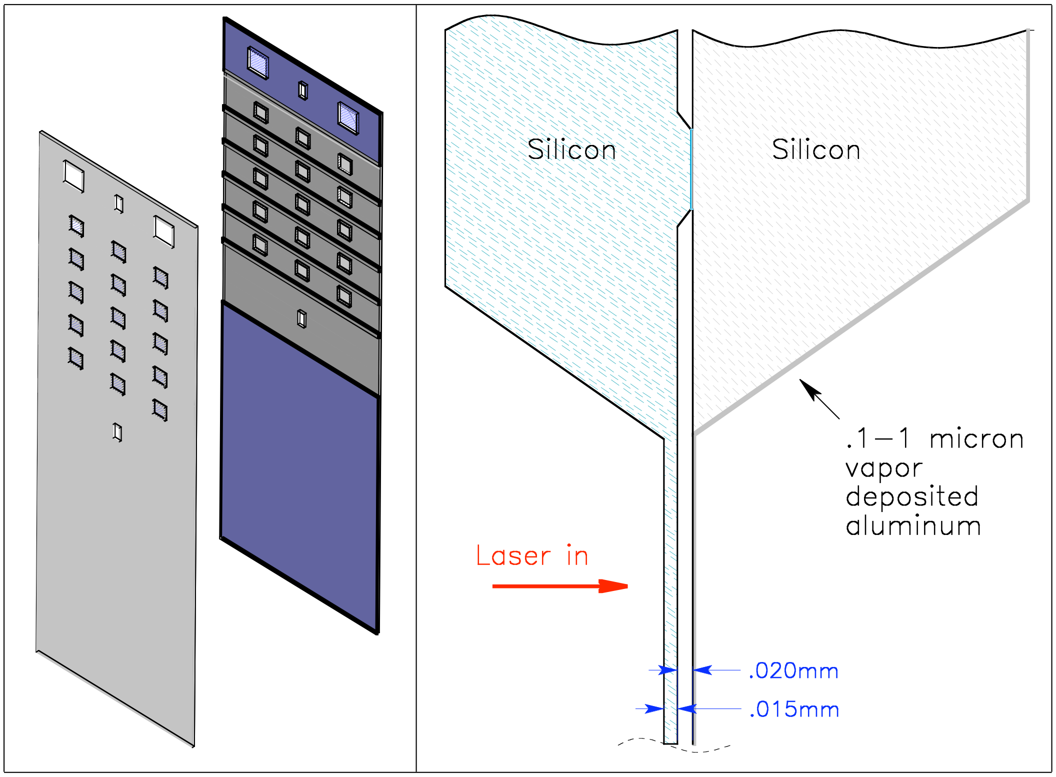

Figure 6.2: Structure of targets for $K_\alpha$ heating experiments on JanUSP. Etching the target foils out of a thicker wafer allowed us to use the wafer itself as a frame. On the source side, the Si was etched down to ∼15 $\mu m$ . The 20 $\mu m$ spacers were also etched from silicon from the other side. On the sample side, the silicon was etched all the way down to a 50 nm$Si_3N_4$base, upon which the Al was vapor deposited. Windows were sufficiently spaced so that shock waves from the 10 J laser would not affect adjacent windows.

to measure the x-rays in the first experiment in the absence of a photon counting CCD. Doubling and spatial filtering of the probe beam was used only in the second experiment. In both experiments, timing of the probe was achieved by the technique of air breakdown (section 5.3.2).

### 6.1.1 Target parameters

As discussed in section 4.3.3, our desire to study the x-ray heating of aluminum lead us to heat using the $K_\alpha$ x-rays of silicon. Besides being optimal for heating aluminum, silicon is also convenient as a target because the thin, laser irradiated part can be etched out of a larger wafer, which can act as a supporting frame, and will stand rigid and flat at the thicknesses we use $\gtrsim 10\,\mu m$. Our $K_\alpha$ heating targets at JanUSP were designed in collaboration with the target fabrication team there, and made entirely from the etching of Si and $Si_3N_4$, with the Al sample formed by vapor deposition on a negligibly thin (with respect to photon absorption) layer of $Si_3N_4$. In the first experimental run we used an Al sample layer of 100 nm; in the second[1], the sample was 100 nm Ti. Both materials absorb Si $K_\alpha$ at a similar rate. Our target design is shown in figure 6.2.

### 6.1.2 Laser parameters

In the summer 2002 experiments, the average laser energy in a system shot was $\sim$ 10J. The pulse contrast appeared to be poor, based on experimental results (see section 6.1.5), until a pulse cleaner was brought online. The exact level of the prepulse was unknown, but it was sufficient to deposit enough energy into the source foil to allow it to heat the sample foil before the main pulse arrived, indicating that the contrast was probably worse than $10^{-4}$ relative to the main. In the spring 2003 experiments, damage to the optics in the laser chain kept the laser energy below 6 J, with most shots occurring near 3 J. The laser pulse duration was stretched to .3 - 1 ps in order to keep the intensity down. Since it was picked off within the target chamber, the probe had the same pulse length as the main pulse. In addition to stretching the pulse, we also decreased the intensity by shooting the target out of focus. Beam profile images are shown in figure 6.3. Because the JanUSP target

---

[1] the target designers attempted also to make $1\,\mu m$ Al for that run, but the surfaces became very granular and did not cleanly reflect our probe

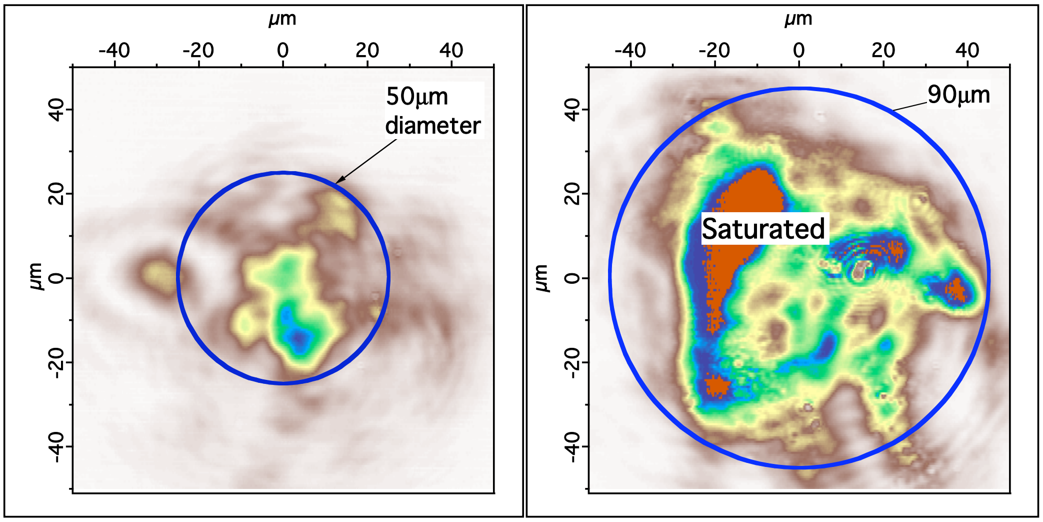

Figure 6.3: Beam profile of the slightly defocused JanUSP laser. Left: By taking the beam ∼100 $\mu m$ out of focus, a ∼50 $\mu m$ diameter beam was achieved. Based on the image, the intensity was estimated at $8 \times 10^{17}\,W/cm^2$ peak and $3 \times 10^{17}\,W/cm^2$ average inside the 50 $\mu m$ diameter circle. By comparison, a Gaussian wave would have approximately $5.1 \times 10^{17}\,W/cm^2$ peak and $3.1 \times 10^{17}\,W/cm^2$ average intensity, indicating that our defocused beam had hot spots relative to the smooth Gaussian case. The hotspot problem gets worse as we try to go to larger beam sizes (right): a beam with a geometric focus of 90 $\mu m$ only appears to be so large by saturating the image: the peak to average beam intensity ratio becomes even greater.

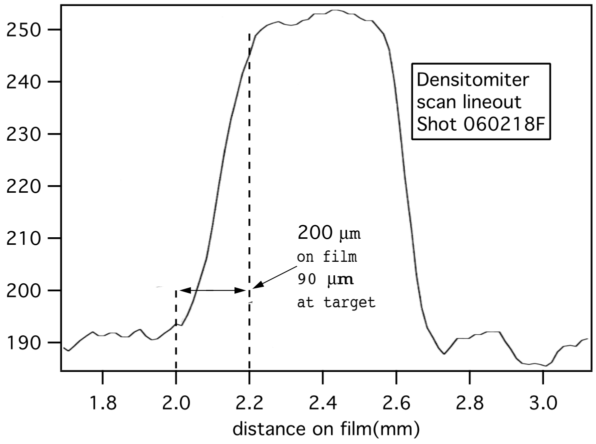

Figure 6.4: Densitometer scan of pinhole film from a 10 J shot in the Summer 2002 JanUSP experiment.

chamber used a short focal length, low f/# optic to obtain the highest possible intensity, decreasing the focal spot size to $\sim 100\,\mu m$ took the laser far outside of its Raleigh range and, as a consequence, the beam intensity profile was not smooth. In all cases, we moved the target towards the parabola to defocus.

In general a tightly focusing optic is less well suited for producing a large laser spot, and a soft focusing, high f/# parabola would be preferable for these purposes. High yield $K_\alpha$ generation is not the only application for which the intensity of a tightly focused $\gtrsim$100 TW would be excessive. For example, in the generation of fusion neutrons from deuterium clusters, any intensity beyond what is needed to fully strip the clusters is excessive, and it is then preferable to increase the focal volume to increase the overall yield. Aside from softer focusing, adaptive optics (i.e. a deformable mirror) could help produce a smoother spot away from best focus.

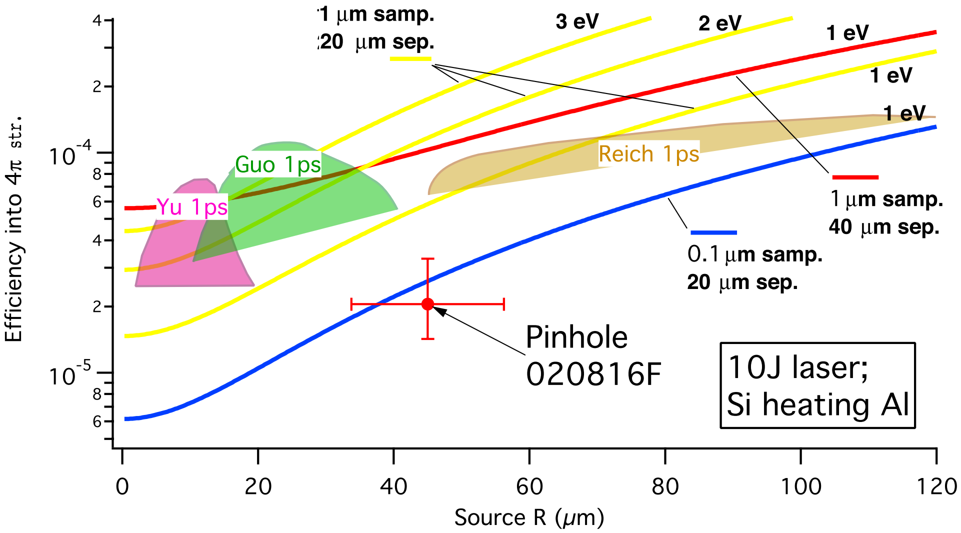

Figure 6.5: Efficiency and spot size of Si $K_\alpha$ from a 10 J shot on JanUSP. RECALL: The contours are as in figure 4.2, labeled by the energy to which the sample foil can be heated with efficiencies along each contour, as well as the sample thickness and source-sample separation. The colored shaded regions are as in figure 4.15, indicating the optimization ranges of various laser-to-electron scaling theories.

### 6.1.3 Pinhole x-ray measurement

We measured the x-ray flux in the 2002 experiments using a pinhole camera (section 5.2.4). The pinhole itself was 200 $\mu m$ in diameter, meaning that it could not resolve a spot as small as our $K_\alpha$ source. In fact, the pinhole acted more like a knife edge, and it was only by the rising edge of the pinhole image that we were able to determine the source size as about $90 \pm 20\,\mu m$ (see figure 6.4). We used absolutely calibrated, double sided Kodak DEF film, and a densitometer scan together with our estimate of the spot size, an estimate of the high-energy bremsstrahlung levels, and consideration of our filters ($3\,\mu m$ Ti), we estimated a flux of $3.3 \pm 1 J/cm^2$ silicon $K_\alpha$ . From a shot energy of 10.31 J, this indicates an efficiency of $\approx 2.0 \times 10^{-5}$. In figure 6.5 I put this number into the perspective of the analysis in section 4.3.3. We see that this flux was very nearly enough to heat our 100 nm Al target to 1 eV/atom by $K_\alpha$ alone.

### 6.1.4 Photon counting measurements

A photon counting CCD was fielded in the spring 2003 experiment. The shot energies were low, between 1 and 5 J, and the $K_\alpha$ efficiency was also lower, so that even scaled up to 10 J the $K_\alpha$ output would be by far insufficient to heat a sample foil of $.1\,\mu m$ Al. Our available sample foils were $.1\,\mu m$ Ti and $1\,\mu m$ Al, so the expected heating by $K_\alpha$ was even less. The $K_\alpha$ photon counting measurements are shown in the context of our earlier plots in figure 6.6.

Silicon $K_\alpha$ photons have a low enough energy so that the background caused by the 3-5 J shots on JanUSP nearly swamped the CCD, and the $K_\alpha$ peaks were difficult to discern for all shots above about 3 J, regardless of laser spot size. Time constraints didn't permit an optimization of the procedures described in section 5.2.5 for minimizing the background on the CCDs[2], but in general Si $K_\alpha$ is very

---

[2] In particular, lining the sides of the tube and chamber with lead bricks would have been a huge

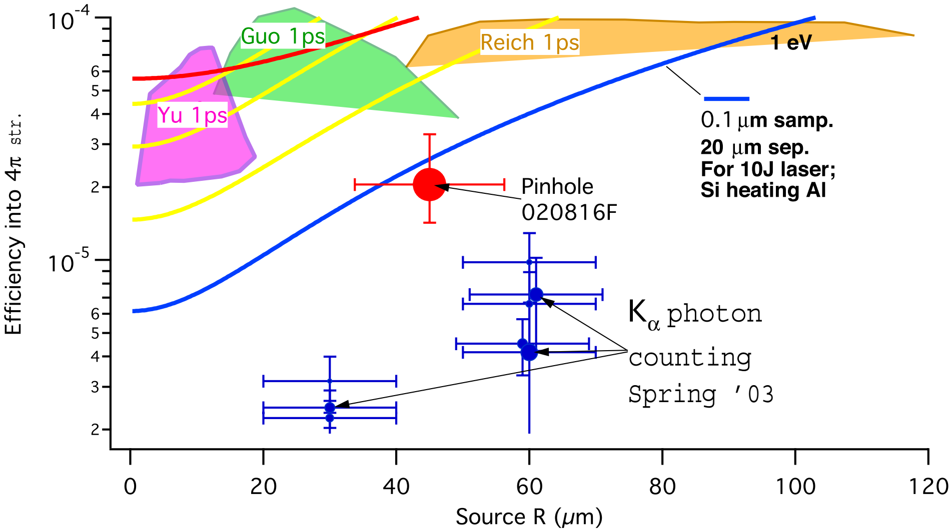

Figure 6.6: Photon counting measurements on Calisto from spring 2003 were low in terms of efficiency, and laser energy was also low. The size of the data points indicates the laser energy, with the pinhole shot at 10J, and the photon counting shots between 1 and 5 J. RECALL: The contours are as in figure 4.2, labeled by the energy to which the sample foil can be heated with efficiencies along each contour, as well as the sample thickness and source-sample separation. The colored shaded regions are as in figure 4.15, indicating the optimization ranges of various laser-to-electron scaling theories. The efficiencies of the shaded regions and contours reference 10 J, whereas the data points are from lower energies (except for the pinhole shot).

difficult to see by photon counting as the laser energy approaches 10 J, even when the focal spot size is greatly increased.

The reasons for the Si K$_\alpha$ efficiency being higher in the summer 2002 measurement by pinhole camera, relative to the spring 2003 measurements by photon counting are uncertain, however:

- We noted that in the latter experiments, the targets provided had a visibly grainy surface, left from the etching process, which may have effectively thickened the target by an unacceptable amount.
- It is also possible that we underestimated the integrated bremsstrahlung flux in calculating the K$_\alpha$ in the pinhole measurement, implying an overestimation of the K$_\alpha$ .
- Finally, the issues with the laser which drove down the energy for the shot run may have affected other aspects of laser performance, including pulse cleanliness. If a large preplasma was in place on the front of the source target, this could have negatively affected the K$_\alpha$ output.

### 6.1.5 Expansion measurements

Expansion on the JanUSP K$_\alpha$ heating shots was measured using a probe beam picked off from the edge of the main beam in the target chamber (fig. 6.1). As such, we did not have reference images of the target window from before each shot, as that would have also delivered energy on target. A motorized beam block would have worked to stop the main beam, but the excellent flatness of our targets made it possible to measure expansion without a reference phase[3].

---

project.

[3] In retrospect, a beam block would have been a good idea because reference phase is always useful.

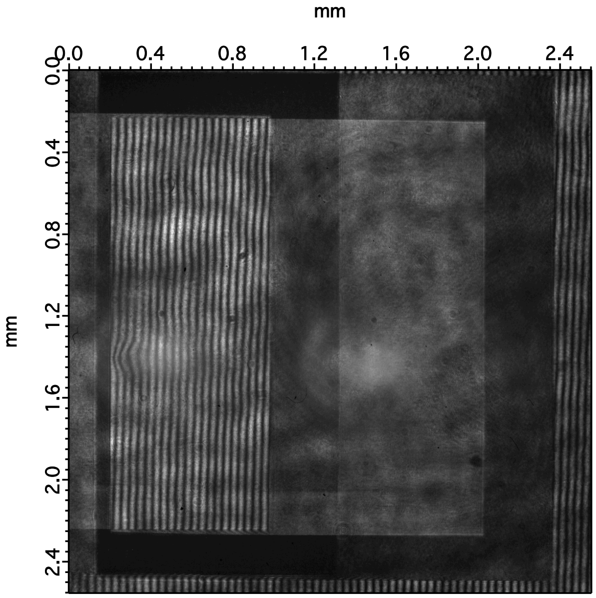

Figure 6.7: Full image from the interferometer on JanUSP, showing the dual images of the target window.

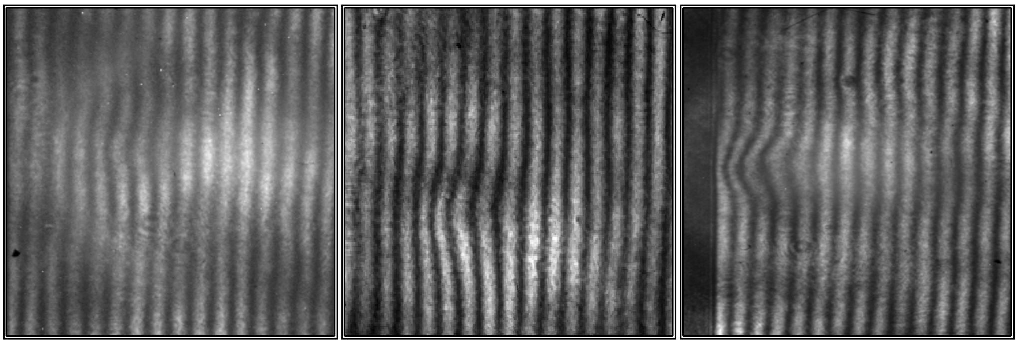

Figure 6.8: Example interference images from the JanUSP shots, showing increasing levels of expansion, left to right.

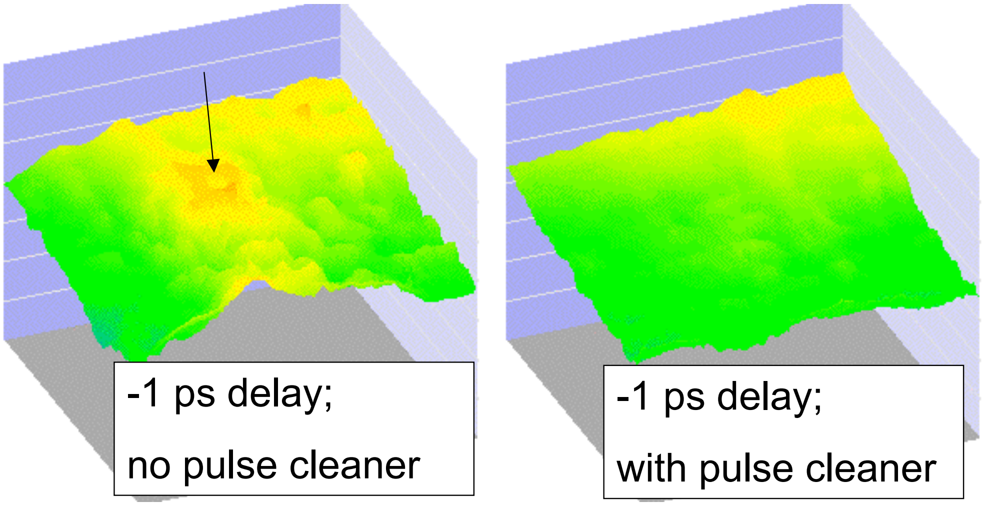

Figure 6.9: Phase map images of the expansion region at a probe delay of -1 ps (e.g. before laser arrival). Left: without a pulse cleaner in place, very clear heating of the sample has occurred well before the main pulse. Right: with a pulse cleaner installed, no visible heating occurs before the laser arrival, as would be expected.

### Pulse cleanliness

At the beginning of the first run, we found that heating of our sample layer was occurring before the arrival of the main laser pulse. Even to the maximum negative delay of the problem, 82 ps before main pulse arrival, damage was still seen. As seen in figure 6.9, installation of a pulse cleaner [NIT$^+$98] reduced the pre-pulses of the laser sufficiently to give the expected result that no heating of the sample should occur before the arrival of the main pulse.

### Faster than expected expansion

Even after the pulse cleaner was brought online, the expansion of the sample was much more dramatic than expected based on $K_\alpha$ heating alone. Clearly, a heating mechanism other than x-rays was dominating in our full energy shots. Figure 6.10 shows the rate of expansion of 0.1 $\mu m$ Al, measured by a series of time-delayed interferometry shots in the summer 2002 experiments, compared to the measurement

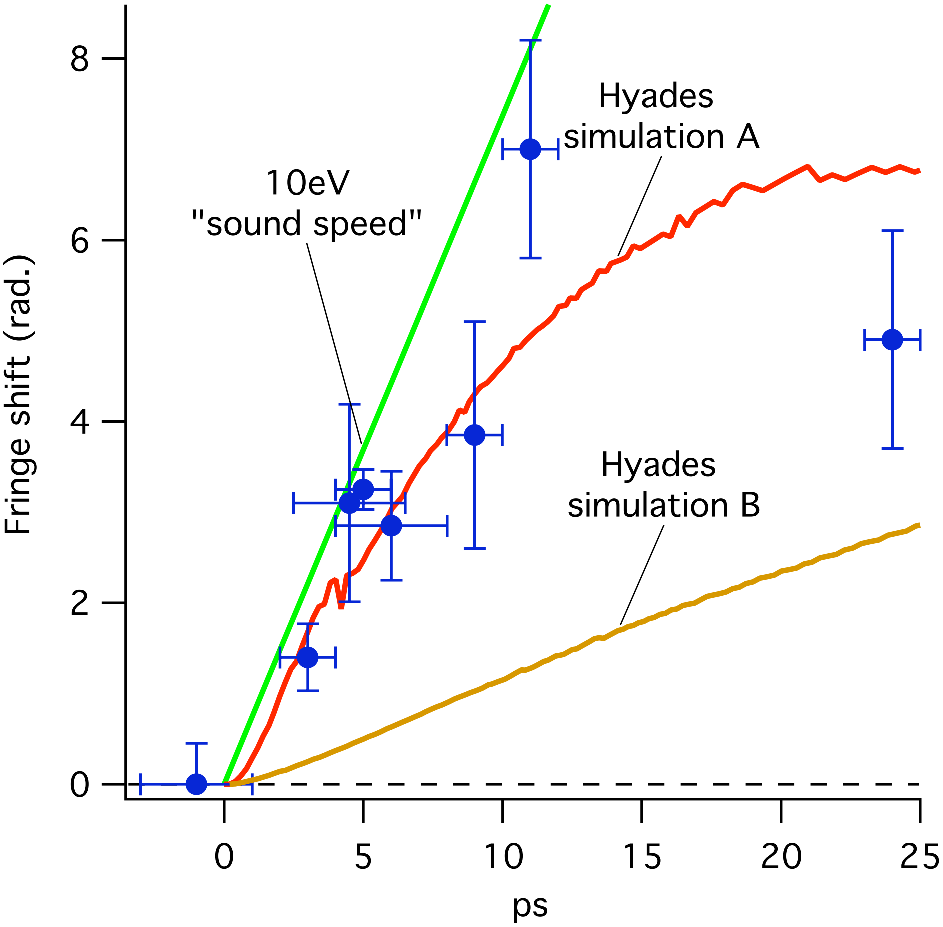

Figure 6.10: Measured and simulated expansion of the heated Al sample foils. "Hyades simulation A" shows the phase shift in the probe, caused by target expansion, in a simulated 100nm Al foil heated such that its ion temperature reaches 10 eV. In "Hyades simulation B," the ion temperature only reaches 2.5 eV, much hotter than could be attributed to $K_\alpha$ heating, but still shows much slower expansion than indicated by the interferometry measurement. Hyades simulation curve A rounds off when rarefaction waves from either side of the simulated sample foil (.1 $\mu m$ thick) meet, destroying self-similar flow.

simulated in the 1-D Lagrangian code Hyades [LL94]. The simulated expansion which best matches the data required heating of the sample, through the electrons, to the point that the ion temperature reached 10 eV. A second simulation, for which the ion temperature only reaches 2.5 eV (which is still more than predicted from $K_\alpha$ heating) is shown to expand much more slowly than what we measured. A cursory measurement of the protons with RCF film confirmed that a small but significant number of $> 1$ MeV protons were generated by our source, despite efforts to decrease the intensity to $\sim 2 \times 10^{17} W/cm^2$. A 1 MeV proton can cross a $20 \mu m$gap in approximately 1.4 ps.

For the spring 2003 run, in which the laser energy was lower and we further reduced intensity by increasing focal spot size, we again observed heating far above what would be expected from the $K_\alpha$ x-rays alone but there was also strong evidence of a delay between the laser shot and the onset of expansion, which suggests heating by slow protons (see figure 6.11). We used a larger focal spot than was used to heat the Al sample, in an effort to reduce any proton generation. It appears that we succeeded in reducing the temperature of the proton distribution, but that very strong heating did occur nonetheless.

Besides protons, it is also possible that the hot electrons in the source foil were not sufficiently stopped by the vacuum gap, as initially believed. The calculations of Fill, *et al.*(section 4.3.5) do predict that electron heating should be less than $K_\alpha$ heating for an optimized shot. However, recall that his analytic models suppose either a mono-energetic beam of electrons or a delta function in time. Neither of these conditions fully hold in reality, and removing them could lead to a larger number of escaping electrons. This was demonstrated experimentally by Stein and Fill , *et al.*[SFH$^+$04], who used a Cerenkov medium spaced from a laser irradiated source to detect electrons independently from other sources.

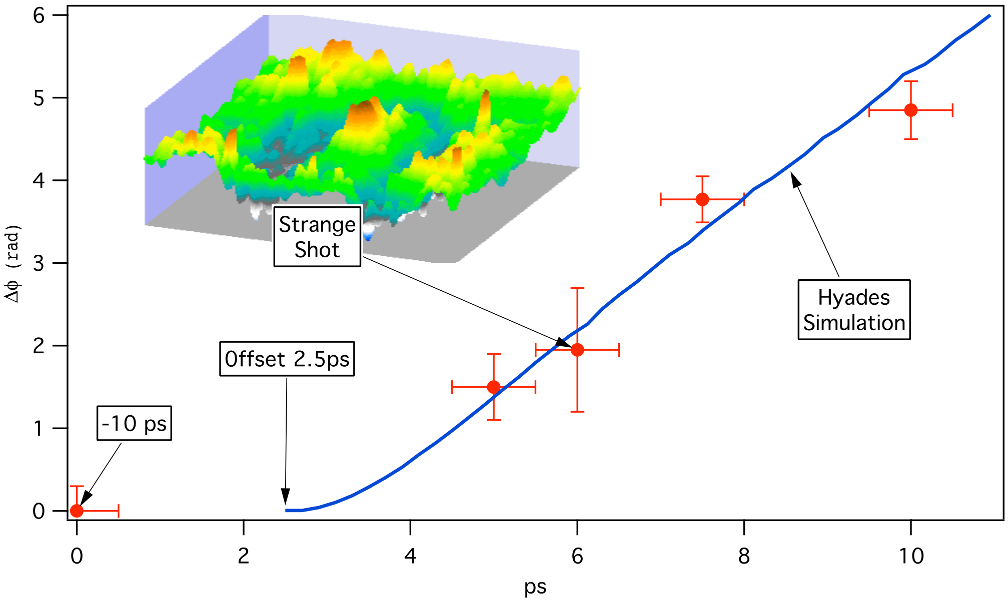

Figure 6.11: Expansion measurements of a Ti sample spaced 20 $\mu m$ from the Si source (same as in Al sample shots). The Hyades simulation indicates the phase shift from sample expansion calculated for a Ti foil heated to the point that the peak ion temperature reaches 12 eV, but with the heating source offset 2.5 ps. Although little more than a curiosity, since it was only observed once, I show inset the phase map of a "strange" shot in which the expanding region is surrounded spatially by a depressed region in the target (a negative phase shift region), of about twice the diameter of the expanding spot. For only $K_\alpha$ photons to heat to this degree would require a conversion efficiency of $\gtrsim 5 \times 10^{-4}$. Returning to figure 4.11 (with Ti absorbing Si $K_\alpha$ at a similar rate to Al), we see that this would basically require $\sim$100% conversion efficiency into electrons of energies between 30keV and 40keV, which should be considered impossible.

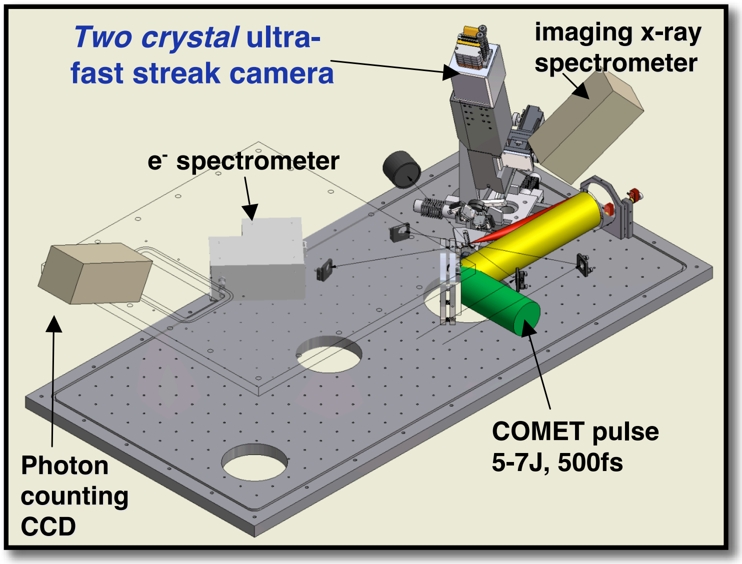

Figure 6.12: Layout of the LAEPRI 2004 experiment. The photon counting CCD was in the laser plane and further away from the target than depicted here. The FSSR1D and streak camera observed the target front, while the photon counting and electron spectrometer diagnostics viewed the back side.

## 6.2 LAEPRI 2004

The Laser Absorption and Energy Partitioning at Relativistic Intensities (LAEPRI2004) experiment aimed to study the partitioning of laser energy at $> 10^{18}\ W/cm^2$ into front side plasma and fast electrons by measuring the characteristic x-rays of both simultaneously. The primary diagnostic was the ultrafast T-Rex streak camera, set up to observe the $\mathrm{He}_\alpha$ of an Al ablater layer simultaneously with the $\mathrm{K}_\alpha$ of a Ti layer underneath. In addition, a spherical crystal spectrometer (FSSR1D) was employed to give both high-resolution spectral and spatial information about the Ti $\mathrm{K}_{\alpha 1}$ and $\mathrm{K}_{\alpha 2}$, and a photon counting CCD gave the absolute flux of Ti $\mathrm{K}_\alpha$ from the target back side.

### 6.2.1 Converting COMET to a target shooter

For this experiment, the COMET laser (sec. 3.2.3) was converted into a target shooter to substitute for the ailing JanUSP laser. This involved the installation of a new target chamber with a parabola focusing optic and correction of grating astigmatism, as described in section 5.1.1. The grating astigmatism had gone unnoticed because the COMET short pulse beam was intended to deliver a line focus anyway. Pulse cleanliness had also not been a concern when COMET was operated as an x-ray laser since a long scale length plasma is desired. We found strong evidence of a very significant prepulse throughout this experiment, but had no means to correct it within the schedule of the experiment[4].

### 6.2.2 Photon counting measurements

Efficiency of laser energy conversion into titanium $K_\alpha$ and $K_\beta$ was measured with a photon counting CCD for a variety of focal spot sizes ahd shot energies. Figure 6.13 shows examples of the photon counting histograms taken, and figure 6.14 shows the reduced data of $K_\alpha$ /$K_\beta$ efficiency vs. laser spot size. The majority of shots were taken before the compressor grating parallelism problem was fixed and thus had a focal spot which was much wider than it was tall (figure 5.3). With the focal spot fixed, full energy shots produced too much background on the counting CCD to be seen, so only those tightly focused shots taken at lower energy or with an intentionally defocused spot show up on the plot. Finally a number of shots were taken with an intentional high energy, long timescale (5 J, 400 ps) prepulse, and these showed the signal of a multiply ionized plasma, in the form of satellites in the $He_\alpha$ range.

---

[4] It was later discovered that the prepulse was caused by a thin film polarizing mirror in the laser chain that had been installed backwards.

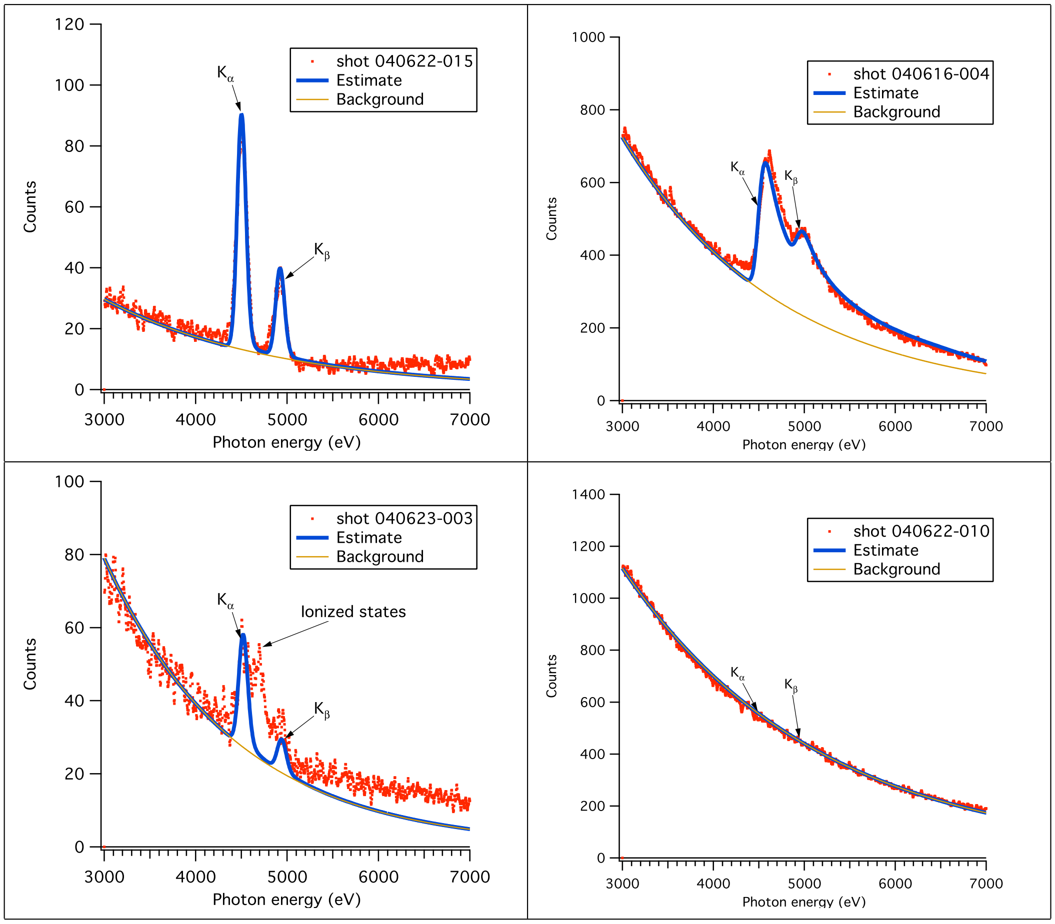

Figure 6.13: Examples of $K_\alpha$ histograms from the LAEPRI shots. TOP LEFT: a good histogram coming from a moderate ($\sim$ 4J) energy shot not at tightest focus ($\sim 1.25\times10^{17} W/cm^2$), on $12 \mu m$ Ti; TOP RIGHT: A $>$ 7J shot, not at tightest focus, exhibiting very high $K_\alpha$ /$K_\beta$ and background. The peaks blend together because of multiple counts (see section 5.2.5); BOTTOM LEFT: A shot in which an intentional long-pulse prepulse (arriving 400 ps ahead) was used. Ionized states of Ti (at least up to $He_\alpha$ ) are seen in the spectrum; BOTTOM RIGHT: a tightly focused, high energy shot swamps the $K_\alpha$ signal with background.

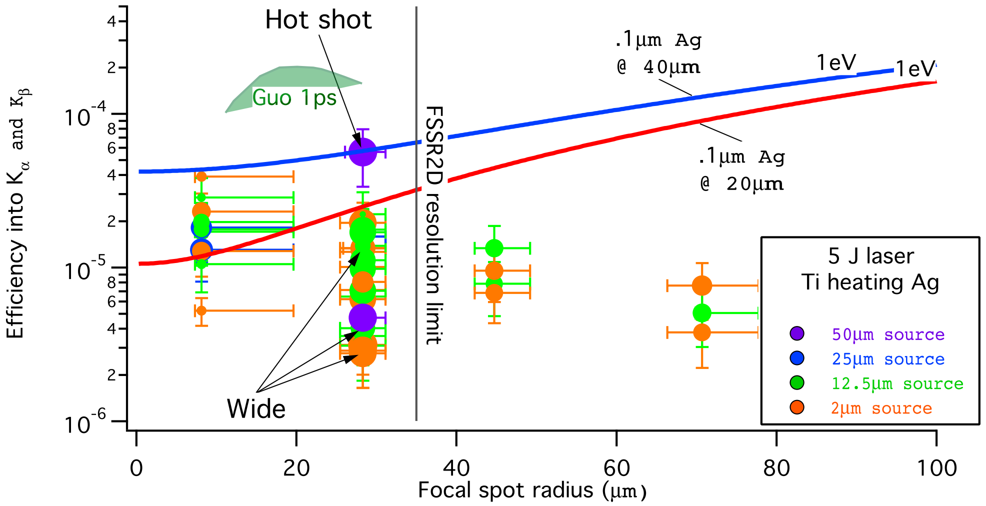

Figure 6.14: $K_\alpha$ and $K_\beta$ photon counting results from LAEPRI04. The size of the data points indicate their energies, between 1.5 J and 7 J. The shots labeled "wide" were taken before the grating parallelism was fixed, and had a 4:1 width to height ratio. The "radius" was calculated from $r = \sqrt{A/\pi}$, where $A$ is the $1/e^2$ area. The shot labeled "hot shot" was an inexplicably high energy shot ($> 7$ J) which damaged a rod in the laser. In addition to high $K_\alpha$ and $K_\beta$ that particular shot showed abnormally high bremsstrahlung, integrating to 2x the $K_\alpha$ /$K_\beta$ flux, and stronger than normal electrons. The spatial resolution limit of the FSSR2D imaging x-ray spectrometer was set by the pixel size on its CCD.

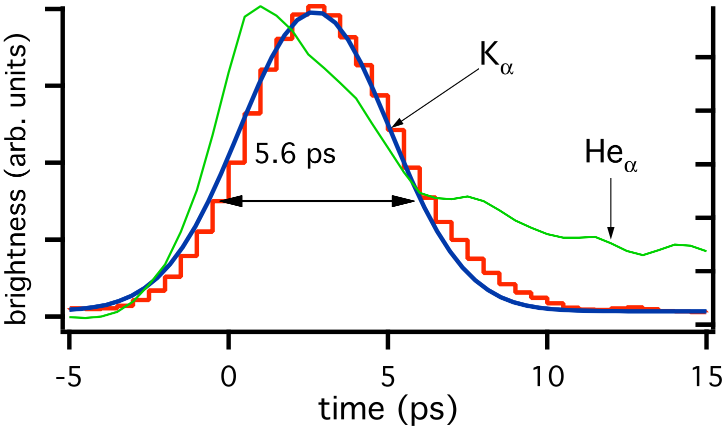

Figure 6.15: Lineout of Ti $K_\alpha$ on a typical shot. The signal is fit very easily to a Gaussian of FWHM 5.6 ps. Jagged edges of the lineout indicate pixel widths. Al $He_\alpha$ from the same shot is superimposed on the same timescale, and exhibits a similar initial pulsewidth to the $K_\alpha$ but persists at the low level at the right of the graph for several 10s of ps.

### 6.2.3 X-ray streak camera results

The T-Rex x-ray streak camera (section 5.2.2) successfully resolved the $He_\alpha$ of aluminum and $K_\alpha$ from the front side of the titanium target with temporal resolution to $< 1$ ps. Figure 6.15 shows a line-out of the $K_\alpha$ generated in a typical shot on 12.5 $\mu m$ Ti with a 1000ÅAl overlayer. The plot indicates a FWHM duration of 5.6 ps. This is considerably longer than the nominal FWHM ($\sim$ 500 ps) of the laser pulse, but it is possible that the laser profile had wings out to ±3ps of sufficient intensity to drive $K_\alpha$ photons. The hot electrons originate from within the Al front layer, and the $He_\alpha$ emission from that has a peak on a similar timescale to the $K_\alpha$ , before reaching a steady emission that persists for several tens of picoseconds. The long $K_\alpha$ pulsewidth could also be a sign of recirculating hot electrons (sec. 4.3.5). On the other hand, the significant prepulse on COMET may have contributed to a longer $K_\alpha$ pulsewidth. It was determined that space charge effects within the streak

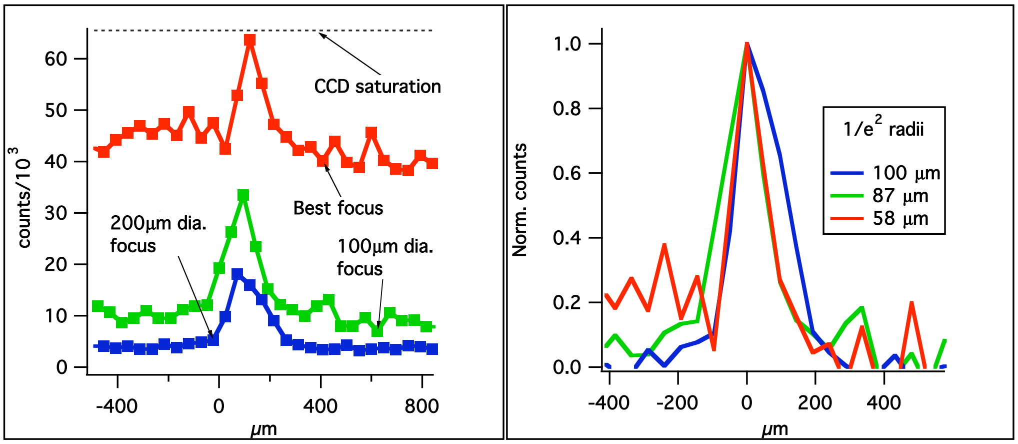

Figure 6.16: Lineouts in the spatial direction of $K_{\alpha 2}$ from titanium foils shot on COMET. Red curve: best focus, giving a spot source size with $1/e^2$ radius $\lesssim 58\,\mu m$. Because the camera was approaching saturation, we know that pixel bleeding artificially increased the apparent size of this source, the above example being the least bled source; Green curve: target shot with $\sim 100\,\mu m$ diameter focal spot; blue line: shot with $\sim 200\,\mu m$ diameter focal spot. The $1/e^2$ radii were determined by Gaussian fit.

camera should not have been responsible for an illusion of pulse broadening. Riley, *et al.*[RKPdS$^+$06] observed a similar long pulsewidth to $K_\alpha$ using a fast x-ray streak camera (2 ps resolution).

### 6.2.4 Imaging x-ray spectrometer results

The imaging x-ray spectrometer was run with a vacuum compatible compact x-ray CCD, built at LLNL. The layout of the target chamber precluded using the crystal in the FSSR-2D configuration for spatial magnification, and hence the FSSR-1D configuration was used, with the image of the source de-magnified to 52%. As such, a single pixel width represented 48 $\mu m$ , setting the best-case of spatial resolution.

### Spatial extent of the source

Because the spatial resolution was somewhat poor, precise spatial information about our sources was not obtained. We were able to confirm a difference in spot size between tightly focused and defocused laser shots (figure 6.16), but even this pushes the resolution limit of the camera. Shots taken with a tight focal spot mostly saturated the camera, which led to pixel bleeding in the spatial direction. Hence, the measurement of $58\mu m$ for the source in the tightly focused case is an upper limit, and the actual source size is probably smaller. The spatial extent of the $\mathrm{K}_{\alpha 1}$ and $\mathrm{K}_{\alpha 2}$ must be the same, and hence the $\mathrm{K}_{\alpha 2}$ spatial extent is used to judge the $\mathrm{K}_{\alpha 1}$ extent as well. However, satellites of $\mathrm{K}_{\alpha 1}$ exist only where the titanium is hot enough to be multiply ionized, and through a combination of not being bright enough to saturate and actually being smaller in spatial extent because of radially decreasing temperature, the satellites were typically a single pixel in width, or $\lesssim 48\,\mu m$ .

### Spectral information

The CCD was deliberately oriented such that pixel bleeding would occur along the spatial direction and not the spectral direction, so that saturated images would still allow resolution of sattelites of $\mathrm{K}_{\alpha 1}$ . The spectral resolution was $\lambda/\Delta\lambda \approx 3800$.

The spectral data became the subject of a very interesting analysis, led by S. Hansen [HFP+05], in which the average temperature over the foil thickness was determined to within ±5 eV using a self-consistent-field model. The temperatures of the bulk foil material were in the range of 25 - 40 eV, which is of course indicative of warm dense matter.

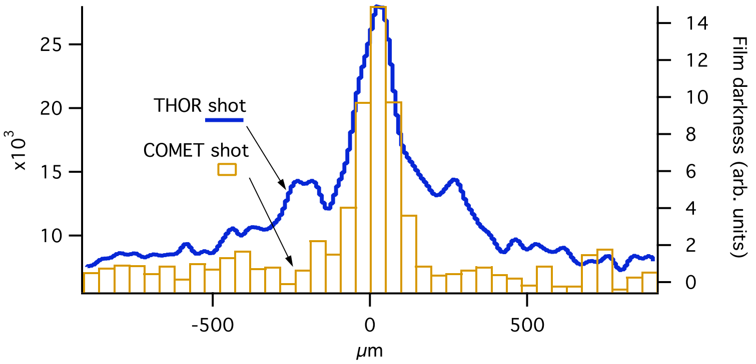

Figure 6.17: FSSR1D spatial lineouts of $K_\alpha$ from the COMET and THOR experiments. The THOR shot clearly exhibits side wings of outer diameter 200 $\mu m$ . The COMET shot lineout is displayed with bars to emphasize the scale of its resolution.

## 6.3 THOR experiments

We performed a series of x-ray characterization experiments on the THOR laser in 2005. Details of these experiments can be found in the masters thesis of S. Kneip [Kne05]. I will briefly outline some of the more notable results here.

### 6.3.1 Resolving spatial features in $K_\alpha$

A very similar FSSR-1D to the one fielded on COMET was operated on THOR by Dr. S. Pikuz of Lomonosov Moscow State University. By using film[5] instead of a CCD, and using less magnification than in the COMET experiments, we were able to obtain superior spatial resolution and observe an interesting feature in laser generated titanium $K_\alpha$ which might have been harder to see using a CCD. Figure 6.17 shows the lineout along the spatial dimension of $K_{\alpha 1}$ from a shot at 0° onto a flat foil of Ti, compared to the lineout from a shot on COMET. The foil thicknesses ($\sim$ 12 $\mu m$ ) and laser intensities ($10^{19}$ $W/cm^2$) were approximately the same, but the energies were different by an order of magnitude (5 J on COMET, 500mJ on

---

[5] Kodak RAR 2492

THOR), and the COMET shot was taken at an incidence angle of 45°. We see the interesting result that the THOR lineout has "wings" with an outer diameter of about $500\,\mu m$, surrounding the inner peak of diameter $\sim 150\,\mu m$. The $\mathrm{K}_\alpha$ measured on COMET has a much sharper spatial fall-off. What is interesting in the THOR shot is that the $\mathrm{K}_\alpha$ spatial profile exhibits a definite dip, indicating two distinct regions of $\mathrm{K}_\alpha$ emission (if we assume axial symmetry).

A similar effect was observed by Burgess, *et al.*[BLN85] under vastly different laser conditions and at a 45° laser incidence. In their case, a 200 $\mu m$ diameter gold disk was irradiated at 45° by a 2J, 20ps laser pulse, and x-ray emission was measured by penumbral imaging to have strong emission at the center of the target and also on the edges of the disk, with a low emission region in between. This effect was attributed to strong laser-generated magnetic fields on the front side of the target bending backwards traveling hot electrons in an arching path back to the target. This implied magnetic fields on the order of $10^6$ Gauss. This explanation would not explain why the COMET shot saw no sign of these wings.

Koch, *et al.*[KKF$^+$02] observed a columnar shape to $\mathrm{K}_\alpha$ output when a plastic target with buried metal tracer layers was irradiated by a petawatt laser pulse. They explained this phenomenon in terms of a Weibel-like instability for hot electrons propagating through the insulating plastic. Furthermore, their model relied on the laser driver being on for $\gtrsim$ 500 fs. These conditions don't apply to our measurement.

An electron fountain effect at the back side of a target is seen by A. Pukhov [Puk01] in 3D PIC simulations designed to study back surface proton acceleration. Electrons leaving the back surface generate a strong azimuthal magnetic field which tends to keep them columnated, but as they're pulled back by the electric fields, they fountain out, rather than returning straight back, and further contribute to the magnetic field.

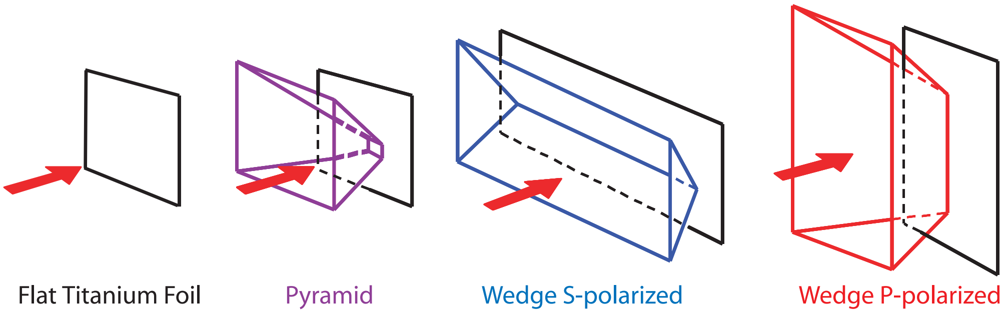

Figure 6.18: The various target geometries employed in our experiments. Left to right, a flat foil of titanium, a pyramid etched into Si with the Ti foil at its tip, the s-wedge and the p- wedge. The latter two have the same shape but are named after their orientation relative to the laser polarization.

### 6.3.2 Shaped targets

We also studied the effects of re-entrant conical targets, inspired by the fast ignitor concept [KNM$^+$01] and simulations by Y. Sentoku [SMR$^+$04]. Given the prohibitive cost of the free-standing gold targets used in fast ignitor targets, we elected to produce our own variety of cones by anisotropic etching of silicon. This produces a square-base cone pit in a silicon wafer with a sharp tip which can be etched down to within microns of the wafer's back surface. It is also possible to make "1-dimensional" cone targets by extending the tip of the cone to a line, which can then be oriented for s- or p- polarization (figure 6.18). The 70.5° cone angle was too wide to expect any significant surface electron guiding [NKNM04], but reflection of laser light towards the tip can lead to an enhancement in laser intensity there.

For our experiments we affixed a $K_\alpha$ fluorescing layer of titanium (11 $\mu m$ or 25 $\mu m$ thick) to the back surface of the target to give a signature of the fast electrons emitted from the cone tip. Complimentary 1-D PIC simulations were performed by Dr. Y. Sentoku of the University of Nevada at Reno. The hard (>100 keV) x-ray temperature was measured by an array of scintillator/photomultiplier detectors with different filtering. The $K_\alpha$ yield was measured by a von Hamos crystal

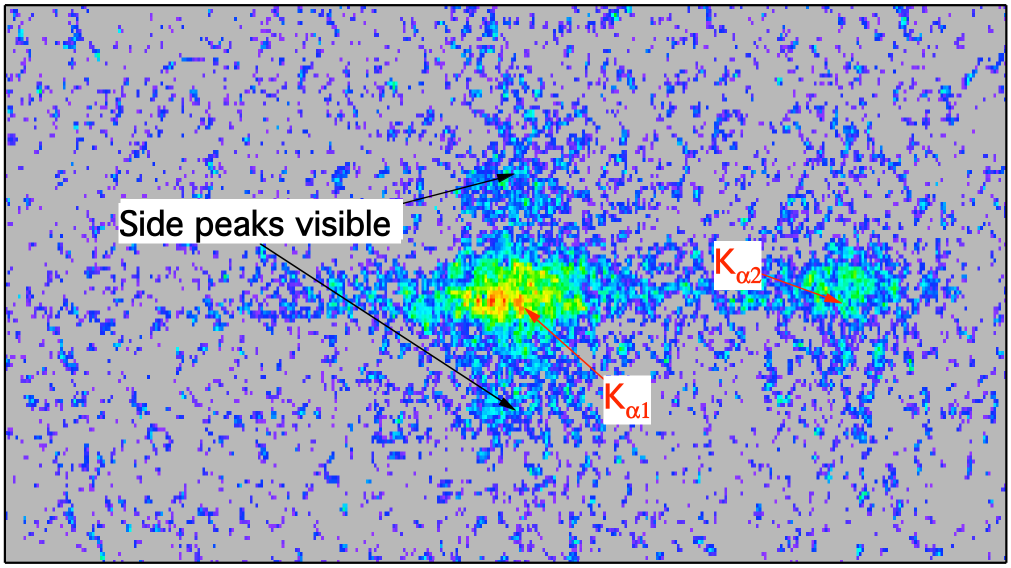

Figure 6.19: FSSR1D image of $K_\alpha$ in titanium, displaying side peaks (see section 5.2.3).

spectrometer. Somewhat surprisingly, we found the trends in these two measurements to be opposite between cones, s-wedges, and p-wedges: p-wedges exhibited the strongest hard x-ray spectrum and the weakest $K_\alpha$ , while s-wedges exhibited the opposite extremes, with cones falling in the middle. The PIC simulations predicted that the p-wedges indeed absorbed more laser energy, but this laser energy came in the form of very hot electrons which emit large amounts of bremsstrahlung but have a low cross section for K-shell ionization. The simulated s-wedges on the other hand, showed pressure heating near the wedge tip to temperatures of several keV, a temperature high enough to send K-shell ionizing hot electrons into the titanium layer.

The FSSR1D imaging the back side of a titanium-backed cone target showed that the presence of the cone removed the wings from the spatial profile of $K_\alpha$ (figure 6.20). This would seem to support the idea that the wings are generated from electron motion at the front side of the target, which the cone geometry would

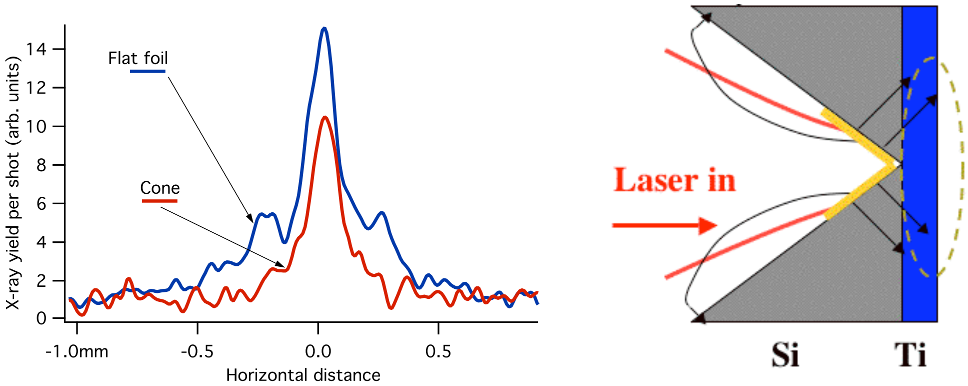

Figure 6.20: Left: $K_\alpha$ imaging of the emission from a Si cone target shows no sign of the wings seen from a flat Ti foil. Right: if the wing effect is generated on the front side, blocking of electrons by bulk silicon could explain their absence in cone shots.

prevent, but this is not conclusive. What is certain is that the cone suppresses the wings to form a more point-like source, which is often desirable.

## 6.4 Prospects for $K_\alpha$ heating

In the next chapter I will describe the approach of proton heating, which we ultimately used to achieve the goal of producing and diagnosing well-characterized warm dense matter states. We have found that, although $K_\alpha$ x-rays should in principle be able to heat material to the lower warm dense matter temperatures, there are a number of serious obstacles to this experiment:

- First and foremost, heating mechanisms other than $K_\alpha$ x-rays have dominated in these experiments. If this is in fact heating by MeV protons, this effect could be significantly reduced by cleaning hydrocarbons and water contamination from the source either by ion sputtering gun [APM$^+$04] (which would require a mechanism to move the sample in and out of position) or by ohmic heating. One might suggest increasing the vacuum gap to allow more time for x-ray heating before protons arrive. However, as we've seen the K$_\alpha$ flux falls off quickly as we increase the gap, and even a 100 $\mu m$ gap wouldn't buy much time, but would reduce the K$_\alpha$ excessively.

- A barrier layer would stop lower energy K$_\alpha$ x-rays more readily than fast protons. This would preclude using this technique for photons heating low Z materials such as Al, but might work with higher Z source and sample.
- We've seen evidence that any K$_\alpha$ source will be extended in time as we increase our laser energy and K$_\alpha$ output. This takes away one of the key advantages to K$_\alpha$ heating.
- Relativistic hot electrons are not favorable for generating K$_\alpha$ , particularly in the low-Z sources which would be needed to heat low-Z materials, such as Al, by K$_\alpha$ . But it is these electrons that are favorably guided in the cone geometry [SMR$^+$04]. Higher Z sources and samples might be aided by cone guiding.
- As seen in section 4.3, for very high Z materials such as Ag, the fraction of bremsstrahlung energy at higher photon energy than the K$_\alpha$ begins to overtake the energy emitted from K$_\alpha$ even in the optimized case. Bremsstrahlung heating would take away the advantage of the narrow band K$_\alpha$ source.
- Refocusing of K$_\alpha$ with grazing incidence optics (e.g. an ellipsoid) would eliminate the problem of protons (especially if a barrier were used), but this technique is likely to reduce K$_\alpha$ flux by at least an order of magnitude, because of imperfect re-imaging, and a small collection solid angle.

If well-characterized heating to WDM states by K$_\alpha$ photons is to be achieved, it will likely involve a cleaned source foil or cone of medium-high Z (e.g. Cu) heating a sample foil of still higher Z, using a high-energy petawatt class laser with a very large and smooth focal spot. Electrons and protons leaving the source target will have to be carefully characterized, and the laser-to-$K_\alpha$ efficiency will have to be fully optimized.

We now shift our attention to deliberately heating via MeV protons through which temperatures exceeding 10 eV are easily achieved.

# Chapter 7

# Proton heating experiments

As discussed in the last chapter, our early experiments showed strong evidence of heating by MeV protons far above the level of any heating by $K_\alpha$ photons. Shortly after those experiments, Patel, *et al.*[PMK$^+$03] published results of an experiment on JanUSP in which they demonstrated proton heating to warm dense matter temperatures using streaked optical pyrometry (section 5.5). Based on our previous experiments, we decided that the apparent merits of $K_\alpha$ heating were outweighed by the superior heating capability of protons. Indeed, it would be a bigger challenge to avoid proton heating than it is to implement it. The featured results of this chapter, and of this thesis, are the first simultaneous measurements of a pressure-related quantity (the rate of expansion) together with the temperature (through the thermal self-emission), of isochorically heated warm dense matter.

## 7.1 Calisto shots

Initial proton heating shots were performed on Calisto (formerly JanUSP). During the experiment we had access to an independently air-compressed and frequency-doubled probe beam, as well as a C1587 streak camera (section 5.5.3). For some of

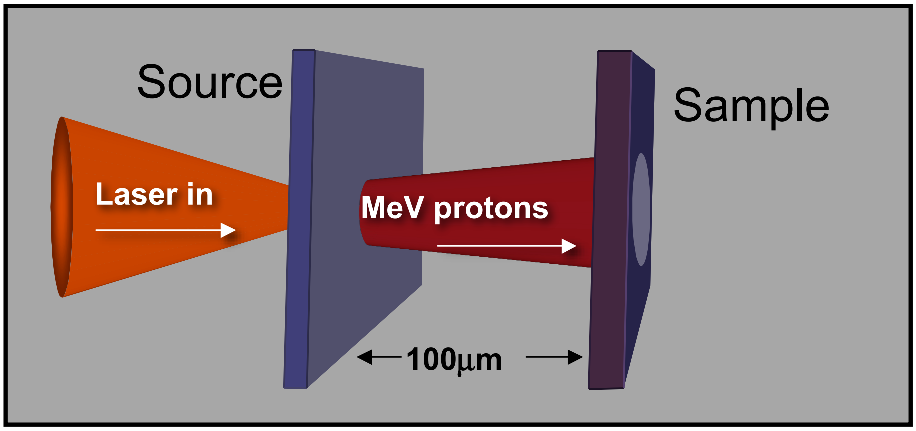

Figure 7.1: Basic schematic of the proton heating experiment.

the shots, the SOP was spectrally resolved using a prism spectrometer, and set up as described in section 5.5.6. For others, the prism and slit were removed to produce a simple imaging SOP. The probe beam was also timed using the streak camera, as described in section 5.3.2.

### 7.1.1 Target design

For the Calisto experiments, we[1] fabricated our targets from Si wafers at the UT Microelectronics Research Center[2]. A schematic of the targets is shown in figure 7.3. The source side of the target was coated with 150 nm Au to prevent scattering of the laser precurser through the target, since Si is transparent to 800nm light until ionized.

### 7.1.2 Effects of a prepulse

The Calisto/JanUSP laser was used for many successful proton experiments in years past [PMK$^+$03, BMC$^+$04, APM$^+$04]. However, its capacity to produce high quality

---

[1] Specifically, Byoung Ick Cho

[2] `http://www.mrc.utexas.edu/index.html`

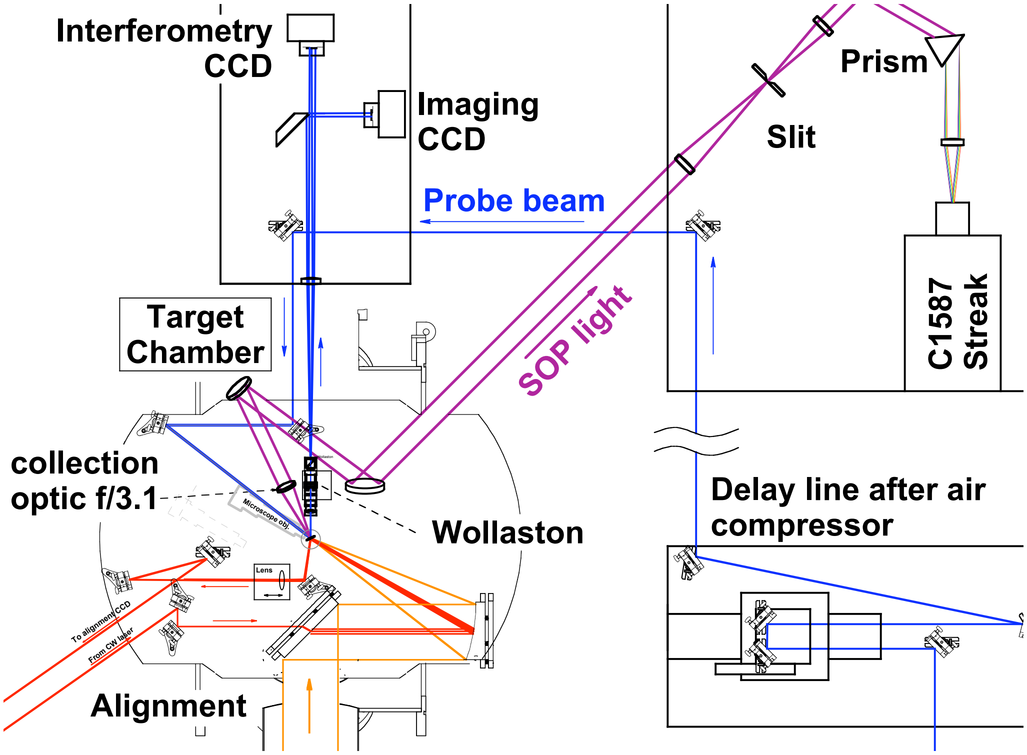

Figure 7.2: Layout of the Calisto proton heating experiment. We used an independently air-compressed and doubled probe beam and a Wollaston prism interferometer with two CCDs to seperately observe the phase and reflectivity of the sample at 400nm. A prism spectrometer front end to a streak camera observing the back side of the target acted as a spectrally-resolved SOP. For some shots, the prism and slit were removed, returning us to an imaging SOP.

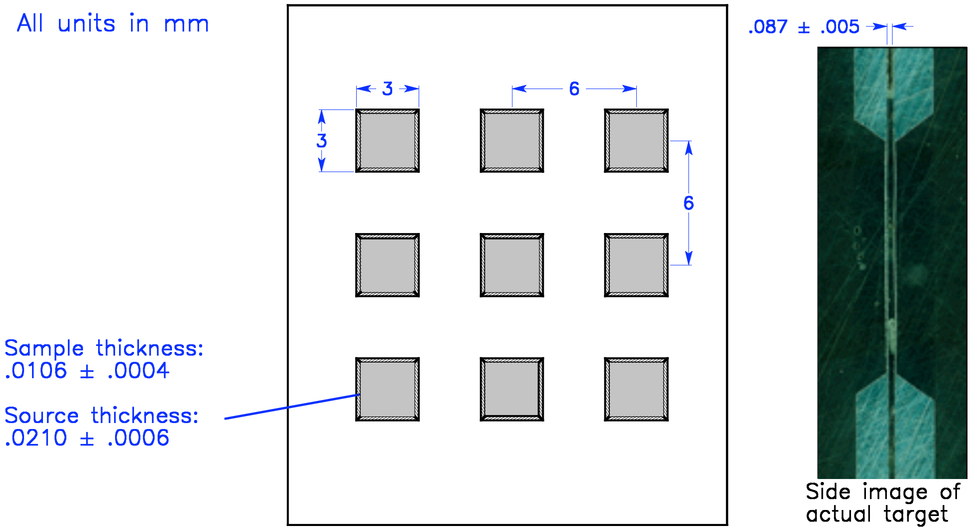

Figure 7.3: Target design for the Calisto proton heating experiments. Windows were 3 mm on a side and etched down to 20 $\mu m$ for the source and 10 $\mu m$ for the sample. A single target consisted of two pieces of wafer adhered together with their etched sides facing outward. The spacing of $\approx 85\,\mu m$ was maintained by using single strips of scotch double-sided tape, cat. 665, which we found to be exceptionally stable in thickness compared to other options. High magnification cross-section images of the targets were used to determine thicknesses and variations. In some shots, the Si source window was broken out and replaced with a 4 $\mu m$ Au foil, which gave slightly higher proton yeild.

energetic proton beams has diminished over the years. Our suite of diagnostis provided clear evidence that the ability of Calisto to produce quality proton beams from laser foil interaction is now severly diminished by the presence of a significant prepulse[3]. As demonstrated by Wilks and Mackinnon, *et al.*[MBH$^+$01, WLC$^+$01], a preformed plasma on the back surface of a proton source target destroys its ability to produce multi-MeV proton beams, drastically reducing not only its maximum (cut-off) energy, but also the conversion efficiency. Our interferometer clearly measured a significant plasma on the back side of the source foil in advance of the main laser pulse, and our SOP directly measured the laser prepulse in mJ shots as well as its effects on a target in full energy shots, and RCF film stack diagnostics showed the greatly diminished and distorted proton/ion beam and further evidence that this was caused by a prepulse. Evidence of a prepulse from the interferometery/reflectivity probe is shown in figure 7.4. With the probe arriving 30ps before the main pulse, substantial plasma effects are already occuring on the back surface of the source foil. On the earlier JanUSP experiments, we performed similar tests of the bare source foil and found no such signs of disturbance before the arrival of the main pulse[4]. This suggests that the prepulse is a new phenomenon which did not hinder proton generation during the $K_\alpha$ heating experiments. Evidence of a strong prepulse from the spectral streak camera is shown in figure 7.5. Direct measurement of the laser from scattering at the target plane indicated that the prepulse existed 100 ps before the main pulse, and also had a symmetric post pulse of slightly higher brightness, and as well as another post pulse twice as far out. The same timing was seen in a system shot on a bare source target, where at -100 ps a small amount of prepulse light scatters through the 20 $\mu m$ Si target, which is overlayed with a 600 ÅAu but still slightly transmissive of 800 nm light. In the prepulse, signs of thermal emission

---

[3] The reader may recall that a prepulse problem in an earlier experiment was fixed by use of a pulse cleaner. In these experiments, that same pulse cleaner no longer worked in that capacity, being needed instead as an ordinary amplifier.

[4] This was with the pulse cleaner.

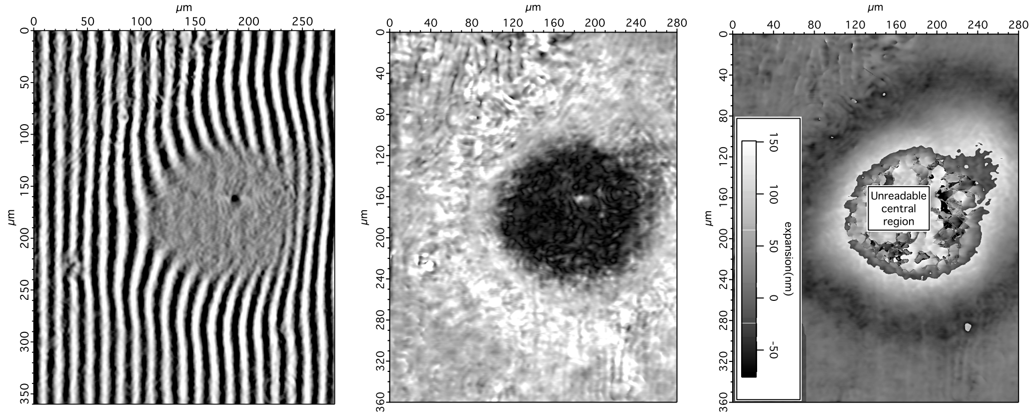

Figure 7.4: The back surface of a silicon source target irradiated by a system shot, with probe delayed -30ps relative to main. Left: Interference fringes on shot show clear deviation; Center: reflectivity, after dividing out the pre-shot reference image, shows strong a strong darkening region; Right: expansion calculated from the phase of interferometry minus the phase of a pre-shot reference image. In the darkest region, the phase cannot be interpreted. A “depressed” region in the phase map shows up as a dark halo on the phase map, of about 250 $\mu m$ diameter. The cause of this is currently unknown, although it could be a plasma effect, with sub-critical density plasma eminating from the central expanding region causing a negative phase shift in transmission.

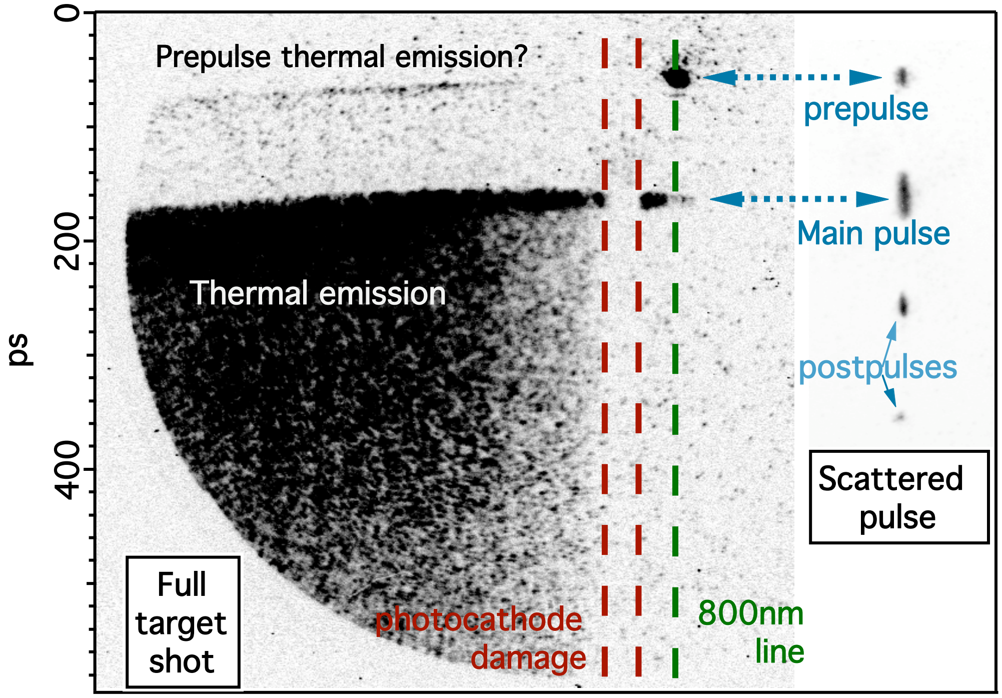

Figure 7.5: Evidence of substantial preulse from the spectral SOP. Two streak images are shown. On the left side is an actual system shot on a bare source target showing a precursor, with strong emission at 800nm and some emission at other wavelengths, followed by the expected termal emission. On the right side is the streak of the main pulse scattered off of a tissue, showing pre-, main, and post-pulses. The main pulse appears broad because its signal is saturated and therefore space charge effects took place within the streak camera.

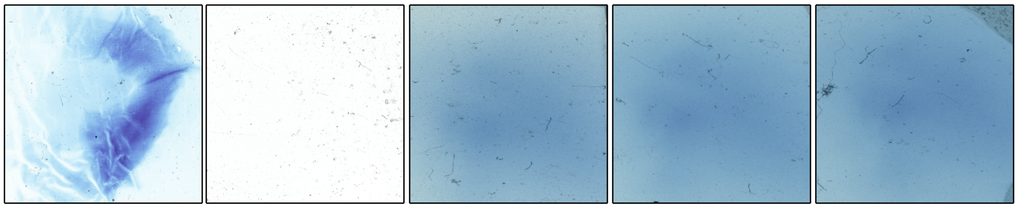

Figure 7.6: Scans of an example RCF stack. Left to right = top to bottom: First two films are Gafchromic HD film oriented with active layer towards target. Last four films are Gafchromic HS, which is similar to MD55. The first film shows protons and ions in a pattern that suggests a broken surface on the source. No protons or ions penetrate to the second layer. Consecutive HS films have approximately the same degree of exposure, which is attributed to electrons

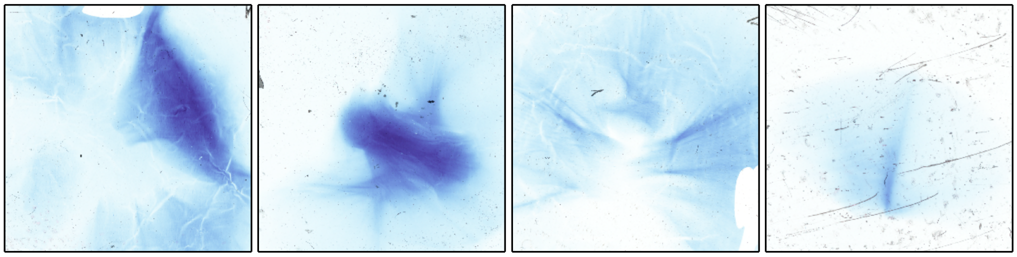

Figure 7.7: Scans of additional front layer films from a variety of system shots, this time on Au. Each film display a unique pattern apparently representing a disturbed surface at the time of proton generation.

are seen in the source target, indicating that it's been heated to eV temperatures. At the time of main pulse arrival, the source foil is heated to very high temperatures very rapidly, as expected.

As mentioned in section 5.4.1, evidence of a prepulse was also present in RCF measurements of the proton output from source foils. Figure 7.6 shows a full stack of six films deep. The films were wrapped in 10 $\mu m$ Al. The first two films are Gafchromic high density (HD) film with the active layer facing the target, and the last four films are Gafchromic high sensitivity (HS) film. HD films are asymmetric and have $< 1$ $\mu m$ of gel before their 6.5 $\mu m$ active layer, and 100 $\mu m$ of plastic behind. HS films have 100 $\mu m$ of plastic on either side of a 40 $\mu m$ active layer. The fact that no protons expose the second RCF film indicates that the cutoff energy is less than 4 MeV. Clouding of the HS layers is consistent with hot electrons, which have long range in the film material and thus deposit uniformly throughout the stack (invisible in the HD films because they have far less active material). The presence of significant electrons indicates that we would have expected a large amount of high energy protons, had the back surface of the source not been disturbed by the prepulse. Thus, significant electron exposure of the film stack without protons is considered another telltale sign of a prepulse[5].

### 7.1.3 Energy deposition from RCF films

The RCF scans shown previously in figure 5.28 were the best proton signals measured during the calisto run, and we use them to determine what type of heating we could expect in our sample foil, at most. The 10 $\mu m$ Al wrapped around the RCF stack is similar to the 10 $\mu m$ of Si material in our sample, and since we are interested mostly in the heating near the back surface, the dosage in the RCF stack should be closely related to the dosage at the back of a sample layer. From the OD of the film we obtain a dose in Gy (J/kg), which was shown in figure 5.28. That stopping power is given in MeV cm$^2$/g means that the dosage can essentially be scaled down based on relative areas being exposed. If we suppose that at a 100 $\mu m$ distance the protons are concentrated in a 100 $\mu m$ spot on the sample and came from a similar size source so that they haven't had a chance to spread out angularly yet, we can approximate that the visible dosage on the film would have been uniformly distributed within a $\sim 100 \mu m$ spot on the sample. With these assumptions, the films in figure 5.28 suggest that the Si source would dose a Si sample to $\approx .12 eV/atom$, while the Au source would dose to $\approx .36 eV/atom$. This is assuming that the forward-projected protons are responsible for the majority of the heating. However, it is possible that slower

---

[5] This comes from personal conversation with Dr. P.K. Patel at LLNL

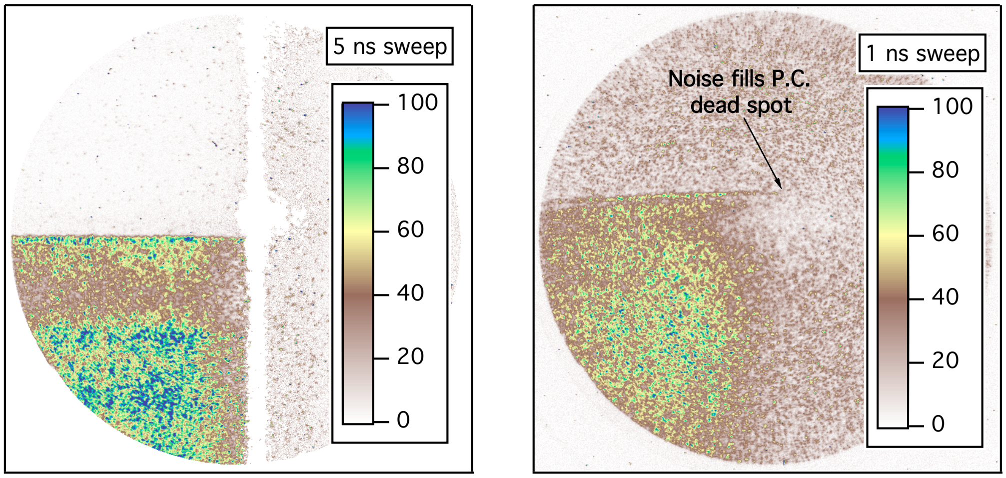

Figure 7.8: Raw spectral SOP images from Si samples heated by Au source targets. LEFT: 5ns sweep; RIGHT: 1ns sweep. The lower left quadrant of each circle contains the SOP data. The vertical dividing line is a result of the damaged photocathode. *Both images are shown on the same scale.* In the faster sweep speed, there is additional noise on top of the reduced signal. The noise level is confirmed by the presence of signal within the photocathode dead region, which would be completely empty in the absence of noise. The blanking (noise preventing) circuitry of the streak camera is different for the higher sweep rates, and may not have been functioning properly in this older streak unit.

protons released at wider angles than 20° could have contriubted to heating. These energy deposition levels are also so small that other sources such as bremsstrahlung and hot electrons might have significantly contributed to the total heating level. Indeed, the SOP seemed to indicate slightly higher temperatures than estimated here.

### 7.1.4 Spectral SOP results and interpretation

The spectral SOP (see section 5.5.6) successfully detected the thermal emission from proton heated samples for sweep speeds of 1 ns or slower. Two example images are shown in figure 7.8, which represent the highest measured temperatures, obtained using Au source foils. The lower left quadrant of each image contains the spectrally

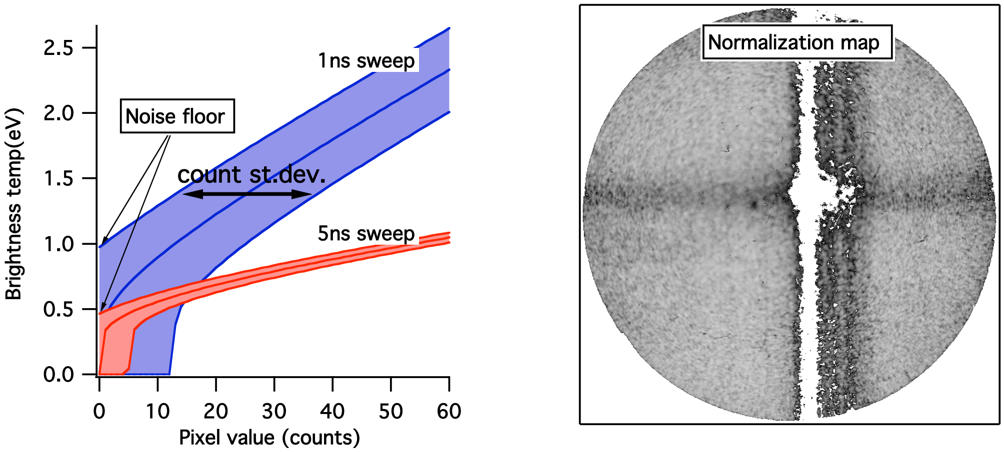

Figure 7.9: LEFT: Plot of photon counts to brightness temperature for the two images. Horizontal width of the bands indicate the standard deviation in noise level in regions where no signal should be present. This noise leads to a blindness to temperatures less than ∼ 1eV for the 1 ns sweep time and ∼ .5 eV for the 5 ns sweep time. RIGHT: The normalization map, used to account for photocathode damage and MCP dimming, was produced using uniform white light exposure at a slow sweep speed.

dispersed light from about 450nm to 700nm, cut off at the photocathode damage region. We attempted to time the streak camera so that it would capture the emission at the midpoint of the sweep, in order to see the initial rise in teperature across as much bandwidth as possible.

On our streak unit the signal to noise ratio decreased as the sweep speed increased not only because of weaker signal but also because of increasing noise[6]. As a result, shots at the fastest (300ps) sweep speed did not produce meaningful data. Figure 7.9 shows two aspects of the calibration proccess. First, the conversion of pixel counts on the streak camera CCD to brightness temperature (shown for 633 nm), based on a full calibration of the system, gives a picture of the minimum measureable temperature. The relatively low sensitivity and high noise levels of the

---

[6] According to Hamamatsu, the “blanking circuitry”, which controls against stray electrons, changes modes below 2 ns.

streak camera we were using limited us to about .5 eV and 1 eV for the minimum discernable temperature in 5 ns and 1 ns sweeps, respectively. This is based only on the standard deviation in the noise in a region of the sweep that should be blank (upper left quadrant in figure 7.8 images). The damaged photocathode and faded MCP are handled by a flatfield normalization map, obtained from uniform white light illumination in a slow speed sweep.

We find that the heated samples did reach temperatures near 1 eV. Scaled sweep images and lineouts of the example shots are shown in figure 7.10. The noise level and uncertainty in calibration prevented us from resolving the details of the temporal evolution. However we can place the temperature at 1 ±.5 eV, which is slightly higher than predicted from the proton RCF, but considerably lower than seen in the x-ray heating experiments.

### 7.1.5 Expansion measurements

Expansion was very slow compared to what was seen in the x-ray heating experiments (6.1.5), but still measureable for long delay times, and consistent with Si at $\lesssim$ 1eV. Apparently the heating was quite variable because the degree of expansion does not fit nicely on a single line, and most expansion measurements showed much slower growth than would be expected from a 1eV temperature (figure 7.11). In the experiment described in the next section, we employed a chirped pulse interferometer to get a full time history of expansion in a single shot.

## 7.2 Titan experiment

The Titan experiment was very successful in that it clearly produced and characterized in a clean and consitent manner states of volumetrically heated warm dense matter. Unlike the previous experiments, a single shot gave a complete time history of both the expansion and the brightness temperature from our proton heated tar-

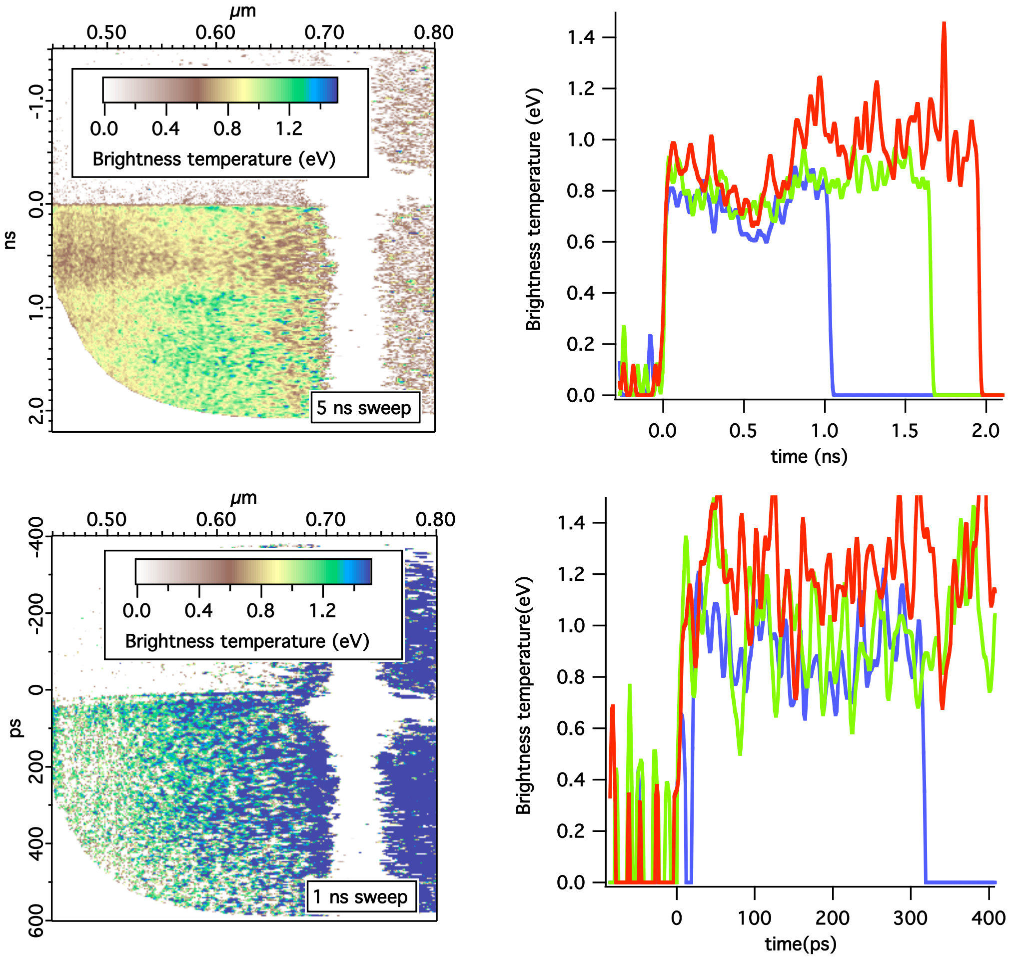

Figure 7.10: Scaled data from the two example spectral SOP measurements. IMAGES: Axes scaled to wavelength in $\mu m$ and time along the x and y axes, and brightness scaled to the brightness temperature calculated from pixel values. The images are not perfectly uniform along single-time lineouts in part because the emissivity of the target is not taken into account. PLOTS: Vertical lineouts of the data for 3 different wavelengths (Blue = 470 nm, Green = 532 nm, Red = 633 nm). In the 5 ns scan, an initial peak followed by a slow dropoff and a gradual rise can be seen. In the 1 ns scan, the noise is much greater and a temporal progression is harder to discern.

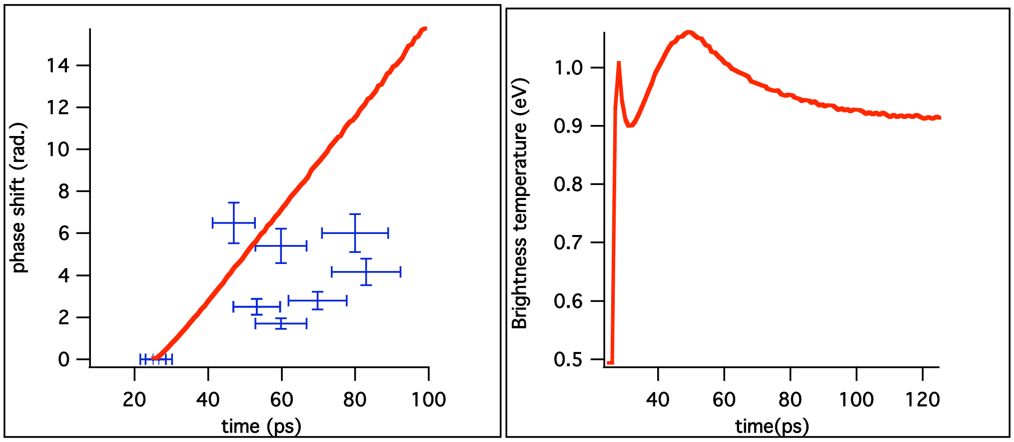

Figure 7.11: LEFT: Phase vs. time measured with a 400nm probe, with a Hyades hydro simulation of the same assuming a delay corresponding to the 200 keV proton arrival time. Right: The brightness temperature for this simulation.

get. With a measure of the proton spectrum, we were able to tie together all three measurements with a single free parameter.

### 7.2.1 Experimental layout

The Titan experimental layout is shown in figure 7.12 An independently compressed, partially chirped probe beam is delivered to the back surface of the target and timed by path length to be synchronized with the main laser pulse. The probe reflects from our target and is relay-imaged out of the chamber to the interferometer front end of the CPI, in which that image is relayed onto the slit of a spectrometer, giving the 1-D temporal, 1-D spatial image of the target back surface (sec. 5.3.7). A 90/10 beamsplitter takes a small fraction of the beam to monitor the image plane that is projected on the slit, and thus gives the 2D image. This diagnostic is only used to verify alignment however, since the fringes from the chirped pulse will be blurred on a simple 2D image. We discovered that a wall of lead bricks were neccessary to protect the CCD from malfunction on system shots, as discussed in section 3.2.4.

We set up a monochromatic SOP with its collection optic above the plane

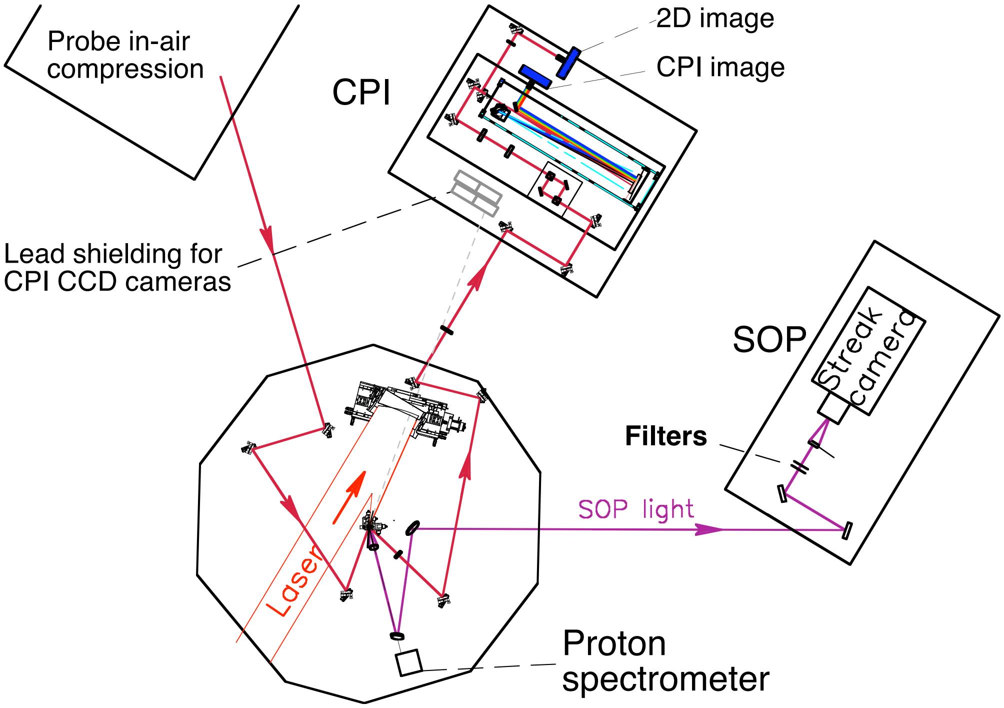

Figure 7.12: Top overview of the Titan experimental layout, described in the text.

as described in section 5.5.4. We used a 1:1 magnification onto the C7700 high dynamic range streak camera. The sensitivity of this camera was such that filters of 1.5 ND, in addition to the 10nm bandwidth 468nm interference filter, were needed to keep signal below saturation on system shots.

A proton spectrometer, fielded by Dr. H. Chen also gave data that was used in our analysis. It was aligned directly behind target normal and several feet behind the target. Other diagnostics on this experiment incude an array of electron spectrometers encircling the target at the same distance as the proton spectrometer, a Von Hamos spectrometer[7], behind the target and below the target plane, tuned to Al $K_\alpha$ , and a streak-camera based ion time of flight spectrometer still in development.

Although not depicted here, a series of alignment beams aided in finding best focus. The stable-breadboard design of the Titan target chamber (sec. 3.2.4) made alignment reliable and consistent.

### 7.2.2 Laser conditions

At the time of our experiment, Titan was capable of delivering 150 J in a ~600 ps pulse at 1 $\mu m$ . An f/3 parabola achieved $< 10\,\mu m$ focal spot diameter. We ran the laser at 100 J to reduce the turnaround time from nuclear activation within the chamber and to reduce the odds of electromagnetic pulses disabling our electronic diagnostics. The probe beam was left partially stretched to approximately[8] 158 ps.

### 7.2.3 Target design

Our targets were designed and fabricated at LLNL. As shown in figure 7.13, the target window is etched out of a $400\mu m$thick wafer of Si. The $400\mu m$thickness serves

---

[7] These diagnostics are part of a separate and ongoing experimental campaign to measure proton stopping power in warm dense matter.

[8] A 60 ps pulse was desired but a miscalculation involving a previous experiment that used a stretched main beam was not realized until setup and timing were already done.

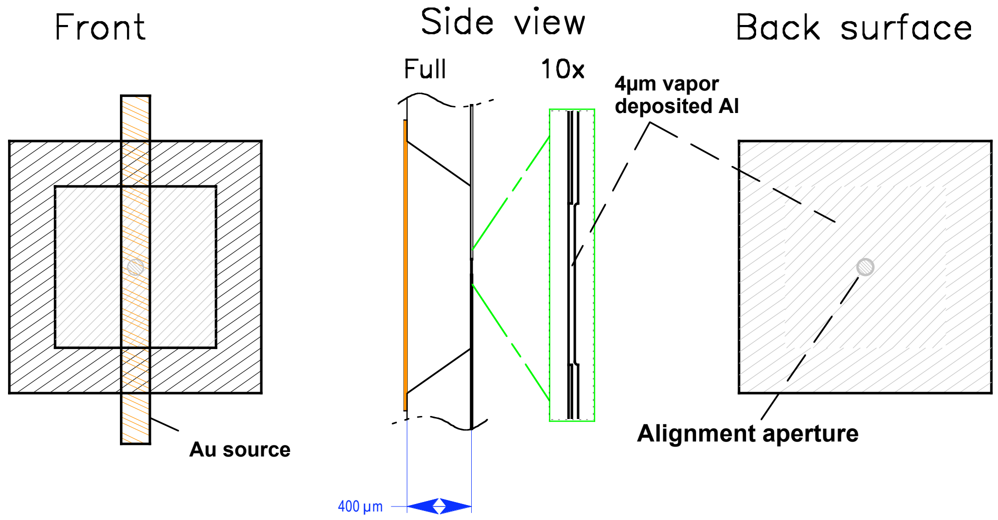

Figure 7.13: The target window and source foil for the Titan experiments. The window was 1 mm across and 400 $\mu m$ deep. The back surface was layered with .5 $\mu m$ Au below 2 $\mu m$-4 $\mu m$ Al, except in the aperture region, where the Au was first etched away. The Au source foil was thin enough so that, with pump laser incident at an angle, the aperture could be brought to the focal position of the laser, allowing us to align the target using the encoded target manipulation stages.

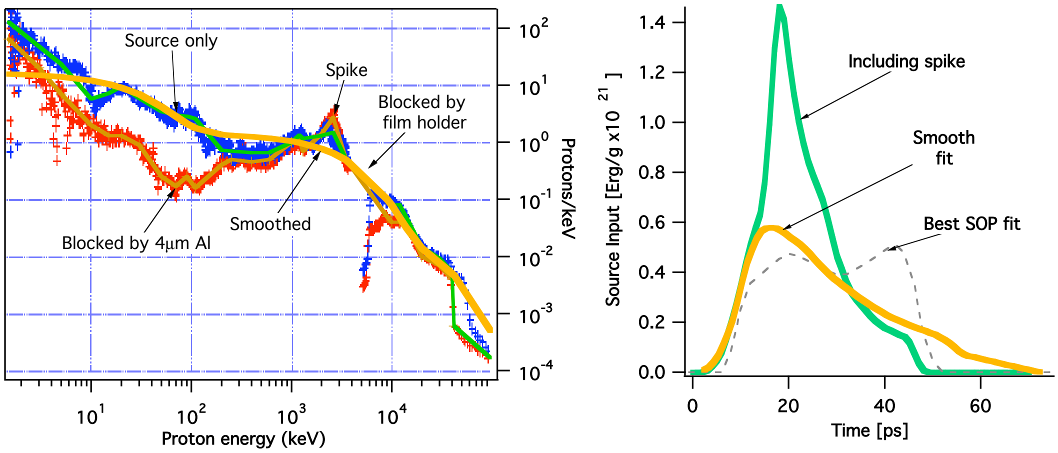

Figure 7.14: LEFT: Two proton spectra measurements from system shots on Titan. The red trace is from a shot in which a sample layer was present; the blue curve is from a bare sample shot. They are consistent with the absorption of the sample layer. A blocked region and associated spike are labeled. RIGHT: The implied time history of heat deposition from the smoothed and traced spectra, and an artificial proton spectrum that best fit the SOP.

as the source-sample spacing, as the source foil was a thin strip of 17 $\mu m$ thick Au. The sample started with a backing of 500nm thick Au into which a 100 $\mu m$ diameter alignment aperture was etched. Between 2$\mu m$and 4$\mu m$of Al was then deposited over the back surface. The foil inside the aperture wrinkled, and so the 100 $\mu m$ outline was visible on both sides, aiding greatly in alignment of both the SOP and the FDI.

### 7.2.4 Proton spectra

We did not use proton RCF on this experiment, but it was well-established that excellent proton beams could be produced on Titan, darkly exposing several layers in a film stack with a circular proton beam, using ∼15$\mu m$Au targets[Ng07]. We instead used a magnetic proton spectrometer with an image plate detector to produce a spectrum from 10 keV to 100 MeV.

Two example proton spectra are shown in figure 7.14. We found these spectra

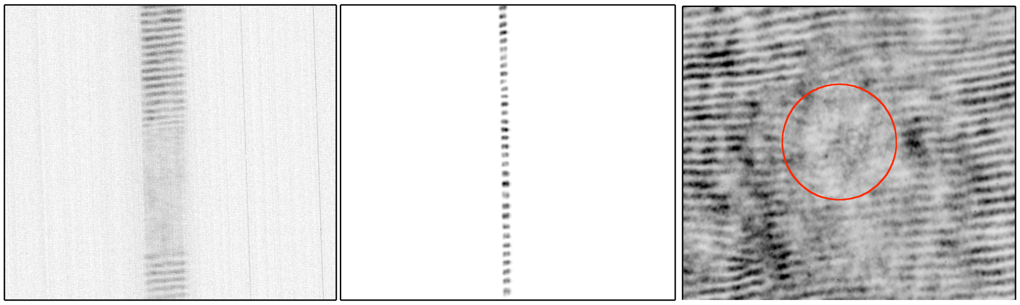

Figure 7.15: Some example images from the setup and alignment of the Titan CPI. LEFT: The target alignment aperture lined up with a partially opened slit, illuminated with CW light to form an image on the CPI camera. CENTER: Closed slit, illuminated with CW light. RIGHT: On-shot output of the 2D imaging camera, showing the extent of the plasma.

to have a common "spike" feature at about 2 MeV, adjacent to a gap in the spectrum at about 4 MeV caused by the film holder. We believe that the spike is associated with the film holder gap and not an actual peak in the proton spectrum. For this reason we use a 3-Maxwellian fit to the proton spectrum in our simulations. This assumption about the spectrum is supported by our simulations, where the proton temporal profile of the smoothed fit gives much better agreement with our other diagnostics. It is also reasonable because a peak in the spectrum is not expected, and if it were real, we would hardly expect it to appear at the exact same energy every time.

### 7.2.5 CPI results and interpretation

In figure 7.15 are shown some setup images from the Titan CPI, showing the aperture and a closed slit illuminated with CW probe light, as well as an image from the 2D CCD camera, which allowed us to verify after a shot that we were aligned to the central region of proton heating.

The CPI was successfully timed and aligned to show the expansion of our heated target foil, including the intial onset of heating. Some examplle raw inter-

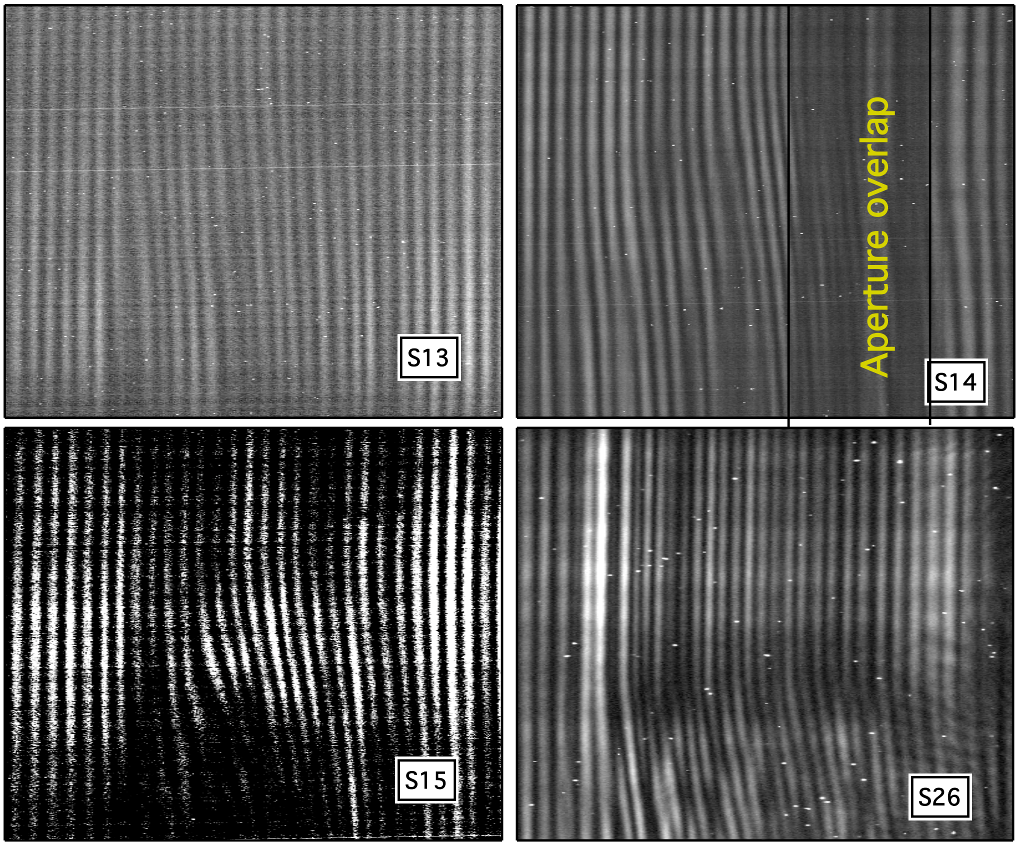

Figure 7.16: Examples of raw CPI data. Time goes from top to bottom on these images, and one can see vertical fringes bending to the right, indicating expansion with time. The height of each image represents about 75 ps.

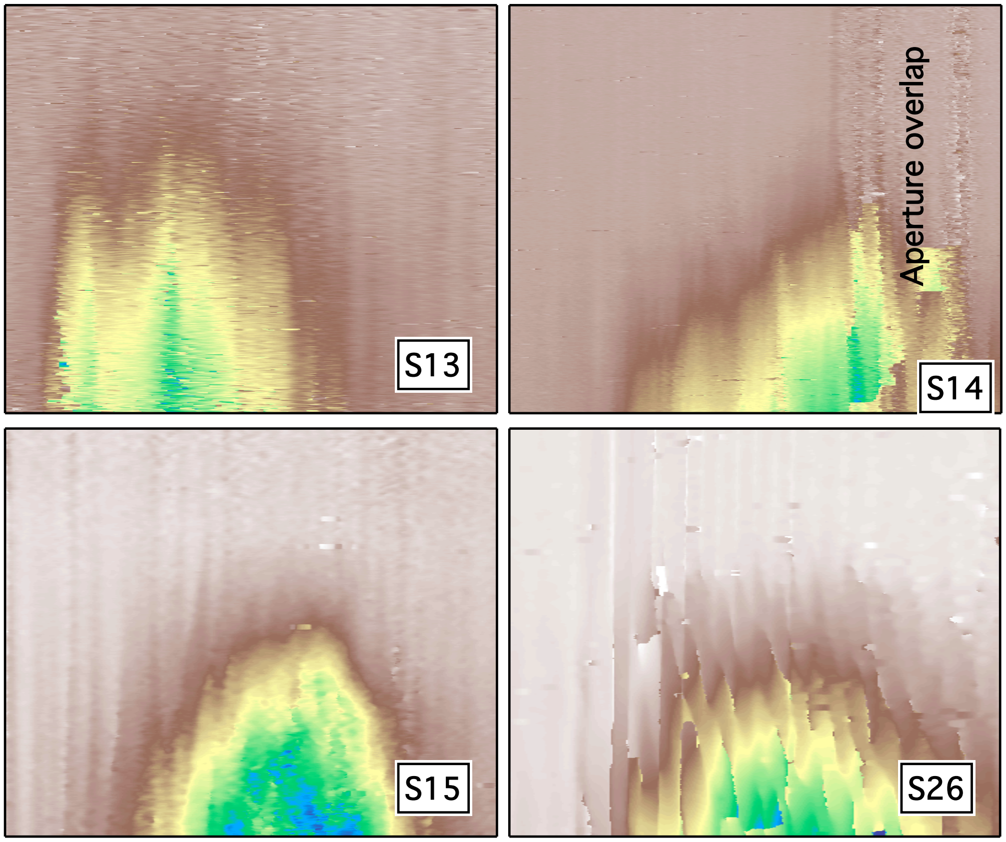

Figure 7.17: Unwrapped phase images for the CPI. Some mottling is evident from imperfect phase unwrapping caused by regions of poor fringe contrast, but these show up only at late times and are clear $2\pi$ phase jumps that are easily accounted for.

ferograms are shown in figure 7.16. In S14 we see the disadvantage of having the alignment aperture on the target itself: Inadvertently leaving it within the range of target that was heated, we not only created an unreadable region in the interference image, but also produced a region where the target is hotter, leading to a strong disagreement between the SOP and CPI.

In figure 7.17 are shown direct unwrapped phase maps of the interference images, using also the pre-shot reference images. A nice picture of a target that is expanding with time, with a clear region of fastest expansion can be seen in all

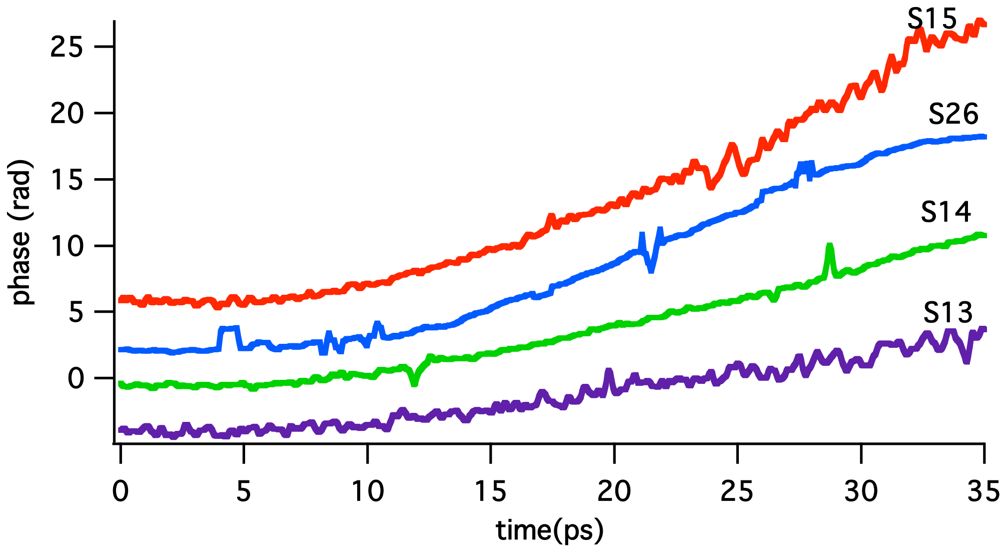

Figure 7.18: Vertical lineouts reconstructed [GAR+01] to give phase shift as a function of time. The curves are vertically offset. Labels on each curve are the shot numbers for the Titan run.

images.

In figure 7.18 are the phase shift as a function of time from vertical lineouts of the CPI phase, following reconstruction [GAR+01]. Except for a few blips of noise, the expansion is rather smooth, with different rates on different shots.

When properly aligned and calibrated as in our Titan shot run, the CPI gives in a single shot what it would have taken a series of shots to achieve with the 2-D interferometer used in previous experiments. Setup is considerably more complicated, but the advantage is clear: from the 4 shots seen above, the expansion rates were different, and were not proportional to laser energy. Indeed, S13 showed the slowest expansion from the second highest laser energy at 103 J, while shot 15 had the fastest expansion (tied with S26) with the lowest laser energy at 86 J. S26 had 93 J while S14 had 108 J. If these shots had been used to produce single delay 2-D expansion images, there would have been a great deal of scatter, as was seen in many of the previous experiments.

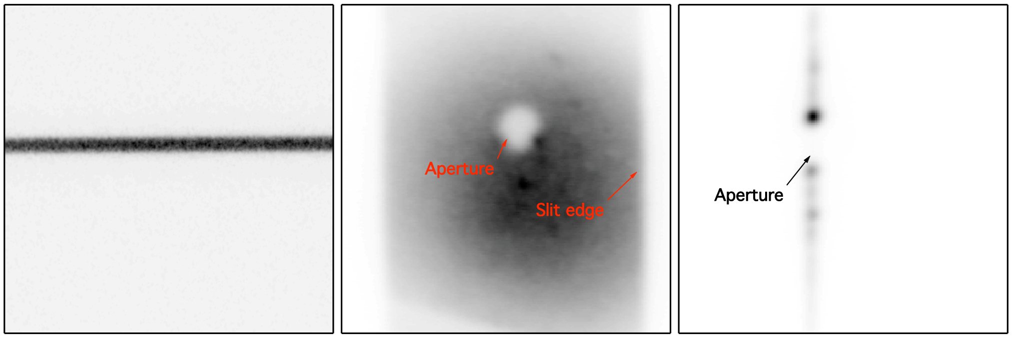

Figure 7.19: Images from the setup of the SOP on Titan. LEFT: An example streak of CW light from calibration sweeps, exhibiting excellent signal-to-noise ratio and dynamic range. CENTER: An image of the 100 $\mu m$ aperture at target chamber center, illuminated by diffuse white light, in focus mode with slit wide. RIGHT: Slit closed around aperture, a part of the alignment procedure.

Since our vacuum gap is large and velocity dispersion causes the protons to deposit energy over a rather long time period compared to what we would prefer, it is convenient that our temperature measurement, the SOP also gives a full time history on a single shot.

### 7.2.6 SOP results and interpretation

As mentioned in section 5.5 the C7700 streak camera on Titan had $10^3\times$ better sensitivity and 10× better dynamic range than the previous model of streak camera used, as well as a completely uniform detection plate and photocathode. Figure 7.19 shows some images from the setup of the streak camera, showing calibration and alignment.

In figure 7.20 are shown some SOP streaks from various system shots. The height of each image corresponds about .96 mm in the target plane. The spatial extent of the heated regions were similar to 330 $\mu m$ across (FWHM), comparable to the 400 $\mu m$ spacing between source and sample, and in agreement with the spatial scale measured on the CPI. All system shots were taken with a 500 ps sweep window,

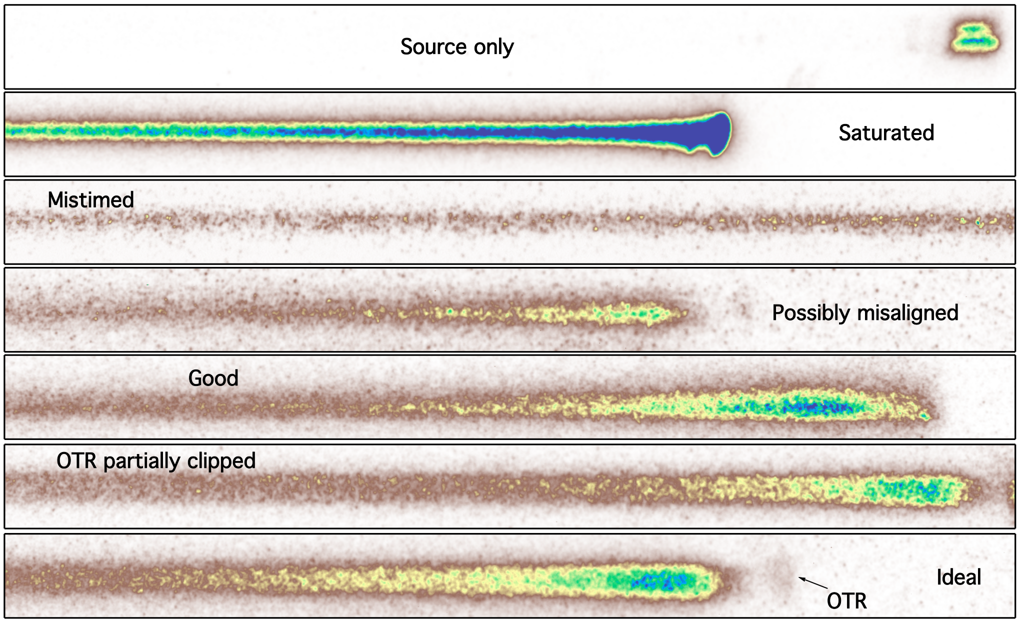

Figure 7.20: Example streak images on a system shot. SOURCE ONLY: 17$\mu m$source foil with no sample foil. A very large amount of ND is used and we see that the emission lasts only a short time but is much brighter than the other streaks shown here, accounting for the ND. SATURATED: If insufficient filtering is used (in this case 0.5 ND compared to 1 and 1.5 ND used on the other shots), the SOP signal will become saturated an unuseable. MISTIMED: We must time within a window of 500ps, which is easy to miss with electronic timing if the path length from the fast photodiode is off by even a cm, or something affects the rise time of the signal pulse. POSSIBLY MISALIGNED: This image appears good but may have been misaligned: the spatial extent of the sweep is narrower than other shots. GOOD: A well aligned and timed shot. However the OTR is strong and blurs in somewhat with the main shot. OTR PARTIALLY CLIPPED: The full thermal emission is seen, but the OTR is partially clipped at the edge of the image. IDEAL: A shot in which the full OTR and thermal emission can be seen.

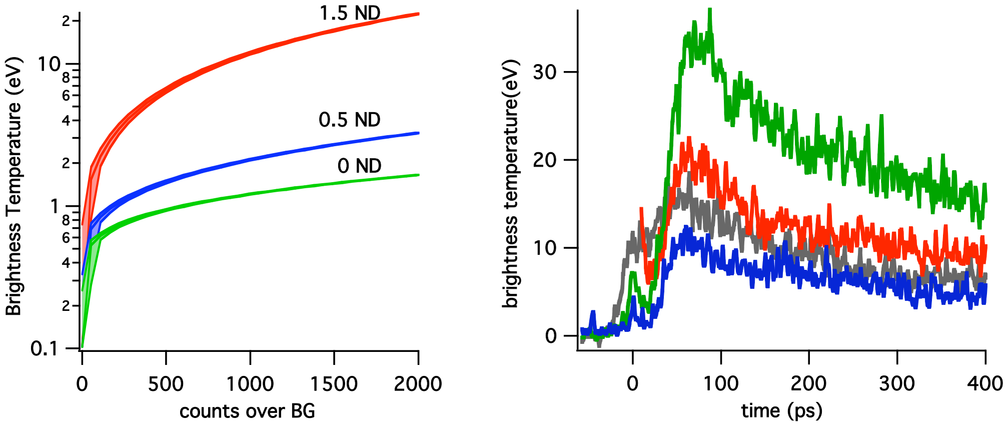

Figure 7.21: Interpretation of the SOP as brightness temperature. LEFT: The equivalent figure to 7.9, showing much less effect from background noise, and at a faster sweep speed. The C7700 blanking circuitry functioned properly, keeping the signal to noise ratio low at the fastest sweep speed. RIGHT: Example lineouts from various streak images, showing an OTR pulse at time 0 followed by quickly rising thermal emission. Note that in the grey curve the OTR is very strong and begins to blur with the second peak.

shown in its entirety in each of the images in the figure.

Figure 7.21 shows the interpretation of the SOP images as brightness temperature. Electron noise does not significantly affect our measurements as it did in the Calisto SOP, and we are subject only to the uncertainty in our calibration. Taking all factors into account, that uncertainty was $\sim 15\%$. This higher sensitivity would allow for higher magnification in future experiments of this type.

### 7.2.7 HYADES simulation comparison

We test our data against the predictions of some of the leading equations of state by way of the 1-dimensional radiative Lagrangian hydrodynamic code Hyades [LL94]. The code is designed to deal with dense, cooler plasmas, and can operate within the WDM regime so long as a defined EOS is available. Available in our copy were the QEOS [MWYZ88] and the Sesame EOS tables for various materials [Mon84], as well as several ionization models. In simulating our experimental results, we had three parameters:

1. Equation of state model. Our available EOS models were ideal gas, QEOS, and LANL Sesame table # 3718 for Al.
2. Ionization model. The default model of Saha ionization [ZBD00], but a Thomas-Fermi model is also available. The QEOS uses its own version of the Thomas-Fermi model, precluding selection of an alternate model.
3. The total number of protons in the measured spectrum (figure 7.14) to use as an energy source.

### Determining the proton number

This last item was achieved for each combination of EOS and ionization model by entering the protons as a timed energy source into the simulation. Protons can be modeled as a source of energy to the electrons of the sample material. Based on proton stopping power [BCZC05], we calculated the energy deposition with time and depth into the foil producing a plot such as the one shown in figure 7.14, multiplied by a constant, and converted it into the Hyades format. For each EOS and ionization model, we changed this constant until the calculated brightness temperature (see section 5.5.1) best matched the data from our SOP. As seen in figure 7.22, the temporal profile of brightness temperature emission can be matched, by iterating the scalar multiple of proton number in each of the models, but only if a smooth three-Maxwellian fit to the proton data is used: if a direct trace of the proton data, including the aforementioned "spike," the simulation fails to converge to within error of the data.

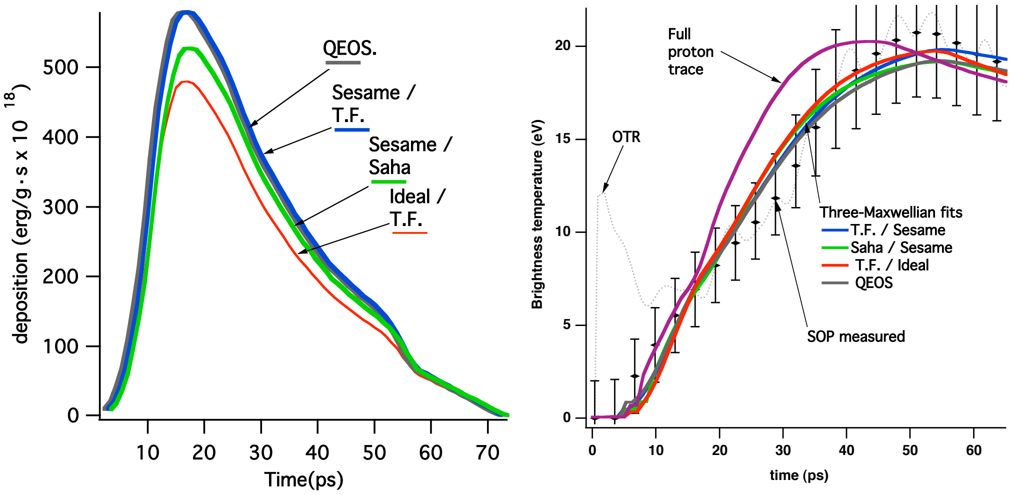

Figure 7.22: Matching the measured brightness temperature to Hyades simulation for various models. LEFT: Energy deposition profiles used for the various models (see figure 7.14 for "full trace"). The difference is significant, as the SOP data would not be matched if a different energy deposition profile were used (e.g., Sesame/Saha using the QEOS dose rate profile). RIGHT: Various models and data for the brightness temperature. OTR is removed from the data by a Gaussian fit. Error bars on the data represent the range of the noise plus the error in our brightness temperature calibration (20% at the peak temperature).

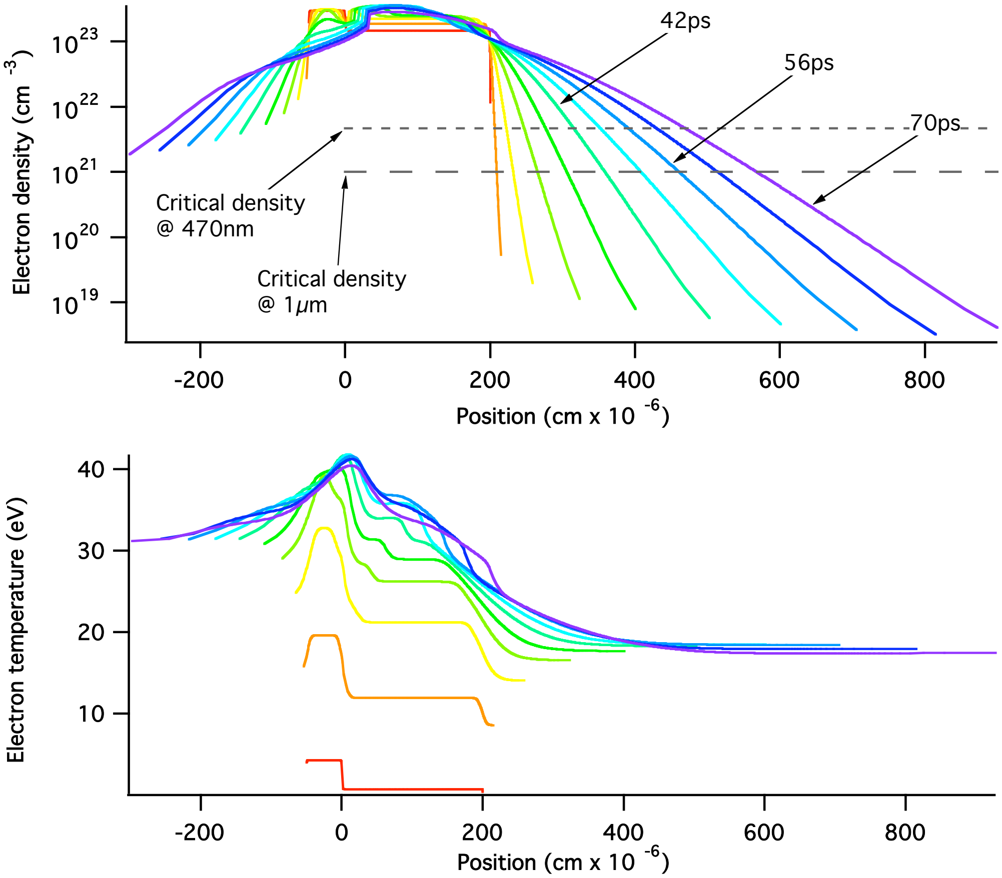

Figure 7.23: Time slices from the Hyades simulation of S15, in 7ps intervals. TOP: Electron density vs. position in the target normal direction. Left of the 0 position is the 0.5 $\mu m$ Au, which can be seen as an electron density that is initially higher than the Al. BOTTOM: Electron temperature vs. position. The Au is more strongly heated because it absorbs the protons more strongly. However the heat wave from the Au never reaches the position of the critical density surface.

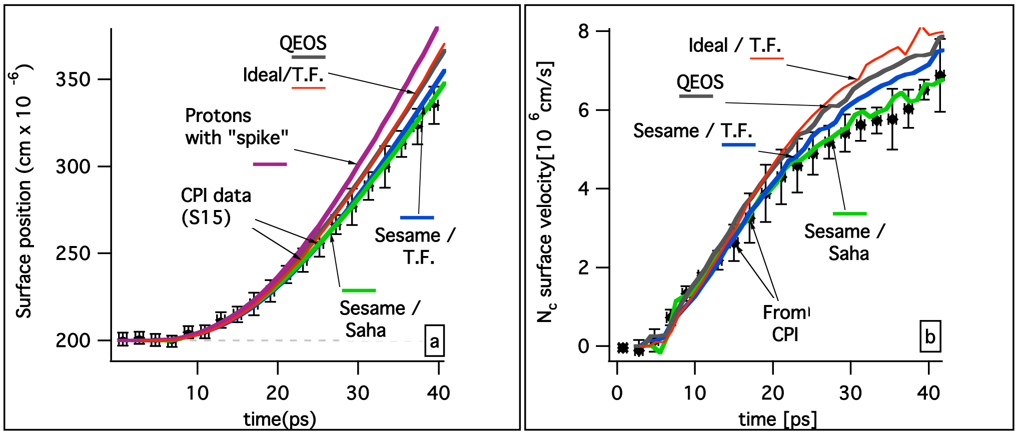

Figure 7.24:

### Agreement with CPI

Once the simulation is run to produce the match shown in figure 7.22, the simulation is already completely determined and no tweaks can be made to fit the CPI data. Thus the physics must be correct, specifically the EOS model must predict the correct pressures and ionization state to give the right prediction of the CPI measurement, given a foil that emits consistently with the SOP data. This is a strong constraint, but if it doesn't work then there is something wrong either with our data or the simulation.

We find that the simulation can in fact fit both the CPI and SOP data with energy input from the measured protons, and that the degree of agreement depends on the specific model used. The expansion simulation and data are shown in figure 7.24. We see that when Hyades is run with the Sesame Al EOS and its default ionization model (based on Saha), we find the best match to our expansion data. The fit is also good when the optional Thomas Fermi ionization model is used, although this fit seems to break down at later times. QEOS seems to diverge the most, although it is also within error for the first 20 ps of expansion.

To give a quantitative description of how well the model fits our measured data, we consider the statistical correlation between the data, and the simulation curves, which are treated as the ideal function. We can calculate the $\chi^2$ figure across the data points shown, and compare this to the $\chi^2$ of hypothetical data that matches perfectly the *shape* of the simulated curve, but is scaled by some percent. The value of this percentage which gives the same $\chi^2$ figure as the actual data becomes our figure of merit. In this way, we find that we were able to match the SOP data within 10% for all models in the first step, and that the expansion velocity was accurate to within 7% for the Sesame model, and 20% for the QEOS model. If we restrict our view to the first 20 ps of expansion, these later two numbers reduce to 2.5% and 20%, respectively.

## 7.3 Sandia Petawatt experiment

We have taken the first steps towards establishing this experiment at the 100 TW target chamber at Sandia national laboratories. We built a new CPI similar to the one at Titan, but using an inverting Michelson interferometer instead of a Mach Zehnder on the front end. The facility has two Hamamatsu streak cameras, a C7700 identical to the one used on Titan, and a FESCA 200 sub-picosecond unit.

### 7.3.1 Targets

Our targets were 3 $\mu m$ Al sputtered on a thin polished Si backing which was subsequently etched away. The windows looked quite similar to the targets used on Calisto, but with Al as the sample instead of Si. The windows were 2 mm across, and at this size the sputtering and etching proccess did cause them to warp to some extent. With the ability to take reference probe images this wasn't too much of a problem, but flatter targets would have been preferable. This could be obtained with a slower etching proccess or smaller windows. The source foil was 20 $\mu m$ Al foil, spaced 100 $\mu m$ from the sample.

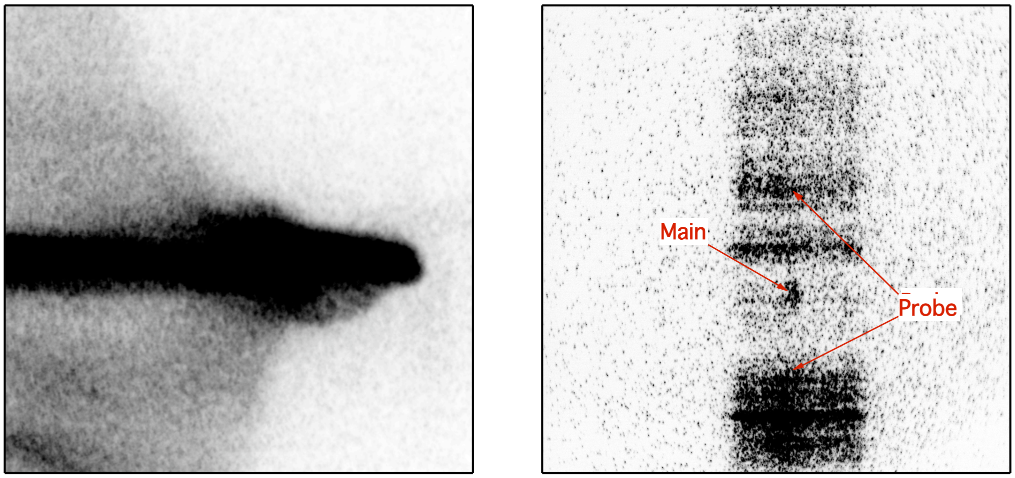

Figure 7.25: Images from the Sandia SOP. LEFT: Replacing the narrow band interference filter with a 650nm SWP filter on a system shot led to a saturated signal, whereas the interference filter apparently let in insufficient light. RIGHT: By shooting the main pulse through an aperture and reflecting the probe pulse into the streak camera, we were able to show the relative timing, aiding with the setup of the CPI.

### 7.3.2 SOP

As discussed in section 5.5.3, we were unable to obtain SOP data using the FESCA 200 streak camera. The lower photocathode sensitivity to visible light combined with the higher f/# (5 vs. 3 for the C7700 SOP) combined such that obtaining the same signals as on Titan would require a 1.9dB increase in the light signal. However, since we were using 1.5 ND on Titan and seeing ample signal, we still expected to see some sign of a streak signal on the FESCA, albeit not at the fastest sweep speed. By monitoring the gate signals of the streak camera on shot, using an oscilloscope in an electromagnetically isolated box, we determined to a fair level of certainty that the triggering on system shots was functioning properly, and hence it was most likely insufficient light signal that caused the SOP diagnostic to fail. Figure 7.25 shows that we actually get too much light if we don't filter, using only an SWP to out the fundamental, rather than an interference filter. Also in the figure is an image

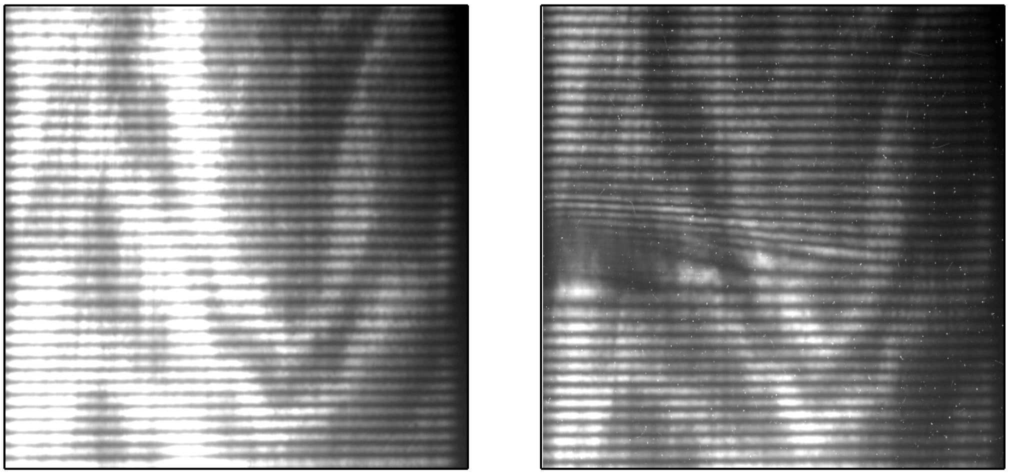

Figure 7.26: Example raw CPI images. The light level was only slightly lower for the system shot here, as the pointing stability problem was nearly resolved and we also minimized the time between taking the reference shot and the system shot.

depicting the streak camera's utility in finding the relative probe/main timing.

There is a C7700 available at Sandia. It would also be possible to utilize the FESCA 200 as an SOP streak camera at its fastest speed using lower wavelengths, as they will be brighter in thermal emission, and the FESCA has a sensitivity peaks at 320 nm.

### 7.3.3 CPI data

The CPI probe beam was chirped to 35 ps and reflected at an angle of 15° from normal. Example reference and shot images are shown in figure 7.26. An alignment stability problem which caused the beam to drift and greatly reduce the illumination on a system shot is being addressed, and was mostly solved by the end of the shot run. The shots showed expansion rates comparable and slightly higher than what was seen on Titan (figure 7.27). Reference phase subtraction was less successful in producing a flat background than in the Titan shot runs, probably because of the probe beam pointing instability. However from the expansion it is quite clear that

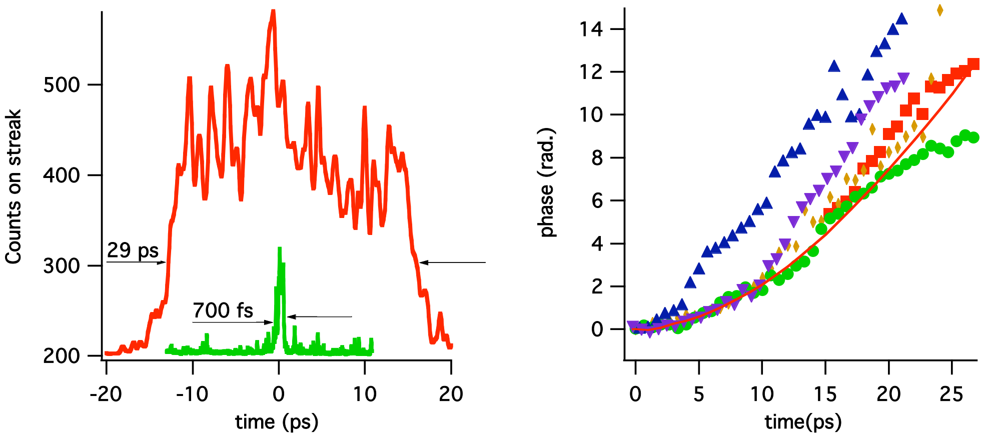

Figure 7.27: LEFT: Timescales of the probe and main pulse as measured by the FESCA 200 streak camera. RIGHT: Expansion vs. time for several system shots (points), and a Hyades simulation with similar conditions to those used in the Titan analysis, exhibiting a peak electron temperature >20 eV (smooth line).

we were reaching temperatures that exceeded 20 eV.

### 7.3.4 Prospects for the Sandia experiment

The CPI diagnostic remains intact, stored at Sandia. There are many ways in which this experiment could be improved in future runs.

- A functioning SOP can be made with the C7700 streak camera. With a good body of data from the C7700 it could be possible to determine a regime in which the faster FESCA could operate.

- With the replacement of a few optics, the probe beam can obtain sufficient energy for the CPI to be run at $2\omega$, allowing for probing of a higher density critical surface, and the possibility of using Si as a sample material. The probe pointing stability will have to be improved before this step is taken.

- A good measure of the proton spectrum turned out to be an integral part of the analysis of the Titan data. Time did not permit us to use it, but a simple

Thompson parabola was available at Sandia, and such a diagnostic would be very useful in understanding what's going on in the shots.

- With a slight change in the imaging, both images from the inverted Michelson could fit on the CCD at once, giving either redundant expansion data or reflectivity.
- The expansion data show some signs of the influence of slow ions. A thick barrier layer could help to prevent that. Technically that barrier could simply be the Si substrate that the Al is deposited onto; we could simply leave some of it instead of etching it all away.

With refinements on the Sandia experiment, we are sure to improve on the results seen at Titan. The foundation is certainly there to build up a good body of data for experimentally testing the EOS of isochorically headed Al.

# Chapter 8

# Conclusions

The goal of this work has been to experimentally probe isochorically heated warm dense matter to test the equation of state. Specifically, we looked at two techniques for heating a sample foil with ultrafast laser generated secondary radiation from a nearby source foil, $K_\alpha$ x-rays and MeV protons. Characterizing the internal energy or temperature, together with the hydrodynamic expansion, we produce data that tests the well-established equations of state in the difficult pressure and density range of warm dense matter.

## 8.1 X-ray heating

The prospect of heating with laser generated x-rays was attractive for two reasons. First, because the $K_\alpha$ and $K_\beta$ lines are very sharp, the photons travel in a straight line path to a detector, and their absorption in matter is well-understood, it is in principle a simple task to back out the internal energy deposition from a measurement of the x-rays. Second, because $K_\alpha$ and $K_\beta$ are driven by the ultrafast laser pulse and travel at the speed of light without velocity dispersion, the x-rays would in theory provide a sub-ps pulse, making the heating highly isochoric. I showed in chapter 4 that modeling based on the literature of laser coupling into hot electrons traveling through a foil indicated that sufficient K$_\alpha$ flux to heat into the 1eV range was possible on a 10 J laser, but only if our source and sample foils were within about 30 $\mu m$ of each other, and the focal spot of the laser could be smoothly defocused to a spot with 10s of $\mu m$ diameter, much larger than the typical few $\mu m$ diameter spots of typical ultraintense laser systems. I also highlighted the importance of using the right combination of source and sample materials.

Some potential issues were highlighted in chapter 4, namely that, as laser energy increases, our ability to heat low-Z materials such as Al using K$_\alpha$ does not improve substantially above about 10 J because the laser spot must increase proportionally, decreasing the intensity for a given K$_\alpha$ output. For higher energies, higher-Z materials would be more suitable for K$_\alpha$ heating experiments of this kind. However, it was noted that the relative flux of bremsstrahlung would increase in the higher-Z regime, making the experiment less clean, even when considering x-rays only and ignoring other factors.

In chapter 6, we saw that proton heating dominated even though we defocused to nominal intensities outside of the optimal proton generation range (although we could not produce a very clean focal spot at these sizes). We further saw that the K$_\alpha$ output was weaker and more spread out in time than expected.

I suggested that, to go forward with the x-ray heating experiment would call for higher energies, cleaner and larger focal spots, and higher-Z materials than were attempted in this experiment. Furthermore, contaminant layers must be cleaned from a source foil to prevent proton production. The rapid falloff of K$_\alpha$ intensity with distance limits our options for getting creative. Because K$_\alpha$ sources are useful for many other applications I suggest that they should still be studied on higher energy laser systems, but not with isochoric heating as a primary goal.

## 8.2 Proton heating

In switching to proton heating we lose the two advantages which were ostensibly held by $K_\alpha$ heating. The proton energies are distributed over a smooth energy distribution and vary along their spatial profile, and diagnostics of the proton beam would not determine the energy deposition to sufficient precision. Thus it was necessary for us to acquire a high quality ultrafast streak camera for an optical pyrometry diagnostic, a difficult task. Velocity dispersion meant also that our heating source was less perfectly instantaneous. However, protons allowed us to reach much higher temperatures than $K_\alpha$ heating could have, and this lends a great deal of flexibility to the experiment.

In the final proton heating experiments, we employed single-shot time resolved measurements of the heated sample. Together with a measure of the proton spectrum, we were able to correlate these measurements beautifully through comparison with a 1-D hydrodynamics code running on various equation of state models. We found that the most carefully formulated and well-regarded EOS, the SESAME EOS, together with the most detailed ionization balance model, based on Saha ionization, best fit our measurements.

There are many ways in which one could expand upon the proton heating experiment. First, by varying the thickness of our sample layer, or equivalently by placing various thicknesses of foil at the front side of the sample, we can both vary the degree of heating by protons and reduce the influence of late-arriving slower protons. Using a gap closer to 100 $\mu m$ rather than the 400 $\mu m$ used on Titan would also help in producing shorter heating times.

Further refinement of our diagnostics can occur as this experiment continues. In particular, more and various calibrations of the SOP diagnostic would help reduce the error in the temperature measurement. Further cleaning up and stabilizing of the probe beam would improve the quality of interference fringes in the CPI, improving precision in the expansion measurement.

Aside from improving on the experiment in its current form, there are several other diagnostics which could be usefully added. For example, we will be interested in probing parts of the plasma profile than the critical density surfaces we were limited to in our experiment. This can be done by looking at different wavelengths, e.g., with harmonics of the probe beam (maybe even simultaneously), and UV wavelengths in the streak camera. We can also observe the hydrodynamic expansion of the isentrope at later times ($\sim$ 100ps) by profilometery, as suggested by Foord, *et al.*[FRS04], either through proton or x-ray radiography. Also, by using a spherically shaped source target [PMK+03] would allow us to reach still higher temperatures, at which the $K_\alpha$ spectroscopy temperature determination technique of Hansen, *et al.*[HEF+07] could be employed.

Finally, the optical properties of WDM [PHK+06] are also very interesting, and we could study these at the wavelength of our SOP, to improve our temperature measurement, and also at high harmonics, using HHG from gas jets .

## 8.3 Conclusion

In conclusion, we have taken steps towards further improving our knowledge of the equation of state in the important and difficult regime of warm dense matter. As the body of data across the warm dense matter regime expands, we will come closer to our goal of filling that void, improving both our understandings of the inner workings of warm dense matter, and our ability to understand and the behavior of systems that pass through this regime, which, among other things, will be a step in the direction of fusion power.

# Bibliography

[AAB$^+$06] S. Amoruso, G. Ausanio, R. Bruzzese, L. Gragnaniello, L. Lanotte, M. Vitiello, and X. Wang. Characterization of laser ablation of solid targets with near-infrared laser pulses of 100 fs and 1 ps duration. *Applied Surface Science*, 252(13):4863–4870, Apr 2006.

[Abe59] R. Abe. Giant Cluster Expansion Theory and Its Application to High Temperature Plasma. *Progress of Theoretical Physics*, 22:213–226, August 1959.

[ADK86] M. V. AMMOSOV, N. B. DELONE, and V. P. KRAINOV. Tunnel ionization of complex atoms and atomic ions in a varying electromagnetic-field. *ZHURNAL EKSPERIMENTALNOI I TEORETICHESKOI FIZIKI*, 91(6):2008–2013, Dec 1986.

[AFA$^+$06] P. Antici, J. Fuchs, S. Atzeni, A. Benuzzi, E. Brambrink, M. Esposito, M. Koenig, A. Ravasio, J. Schreiber, A. Schiavi, and P. Audebert. Isochoric heating of matter by laser-accelerated high-energy protons. *Journal De Physique Iv*, 133:1077–1079, 2006.

[APM$^+$04] M. Allen, P. K. Patel, A. Mackinnon, D. Price, S. Wilks, and E. Morse. Direct experimental evidence of back-surface ion acceleration from laser-irradiated gold foils. 93(26), 2004. 265004.

[APW+06] T. Ao, Y. Ping, K. Widmann, D. F. Price, E. Lee, H. Tam, P. T. Springer, and A. Ng. Optical properties in nonequilibrium phase transitions. *Physical Review Letters*, 96(5):055001, 2006.

[BA53] H.A. Bethe and J. Ashkin. *Passage of Radiations through Matter.* Experimental Nuclear Physics, vol. I. Wiley, New York, 1953.

[BBG+04] E. Breschi, M. Borghesi, M. Galimberti, D. Glulletti, L. A. Gizzi, and L.l Romagnani. A new algorithm for spectral and spatial reconstruction of proton beams from dosimetric measurements. *Nuclear Instruments & Methods In Physics Research Section A-Accelerators Spectrometers Detectors And Associated Equipment*, 522(3):190–195, 2004.

[BCS+02] M. Borghesi, D. H. Campbell, A. Schiavi, M. G. Haines, O. Willi, A. J. MacKinnon, P. Patel, L. A. Gizzi, M. Galimberti, R. J. Clarke, F. Pegoraro, H. Ruhl, and S. Bulanov. Electric field detection in laser-plasma interaction experiments via the proton imaging technique. *Physics Of Plasmas*, 9(5):2214–2220, 2002. Part 2.

[BCZC05] M.J. Berger, J.S. Coursey, M.A. Zucker, and J. Chang. Stopping-power and range tables for electrons protons, and helium ions, 2005. http://www.physics.nist.gov/PhysRefData/Star/Text/contents.html.

[BDGR97] A. R. Bell, J. R. Davies, S. Guerin, and H. Ruhl. Fast-electron transport in high-intensity short-pulse laser-solid experiments. *PLASMA PHYSICS AND CONTROLLED FUSION*, 39(5):653–659, May 1997.

[BKN97] A. Braun, S. Kane, and T. Norris. Compensation of self-phase modulation in chirped-pulse amplification laser systems. *Optics Letters*, 22(9):615–617, May 1997.

[BLN85] M. D. J. Burgess, B. Lutherdavies, and K. A. Nugent. An experimental-study of magnetic-fields in plasmas created by high-intensity one micron laser-radiation. *Physics Of Fluids*, 28(7):2286–2297, 1985.

[BMC$^+$04] M. Borghesi, A. J. Mackinnon, D. H. Campbell, D. G. Hicks, S. Kar, P. K. Patel, D. Price, L. Romagnani, A. Schiavi, and O. Willi. Multi-mev proton source investigations in ultraintense laser-foil interactions. *Physical Review Letters*, 92(5):055003, 2004. 055003.

[BMKB$^+$99] A. Benuzzi-Mounaix, M. Koenig, J. M. Boudenne, T. A. Hall, D. Batani, F. Scianitti, A. Masini, and D. Di Santo. Chirped pulse reflectivity and frequency domain interferometry in laser driven shock experiments. *Phys. Rev. E*, 60(3):R2488–R2491, Sep 1999.

[Boy92] R.W. Boyd. *Nonlinear Optics*. Academic Press, 1992.

[BPS] R. Benattar, C. Popovics, and R. Sigel. Polarized light interferometer for laser fusion studies. *Review of Scientific Instruments*, 50(12):1583.

[Bru87] F. Brunel. Not-so-resonant, resonant absorption. *Physical Review Letters*, 59(1):52, 1987. 00319007 Accession Number: 2974388; Publication Date: 6 July 1987; ISSN: 00319007; Pages: 52-5; CODEN: PRLTAO; Key Phrase Headings: resonant absorption; intense electromagnetic wave; sharply bounded overdense plasma; strong energy absorption; Classification: A5225P Emission, absorption, and scattering of radiation in plasma; A5240D Electromagnetic wave propagation in plasma; Treatment: Experimental; Number of References: 13; Publication Type: Journal Paper; Language: English; Abstract Number: A87117710; Entry Date: 20001012.

[BW75] M. Born and E. Wolf. *Principles of Optics.* Pergamon Press, Oxford, 1975.

[CB97] G. Chabrier and I. Baraffe. Structure and evolution of low-mass stars. *Astronomy and Astrophysics*, 327(3):1039–1053, Nov 1997.

[CDSC+98] G. W. Collins, L. B. Da Silva, P. Celliers, D. M. Gold, M. E. Foord, R. J. Wallace, A. Ng, S. V. Weber, K. S. Budil, and R. Cauble. Measurements of the equation of state of deuterium at the fluid insulator-metal transition. *SCIENCE*, 281(5380):1178–1181, Aug 1998.

[CFR+05] T. E. Cowan, J. Fuchs, H. Ruhl, Y. Sentoku, A. Kemp, P. Audebert, M. Roth, R. Stephens, I. Barton, A. Blazevic, E. Brambrink, J. Cobble, J. C. Fernandez, J. C. Gauthier, M. Geissel, M. Hegelich, J. Kaae, S. Karsch, G. P. Le Sage, S. Letzring, M. Manclossi, S. Meyroneinc, A. Newkirk, H. Pepin, and N. Renard-LeGalloudec. Ultralow emittance, high current proton beams produced with a laser-virtual cathode sheath accelerator. *Nuclear Instruments & Methods In Physics Research Section A-Accelerators Spectrometers Detectors And Associated Equipment*, 544(1-2):277–284, 2005.

[CHGA+01] J. Collier, C. Hernandez-Gomez, R. Allott, C. Danson, and A. Hall. A single-shot third-order autocorrelator for pulse contrast and pulse shape measurements. *Laser And Particle Beams*, 19(2):231–235, Jun 2001.

[CHGR$^+$99] J. Collier, C. Hernandez-Gomez, I. N. Ross, P. Matousek, C. N. Danson, and J. Walczak. Evaluation of an ultrabroadband high-gain amplification technique for chirped pulse amplification facilities. *APPLIED OPTICS*, 38(36):7486–7493, Dec 1999.

[CM78] C.W. Cranfill and R. More. Ioneos: A fast, analytic ion equation-of-state routine. Informal Report LA-7313-MS, Los Alamos National Laboratory, 1978. Online at `http://www.fas.org/sgp/othergov/doe/lanl/lib-www/la-pubs/00309855.html`.

[CM06] J. Clerouin and S. Mazevet. Exploring warm dense matter using quantum molecular dynamics. *Journal De Physique IV*, 133:1071–1075, Jun 2006.

[CoHEDPP03] National Research Council Committee on High Energy Density Plasma Physics, Plasma Science Committee. *Frontiers in High Energy Density Physics: The X-Games of Contemporary Science*. The National Academies Press, 2003.

[CP00] G. H. Chan and W. V. Prestwich. Dose measurement based on spectral chi-square minimization using gafchromic md-55 film. *Physics In Medicine And Biology*, 45(7):1851–1861, 2000.

[CTB82] E. Casnati, A. Tartari, and C. Baraldi. An empirical-approach to k-shell ionization cross-section by electrons. *Journal Of Physics B-Atomic Molecular And Optical Physics*, 15(1):155–167, 1982.

[CZM93] Y. H. Chuang, L. Zheng, and D. D. Meyerhofer. Propagation of light-pulses in a chirped-pulse-amplification laser. *IEEE Journal of Quantum Electronics*, 29(1):270–280, Jan 1993.

[Dap03] Maurizio Dapor. *Electron-Beam Interactions with Solids: Application of the Monte Carlo Method to Electron Scattering Problems.* Springer-Verlag Berlin Heidelberg, 2003.

[Dav01] J. E. Davis. Event pileup in charge-coupled devices. *Astrophysical Journal*, 562(1):575–582, Nov 2001.

[DBHG97] J. R. Davies, A. R. Bell, M. G. Haines, and S. M. Guérin. Short-pulse high-intensity laser-generated fast electron transport into thick solid targets. *Phys. Rev. E*, 56(6):7193–7203, Dec 1997.

[DDK$^+$05] J. P. Davis, C. Deeney, M. D. Knudson, R. W. Lemke, T. D. Pointon, and D. E. Bliss. Magnetically driven isentropic compression to multimegabar pressures using shaped current pulses on the z accelerator. *PHYSICS OF PLASMAS*, 12(5):056310, May 2005.

[Des03] Michael P. Desjarlais. Density-functional calculations of the liquid deuterium hugoniot, reshock, and reverberation timing. *Phys. Rev. B*, 68(6):064204, Aug 2003.

[DLO$^+$00] J. Dunn, Y. Li, A.L. Osterheld, J. Nilsen, J.R. Hunter, and V.N. Shlyaptsev. Gain saturation regime for laser-driven tabletop, transient ni-like ion x-ray lasers. *Physical Review Letters*, 84(21):4834–7, 22 May 2000.

[Dra06] R. P. Drake. *High-Energy-Density Physics: Fundamentals, Inertial Fusion, and Experimental Astrophysics.* Springer-Verlag Berlin Heidelberg, 2006.

[ESS02] F. Ewald, H. Schwoerer, and R. Sauerbrey. K-alpha-radiation from relativistic laser-produced plasmas. *Europhysics Letters*, 60(5):710–716, Dec 2002.

[Fil01] E. E. Fill. Analytical theory of pulsed relativistic electron beams entering a vacuum. *Physics Of Plasmas*, 8(10):4613–4617, 2001.

[Fil04] E. E. Fill. Kinetics of ultrashort relativistic electron pulses emitted from solid targets. *Physical Review E*, 70(3), 2004. Part 2 036409.

[Fil05] E. E. Fill. Ultrashort-pulse laser plasmas: Fraction of hot electrons escaping from the target and electron spectra in planar and spherical geometry. *Physics Of Plasmas*, 12(5):052704, 2005.

[FKL+75] D. W. Forslund, J. M. Kindel, Kenneth Lee, E. L. Lindman, and R. L. Morse. Theory and simulation of resonant absorption in a hot plasma. *Phys. Rev. A*, 11(2):679–683, Feb 1975.

[FMU+01] T. Feurer, A. Morak, I. Uschmann, Ch Ziener, H. Schwoerer, Ch Reich, P. Gibbon, E. Förster, R. Sauerbrey, K. Ortner, and C. R. Becker. Femtosecond silicon k alpha pulses from laser-produced plasmas. *Physical Review E*, 65(1):016412, 2001. Copyright (C) 2006 The American Physical Society Please report any problems to prolaaps.org PRE.

[FRS04] M. E. Foord, D. B. Reisman, and P. T. Springer. Determining the equation-of-state isentrope in an isochoric heated plasma. *Review Of Scientific Instruments*, 75(8):2586–2589, 2004.

[FWS+98] D. N. Fittinghoff, B. C. Walker, J. A. Squier, C. S. Toth, C. Rose-Petruck, and C. P. J. Barty. Dispersion considerations in ultrafast cpa systems. *IEEE Journal of Selected Topics In Quantum Electronics*, 4(2):430–440, Mar-Apr 1998.

[Gaf] Gafchromic$^{\mathrm{TM}}$md-55 radiochromic dosimetry film for high-energy photons: Configuration, specifications, and performance data.

online at `http://www.ispcorp.com//products/dosimetry/content/gafchromic/index.html`.

[GAR$^{+}$96] J. P. Geindre, P. Audebert, A. Rousse, J. C. Gauthier, A. Y. Faenov, T. A. Pikuz, S. A. Pikuz, and T. A. Shelkovenko. Fssr mica spherical crystal spectrometer with ccd detector for high-resolution x-ray spectroscopy of femtosecond laser produced plasma. *Physica Scripta*, 53(6):645–647, Jun 1996.

[GAR$^{+}$01] J. P. Geindre, P. Audebert, S. Rebibo, G. Grillon, Chambaret J.-P., and J. C. Gauthier. Single-shot spectral interferometry of femtosecond laser-produced plasmas. *Laser And Particle Beams*, 19:67–73, 2001.

[GB92] Paul Gibbon and A. R. Bell. Collisionless absorption in sharp-edged plasmas. *Phys. Rev. Lett.*, 68(10):1535–1538, Mar 1992.

[GF96] P Gibbon and E Förster. Short-pulse laser - plasma interactions. *Plasma Physics and Controlled Fusion*, 38(6):769–793, 1996.

[GG02] Fran çois Gygi and Giulia Galli. Electronic excitations and the compressibility of deuterium. *Phys. Rev. B*, 65(22):220102, Jun 2002.

[Gin64] V. L. Ginzburg. *The Propagation of Electromagnetic Waves in Plasmas.* Pengram, 1964.

[GP98] D.C. Ghiglia and M.D. Pritt. *Two-Dimensional Phase Unwrapping: Theory, Algorithms, and Software.* John Wiley and Sons, Inc., 1998.

[Gro71] R. Grover. Liquid metal equation of state based on scaling. *Journal of Chemical Physics*, 55(7):p3435 – 3441, 1971.

[GSWB01] T. Guo, C. Spielmann, B. C. Walker, and C. P. J. Barty. Generation of hard x rays by ultrafast terawatt lasers. *REVIEW OF SCIENTIFIC INSTRUMENTS*, 72(1):41–47, Jan 2001.

[GZK$^+$06] P. M. Gu, B. Zhang, M. H. Key, S. P. Hatchett, T. Barbee, R. R. Freeman, K. Akli, D. Hey, J. A. King, A. J. Mackinnon, R. A. Snavely, and R. B. Stephens. Measurements of electron and proton heating temperatures from extreme-ultraviolet light images at 68 ev in petawatt laser experiments. *Review of Scientific Instruments*, 77(11):113101, Nov 2006.

[HAC$^+$06] B. M. Hegelich, B. J. Albright, J. Cobble, K. Flippo, S. Letzring, M. Paffett, H. Ruhl, J. Schreiber, R. K. Schulze, and J. C. Fernandez. Laser acceleration of quasi-monoenergetic mev ion beams. *NATURE*, 439(7075):441–444, Jan 2006.

[HEF$^+$07] J. F. Hansen, M. J. Edwards, D. H. Froula, A. D. Edens, G. Gregori, and T. Ditmire. Laboratory observation of secondary shock formation ahead of a strongly radiative blast wave. *ASTROPHYSICS AND SPACE SCIENCE*, 307(1-3):219–225, Jan 2007.

[Hem79] W. F. Hemsing. Velocity sensing interferometer (visar) modification. *Review of Scientific Instruments*, 50(1):73–78, 1979.

[HFP$^+$05] S. B. Hansen, A. Ya. Faenov, T. A. Pikuz, K. B. Fournier, R. Shepherd, H. Chen, K. Widmann, S. C. Wilks, Y. Ping, H. K. Chung, A. Niles, J. R. Hunter, G. Dyer, and T. Ditmire. Temperature determination using k alpha spectra from m-shell ti ions. *Physical Review E (Statistical, Nonlinear, and Soft Matter Physics)*, 72(3):036408, 2005.

[HGD01] B. L. Henke, E. M. Gullikson, and J. C. Davis. X-ray interactions: photoabsorption, scattering, transmission, and reflection at e=50-30000 ev, z=1-92. *Atomic Data and Nuclear Data Tables*, 54(2):181–342, 0701. `http://henke.lbl.gov/optical_constants/`.

[HGMD07] G. Hays, E. Gaul, M. Martinez, and T. Ditmire. Novel broad spectrum neodymium doped laser glasses for high-energy chirped-pulse amplification. *Applied Optics*, Accepted for publication April 2007.

[Hol84] K. S. Holian. Sesame eos. Technical Report LA-10160-MS UC-34, Los Alamos National Laboratory, 1984.

[Hom98] C Hombourger. An empirical expression for k-shell ionization cross section by electron impact. *Journal of Physics B: Atomic, Molecular and Optical Physics*, 31(16):3693–3702, 1998.

[HRJ$^+$70] W.G. Hoover, M. Ross, K.W. Johnson, D. Henderson, J.A. Barker, and B.C. Brown. Soft-sphere equation of state. *Journal of Chemical Physics*, 52(10):p4931 – 4941, 1970.

[HSGD75] W.G. Hoover, G. Stell, E. Goldmark, and G.D. Degani. Generalized van der waals equation of state. *Journal of Chemical Physics*, 63(12):p5434 – 5438, 1975.

[Hua87] K. Huang. *Statistical Mechanics.* John Wiley & Sons, New York, 1987.

[HUB81] W. B. HUBBARD. Interiors of the giant planets. *SCIENCE*, 214(4517):145–149, 1981.

[Hub00] J.D. Huba. Nrl plasma formulary. Naval Research Laboratory, 2000.

[Hut87] I.H. Hutchinson. *Principles of Plasma Diagnostics.* Cambridge Univesity Press, New York, 1987.

[HVC$^+$02] D. L. Hanson, R. A. Vesey, M. E. Cuneo, J. L. Porter, G. A. Chandler, L. E. Ruggles, W. W. Simpson, J. Torres, J. McGurn, D. Hebron, S. C. Dropinski, J. H. Hammer, G. R. Bennett, H. Seaman, T. L. Gilliland, and D. G. Schroen. Measurement of radiation symmetry in z-pinch-driven hohlraums. *Physics of Plasmas*, 9(5):2173–2181, May 2002.

[HW98] R.D. Hazeltine and F.L. Waelbroeck. *The Framework of Plasma Physics.* Perseus Books, 1998.

[Ich82] S. Ichimaru. Strongly coupled plasmas - high-density classical plasmas and degenerate electron liquids. *Reviews of Modern Physics*, 54(4):1017–1059, 1982.

[IIT87] S. Ichimaru, H. Iyetomi, and S. Tanaka. Statistical physics of dense-plasmas - thermodynamics, transport-coefficients and dynamic correlations. *Physics Reports-Review Section Of Physics Letters*, 149(2-3):91–205, May 1987.

[Inc02] Sumita Optical Glass Inc. Optical glass data book version 3.03, 2002.

[Jac98] John David Jackson. *Classical Electrodynamics.* John Wiley and Sons, Inc., 1998.

[KHB$^+$04] M. D. Knudson, D. L. Hanson, J. E. Bailey, C. A. Hall, J. R. Asay, and C. Deeney. Principal hugoniot, reverberating wave, and mechanical reshock measurements of liquid deuterium to 400 gpa using plate impact techniques. *PHYSICAL REVIEW B*, 69(14):144209, Apr 2004.

[Kit58] *Kittel, Charles.* Dover Publications, 1958.

[KKF$^+$02] J. A. Koch, M. H. Key, R. R. Freeman, S. P. Hatchett, R. W. Lee, D. Pennington, R. B. Stephens, and M. Tabak. Experimental measurements of deep directional columnar heating by laser-generated relativistic electrons at near-solid density. *Physical Review E (Statistical, Nonlinear, and Soft Matter Physics)*, 65(1):016410/1, 2002.

[KM59] H. W. KOCH and J. W. MOTZ. Bremsstrahlung cross-section formulas and related data. *Rev. Mod. Phys.*, 31(4):920–955, Oct 1959.

[KM98] O. A. Konoplev and D. D. Meyerhofer. Cancellation of b-integral accumulation for cpa lasers. *IEEE Journal of Selected Topics In Quantum Electronics*, 4(2):459–469, Mar-Apr 1998.

[Kne05] Stephan Kneip. X-ray and hot electron enhancement with advanced targets irradiated by ultra-high intensity laser. Master's thesis, University of Texas at Austin, 2005.

[KNM$^+$01] R. Kodama, P. A. Norreys, K. Mima, A. E. Dangor, R. G. Evans, H. Fujita, Y. Kitagawa, K. Krushelnick, T. Miyakoshi, N. Miyanaga, T. Norimatsu, S. J. Rose, T. Shozaki, K. Shigemori, A. Sunahara, M. Tampo, K. A. Tanaka, Y. Toyama, T. Yamanaka, and M. Zepf. Fast heating of ultrahigh-density plasma as a step towards laser fusion ignition. *Nature*, 412(6849):798, 2001.

[Kog] U. Kogelschatz. Application of a simple differential interferometer to high current arc discharges. *Applied Optics*, 13(8):1749.

[Kra01] M. O. Krause. Atomic radiative and radiationless yields for k and l shells. *Journal of Physical and Chemical Reference Data*, 8(2):307–327, 0101.

[Kru88] William L. Kruer. *The Physics of Laser Plasma Interactions.* Addison-Wesley, 1988.

[LBC$^+$01] R. W. Lee, H. A. Baldis, R. C. Cauble, O. L. Landen, J. S. Wark, A. Ng, S. J. Rose, C. Lewis, D. Riley, J. C. Gauthier, and P. Audebert. Plasma-based studies on 4$^{\text{th}}$ generation light sources. In *AIP Conference Proceedings*, volume 581, page 45, Arcidosso, Italy, 2001.

[LBKC00] Thomas J. Lenosky, Scott R. Bickham, Joel D. Kress, and Lee A. Collins. Density-functional calculation of the hugoniot of shocked liquid deuterium. *Phys. Rev. B*, 61(1):1–4, Jan 2000.

[LIN95] J. LINDL. Development of the indirect-drive approach to inertial confinement fusion and the target physics basis for ignition and gain. *PHYSICS OF PLASMAS*, 2(11):3933–4024, Nov 1995.

[LL94] J. T. LARSEN and S. M. LANE. Hyades - a plasma hydrodynamics code for dense-plasma studies. *J. Quant. Spectrosc. Ra*, 51(1-2):179–186, Jan-Feb 1994.

[LMC92] J. D. LINDL, R. L. MCCRORY, and E. M. CAMPBELL. Progress toward ignition and burn propagation in inertial confinement fusion. *PHYSICS TODAY*, 45(9):32–40, Sep 1992.

[LMHK$^+$03] R. W. Lee, S. J. Moon, Chung Hyun-Kyung, W. Rozmus, H. A. Baldis, G. Gregori, R. C. Cauble, O. L. Landen, J. S. Wark, A. Ng, S. J. Rose, C. L. Lewis, D. Riley, J. C. Gauthier, and P. Audebert. Finite temperature dense matter studies on next-generation light sources. *Journal of the Optical Society of America B (Optical Physics)*, 20(4):770, 2003.

[MAD$^+$02] P. Monot, T. Auguste, S. Dobosz, P. D'Oliveira, S. Hulin, M. Bougeard, A. Ya. Faenov, T. A. Pikuz, and I. Yu. Skobelev. High-sensitivity, portable, tunable imaging x-ray spectrometer based on a spherical crystal and mcp. *Nuclear Instruments & Methods in Physics Research Section A: Accelerators, Spectrometers, Detectors and Associated Equipment*, 484(1-3):299–311, 2002.

[Mah02] J.R. Mahan. *Radiation Heat Transfer: A Statistical Approach.* John Wiley & Sons, New York, 2002.

[Mal04] Alexandre S. Maltsev. Above threshold ionization with ultrahigh intensity laser light. Master's thesis, The University of Texas at Austin, 2004.

[Mar00] M. P. Marder. *Condensed Matter Physics.* Wiley, New York, 2000.

[May77] J.E. Mayer. *Statistical Mechanics.* John Wiley & Sons, New York, 2 edition, 1977.

[May94] F. Mayinger. *Optical measurements : techniques and applications*, page 77. Berlin ; New York : Springer-Verlag, 1994.

[MBH$^+$01] A. J. Mackinnon, M. Borghesi, S. Hatchett, M. H. Key, P. K. Patel, H. Campbell, A. Schiavi, R. Snavely, S. C. Wilks, and O. Willi. Effect of plasma scale length on multi-mev proton production by intense laser pulses. *Physical Review Letters*, 86(9):1769–1772, 2001.

[McC82] G.H. McCall. Calculation of x-ray bremsstrahlung and characteristic line emission produced by maxwellian electron distribution. *J. Phys. D*, 15:823–831, 1982.

[MF89] H. M. Milchberg and R. R. Freeman. Light-absorption in ultrashort scale length plasmas. *Journal of the Optical Society of America B (Optical Physics)*, 6(7):1351–1355, Jul 1989.

[MGA$^+$01] S. V. Milton, E. Gluskin, N. D. Arnold, C. Benson, W. Berg, S. G. Biedron, M. Borland, Y. C. Chae, R. J. Dejus, P. K. Den Hartog, B. Deriy, M. Erdmann, Y. I. Eidelmann, M. W. Hahne, Z. Huang, K. J. Kim, J. W. Lewellen, Y. Li, A. H. Lumpkin, O. Makarov, E. R. Moog, A. Nassiri, V. Sajaev, R. Soliday, B. J. Tieman, E. M. Trakhtenberg, G. Travish, I. B. Vasserman, N. A. Vinokurov, X. J. Wang, G. Wiemerslage, and B. X. Yang. Exponential gain and saturation of a self-amplified spontaneous emission free-electron laser. *Science*, 292(5524):2037–2041, Jun 2001.

[MM96] G. Malka and J. L. Miquel. Experimental confirmation of ponderomotive-force electrons produced by an ultrarelativistic laser pulse on a solid target. *Phys. Rev. Lett.*, 77(1):75–78, Jul 1996.

[MNG$^+$04] M. J. Mead, D. Neely, J. Gauoin, R. Heathcote, and P. Patel. Electromagnetic pulse generation within a petawatt laser target chamber. *Review of Scientific Instruments*, 75(10):4225–4227, Oct 2004.

[MNP$^+$00] W. Mroz, P. Norek, A. Prokopiuk, P. Parys, M. Pfeifer, L. Laska, M. P. Stockli, D. Fry, and K. Kasuya. Method of processing ion energy distributions using a thomson parabola ion spectrograph with a microchannelplate image converter camera. *Review of Scientific Instruments*, 71(3):1417–1420, Mar 2000.

[Mon84] V. Montoya. *T-4 Handbook of Material Properties Data Bases, Vol Ic: Equations of State.* Los Alamos National Laboratory, 1984.

Online at `fas.org/sgp/othergov/doe/lanl/lib-www/la-pubs/00321144.pdf`.

[Mor91] R. M. More. Atomic physics of laser-produced plasma. In A. M. Rubenchik and Witkowski, editors, *Physics of Laser Plasma*, volume 3 of *Handbook of Plasma Physics*. Elsevier Science Publishing Company, Inc., NY, 1991.

[MPT$^+$04] A. J. Mackinnon, P. K. Patel, R. P. Town, M. J. Edwards, T. Phillips, S. C. Lerner, D. W. Price, D. Hicks, M. H. Key, S. Hatchett, S. C. Wilks, M. Borghesi, L. Romagnani, S. Kar, T. Toncian, G. Pretzler, O. Willi, M. Koenig, E. Martinolli, S. Lepape, A. Benuzzi-Mounaix, P. Audebert, J. C. Gauthier, J. King, R. Snavely, R. R. Freeman, and T. Boehlly. Proton radiography as an electromagnetic field and density perturbation diagnostic (invited). *Review Of Scientific Instruments*, 75(10):3531–3536, 2004. Part 2.

[MR79] A.K. McMahan and M. Ross. *High-Pressure Science and Technology*. Plenum, NY, 1979.

[MSB$^+$88] P. Maine, D. Strickland, P. Bado, M. Pessot, and G. Mourou. Generation of ultrahigh peak power pulses by chirped pulse amplification. *IEEE Journal of Quantum Electronics*, 24(2):398–403, Feb 1988.

[MSP$^+$02] A. J. Mackinnon, Y. Sentoku, P. K. Patel, D. W. Price, S. Hatchett, M. H. Key, C. Andersen, R. Snavely, and R. R. Freeman. Enhancement of proton acceleration by hot-electron recirculation in thin foils irradiated by ultraintense laser pulses. *Physical Review Letters*, 88(21):215006, 2002. 215006.

[MWYZ88] R. M. More, K. H. Warren, D. A. Young, and G. B. Zimmerman. A new quotidian equation of state (qeos) for hot dense matter. *Physics Of Fluids*, 31(10):3059–3078, 1988.

[MYS$^+$91] W.L. McLaughlin, C. Yundong, C.G. Soares, A. Miller, G. Vandyk, and D.F. Lewis. Sensitometry of the response of a new radiochromic film dosimeter to gamma-radiation and electron-beams. *Nuclear Instruments & Methods In Physics Research Section A-Accelerators Spectrometers Detectors And Associated Equipment*, 302(1):165–176, Apr 1991.

[NAP$^+$05] A. Ng, T. Ao, F. Perrot, M. W. C. Dharma-Wardana, and M. E. Foord. Idealized slab plasma approach for the study of warm dense matter. *Laser And Particle Beams*, 23(4):527–537, 2005.

[Ng:02] *IEEE Conference Record - Abstracts. 2002 IEEE International Conference on Plasma Science (Cat. No.02CH37340).* IEEE, 2002.

[Ng07] A. Ng. Titan leads the way in laser matter science, January 2007.

[NIT$^+$98] M. Nantel, J. Itatani, A. C. Tien, J. Faure, D. Kaplan, M. Bouvier, T. Buma, P. Van Rompay, J. Nees, P. P. Pronko, D. Umstadter, and G. A. Mourou. Temporal contrast in ti : Sapphire lasers: Characterization and control. *IEEE Journal of Selected Topics In Quantum Electronics*, 4(2):449–458, Mar-Apr 1998.

[NKNM04] T. Nakamura, S. Kato, H. Nagatomo, and K. Mima. Surface-magnetic-field and fast-electron current-layer formation by ultraintense laser irradiation. *Physical Review Letters*, 93(26), 2004. 265002.

[OCR$^+$05] K. Osvay, M. Csatari, I. N. Ross, A. Persson, and C. G. Wahlstrom. On the temporal contrast of high intensity femtosecond laser pulses. *LASER AND PARTICLE BEAMS*, 23(3):327–332, Sep 2005.

[PCC$^+$99] T. W. Phillips, M. D. Cable, T. E. Cowan, S. P. Hatchett, E. A. Henry, M. H. Key, M. D. Perry, T. C. Sangster, and M. A. Stoyer. Diagnosing hot electron production by short pulse, high intensity lasers using photonuclear reactions. *Review of Scientific Instruments*, 70(1):1213–1216, Jan 1999.

[PDS94] M. D. Perry, T. Ditmire, and B. C. Stuart. Self-phase modulation in chirped pulse amplificiation. *Optics Letters*, 19(24):2149–2151, Dec 1994.

[PHA$^+$01] A. Poppe, R. Holzwarth, A. Apolonski, G. Tempea, C. Spielmann, T. W. Hansch, and F. Krausz. Few-cycle optical waveform synthesis. *Applied Physics B - Lasers and Optics*, 72(3):373–376, Feb 2001.

[PHK$^+$06] Y. Ping, D. Hanson, I. Koslow, T. Ogitsu, D. Prendergast, E. Schwegler, G. Collins, and A. Ng. Broadband dielectric function of nonequilibrium warm dense gold. *Physical Review Letters*, 96(25), 2006. 255003.

[PIK$^+$04] H. S. Park, N. Izumi, M. H. Key, J. A. Koch, O. L. Landen, P. K. Patel, T. W. Phillips, and B. B. Zhang. Characteristics of high energy k alpha and bremsstrahlung sources generated by short pulse petawatt lasers. *Review of Scientific Instruments*, 75(10):4048–4050, Oct 2004.

[PMK$^+$03] P. K. Patel, A. J. Mackinnon, M. H. Key, T. E. Cowan, M. E. Foord, M. Allen, D. F. Price, H. Ruhl, P. T. Springer, and R. Stephens.

Isochoric heating of solid-density matter with an ultrafast proton beam. *Physical Review Letters*, 91(12):125004, 2003.

[PTL$^+$81] R.H. Pratt, H.K. Tseng, C.M. Lee, L. Kissel, C. MacCallum, and M. Riley. Bremsstrahlung energy spectra from electrons of kinetic energy 1 kev $\geq$ T$_1$ $\geq$ 2000 kev incident on neutral atoms 2 $\geq$ Z $\geq$ 92. *Atomic Data Nucl. Data Tables*, 20(175), 1981. Errata in 26, 477.

[Puk01] A. Pukhov. Three-dimensional simulations of ion acceleration from a foil irradiated by a short-pulse laser. *Phys. Rev. Lett.*, 86(16):3562–3565, Apr 2001.

[QEA02] B. L. Qian and H. E. Elsayed-Ali. Electron pulse broadening due to space charge effects in a photoelectron gun for electron diffraction and streak camera systems. *Journal of Applied Physics*, 91(1):462–468, Jan 2002.

[RD73] F. J. Rogers and H. E. DeWitt. Statistical mechanics of reacting coulomb gases. *Phys. Rev. A*, 8(2):1061–1076, Aug 1973.

[Rei98] L. E. Reichl. *A Modern Course in Statistical Physics.* John Wiley and Sons Inc., New York, 2 edition, 1998.

[RGUF00] C. Reich, P. Gibbon, I. Uschmann, and E. Forster. Yield optimization and time structure of femtosecond laser plasma k alpha sources. *Physical Review Letters*, 84(21):4846–4849, 2000.

[RKPdS$^+$06] D. Riley, F. Y. Khattak, O. A. M. B. Percie du Sert, R. J. Clarke, E. J. Divall, M. Edwards, P. S. Foster, C. J. Hooker, A. J. Langley, P. Mistry, D. Neely, J. Smith, C. Spindloe, G. J. Tallents, and M. Tolley. Efficient k-[alpha] and he-[alpha] emission from ti foils irradiated with 400 nm, 45 fs laser pulses. *Journal of Quantitative Spectroscopy and Radiative Transfer*, 99(1-3):537–547, 2006.

[RM06] S. D. Rothman and J. Maw. Characteristics analysis of isentropic compression experiments (ice). *Journal De Physique IV*, 134:745–750, Aug 2006.

[Rog00] F. J. Rogers. Ionization equilibrium and equation of state in strongly coupled plasmas. *Physics of Plasmas*, 7(1):51–58, Jan 2000.

[Ros80] M. Ross. Extension of liquid-metal theory to dense partially ionized plasmas. *Physical Review B (Condensed Matter)*, 21:3140–3151, April 1980.

[Rou62] C. A. Rouse. Ionization-Equilibrium Equation of State. III. Results with Debye-Hückel Corrections and Planck's Partition Function. *Astrophysical Journal*, 136:636, September 1962. Available online without subscription: Provided by the Smithsonian/NASA Astrophysics Data System.

[RY97] F. J. Rogers and D. A. Young. Validation of the activity expansion method with ultrahigh pressure shock equations of state. *Physical Review E*, 56(5):5876–5883, 1997. Part B.

[SAB$^+$04] R. Shepherd, P. Audebert, R. Booth, B. Young, J. Bonlie, D. Nelson, S. Shiromizu, D. Price, D. Norman, J. Dunn, K. Widmann, and P. Springer. Time resolved spectroscopy of ultrashort pulse laser generated x rays using von hamos crystal spectroscopy. *Review of Scientific Instruments*, 75(10):3765–3767, Oct 2004.

[SB85] S. M. SELTZER and M. J. BERGER. Bremsstrahlung spectra from electron interactions with screened atomic-nuclei and orbital electrons. *NUCLEAR INSTRUMENTS & METHODS IN PHYSICS RESEARCH SECTION B-BEAM INTERACTIONS WITH MATERIALS AND ATOMS*, 12(1):95–134, 1985.

[SBP+95] R. Shepherd, R. Booth, D. Price, M. Bowers, D. Swan, J. Bonlie, B. Young, J. Dunn, B. White, and R. Stewart. Ultrafast x-ray streak camera for use in ultrashort laser-produced plasma research. *Review of Scientific Instruments*, 66(1):719–721, Jan 1995.

[SFH+96] B. C. Stuart, M. D. Feit, S. Herman, A. M. Rubenchik, B. W. Shore, and M. D. Perry. Nanosecond-to-femtosecond laser-induced breakdown in dielectrics. *Phys. Rev. B*, 53(4):1749–1761, Jan 1996.

[SFH+04] J. Stein, E. Fill, D. Habs, G. Pretzler, and K. Witte. Hot electron diagnostics using x-rays and cerenkov radiation. *LASER AND PARTICLE BEAMS*, 22(3):315–321, Sep 2004.

[SGJ+06] C. Stoeckl, V. Y. Glebov, P. A. Jaanimagi, J. P. Knauer, D. D. Meyerhofer, T. C. Sangster, M. Storm, S. Sublett, W. Theobald, M. H. Key, A. J. MacKinnon, P. Patel, D. Neely, and P. A. Norreys. Operation of target diagnostics in a petawatt laser environment (invited). *Review of Scientific Instruments*, 77(10):10F506, Oct 2006.

[Sie86] A.E. Siegman. *Lasers.* University Science Books, 1986.

[SKH+00] R. A. Snavely, M. H. Key, S. P. Hatchett, T. E. Cowan, M. Roth, T. W. Phillips, M. A. Stoyer, E. A. Henry, T. C. Sangster, M. S. Singh, S. C. Wilks, A. MacKinnon, A. Offenberger, D. M. Pennington, K. Yasuike, A. B. Langdon, B. F. Lasinski, J. Johnson, M. D. Perry, and E. M. Campbell. Intense high-energy proton beams from petawatt-laser irradiation of solids. *Physical Review Letters*, 85(14):2945–2948, 2000.

[SM85] D. Strickland and G. Mourou. Compression of amplified chirped optical pulses. *Optics Communications*, 55(6):447–449, 1985.

[SMR$^+$04] Y. Sentoku, K. Mima, H. Ruhl, Y. Toyama, R. Kodama, and T. E. Cowan. Laser light and hot electron micro focusing using a conical target. *Physics of Plasmas*, 11(6):3083, 2004.

[SMV$^+$96] J. M. Soures, R. L. McCrory, C. P. Verdon, A. Babushkin, R. E. Bahr, T. R. Boehly, R. Boni, D. K. Bradley, D. L. Brown, R. S. Craxton, J. A. Delettrez, W. R. Donaldson, R. Epstein, P. A. Jaanimagi, S. D. Jacobs, K. Kearney, R. L. Keck, J. H. Kelly, T. J. Kessler, R. L. Kremens, J. P. Knauer, S. A. Kumpan, S. A. Letzring, D. J. Lonobile, S. J. Loucks, L. D. Lund, F. J. Marshall, P. W. McKenty, D. D. Meyerhofer, S. F. B. Morse, A. Okishev, S. Papernov, G. Pien, W. Seka, R. Short, M. J. Shoup, M. Skeldon, S. Skupsky, A. W. Schmid, D. J. Smith, S. Swales, M. Wittman, and B. Yaakobi. Direct-drive laser-fusion experiments with the omega, 60-beam, ¿40 kj, ultraviolet laser system. *Physics of Plasmas*, 3(5):2108–2112, May 1996.

[SRU$^+$02] D. Salzmann, Ch Reich, I. Uschmann, E. Forster, and P. Gibbon. Theory of ka generation by femtosecond laser-produced hot electrons in thin foils. *Physical Review E (Statistical, Nonlinear, and Soft Matter Physics)*, 65(3):036402/1, 2002.

[SSB82] R. M. Sternheimer, S. M. Seltzer, and M. J. Berger. Density effect for the ionization loss of charged particles in various substances. *Phys. Rev. B*, 26(11):6067–6076, Dec 1982.

[STS$^+$04] C. Stoeckl, W. Theobald, T. C. Sangster, M. H. Key, P. Patel, B. B. Zhang, R. Clarke, S. Karsch, and P. Norreys. Operation of a single-photon-counting x-ray charge-coupled device camera spectrometer in a petawatt environment. *Review of Scientific Instruments*, 75(10):3705–3707, Oct 2004.

[SYN$^+$06] T. Sasaki, Y. Yano, M. Nakajima, T. Kawamura, and K. Horioka. Warm-dense-matter studies using pulse-powered wire discharges in water. *Laser And Particle Beams*, 24(3):371–380, Sep 2006.

[TIK82] M. Takeda, H. Ina, and S. Kobayashi. Fourier-transform method of fringe-pattern analysis for computer-based topography and interferometry. *Journal Of The Optical Society Of America*, 72(1):156–160, 1982.

[Tra83] K. S. Trainor. Construction of a wide-range tabular equation of state for copper. *Journal of Applied Physics*, 54(5):2372–2379, 1983.

[Vau86] D. Vaughan. X-ray data booklet. Technical Information Department, Lawrence Berkeley Laboratory, Berkeley, California 94720, 1986. Available online at: http://xdb.lbl.gov/.

[WAF$^+$04] K. Widmann, T. Ao, M. E. Foord, D. F. Price, A. D. Ellis, P. T. Springer, and A. Ng. Single-state measurement of electrical conductivity of warm dense gold. *Physical Review Letters*, 92(12):125002, 2004. 125002.

[WBK$^+$01] K. B. Wharton, C. D. Boley, A. M. Komashko, A. M. Rubenchik, J. Zweiback, J. Crane, G. Hays, T. E. Cowan, and T. Ditmire. Effects of nonionizing prepulses in high-intensity laser-solid interactions. *Phys. Rev. E*, 64(2):025401, Jul 2001.

[WGF+01] K. Widmann, G. Guethlein, M. E. Foord, R. C. Cauble, F. G. Patterson, D. F. Price, F. J. Rogers, P. T. Springer, R. E. Stewart, A. Ng, T. Ao, and A. Forsman. Interferometric investigation of femtosecond laser-heated expanded states. *Physics Of Plasmas*, 8(9):3869–3872, 2001.

[WHW+98] K. B. Wharton, S. P. Hatchett, S. C. Wilks, M. H. Key, J. D. Moody, V. Yanovsky, A. A. Offenberger, B. A. Hammel, M. D. Perry, and C. Joshi. Experimental measurements of hot electrons generated by ultraintense ($> 10^{19} w/cm^2$) laser-plasma interactions on solid-density targets. *PHYSICAL REVIEW LETTERS*, 81(4):822–825, Jul 1998.

[WK97] S. C. Wilks and W. L. Kruer. Absorption of ultrashort, ultra-intense laser light by solids and overdense plasmas. *IEEE JOURNAL OF QUANTUM ELECTRONICS*, 33(11):1954–1968, Nov 1997.

[WLC+01] S. C. Wilks, A. B. Langdon, T. E. Cowan, M. Roth, M. Singh, S. Hatchett, M. H. Key, D. Pennington, A. MacKinnon, and R. A. Snavely. Energetic proton generation in ultra-intense laser-solid interactions. *Physics Of Plasmas*, 8(2):542–549, 2001.

[WR] Inc. Wolfram Research. Optica mathematica package.

[YB83] B. Yaakobi and A. J. Burek. Crystal diffraction systems for x-ray spectroscopy, imaging, and interferometry of laser fusion-targets. *IEEE Journal of Quantum Electronics*, 19(12):1841–1854, 1983.

[YJKK99] J. Yu, Z. Jiang, J. C. Kieffer, and A. Krol. Hard x-ray emission in high intensity femtosecond laser-target interaction. *PHYSICS OF PLASMAS*, 6(4):1318–1322, Apr 1999.

[YMUM06] H. Yoneda, H. Morikami, K. Ueda, and R. M. More. Ultra-short pulse laser pump-probe experiments for investigation of warm dense plasmas. *Journal Of Quantitative Spectroscopy & Radiative Transfer*, 99(1-3):690–696, May-Jun 2006.

[ZBD00] M. R. Zaghloul, M. A. Bourham, and J. M. Doster. A simple formulation and solution strategy of the saha equation for ideal and nonideal plasmas. *Journal Of Physics D-Applied Physics*, 33(8):977–984, 2000.

[ZHMK95] J. P. Zhou, C. P. Huang, M. M. Murnane, and H. C. Kapteyn. Amplification of 26-fs, 2-tw pulses near the gain-narrowing limit in ti-sapphire. *Optics Letters*, 20(1):64–66, Jan 1995.

[ZR66] Y. B. Zeldovich and Y. P. Raizer. *Physics of Shock Waves and High-Temperature Hydrodynamic Phenomena.* Academic Press, New York, 1966.

# Vita

Gilliss McNaughton Dyer was born in Lihue, Hawaii on August 18, 1978, the son of Michael and Charlene Dyer. After completing his work at Iolani High School, Honolulu, Hawaii he entered New College of the University of South Florida in Sarasota, Florida where he majored in Mathematics and Physics. In fall of 2000 he entered the Physics graduate program of the University of Texas at Austin.

Permanent Address: 1904 Rosetti Dr. Austin TX 78752

This dissertation was typeset with $\LaTeX\,2_\varepsilon$[1] by the author.

---

[1] $\LaTeX\,2_\varepsilon$ is an extension of $\LaTeX$. $\LaTeX$ is a collection of macros for $\TeX$. $\TeX$ is a trademark of the American Mathematical Society. The macros used in formatting this dissertation were written by Dinesh Das, Department of Computer Sciences, The University of Texas at Austin, and extended by Bert Kay, James A. Bednar, and Ayman El-Khashab.